

**Static, Dynamic and Levitation  
Characteristics of Squeeze Film  
Air Journal Bearing: Designing,  
Modelling, Simulation and Fluid Solid  
Interaction**

A thesis submitted for the degree of  
Doctor of Philosophy

by

**Chao Wang**

School of Engineering and Design

Brunel University

**Abstract**

**July 2011**

## **Abstract**

## **Abstract**

Bearings today need to be able to run at very high speed, providing high positional accuracy for the structure that it supports, and requiring very little or no maintenance. For this to happen, bearings must have tight tolerances and very low or zero friction during operation. This pushes many traditional contact-type bearings to their limits as they often fail due to friction, generating heat and causing wear.

By comparison, existing non-contact bearings fare better because of their very low or zero friction. But some have their own problem too. For example, the fact that aerostatic bearings require an air supply means having to use a separate air compressor and connecting hoses. This makes the installation bulky. Aerodynamic and hydrodynamic bearings cannot support loads at zero speed. Both hydrodynamic and hydrostatic bearings may cause contamination to the work-pieces and the work environment because of the use of lubricating fluid.

A potential solution to the above-mentioned problems is the new squeeze film air bearing. It works on the rapid squeeze action of an air film to produce separation between two metal surfaces. This has the benefit of being compact with a very simple configuration because it does not require an external pressurized air supply, can support loads at zero speed and is free of contamination.

For this research, two squeeze film air journal bearings, made from material of Al 2024 – T3 and Cu - C101 with the same geometry, were designed. The bearing is in the shape of a round tube with three fins on the outer surface and the journal, a round rod. When excited at a certain normal mode, the bearing shell flexes with a desirable modal shape for the squeeze film action. The various modes of vibration of Al bearing were obtained from a finite-element model implemented in ANSYS. Two Modes, the 13<sup>th</sup> and 23<sup>rd</sup>, at the respective frequencies of 16.320 kHz and 25.322 kHz, were identified for further investigation by experiments with respect to the squeeze film thickness and its load-carrying capacity. For Cu bearing, the two Modes are also 13<sup>th</sup> and 23<sup>rd</sup> at the respective frequencies of 12.184 kHz and 18.459 kHz.

## **Abstract**

In order to produce dynamic deformation of the bearings at their modes, a single layer piezoelectric actuator was used as a driver. The maximum stroke length and the maximum blocking force of the single layer piezoelectric actuator were determined using manual calculation and ANSYS simulation.

In the coupled-field analysis, the single layer piezoelectric actuator was mounted on the outside surface of the bearing shell and loaded with an AC and a DC voltage in order to produce the static and dynamic deformation. For the static analysis, the maximum deformation of Al bearing shell is  $0.124\ \mu\text{m}$  when the actuators are driven at the DC of 75 V. For the dynamic analysis, the actuators are driven at three levels of AC, namely 55, 65 and 75V with a constant DC offset of 75V and the driving frequency coincided with the modal frequency of the bearing. The maximum dynamic deformation of Al bearing shell is  $3.22\ \mu\text{m}$  at Mode 13 and  $2.08\ \mu\text{m}$  at Mode 23 when the actuators were driven at the AC of 75 V and the DC of 75 V. Similarly, the FEA simulation was used for analyzing Cu bearing. Furthermore, the dynamic deformation of both Al and Cu bearing at Mode 13 and 23 are validated by experiments.

This research developed two theoretical models that explain the existence of a net pressure in a squeeze film for the levitation. The first model uses the ideal gas law as first approximation whilst the second uses the CFX simulation to provide a more exact explanation.

In terms of the load-carrying capacity, Mode 13 was identified to be better than Mode 23 for both bearings. However, at Mode 13, Al bearing has a higher load-carrying capacity than Cu bearing. This is due to Al bearing having a higher modal frequency and amplitude.

Finally, the coupled-field analysis for fluid solid interaction (FSI) was studied at both Mode 13 and 23 for Al bearing. The findings are that: a) the fluid force in the squeeze film can affect the dynamic deformation of the bearing shell, especially at high oscillation frequency, more at Mode 13 than at Mode 23 due to the relatively high pressure end-leakage in the latter; b) the dynamic deformation of the bearing shell

**Abstract**

increases with the gap clearance in a logarithmic manner at Mode 13; and c) the micron levels of gap clearance provide a damping effect on the dynamic deformation of the bearing shell at Mode 13 and at Mode 23, though much less dominant.

## **Acknowledgements**

# **Acknowledgements**

First of all I would like to express my deepest gratitude to Dr. Y. H. Joe Au for his excellent supervision of my PhD research. I really appreciate his valuable comments, constant support and guidance, and encouragement to complete my research work and to write up the thesis. He has also given me many opportunities to work on related industrial projects to broaden my knowledge in engineering.

I would also like to thank Dr. Yonghuan Xue, who has given me very useful tutorials and practical advice on piezoelectric actuators during the second year of my PhD research. My thanks also go to Dr. Frank Wardle and Professor Kai Cheng; they gave me an opportunity to work on an industrial project related to my PhD work.

Special thanks are due to my friends, Mr. Lei Chen, Dr. Rashidi Ibrahim, Dr Dongming Li, Dr. Haitao Li, Mr. Saiful Ghani and Mr. Rakan Alsharif for their advice and support. I also would like to thank all the department technicians, especially Mr. Paul Yates, who has given me so much technical support in the manufacturing of test bearings and the execution of experiments.

Finally, I dedicate this PhD thesis to the most important people in my life; namely my grandparents, Shuzai Wang and Xianzhong Fu; my parents, Qingxia Fu and Liping Wang; and especially my lovely wife, Mengya Liu, whose unwavering support, love and understanding has sustained me to persevere with my research till completion.

## **Declaration**

## **Declaration**

I declare that, to the best of my knowledge, no portion of the work referred to in this thesis has been submitted in support of an application for another degree or qualification of this or any other university, or other institute of learning.

**Chao Wang**

## Table of Contents

# Table of Contents

Abstract i

Acknowledgements iv

List of Figures .....xi

List of Tables xvii

Abbreviations .....xviii

Nomenclatures .....xix

**Chapter 1 – Introduction.....1**

1.1 Squeeze film bearings .....1

1.2 Aims and objectives .....3

1.3 Thesis structure .....4

**Chapter 2 – Literature review.....6**

2.1 Introduction .....6

2.2 Conventional bearings .....7

2.2.1 Classification of conventional bearings .....7

2.2.2 Contact bearings .....7

2.2.3 Non-contact bearings .....10

2.2.4 Comparison between contact and non-contact bearings .....16

2.3 Novel non-contact bearings using squeeze film effect .....18

2.3.1 Theory of squeeze film effect.....18

2.3.2 Background to squeeze film bearings .....18

2.4 Ideal gas law and adiabatic process .....29

2.4.1 Ideal gas law.....29

2.4.2 Adiabatic process .....30

2.5 Reynolds equation .....30

2.6 Forced vibration.....32

2.7 Driving unit – piezoelectric actuator .....33

2.7.1 Piezoelectric actuator.....33

2.7.2 Piezoelectric effect.....34

2.7.3 Mathematical description for piezoelectric effect .....35

2.7.4 Manufacturer’s data for piezoelectric actuator .....37



<b>Table of Contents</b>	
2.7.5 Piezoelectric actuator types .....	41
2.8 Modal analysis .....	42
2.8.1 Natural frequencies and mode shapes .....	42
2.8.2 Natural frequency measurement .....	43
2.9 Software packages .....	43
2.9.1 Pro-Engineering Wildfire 4.0 .....	43
2.9.2 ANSYS .....	44
2.9.3 CFX.....	45
2.9.4 LabVIEW.....	45
2.10 Summary .....	46
<b>Chapter 3 – Single layer piezoelectric actuator calculation .....</b>	<b>48</b>
3.1 Introduction.....	48
3.2 Single layer piezoelectric actuator calculation .....	48
3.2.1 Maximum stroke length .....	49
3.2.2 Maximum blocking force .....	52
3.3 ANSYS simulation for calculation of single layer piezoelectric actuator .....	53
3.3.1 Elastic matrix.....	55
3.3.2 Permittivity matrix .....	58
3.3.3 Piezoelectric constant matrix .....	59
3.3.4 ANSYS modelling .....	61
3.4 Summary .....	65
<b>Chapter 4 – Modelling structural characteristics and squeeze film effect.....</b>	<b>67</b>
4.1 Introduction.....	67
4.2 Characteristics of beam .....	68
4.2.1 Simple model analysis of a beam and boundary conditions .....	68
4.2.2 Static analysis .....	68
4.2.3 Modal analysis .....	72
4.2.4 Dynamic analysis .....	74
4.2.5 Stress analysis .....	75
4.2.6 Fatigue .....	77
4.3 Principle of squeeze film air bearings .....	78
4.3.1 Theory of squeeze air film .....	78
4.3.2 Ideal gas law.....	79
4.3.3 CFX.....	84

<b>Table of Contents</b>	
4.4 Discussion .....	91
4.4.1 Discussion in characteristics of beam.....	91
4.4.2 Discussion in principle of squeeze film air bearing.....	93
4.5 Summery .....	94
<b>Chapter 5 – Design of squeeze film air bearing and its experiments .....</b>	<b>96</b>
5.1 Introduction.....	96
5.2 Squeeze film air bearings system and process for testing and modelling.....	96
5.3 Design of the proposed squeeze film air journal bearing.....	98
5.4 Experiments design .....	101
5.4.1 Experiment for dynamic characteristics .....	101
5.4.2 Experiment for load–carrying capacity .....	105
5.5 Electrical inputs and mechanical parts.....	107
5.5.1 Signal generator .....	107
5.5.2 Actuator driver and actuator monitor unit.....	108
5.5.3 Oscilloscope .....	108
5.5.4 Piezoelectric actuator .....	109
5.5.5 Squeeze film air journal bearing .....	111
5.5.6 Guide way and guide way holder.....	112
5.6 Signal–pickups.....	112
5.6.1 Capacitive displacement sensor .....	112
5.6.2 Data acquisition card .....	113
5.6.3 LabVIEW user interface.....	114
5.7 Summery .....	115
<b>Chapter 6 – Experimental and theoretical results of proposed squeeze film air journal bearing .....</b>	<b>117</b>
6.1 Introduction.....	117
6.2 Theoretical and experimental results of characteristics of squeeze film air journal bearing .....	118
6.2.1 Material properties of proposed squeeze film air journal bearings .....	118
6.2.2 Static analysis – computer modelling and simulation .....	118
6.2.3 Modal analysis .....	120
6.2.4 Dynamic analysis .....	122
6.3 Load–carrying capacity experiments .....	129
6.3.1 Experiment description.....	129
6.3.2 Load–carrying capacity experiments on Al bearing at Mode 13 and 23.....	130

<b>Table of Contents</b>	
6.3.3 Load-carrying capacity experiments on Cu bearing at Mode 13 .....	133
6.3.4 CFX simulation validations .....	134
6.4 Discussion .....	136
6.5 Summery .....	138
<b>Chapter 7 – Fluid solid interaction (FSI) in coupled– field analysis for squeeze film effect.....</b>	<b>140</b>
7.1 Introduction.....	140
7.2 Fluid solid interaction (FSI).....	141
7.2.1 FSI analysis at Mode 13.....	143
7.2.2 FSI analysis at Mode 23.....	145
7.3 Conclusion.....	147
<b>Chapter 8 – Conclusions and recommendations for further work.....</b>	<b>148</b>
8.1 Conclusions .....	148
8.2 Contributions to knowledge.....	149
8.2.1 Dynamic characteristics of bearing .....	150
8.2.2 Bearing material.....	150
8.2.3 Location for mounting single layer piezoelectric actuator .....	151
8.2.4 Coupled–field analysis between piezoelectric actuator and solid structure .....	151
8.2.5 Fluid solid interaction for analyzing squeeze film effect .....	151
8.3 Recommendations for future work .....	152
<b>References</b>	<b>164</b>
<b>Appendices 172</b>	
<b>Appendix A Piezoelectric coefficient description and measurement data for squeeze film bearings .....</b>	<b>173</b>
<b>Appendix B Engineering drawings 179</b>	
<b>Appendix C Piezoelectric actuator calculation and computer programs .....</b>	<b>184</b>
<b>Appendix D Coupled - field for FSI analysis .....</b>	<b>203</b>
<b>Appendix E List of publications arising from this research.....</b>	<b>207</b>

## List of Figures

# List of Figures

## Chapter 2

Figure 2.1 – The various branches studied in literature review	7
Figure 2.2 – Contact bearing classification	8
Figure 2.3 – Static, Start up and Normal running equilibrium operation condition of aerostatic bearing	11
Figure 2.4 – Hydrodynamic bearing	12
Figure 2.5 – Temperature versus viscosity	13
Figure 2.6 – Working principle of the aerostatic bearing	14
Figure 2.7 – Air bearing spindle with external air pressure supply	15
Figure 2.8 – A linear tubular bearing with two squeeze film bearings on each end sitting on a guide-way, rod	20
Figure 2.9 – Squeeze film gas bearing with counterweight	22
Figure 2.10 – Squeeze film air bearing with elastic hinges	23
Figure 2.11 – Layout of the linear motion bearing	24
Figure 2.12 – Proposed squeeze film test bearing running on a square slider guide	24
Figure 2.13 – A linear guide-way system using ultrasonically vibrated squeeze film gas bearings	26
Figure 2.14 – Squeeze film bearing with elastic hinges and stack piezoelectric actuators: (a) unreformed shape; (b) deformed shape (not to scale)	27
Figure 2.15 – Squeeze film bearing system for supporting a rotation spindle	28
Figure 2.16 – Polarization axis of a piezoelectric ceramic	33
Figure 2.17 – Piezoelectric effect diagram	34
Figure 2.18 – Manufacturer data sheet from Fuji Ceramic Company	38
Figure 2.19 – Orthogonal system describing the properties of a piezoelectric ceramic; axis 3 is the direction of polarization	39
Figure 2.20 – Details of connection for transferring signals to user interface	44

## Chapter 3

### List of Figures

Figure 3.1 – Relationship between free stroke length and blocking force .....	47
Figure 3.2 – Locate the piezoelectric actuator in the orthogonal system .....	48
Figure 3.3 – Compliance and stiffness matrices listed in ANSYS .....	56
Figure 3.4 – Piezoelectric constant list in ANSYS .....	59
Figure 3.5 – Model of the piezoelectric actuator in ANSYS .....	61
Figure 3.6 – Maximum stroke length in X, Y and Z direction with applying 150 V and 0 V on the top and bottom layer of the piezoelectric actuator .....	63
Figure 3.7 – Maximum blocking force in ANSYS simulation .....	64

## Chapter 4

Figure 4.1– Model of rectangle beam with a single layer piezoelectric actuator mounted on top surface .....	67
Figure 4.2 – Static deformation of beam when 150 V DC was applied to the piezoelectric actuator .....	68
Figure 4.3 – Relationship between maximum static deformation and beam thickness .....	68
Figure 4.4 – The force analysis for a piezoelectric actuator bonded onto a beam with thickness .....	69
Figure 4.5 – Static deformation varies linearly with the applied DC voltage .....	70
Figure 4.6 – Mechanical modelling for coupled-analysis between beam and actuator system .....	71
Figure 4.7 – Mode shapes and natural frequencies of beam; colour red indicates maximum deformation and colour blue, no deformation(deformation not to scale) .....	72
Figure 4.8 – Relationship between natural frequency and beam thickness .....	73
Figure 4.9 – Dynamic response of beam when driven at the fundamental natural frequency of 4965.2 Hz .....	74
Figure 4.10 – Dynamic deformation versus beam thickness when excited at natural frequency of beam .....	74
Figure 4.11 – Comparison between static and dynamic beam deformations .....	75
Figure 4.12 – Relationship between dynamic deformation and AC .....	75
Figure 4.13 – Relationship between Dynamic deformation and DC .....	76
Figure 4.14 – Von-Mises stress on the beam based on maximum deformation of 11.884 $\mu\text{m}$ .....	77
Figure 4.15 – Von-Mises stress of beam with beam thickness .....	77

## List of Figures

Figure 4.16 – Von-Mises stress on piezoelectric actuator with beam thickness .....	78
Figure 4.17 – <i>S-N</i> curve of Al 2024-T3 .....	79
Figure 4.18 – Mean pressure ratio versus amplitude ratio –approximate solution Eq.(4.12)	83
Figure 4.19 – Asymmetrical pressure curve with two input parameters and .....	84
Figure 4.20 – Relationship between mean pressure ratio and amplitude ratio	85
Figure 4.21 – Mean pressure ratio versus amplitude ratio – exact solution Eq.(4.7) versus approximate solution Eq.(4.12).....	85
Figure 4.22 – (a) Dimensions of the plates and the air film thickness; and (b) the air film in the rectangular coordinate system used .....	88
Figure 4.23 – Air film thicknesses versus excitation frequency of bottom plate .....	89
Figure 4.24 – Air film thickness versus oscillation amplitude of bottom plate (oscillation frequency at 10 kHz) .....	90
Figure 4.25 – Air film stiffness versus oscillation amplitude .....	91
Figure 4.26 – Air film stiffness versus oscillation frequency .....	92
Figure 4.27 – Steady-state pressure distribution in the x-direction (Figure 4.22(b)) of air film in a period of oscillation of bottom plate in frequency of 10 kHz .....	93
Figure 4.28 – Pressure distribution in the x - direction (Figure. 22(b)) at three levels of excitation frequencies in the steady-state position .....	94
Figure 4.29 – Transition to equilibrium position of top plate for two excitation frequencies of bottom plate at 1 kHz and 10 kHz .....	94
Figure 4.30 – Air flowing velocity between plates during compressive movement	95

## Chapter 5

Figure 5.1 – Squeeze film air bearing system and the processes for testing and modelling .....	101
Figure 5.2 – The bearing with six single layer piezoelectric actuators mounted on three milled flat surfaces .....	104
Figure 5.3 – Schematics of the experimental set-up for measuring the dynamic response of the squeeze film air bearing .....	107
Figure 5.4 – Schematics of the experimental set-up for measuring the mean film thickness between the squeeze film air bearing and the guide way .....	109
Figure 5.5 – Signal generator (S J Electronics) .....	111

### List of Figures

Figure 5.6 – Actuator driver ENP-1-1U (Echo Electronics) and actuator monitor unit ENP-50U (Echo Electronics) .....	112
Figure 5.7 – Oscilloscope HM604 (HAMEG) .....	112
Figure 5.8 – CAD model for single layer piezoelectric actuator .....	113
Figure 5.9 – Physical prototype of the proposed squeeze film air journal bearing with the BNC connection box input to the piezoelectric actuator .....	115
Figure 5.10 – Capacitive displacement probe (MicroSense 5501) and gauging modulud (MicroSense 5810) .....	116
Figure 5.11 – Data acquisition card PCI – 6110 from National Instrument .....	118
Figure 5.12 – User interface for measuring the dynamic response of squeeze film air bearing .....	119

## Chapter 6

Figure 6.1 – Static deformation of the bearing when a 75V DC voltage was applied to the six actuators. (Deformation no to scale).....	123
Figure 6.2 – Static deformation varies linearly with the applied DC voltage .....	123
Figure 6.3 – Comparison of the static deformation between Al bearing and Cu bearing with the various DC voltages .....	124
Figure 6.4 – a) Left - mode shape 13; b) right - mode shape 23.....	125
Figure 6.5 – Set-up for the dynamic deformation measurement .....	127
Figure 6.6 – Dynamic deformation on the fin of the bearing at Mode 13 versus the excitation frequency for the three levels of AC input; the error bars represent $\pm 2$ standard errors .....	128
Figure 6.7 – Dynamic deformation measurement using LabVIEW software .....	129
Figure 6.8 – Dynamic deformation at the edge of Al bearing at Mode 23 versus the excitation frequency for the three levels of AC input .....	130
Figure 6.9 – FEA dynamic modelling for dynamic deformation of mode shape 13.....	131
Figure 6.10 – Comparison between theoretical and experimental dynamic deformation at Mode 13 for Al bearing (DC = 75V and variable AC) .....	132
Figure 6.11– Comparison between theoretical and experimental dynamic deformation at Mode 23 for Al bearing (DC = 75V and variable AC) .....	132
Figure 6.12 – Comparison between Mode 13 and Mode 23 for Al bearing (DC = 75V and variable AC) .....	133

### List of Figures

Figure 6.13 – Dynamic deformation on the fin of Cu bearing at Mode 13 versus the excitation frequency for the three levels of AC input	134
Figure 6.14 – Dynamic deformation on the fin of Cu bearing at Mode 23 versus the excitation frequency for the three levels of AC input	134
Figure 6.15 – Comparison between theoretical and experimental dynamic deformation at Mode 13 for Cu bearing (DC = 75V and variable AC)	135
Figure 6.16 – Comparison between theoretical and experimental dynamic deformation at Mode 23 for Cu bearing (DC = 75V and variable AC)	135
Figure 6.17 – Comparison between the theory and the experiment of dynamic deformation for Al bearing and Cu bearing at Mode 13 (DC = 75V and variable AC)	136
Figure 6.18 – Comparison between the theory and the experiment of dynamic deformation for Al bearing and Cu bearing at Mode 23 (DC = 75V and variable AC)	137
Figure 6.19 – Direction of loading by hanging masses	138
Figure 6.20 – Air film thickness of bearing versus load at four excitation frequencies around Mode 13 of Al bearing	139
Figure 6.21 – Air film stiffness versus load steps for Al bearing driven at Mode 13 with AC 75 V and DC 75 V	140
Figure 6.22 – Air film thickness driven in the variable AC, namely, 55 V, 65 V and 75 V	141
Figure 6.23 – Air film thickness of bearing versus load at four excitation frequencies around Mode 23 of Al bearing	141
Figure 6.24 – Comparison between Mode 13 and Mode 23 in the load-carrying capacity	142
Figure 6.25 – Effect of mass loading on the natural frequency of the bearing, affecting the air film thickness and hence the load -carrying capacity	143
Figure 6.26 – Floating test based on the variable excitation frequencies for copper squeeze film air bearing	143
Figure 6.27 – Comparison between Al bearing and Cu bearing in the load-carrying capacity	144
Figure 6.28 – Air film thickness versus oscillation amplitude at three load levels	145
Figure 6.29 – Comparison of theoretical and experimental for air film thickness	147
Figure 6.30 – Comparison between experimental and theoretical air film stiffness	147

### Chapter 7

Figure 7.1 – Bearing slice from whole squeeze film air journal bearing	153
--	-----



### **List of Figures**

Figure 7.2 – The dynamic deformation of bearing slice .....	154
Figure 7.3 – Dynamic deformation versus oscillation frequency of bearing slice at air film thickness of 5 $\mu\text{m}$ .....	155
Figure 7.4 –Dynamic deformation of bearing slice versus gap clearance .....	156
Figure 7.5 – Dynamic deformation of bearing slice along the length at three levels of gap clearance, 10 $\mu\text{m}$ , 20 $\mu\text{m}$ and 30 $\mu\text{m}$ .....	157
Figure 7.6 – Monitoring points along the length-wise of the bearing slice .....	157
Figure 7.7 – Diagram of coupled-field analysis for FSI .....	158

## List of Tables

## List of Tables

### Chapter 2

Table 2.1 – Comparison between plain bearings and rolling element bearings .....	9
Table 2.2 - Comparison for contact and non – contact bearings .....	16
Table 2.3 - Piezoelectric property definitions .....	36
Table 2.4 - Description of piezoelectric coefficients .....	39

### Chapter 3

Table 3.1- Stroke length in X, Y and Z directions .....	49
Table 3.2- Calculation for the unknown elements of the compliance/ stiffness matrix .....	54

### Chapter 5

Table 5.1 - Function description of instrumentation .....	106
Table 5.2 – Driving conditions for load-carrying capacity experiment .....	110
Table 5.3 – Parameters of single layer piezoelectric actuator .....	114
Table 5.4 – Material properties of bearings .....	115

### Chapter 6

Table 6.1 – Comparison between experimental and theoretical results in natural frequencies for Al bearing and Cu bearing .....	126
--	-----

## Abbreviations

## Abbreviations

AC	Alternative Current
A/D	Analogue-to-Digital
AE	Acoustic Emission
CAD	Computer Aided Design
CCL	CFX Common Language
CFD	Computational Fluid Dynamics
CMM	Coordinate Measure Machine
DAQ	Data Acquisition
DC	Direct Current
FEA	Finite Element Analysis
FTS	Fast Tool Servo
FSI	Fluid Solid Interaction
Hz	Hertz
MEMS	Micro-Electro-Mechanical Systems
MFC	Macro Fibre Composite
NS	Navier – Stoke

## Nomenclatures

## Nomenclatures

$A$	Cross Section Area;
$C$	Material damping;
$c$	Piezoelectric actuator Damping;
	Stiffness Matrix evaluated at constant electric field, i.e. short circuit;
$d_{31}$	Piezoelectric Charge Constant;
$d_{33}$	Piezoelectric Charge Constant;
$d_{15}$	Piezoelectric Charge Constant;
	Electric Displacement Vector; (three components $x, y, z$ )
	Piezoelectric Matrix relating strain/electric field (transposed);
	Piezoelectric Matrix relating strain/electric field;
$e$	Oscillation amplitude;
	Piezoelectric Matrix relating stress/electric field (transposed);
$E$	Dimensional amplitude;
	Piezoelectric Matrix relating stress/electric field;
	Electric Field Vector; (three components $x, y, z$ )
$F_L$	Levitation Force acting on the Top of Plate;
	Maximum Blocking Force;
$g$	Piezoelectric Dielectric Constant;
$h_0$	Average film thickness;
$H$	Normalized film thickness;
$I$	Second Moment of Area;

## Nomenclatures

$K$	Electro – mechanical Coupling Coefficient;
$k$	Actuator Stiffness;
$K_S$	Beam Stiffness;
$k_{33}$	Coupling factor;
$k_p$	Coupling factor;
$k_{31}$	Coupling factor;
$k_t$	Coupling factor;
$k_{15}$	Coupling factor;
$L$	Length of Piezoelectric Actuator;  Length of Piezoelectric Actuator;  Increased Length of Piezoelectric Actuator;  Stroke Length along X axis;  Stroke Length along Y axis;  Stroke Length along Z axis;
$M$	Mass of beam
$m$	Mass;
$m_b$	Mass of bearing;
	Mass of Top Plate;
$N$	Cycles to Failure;  Atmospheric Pressure;
$P$	Absolute Pressure;
$R$	Universal Gas Constant; (8.3145 J/mol K)

## Nomenclatures

	Compliance Matrix evaluated at constant electric field, i.e. short circuit;
	Strain Vector; (six components $x, y, z, yz, xz, xy$ )
$S$	Magnitude of a cyclic stress;
$T$	Absolute temperature;
	Stress vector; (six components $x, y, z, yz, xz, xy$ )
$t$	Thickness of Piezoelectric Actuator;
$u$	Beam Deformation;
$V$	Volume;
$V$	Voltage;
$velTop$	Velocity of Top Plate;
$w$	Width of Piezoelectric Actuator;
$X$	Maximum Stroke Length;
$Y$	Young's Modulus;
	Adiabatic Constant; (Air = 1.4)
	Dielectric Matrix evaluated at constant strain, i.e. mechanically clamped;
	Dielectric Matrix evaluated constant stress, i.e. mechanically free;
	Dielectric Constant;
	Dielectric Constant;
	Relative Dielectric Constant;
$\lambda$	Poisson Ratio;
	Mode coefficient;

## **Nomenclatures**

$\mu$	Dynamic Viscosity;
$\rho$	Density;
	Squeeze number;
	Fatigue Strength;
	Von Mises Stress;
	Non-dimensional time;
$\omega$	Angular velocity;
	Non-dimensional amplitude;

## Chapter 1 – Introduction

### 1.1 Squeeze film bearings

Where there are moving parts, there are bearings. The bearings allow constrained relative motion, typically rotation or linear, between two or more parts. In order to select the correct bearing for an application, the following factors need to be considered [1]:

- (1) Lubrication - gas or liquid;
- (2) Load – its directions, whether radial or axial or both, and its magnitude;
- (3) Speed;
- (4) Temperature - in particular that of the lubricant; and
- (5) Loading condition - vibration and shock loads.

Bearings can be broadly classified into contact and non-contact bearings based on whether or not a direct physical contact actually occurs between two relative moving bearing surfaces. Contact bearings are perhaps more common but they do experience more friction during operation than do the non-contact bearings. The friction creates heat and wear leading to degradation of lubrication and loss of positioning accuracy; in addition the friction consumes power that would otherwise be available for useful work. For this reason, compared to non-contact bearings, contact bearings are used for lower speed application.

Non-contact bearings are the ideal bearings because in theory there is no metal-to-metal contact between the two moving bearing surfaces that are separated by a layer of fluid. The force needed to overcome friction due to the viscosity of the fluid layer is far less than that in the contact bearings. Since there is no wear, there is no heat and hence no change of dimensions due to wear and thermal expansion. Thus, positioning accuracy can be more easily maintained.

In addition, cleanliness can also be easily maintained if oil, as lubricant, is replaced by clean air. This oil-free condition for bearings is essential in machines used for food,



## **Chapter 1 - Introduction**

drug and semiconductor manufacturing and in medical and bio-medical equipment. Other applications can be found in laser scanner motors, hard disc drives and contactless transportation of silicon chips.

Implementation of the principle of non-contact bearing produces aerostatic and aerodynamic bearings, and hydrostatic and hydrodynamic bearings. The difference between aero- and hydro-bearings is in the type of lubricant used; air in the former, and oil in the latter. They do have limitations, however.

Take the example of the aerostatic bearings. They need air compressors and hoses for their satisfactory operation. This ancillary equipment is bulky and not very portable, which can create problem as space is often at a premium particularly in micro- and nano-machining. In addition, the aerostatic bearings require a continuous supply of clean and dry air with the attendant cost in ensuring proper air supply and filtering.

The aerodynamic bearings also have their limitations. For example, at zero speed the load is supported via metal-to-metal contact. At start-up and shut-down, the friction that exists causes surface wear.

The non-contacting phenomenon between two bearing surfaces can also be generated by what is called the 'squeeze-film' effect [2]. This is clearly depicted in the Reynolds equation (see Chapter 2.4). According to the Reynolds equation, if two plates close to each other have oscillating relative motion normal to their surfaces, the air film being squeezed can generate a resistive force large enough to keep the two plates separate. Such bearings require no air compressors, filters or hoses; the whole package, including the power source and the driving element that produces the squeeze film action, can be made very compact.

The research reported in this thesis concerns this squeeze film phenomenon and the means by which the squeeze film effect can be harnessed in the design of journal bearings.

## **Chapter 1 - Introduction**

### **1.2 Aims and objectives**

The aim is to determine the static and dynamic behaviour of the squeeze-film phenomenon so that sufficient engineering knowledge is created for designing a mechanism for generating the squeeze film action and for designing journal bearings that make use of the action. To achieve the aim the following objectives are set:

- To study the driving mechanism for producing the squeeze film action – the piezoelectric actuator was identified and modelled, using ANSYS simulation to calculate two important parameters of maximum stroke length (without constraint at both ends of the actuator) and maximum blocking force (with constraint at both ends) when excited by an electrical power source;
- To conduct a coupled-field analysis between the piezoelectric actuator and a fixed-fixed beam, as an approximation to a bearing shell - to determine the modal shapes and frequencies and the corresponding stress distribution; to evaluate the fatigue life, the static and dynamic deformation of the beam;
- To model the squeeze film action using the ideal gas law and the Reynolds equation - to demonstrate the existence of an asymmetrical pressure distribution which is responsible for the levitation crucial to the operation of non-contacting bearings; to identify critical operating parameters such as the oscillation frequency and amplitude; and to determine their influence on the load-carrying capacity and the air film thickness;
- To design and build a test rig equipped with driving units to power the single layer piezoelectric actuators on a journal bearing to validate the squeeze film effect as predicted by the mathematical modelling and FEA simulation;
- To build a LabVIEW data acquisition program to capture the displacement signal on the bearings from which can be measured the oscillation amplitude and frequency, the modal shape and the air film thickness;

## **Chapter 1 - Introduction**

- To perform experiments to determine the dynamic response of the squeeze film bearings when excited at their modal frequencies;

- To perform experiments to determine the load-carrying capacity of the squeeze film bearings.

### **1.3 Thesis structure**

Chapter 1 introduces contact and non-contact bearings and the reason for researching into a type of non-contact bearing that operates on the ‘squeeze film’ effect. The aim and objectives for the research are explained and the structure of this thesis is presented also in this chapter.

Chapter 2 reviews the historical background and recent development of squeeze film air bearings. Advantages and disadvantages of the existing design of the squeeze film bearings are presented. In addition, theories on the squeeze film effect are introduced.

In Chapter 3, the two important parameters, namely the maximum stroke length and the maximum blocking force associated with the single layer piezoelectric actuator are calculated manually and then using ANSYS simulation.

The coupled-field analysis is presented in Chapter 4. The coupling studied is the one between the piezoelectric actuator (the driver) and a beam (the driven). The FEA modelling includes a modal analysis, static analysis, dynamic analysis, stress analysis and fatigue analysis of the beam with both ends fixed. Using computational fluid dynamics, the squeeze film effect is studied and modelled by two methods: 1) using the ideal gas law as a first approximation, and 2) using the CFX simulation as a much refined study. Significant results obtained from the refined CFX model are discussed and presented as bearing design guidelines.

With the understanding gained from Chapter 3 and Chapter 4, it is now possible to consider how to make use of the findings to design squeeze film air journal bearings. In Chapter 5 is described the reasoning behind the design of two journal test bearings, made from aluminium and copper. It also presents the experimental design, set-up and

## **Chapter 1 - Introduction**

procedure for the dynamic response and load-carrying capacity experiments. The Chapter ends with a description of the electrical inputs to the piezoelectric actuators, the mechanical bearing structure, the measurement instrument and the LabVIEW user interface.

Chapter 6 reports on the theoretical and experimental results of the two proposed journal test bearings focusing on the modal, static and dynamic analyses. It also presents and discusses results of the load-carrying capacity experiments.

Chapter 7 studies the fluid solid interaction between the air film and the bearing shell using the coupled-field analysis. This is focused on the air film effect at Modes 13 and 23 of the journal bearings.

Chapter 8 presents the conclusions to the research, the contributions to knowledge and the recommendations for future work. One of the contributions is the set of guidelines for designing squeeze film air journal bearings.

## **Chapter 2 – Literature review**

### **2.1 Introduction**

In this chapter, a literature review on different topics, as shown in Figure 2.1, is conducted. First, conventional bearings are classified and compared in terms of their design and performance characteristics. Second, a review of the research into the squeeze film bearings by various researchers is presented; it also comprises a survey of the theory that governs the squeeze film action, including the ideal gas law in an adiabatic process and the Reynolds equation. Third, as the squeeze film journal air bearing, which is the object of the PhD research, needs to be characterised in both its static and dynamic performance, it is appropriate to review topics on vibration particularly the forced vibration and modal analysis. Fourth, since the excitation device used to generate the squeeze film action is a piezoelectric actuator which is bonded onto the journal bearing, the mechanical property and transduction characteristic of the piezoelectric actuator are evaluated. Finally, the Chapter ends with a brief description and comment of the software evaluated and subsequently used in the course of the PhD research. These software packages have been used for the modelling and simulation of the piezoelectric actuator, the journal bearing and the coupling between the two, and for data acquisition and analysis of the dynamic response of the journal bearing in experiments.

## Chapter 2 – Literature review

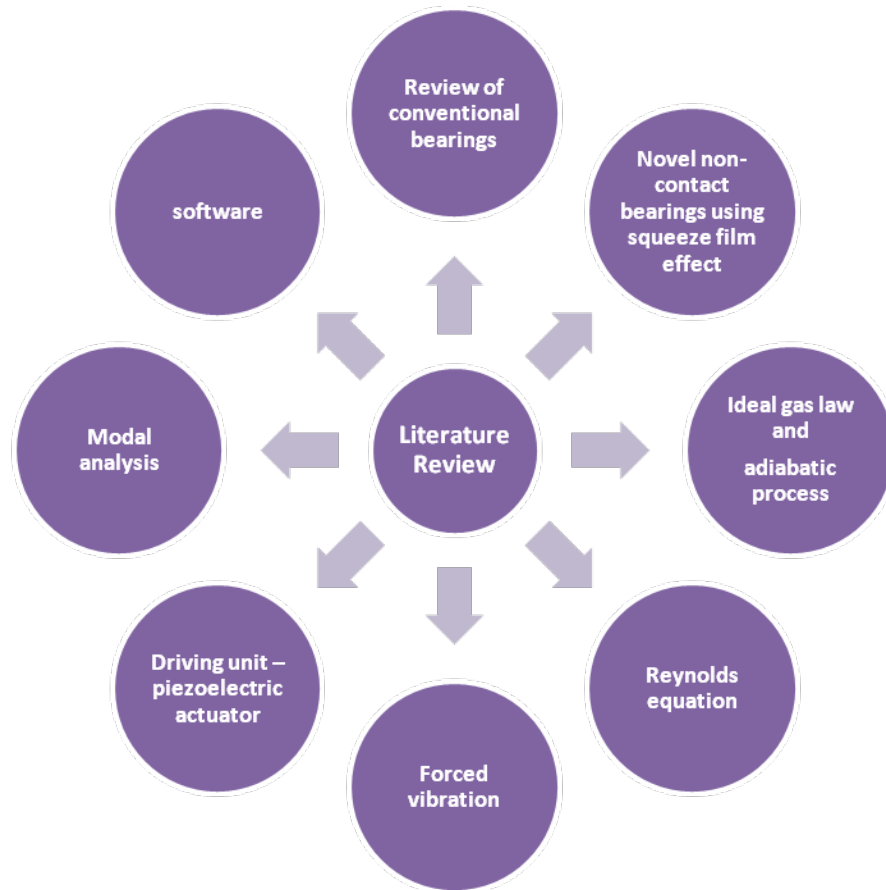


Figure 2.1 – The various branches studied in literature review

### **2.2 Conventional bearings**

#### **2.2.1 Classification of conventional bearings**

There is more than one way to classify bearings. Since the issue of great interest to an engineer is one of friction and its reduction or removal, it is more suitable to classify bearings in terms of the nature of support in a bearing. Thus, broadly speaking there are two classes, namely contact and non-contact bearings. This description enables a squeeze film bearing, the object of interest in this thesis, to be put neatly in the class of non-contact bearings.

#### **2.2.2 Contact bearings**

Contact bearings include plain bearings and rolling element bearings. Examples of the rolling element bearings are ball bearings, straight roller bearings, and taper roller bearings as shown in Figure 2.2. A plain bearing relies on the relative motion between

## Chapter 2 – Literature review

plain surfaces that are either flat or cylindrical. Normally, the material of the plain bearings is softer than the shaft or slider that is supported, in order to allow the bearing to get worn out faster than the shaft or slider. For the rolling element bearings, friction is much reduced between the moving and stationary parts compared with the plain bearing because of the rolling replacing the sliding motion.

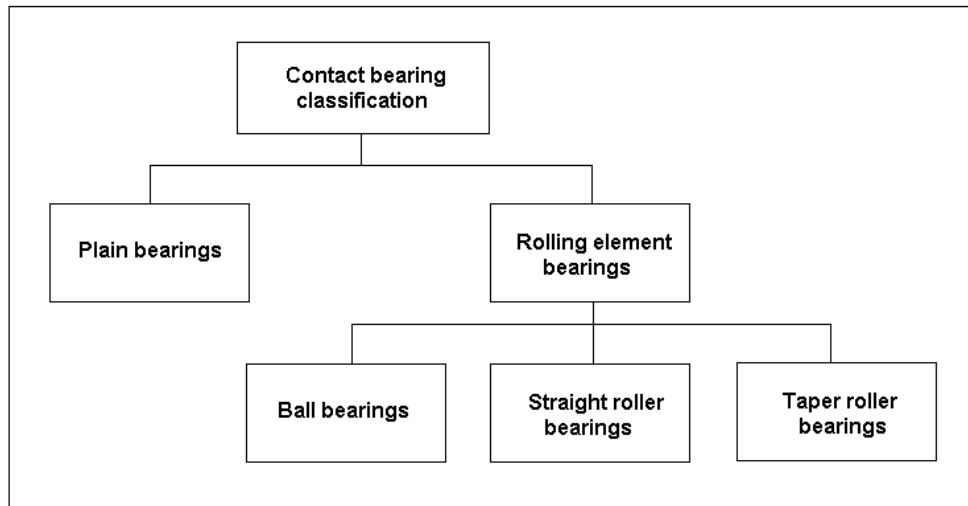


Figure 2.2 – Contact bearing classification.

Amongst the three rolling element bearings presented in Figure 2.2, the ball bearings tend to have lower load-carrying capacity due to smaller contact area that approximates to be a point in the ideal situation. However, the ball bearing can tolerate some misalignment of the inner and outer races. The roller bearings have larger contact area that approximates to be a line. The balls or rollers as the rolling elements can be chosen depending on the loading capacities and operation conditions [3]. The ball bearings can be operated at higher speeds without overheating than the roller bearings; moreover, they are less expensive for lighter loadings, have lower frictional resistance at light loadings and are available in a wider range of sizes. On the other hand, the roller bearings can carry much heavier loads because of the bigger contact area. The other advantage of roller bearings is in their tolerance to shock and impact loadings. The comparison between the plain bearings and roller element bearings is summarised in Table 2.1.

## Chapter 2 – Literature review

Table 2.1 – Comparison between plain bearings and rolling element bearings.

	<b>Plain Bearings</b>	<b>Rolling Element Bearings</b>		
<b>Types</b>	Plain bearing	Ball bearing	Straight roller bearing	Taper roller bearing
<b>Description</b>	Comprising just a bearing surface, without rolling element; usually with lubricant	Comprising inner race, outer race, balls and cage	Comprising inner race, outer race, roller and cage	Comprising inner race, outer race, roller cones and cage
<b>Friction</b>	High relative to rolling element bearing (also depends upon application and lubrication) Coefficient of friction: 0.1 [4]	Low Coefficient of friction: 0.001 [4]	Medium Coefficient of friction: 0.001 [4]	Medium Coefficient of friction: 0.001 [4]
<b>Speed</b>	Low relative to rolling element bearing (no cooling needed)	High (often cooling needed)	Medium (often cooling needed)	Medium (often cooling needed)
<b>Life</b>	Low to high	Medium to high (depends on lubrication and requires maintenance)	Medium to high (depends on lubrication and requires maintenance)	Medium to high (depends on lubrication and requires maintenance)
<b>Load – carrying capacity</b>	Medium Range ( $10^3$ to $2 \times 10^5$ N) [5]	Low relative to roller bearing Range	High Range ( $10^3$ to $2 \times 10^6$ N) [5]	High Range ( $10^3$ to $2 \times 10^6$ N) [5]



## Chapter 2 – Literature review

<b>Misalignment tolerance</b>	Low	High	Low	Low
<b>Cost</b>	Low	Medium	High	High
<b>Lubrication</b>	Requires	Requires less	Requires less	Requires less
<b>Contact area</b>	line	Point	Line	Line

Due to the direct mechanical contact between the rotational and stationary parts, the contact bearings suffer from friction, wear, vibration, heat generation in high speed operating conditions. To avoid those disadvantages, reducing friction is the key because it not only can reduce wear but also overheating. Based on the idea of friction reduction, non-contact bearings will be reviewed next.

### 2.2.3 Non-contact bearings

The non-contact bearings are those which do not have a direct physical contact between the two moving surfaces. Through this significant improvement, the non-contact bearings have features of no wear, hardly any friction except for fluid drag (particular for liquid lubricant), virtually maintenance free, high reliability and much higher positioning accuracy. The most common non-contact bearings are fluid film bearings, which use a thin layer (several microns) of fluid, gas or liquid, for separating two metal surfaces. The non-contact bearings include aerostatic and aerodynamic bearings and hydrostatic and hydrodynamic bearings, the first two based on the gas separating two surfaces and the last two based on the fluid. The function and working principles of the above variable types of the non-contact bearing will be discussed in the following sections [6].

#### 2.2.3.1 Aerodynamic and hydrodynamic bearings

In the aerodynamic bearings, the rotation of the moving part sucks the gas (air) into the inner surface of the bearing in order to form a gas film that is created by the relative motion to generate the pressure differentials not only for supporting the load but also for lubricating [7]. Figure 2.3 shows three operation conditions: static, start up and running.

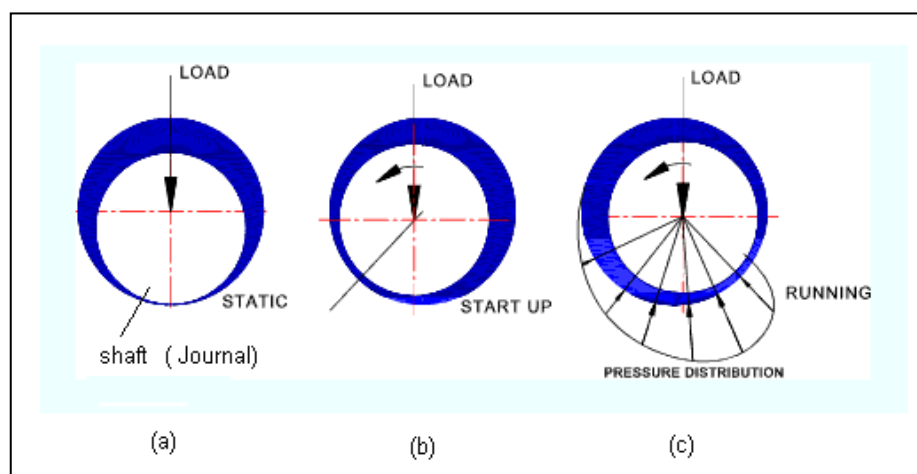
## Chapter 2 – Literature review

From Figure 2.3 (a), it can be observed that the film of lubrication cannot take any load in the static situation. When rotation starts the shaft (journal) moves up until it reaches an equilibrium position; meanwhile, a lubricating wedge is being formed under or around the rotation shaft. As the rotating speed increases, a pressure gradient is created across the gap clearance as shown in Figure 2.3 (c).

The load capacity, an important bearing parameter, depends on the relative speed of the rotating shaft and stationary bearing shell. At very light load and high rotational speed, the shaft will rotate nearly concentrically within the bearing. If the load is increased or the speed reduced, the eccentricity increases as a result of the film thickness being reduced significantly. Any further increase in loading or decrease in rotating speed could cause the failure of aerodynamic conditions due to the surface contact.

So, an evident limitation of the aerodynamic bearing is the high wear rate and excessive friction at start-up and shutdown. It should be used at high rotating speed; otherwise, its life may be shortened. Even at full nominal speed, the aerodynamic bearings are prone to dynamic instability such as the half-frequency whirl. Compared to the rolling element bearing, its stiffness is rather low, which can be a significant disadvantage.

The aerodynamic bearing is used in computer hard drives for supporting a memory disc spun at high speed under a magnetic read/write head. It can also be used in other applications like crankshaft journals.



## **Chapter 2 – Literature review**

Figure 2.3 – Static, Start up and Normal running equilibrium operation condition of aerostatic bearing [8].

The hydrodynamic bearings work on the same principle as the aerodynamic bearings. The only difference between them is the fluid used as lubricant, typically oil for hydrodynamic bearings instead of gas. So, grooves are often cut into the bearing shell to feed oil into the clearance, Figure 2.4. Since oil is virtually incompressible compared to gas, the hydrodynamic bearings have a much higher load-carrying capacity and stability than the aerodynamic bearings of a similar size; moreover, the hydrodynamic bearings have greater stiffness and damping. In other words, they can support a heavier load with greater stability due to the high stiffness of the oil film; the higher damping can prevent excessive vibrations or cushion impulsive shocks during running.

However, for the hydrodynamic bearings not only the rotational speed (which needs to be high) but also the temperature is critical. This is because of the fact that an increase in the oil temperature weakens the intermolecular forces, leading to a reduction in the oil viscosity. Figure 2.5 shows a typical relationship between kinematic viscosity and temperature.

The hydrodynamic bearings suffer similar disadvantages as do their aerodynamic counterparts at static, start up and shutdown. In addition, the integrity of the oil lubricant is also important. Although using oil instead of air increases the load-carrying capacity and film stiffness, yet due to its higher viscosity, the friction or drag associated with shearing an oil film is higher, increasing power consumption [9]. Furthermore, where hygiene and cleanliness are paramount, the use of the hydrodynamic bearings may not be suitable for fear of oil contamination.

## Chapter 2 – Literature review

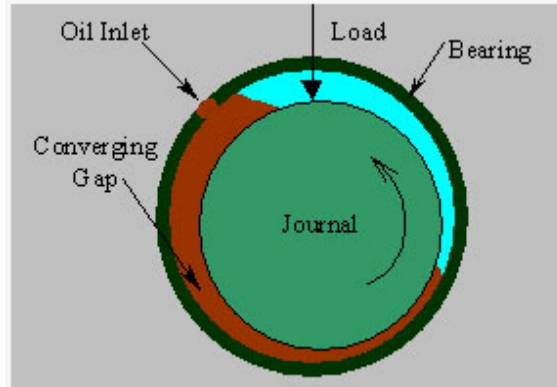


Figure 2.4 – Hydrodynamic bearing [10].

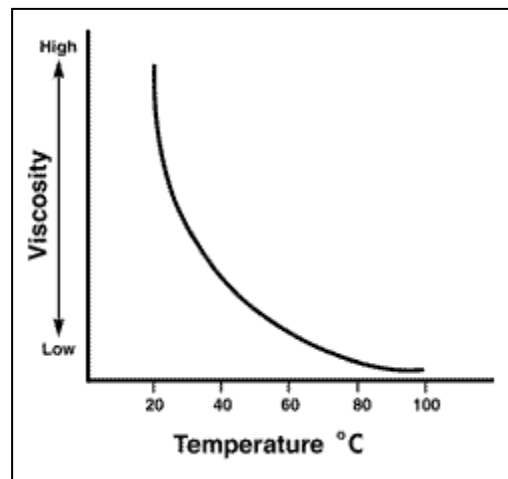


Figure 2.5 – Temperature versus viscosity [9].

### 2.2.3.2 Aerostatic and hydrostatic bearings

Aerostatic bearings use an external air compressor to supply pressurized air into a gap clearance. The gas film in the clearance keeps the two surfaces apart and also acts as a lubricant [11 and 12]. The aerostatic bearings can be classified as either linear air bearings or cylindrical air bearings. The linear air bearings, that can provide translational, are commonly used in micromachining centres, the gantry system in machine tools and high precision coordinate measuring machines, etc. The cylindrical air bearings are used as frictionless rotating support for spindles.

Figure 2.6 shows how an aerostatic bearing works. Without loading, the shaft is concentric in the bearing (ignoring the weight of the shaft), and there is zero pressure difference between the bottom and top halves of the shaft. When an external load is

## Chapter 2 – Literature review

applied to the shaft, the clearance in the bottom half reduces whilst that in the top half increases. So the air flow through the bottom half of the shaft is restricted thus causing the pressure there to increase whilst that at the top half decreases, Figure 2.6 (b). The pressure difference thus created balances the load applied [5].

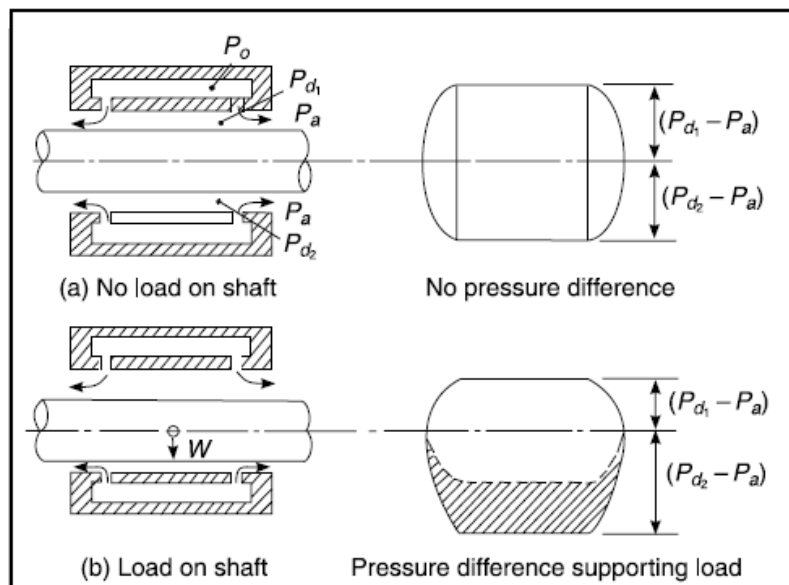


Figure 2.6 – Working principle of the aerostatic bearing [5].

In contrast to the aerodynamic bearings, the air film in the aerostatic bearings can sustain a load even in the static operation condition (zero speed) but they require an external pressurised air supply at all times; and the pressurized air must be properly cleaned and dried. The load-carrying capacity of the aerostatic bearing depends on the net pressure generated inside the bearing clearance, which in turn relies on the pressure in the air supply. In other words, the load-carrying capacity is only limited by the air pressure and the material strength of the bearing housing.

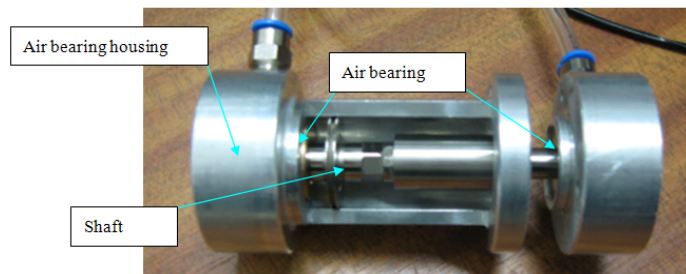
Unlike the aerodynamic bearings, aerostatic bearings do not suffer from excessive friction and wear that occur during the start-up and shutdown stages. In addition, the

## Chapter 2 – Literature review

aerostatic bearings are able to support higher loads than the aerodynamic bearings of a similar size. The aerostatic bearing stiffness and the damping are often much better than the aerodynamic counterparts, being less prone to instability after impulsive shock.

Admittedly, the aerostatic bearing systems are more complex to design, requiring expensive external pressure compressor and air delivery system. In this respect, aerodynamic bearings have far simpler requirements; they do not need compressors to work. Overall, aerostatic bearings deliver superior performance, have longer life expectancy and are noise-free, contamination-free and virtually maintenance-free.

The aerostatic bearings have found popular use in grinding, machining and micro-positioning applications where full functioning at zero speed and absence of friction is essential [5]. The most widely used air bearing applications in machine tools are those involving rotating spindles. One example is given in Figure 2.7; it consists of a shaft and an air bearing housing. The two pipes (inlets) are connected between the air bearing housing and the external air pressure supply (Figure 2.7 (b)) in order to deliver air to the two air bearings on both ends of the shaft.



(a)



(b)

Figure – 2.7 Air bearing spindle with external air pressure supply.

## Chapter 2 – Literature review

The hydrostatic bearings are very similar in working principle to the aerostatic bearings. The one major difference is the lubricant: liquid oil for the former and air for the latter [13]. An external pump is also needed to supply the pressurised liquid to the gap clearance. The hydrostatic bearings have even better stiffness and damping characteristics than the aerostatic bearings. But with the use of liquid, there is a risk of contamination to the machine parts and the environment. The design of the hydrostatic bearings is much more complicated than that of the hydrodynamic bearings. The hydrostatic bearings are typically used in high precision and high speed machine tools.

### 2.2.4 Comparison between contact and non-contact bearings

Table 2.2 provides a summary of the comparison between the contact and non-contact bearings. The assessment is made on the features of bearing stiffness, load-carrying capacity, heat generation, positioning accuracy, operating speed, maintainability, time to failure and cost, amongst others. Each feature is ranked using the descriptors, Excellent, Good, Fair, and Poor; the meaning is as the descriptors suggest.

Table 2.2 - Comparison for contact and non – contact bearings [5 and 6].

Classification	Non-contact bearing				Contact bearing	
	Air lubricant bearing		Oil- lubricant bearing		Plain bearing	Rolling - element bearing
Types	Aero-static	Aero-dynamic	Hydro-static	Hydro-dynamic	Plain	Ball and roller
Working principle	Refer to section 2.2.3.2	Refer to section 2.2.3.1	Refer to Section 2.2.3.2	Refer to section 2.2.3.1	Refer to section 2.2.2	Refer to section 2.2.2
High axial/radial static stiffness	Good	Fair	Excellent	Excellent	Excellent	Excellent
Load-carrying capacity	Good	Poor	Excellent	Good	Excellent	Excellent
Thermal stability	Excellent	Excellent	Good	Fair	Poor	Poor

## Chapter 2 – Literature review

<b>High accuracy of rotation</b>		Excellent	Good	Excellent	Good	Poor	Fair
<b>Operation speed</b>	< 1k rpm	Excellent	Poor	Excellent	Poor	Excellent	Fair
	1k–60k rpm	Excellent	Excellent	Excellent	Excellent	Poor	Good
	> 60k rpm	Excellent	Excellent	Excellent	Excellent	Poor	Poor
<b>Long running Time (Greater than 20,000 hours)</b>		Excellent	Good	Excellent	Excellent	Poor	Poor
<b>Level of maintenance</b>		Good	Excellent	Good	Excellent	Fair	Fair
<b>Contamination Free</b>		Good	Excellent	Poor	Poor	Poor	Poor
<b>Low vibration</b>		Excellent	Excellent	Excellent	Excellent	Fair	Fair
<b>Low running costs</b>		Fair	Excellent	Fair	Good	Good	Good
<b>Frequent starts/stops</b>		Excellent	Poor	Excellent	Poor	Excellent	Excellent
<b>Low starting friction (torque)</b>		Excellent	Poor	Excellent	Fair	Poor	Fair
<b>Wide temperature range</b>		Excellent	Excellent	Poor	Poor	Fair	Fair
<b>Shock resistance</b>		Good	Fair	Excellent	Excellent	Good	Good
<b>Minimum supplied lubricant</b>		Poor	Excellent	Fair	Fair	Good	Excellent
<b>Ease of assembly</b>			Excellent		Excellent	Fair	Fair
<b>Ease of replacement</b>		Poor	Excellent	Poor	Excellent	Excellent	Excellent



## Chapter 2 – Literature review

<b>Small space Area</b>	Poor	Good	Poor	Good	Excellent	Excellent
<b>Purchasing cost</b>	Poor	Fair	Poor	Excellent	Excellent	Excellent

### **2.3 Novel non-contact bearings using squeeze film effect**

#### **2.3.1 Theory of squeeze film effect**

Squeeze air film analysis simulates the effects of air in small gaps (30  $\mu\text{m}$  in this application) between fixed surfaces and structures moving perpendicular to the surfaces in sufficiently high vibration frequencies. Due to such high vibration frequencies, the leakage from the edges is negligible as the air film undergoes cyclical compression and expansion. It can be shown that asymmetrical pressure is created during each cycle such that the mean pressure within the air film is greater than the ambient pressure. This in turn creates the load-carrying capacity through the cyclical and rapid squeeze motion.

#### **2.3.2 Background to squeeze film bearings**

In 1874, Stefan [14] first developed an equation related to the time of descent of a flat round plate onto a smooth flat surface from an initial height. After 12 years, in 1886, Reynolds published his classical theory of hydrodynamic lubrication and while acknowledging the experimental work of Stefan derived the same basic equation for the case of the two parallel circular or elliptical plane surfaces approaching each other without tangential motion. Reynolds combined the stress equations of Stoke with the equations of motion for a viscous fluid and then by neglecting the inertia terms and applying boundary conditions appropriate to the lubricating process, he obtained the well-known Reynolds equation [14], Eq. (2.3).

According to the Reynolds equation, the two parallel plane surfaces, if subjected to a normal oscillatory relative motion at a sufficiently high frequency, can be kept separate due to what is called the ‘squeeze film’ action. If the planes are horizontal and only one plane is made to oscillate, the squeezing action produces a levitation force that lifts the

## **Chapter 2 – Literature review**

upper plane. This is the basis for a new kind of non-contact bearing, the squeeze film bearing.

Based on this theory, in 1964 Salbu [2] constructed a squeeze film bearing. To generate the oscillatory motion at a certain frequency and amplitude, magnetic actuators were used. From the experiments that followed, Salbu observed that at a low oscillation frequency the film force tends to be in phase with the squeeze velocity, but at a higher frequency it is in phase with the squeeze displacement. Because the operation frequency was in the audible range, the bearing was extremely noisy during operation. But the research helps in the understanding of the squeeze film principle applied to the novel squeeze film bearings. The publication of Salbu's research sparked a great interest in the research community.

In the 1960s, a number of patents were filed in the US on the design of squeeze film bearings, such as those from Emmerich [15], Warnock [16] and Farron [17]. All of these designs started using piezoelectric actuators instead of the magnetic actuators to generate the oscillation.

Emmerich's patent described a design that was claimed to achieve appreciably greater oscillation amplitude than ever; the design did also overcome the effect of static friction, which helped to make the piezoelectric driving system more efficient. The design in Farron's patent also avoided the static friction effect by floating the shaft as well as the piezoelectric actuators. In addition, the method can support both the journal and thrust bearings configuration.

All these patented designs, however, use bulky cylindrical piezoelectric actuator stacks, thus taking up a good deal of space. The designs involve many parts that may create complication in assembling. Furthermore, as the designs aim to create uniform oscillation amplitude over the entire bearing surfaces, the amount of power required to drive the actuators is correspondingly high.

In 1986, Mark [18] designed a linear tubular bearing based on the squeeze film effect. A sketch is as shown in Figure 2.8. The bearing consists of a pair of transducer elements each formed from two collinear tubes; the two transducer elements were

## Chapter 2 – Literature review

joined by a cylindrical link. The material of the two collinear tubes can be both piezoelectric ceramic (lead zirconate titanate) material; or one tube piezoelectric and the other an inert material such as molybdenum. An alternating electrical voltage at a certain frequency is applied to the tubes. Under the action of the applied voltage, the outer tube (Tube 2 in Figure 2.8) oscillates in and out along radial direction so that the air in the annular gap clearance is squeezed, producing the squeeze bearing effect. Two bearings on each side can provide a better support to the rod against the pitching motion. Compared to one long actuator tube, this arrangement (Figure 2.8) saves material and mass. But the rolling motion of the linear tubular bearing still exists in this arrangement because of the non-uniform pressure distribution generated by the squeeze film action. The other disadvantage of this design (Figure 2.8) is that the manufacturing cost to produce two collinear tubes with high precision is considerably more expensive, and the piezoelectric actuator (Tube 2) may be damaged if the clearance is too tight during installation. In addition, the piezoelectric actuators used in the research were still quite complicated and difficult to produce. But compared to the designs filed in the US patents of the early 1960s, the design by Mark requires less power to generate sufficient oscillatory amplitude.

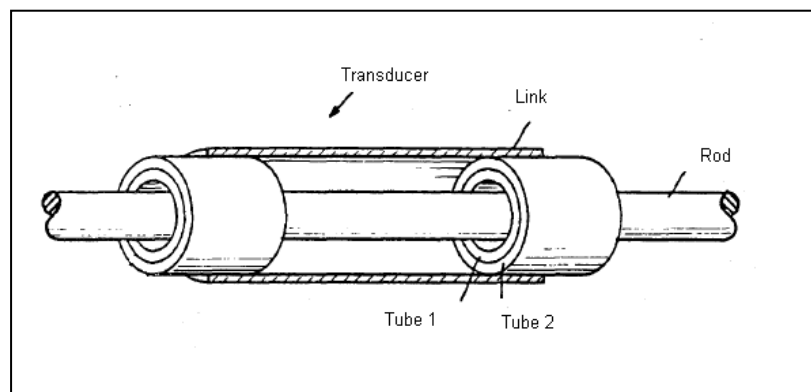


Figure 2.8 – A linear tubular bearing with two squeeze film bearings on each end sitting on a guide-way, rod.

Scranton [19], in his 1987 patent, summarised the drawbacks of the design in the 1960s as being that:

- The conforming surfaces are rigid and heavy;

## Chapter 2 – Literature review

- The transducer which drives the surface of the bearing must be correspondingly massive;
- The power dissipation is high;
- The ratio of bearing weight to load-carrying capacity is too large;
- Because of the relatively large oscillating mass of the bearing itself, it is impossible to make the frequency of oscillation higher than the audible range;
- The oscillatory forces cause excessive vibration of the object supported by the bearing which is frequently an intolerable characteristic of a bearing, especially where precise location of the object is required, as contrasted to oscillation of location of the object.

Scranton [19] suggested bending the piezoelectric actuators in order to excite a flexural vibration mode on the bearing. The design could be made more compact with significantly reduced power consumption. However, Scranton only showed a sketch of the fundamental concept without any implementation.

Yoshimoto [20] proposed a new design of the squeeze film bearing as shown in Figure 2.9. The proposed squeeze film bearing system consists of a slider and a counterweight; the driving units, two stacks piezoelectric actuators, in the middle to connect between the slider and the counterweight. The two stack piezoelectric actuators were driven in a sinusoidal fashion at a certain frequency and amplitude so that both the slider and the counterweight also oscillate in the same sinusoidal fashion at the same frequency as the driving unit. Because the position of the mass of the whole system oscillates up and down with such a high frequency, it produces a thin layer of air film below the slider due to the squeeze film effect levitating the slider above the guide way.

In previous designs the object being levitated was placed on a vibrating surface, and it could be difficult to vibrate a whole long and narrow guide way with sufficient

## Chapter 2 – Literature review

oscillation amplitude at a high enough frequency. In addition, the travelling distance can also be limited by this arrangement. The design as shown in Figure 2.9 does not suffer from this limitation.

The disadvantages of the design in Figure 2.9 are threefold. First, the counterweight adds to the load, making it bulky and harder to levitate. Second, using two stack piezoelectric actuators is more expensive than using their single-layer counterparts, not to mention the higher power consumption. Third, the supported object has the excessive vibration as one of those drawbacks summarized by Scranton.

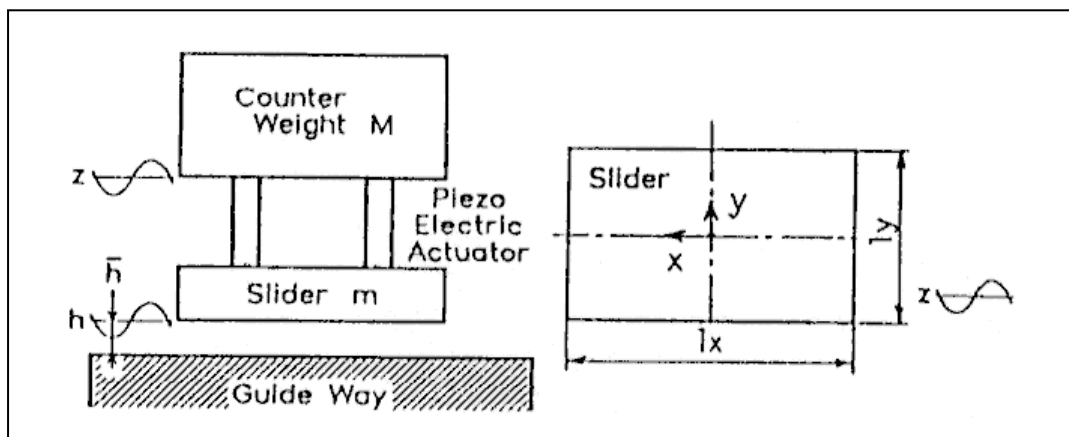


Figure 2.9 – Squeeze film gas bearing with counterweight [20].

In 1995, Yoshimoto [21] introduced a design that used what are called ‘elastic hinges’ in the squeeze film bearing for a linear motion guide as shown in Figure 2.10. The new design includes three elastic hinges and two stack piezoelectric actuators in the middle of the top two elastic hinges. The two stacks actuators were driven to push the top two elastic hinges away to each other in order to oscillate the bottom part vertically. The squeeze film effect can be generated due to the motion of oscillation so that the whole system can be levitated in the air. The advantage of using the elastic hinges can create

## Chapter 2 – Literature review

localised reduction in stiffness – resulting in greater oscillation amplitude. So this design can miniaturize the squeeze film bearing system without using the counterweight. Since there is not a counterweight needed for the requirement of inducing vibration so the arrangement of the piezoelectric actuator can be fixed in horizontal direction as shown in Figure 2.10. The oscillation frequency only up to 2400 Hz lower than the fundamental natural frequency of the system which is in the audible range could induce the noise during operation. The design of the elastic hinges can be a complex matter and they cost more to manufacture. In addition, the stress concentration and the fatigue may cause the failure of the elastic hinges if the oscillation amplitude is quite big or misuse.

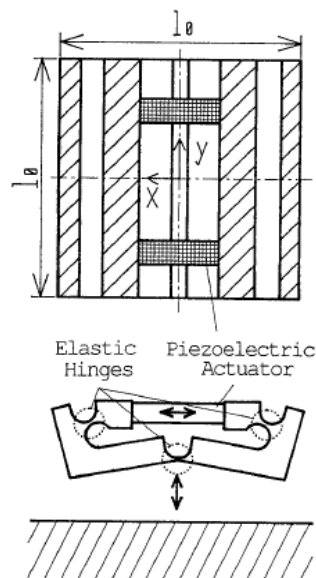


Figure 2.10 – Squeeze film air bearing with elastic hinges [21].

Stolarski [22] following Yoshimoto's idea proposed a self – levitating linear air bearing using the elastic hinges as shown in Figure 2.11. The working principle of this design

## Chapter 2 – Literature review

arrangement (Figure 2.11) was similar to the design in Figure 2.10. But the difference is that the guide way is a solid square block rather than a flat surface, so two stack actuators were necessarily needed on both sides to form two squeeze film bearings in order to avoid the metal contacts horizontally between the guide way and the cartridge. Moreover, the two squeeze film bearings generated by two side plate have not influence on the load-carrying capacity. The operation frequency was also only in the audible range only up to 4000 Hz, which is away from the natural frequencies. Stolarski [23] improved the design in such way as shown in Figure 2.12 that only used two stack piezoelectric actuators on top and two on the bottom without using the actuators on the both side plates. But based on the elastic hinges, the side plates can be deform to form two squeeze film bearing. The operation frequency range was from 500 Hz to 3000 Hz and covered the fundamental natural frequency of 2600Hz. The experimental results were found that the squeeze film air bearing can be operated at the natural frequency and can produce large film thickness. The experimental results also indicated that the air film could not be built when the operation frequency below certain frequency (700 Hz at here). The stack piezoelectric actuator and the elastic hinges were also needed in both designs. The operation frequency can still produce noise in operation.

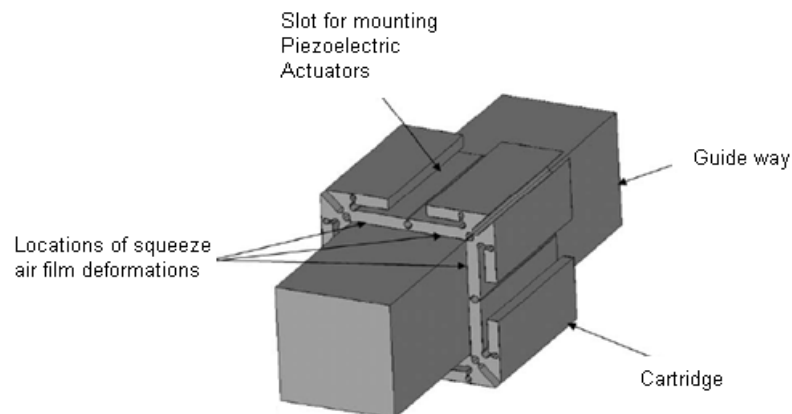


Figure 2.11 – Layout of the linear motion bearing [22].

## Chapter 2 – Literature review

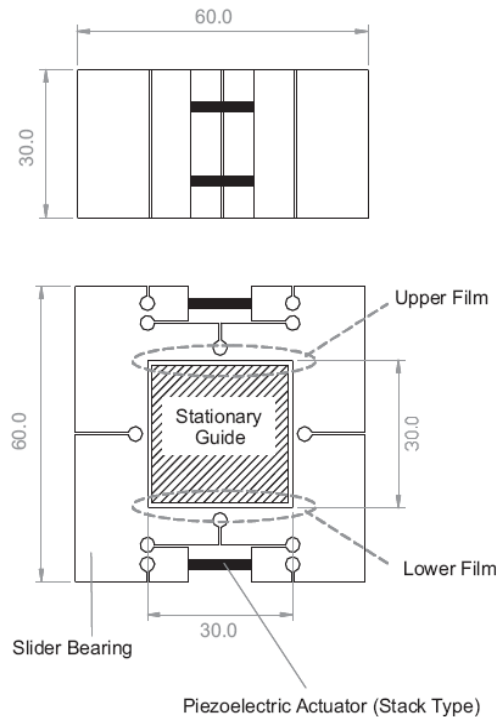


Figure 2.12 - Proposed squeeze film test bearing running on a square slider guide [23].

In 2006, Stolarski [24] presented three novel ideas that are squeeze film action, surface contraction and acoustic levitation [25] for generating a self – levitation between two surfaces from physical fundamentals to practical applications. The three ideas were proven that the levitation could be generated based on the different experimental set-ups. For the squeeze film effect, the paper used the same experimental arrangement as shown in Figure 2.12.

Stolarski [26] also explained the squeeze film effect using both numerical analyses and physical explanations. The asymmetrical pressure distribution in one period can be generated by the squeeze film action deduced from the ideal gas law. This means that the mean pressure beyond the ambient pressure is the key to levitate an object in the air. He also pointed out that incompressible fluid (Oil) could not be used as a lubricant for designing squeeze film bearings due to the symmetrical pressure distribution during rapid squeeze actions. The pressure profile that includes a bumped region and a flat region was also obtained and explained theoretically. The flat region is built due to the repeated compression and expansion action; moreover, it is the main contribution to the



## **Chapter 2 – Literature review**

levitation. The bumpy region may have greater or less pressure than the pressure in the flat region, which depends on the air film being compressed or expanded.

Stolarski [27] also did further investigation on the air film pressure during the squeeze film action on the experimental setup shown in Figure 2.12. A pressure sensor was mounted to the upper surface of the guide for measuring the average dynamic pressure of the upper film at one location. It was found that the asymmetrical film pressure predicted from the Reynolds equation is not always observed in experiments.

In 2006, Yoshimoto [28] introduced a new design of linear motion guide which consists of a guide-way, a cartridge and single layer piezoelectric actuators as shown in Figure 2.13. He reported the research on a newer design in which the bearing was driven by six piezoelectric actuators at the fundamental frequency, at 23.7 kHz, of the bearing. When driven at this frequency the oscillating amplitude of the bearing plate was significantly increased to 1.7  $\mu\text{m}$  measured at the edge of the top plate. The main advantage of this design can avoid the noise generated during operation because the bearing was driven at ultrasonic vibration. Moreover, the design also got rid of the complicated elastic hinges in the squeeze film bearing structure. It not only can significantly reduce the manufacturing cost but also avoid the potential damage of the bearing structure in terms of the stress concentration and the fatigue on the elastic hinges. In addition, the use of the single layer piezoelectric actuators can reduce more power consumption than the stack piezoelectric actuators. But Yoshimoto's work has led to the question of whether better performance can be achieved by driving a bearing at a modal frequency above the fundamental. Moreover, it also has led to question of whether the other mode shapes can also achieve the squeeze film effect and which mode shape has more superior levitation performance.

## Chapter 2 – Literature review

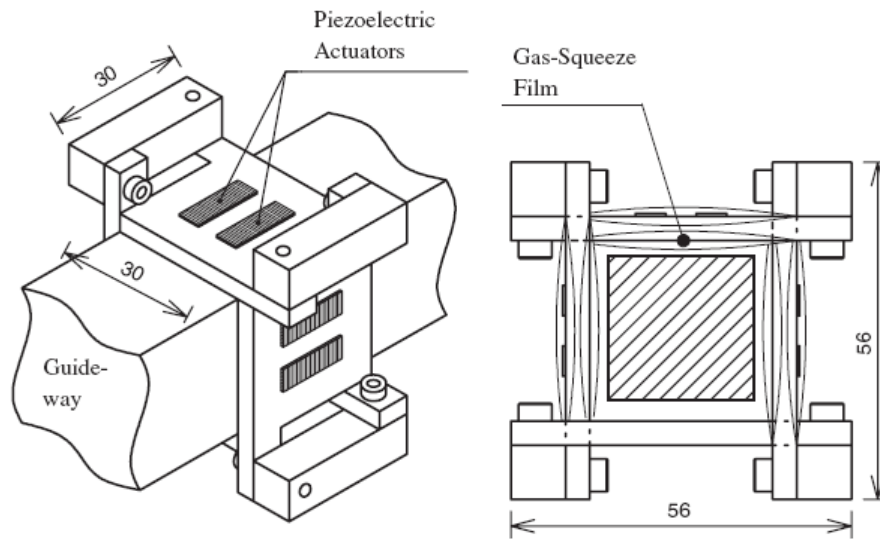


Figure 2.13 - A linear guide-way system using ultrasonically vibrated squeeze-film gas bearings [28].

In 2009, Ono [29] did experiments on Yoshimoto's the linear guide-way as shown in Figure 2.13. A small acrylic ball dropped on the top flat plate as an impulsive load. The experimental results suggested that the response of the cartridge has more oscillations in the thinner film thickness. The experiment also pointed out the approximated dynamic stiffness, obtained from, is much greater than the static stiffness, obtained by measuring the difference in the floating height of the cartridge with load.

Ha [30] reported that the aerodynamic bearing is capable of self-levitation using the squeeze film effect. The aerodynamic bearing system shown in Figure 2.14 (a) consists of a shaft, a bearing housing and stack piezoelectric actuators. In this design the stack actuators were used to deform the bearing housing. The aerodynamic bearing has disadvantage of producing excessive friction and wearing during start-up and shutdown stages. The design used the squeeze film pressure to lift the shaft during two critical stages in order to avoid those two limitations inherited in the aerodynamic bearings. When the spindle reached sufficiently high rotation speed, three lobes were formed as shown in Figure 2.14 (b) by deforming the inner surface area of the bearing in terms of applying a DC voltage to the stack piezoelectric actuators. The bearing can levitate the load of up to 2.18 N, with a vibration amplitude and frequency of 0.45  $\mu\text{m}$  and 1400

## Chapter 2 – Literature review

Hz, respectively. The work done by Ha had explored a novel idea that building the squeeze film effect inside the aerodynamic bearing to overcome its inherent limitations to some extent. Based on the same test rig and working principles, Stolarski [31] did the further research to assess the orbit trajectory path of the rotor upon a perturbation using the numerical method. By analyzing the rotor orbit in the frequency domain, it is able to identify the self-excited whirling instability.

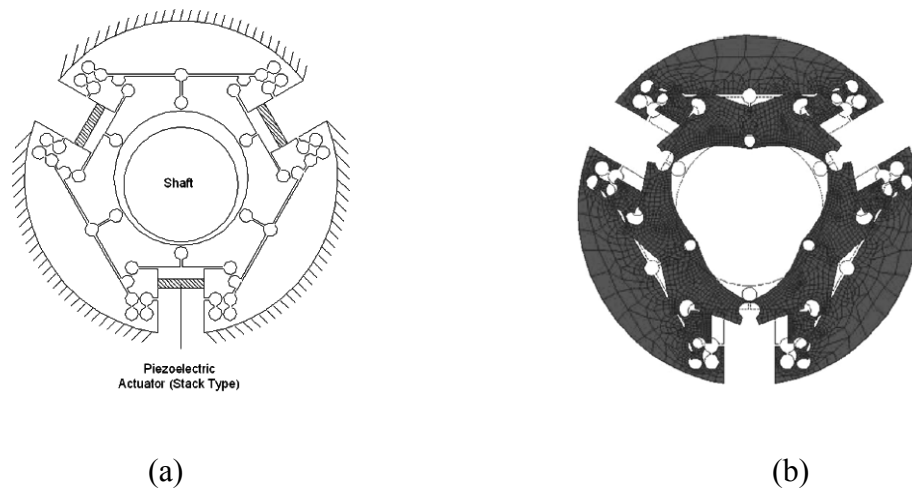


Figure 2.14 – Squeeze film bearing with elastic hinges and stack piezoelectric actuators: (a) unreformed shape; (b) deformed shape (not to scale) [30].

In 2009, Zhao [32] proposed a squeeze film bearing system that consists of a spindle, a bearing housing and three ultrasonic transducers as shown in Figure 2.15. The ultrasonic transducer has the key part –the piezoelectric actuators which were specially designed and fabricated in the requirement of the bearing system. The ultrasonic transducer is the Langevin type transducer [33] which is often used to generate high power and high intensity vibration. The operation frequency is quiet in the ultrasonic range of 20 kHz. The maximum load-carrying capacity can reach up to 51 N when the oscillation amplitude is 10.6  $\mu\text{m}$ . The improvement of the load-carrying capacity proved the point that the squeeze film bearing can be applied to support considerable loading. But in the design only one end of the spindle is supported by the squeeze film bearing but not the other. In other words, not the entire spindle was levitated in the air in terms of the squeeze film effect. Moreover, the three ultrasonic transducers need to

## Chapter 2 – Literature review

be manufactured in the high precision to avoid the discrepancies among them during operation. The piezoelectric actuators were specially design, quite bulky and high power consumption. In this design the size of the housing is difficult to minimize because it has to be very rigid in order to prevent any deformation which may affect the performance of the rotation spindle.

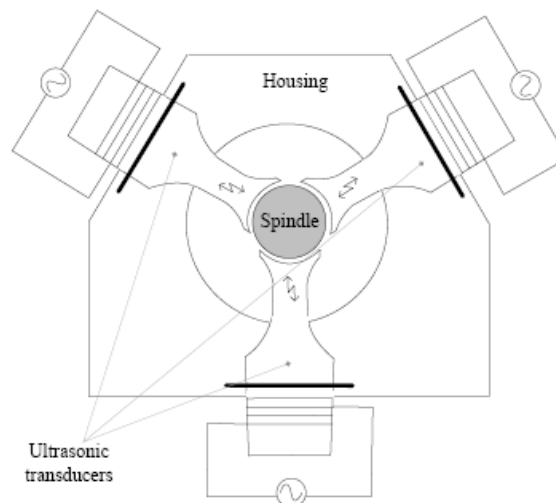


Figure 2.15 – Squeeze film bearing system for supporting a rotation spindle [32].

## 2.4 Ideal gas law and adiabatic process

### 2.4.1 Ideal gas law

An ideal gas is a theoretical gas composed of a set of randomly-moving, non-interacting point particles. The Ideal gas law is the equation of state of a theoretical ideal gas. It is a good approximation to the behaviour of many gases under many conditions, although it has several limitations [34].

The state of an amount of gas is determined by its pressure, volume, and temperature which are related by the equation.

$$(2.1)$$

where,  $p$  is absolute pressure ( $\text{N/m}^2$ , Pa),  $V$  is volume ( $\text{m}^3$ ),  $n$  is amount of substance of the gas,  $R$  is universal gas constant  $8.3145 \text{ J/mol K}$  and  $T$  is absolute temperature (K).

## Chapter 2 – Literature review

### 2.4.2 Adiabatic process

An adiabatic process is a process in which no heat transfer takes place between a system and its surroundings. Zero heat transfer is an idealization, but a process is approximately adiabatic if the system is well insulated or if the process takes place so quickly that there is not enough time for appreciable heat flow to occur [35 and 36]. The adiabatic process for the ideal gas is mathematically described by,

$$(2.2)$$

In Eq. (2.2),  $p$  is the pressure,  $V$  the volume,  $\gamma$  the adiabatic constant equal to 1.4 for air, and  $K$  the constant.

Consider two parallel plates of infinite lateral dimensions separated by a gap; one of the plates oscillates sinusoidal normal to the other at a frequency. If the oscillating frequency is very high, then there is no time for heat transfer to take place and so the process can be regarded as adiabatic.

### 2.5 Reynolds equation

Most gas lubricating films are laminar [37] and have negligible fluid inertia and body forces. Moreover, some assumptions often need to be accepted for simplifications like the lubricant to be Newtonian and the viscosity to be [38 and 39]. In addition, pressure constant along any plane in the lubricant film. At the same time, fluid velocity normal to the surface is negligible and the film gap thickness should be much smaller compared to lateral dimensions. There is no slip at the boundaries, which means the velocity of the lubricant layer adjacent to the boundary is the same as that of the boundary. These assumptions have been accepted universally. By considering the above flow conditions, these much complicated Navier-stokes equations can be simplified into Reynolds equation [40] as shown in the Eq. (2.3). The pressure in the lubricant is governed by the Reynolds equation. In this equation,  $p$  is the pressure (Pa),  $h$  is the

## Chapter 2 – Literature review

lubricant thickness (m),  $\mu$  is the viscosity (Pa .s),  $u$  and  $v$  are two tangential surface velocities (m/s) and  $w$  is normal surface velocity (m/s).

$$(2.3)$$

To study the bearing behaviour of a thin air film between two surfaces, the Reynolds equation, Eq. (2.3), is used.

Stolarski [26] identified three mechanisms from the equation that would show a pressure-generating phenomenon, which gives the bearing its load-carrying capability. The first refers to the ‘physical wedge’ as is found in hydrodynamic bearings where the fluid flows through a wedge; the second requires the two surfaces to contract or expand in-plane in order to create a variable velocity on the bearing surfaces; the third requires that the two bearing surfaces move normal to each other with an oscillating velocity and is known as the ‘squeeze film’ effect.

Stolarski [26] asserted that the pressure generated by the hydrodynamic and squeeze film effects is of a similar order of magnitude and hence the justification for exploring the latter in the design of a new type of bearing. Squeeze film bearings have the significant advantage due to the fact that they do not require air compressors and connecting hoses; the equipment needed for generating the squeeze film action is far smaller and it can be miniaturised to the extent that it becomes a single package with the bearing.

The Reynolds equation can be used to analyze the squeeze film mechanism by neglecting the first and second terms on the right hand side of the Eq. (2.3). The Reynolds equation is normalized into non-dimensional form as

$$(2.4)$$

Where the non-dimensional parameters are given by:

$\bar{h}$ ;  $\bar{u}$ ;  $\bar{v}$ ;  $\bar{w}$  and

## **Chapter 2 – Literature review**

Where,  $p_0$  is the ambient pressure;  $h$  is the average film thickness;  $e$  is the oscillation amplitude;  $\omega$  is the angular velocity of the vibration;  $\epsilon$  is the non-dimensional amplitude;  $S$  is the squeeze number.

As an approximation, Eq. (2.4), though nonlinear, can be linearized by assuming that the oscillation amplitude  $e$  is much smaller than the gap thickness. Furthermore the pressure change  $p$  must be small compared to the ambient pressure  $p_0$ .

The linearized Reynolds equation is widely used in MEMS structure analysis [41 and 42]. Also in optimizing the MEMS structure [43-46], its dynamic behaviour can be simulated in ANSYS using the linearized Reynolds equation to determine the important parameters of damping coefficient and spring stiffness. For instance, the MEMS structure can be perforated to effectively reduce the damping of the oscillating plate in order to maintain the dynamic characteristics for design requirements.

However, the linearized Reynolds equation cannot be used for obtaining the levitation pressure in a squeeze film. This is because when the Reynolds equation is linearized, the important feature of asymmetrical pressure is lost. As a result there is no levitation force for supporting a load. The next paragraph will focus on the important parameters for the non-dimensional Reynolds equation.

The key parameters in the non-dimensional Reynolds equation are the squeeze number and the non-dimensional amplitude for determining the pressure in the squeeze film. If  $S$  approaches to zero, the fluid can escape before it compresses. Therefore, the fluid only adds damping to the system. But if  $S$  goes to infinite, which means the very high oscillation frequency, the fluid is essentially trapped in the gap and behaves more like a spring rather than a damper [47].

### **2.6 Forced vibration**

Given the fact that all the machines that contain moving components may vibrate, the excitation forces transmitted to adjacent components within machines can produce the motion, vibration with different amplitude and frequency. The vibration can also be an unwanted sound, that is, noise when an oscillation frequency is in the audible range;

## **Chapter 2 – Literature review**

and more often, vibration is considered to be undesirable and wasting energy. There are occasions, though not many, where vibration can be put to good use, for example, vibration-assisted machining for improving surface finish and enhancing tool life [48], and vibration bowl feeders for transporting work pieces.

In this research, vibration is deliberately produced by driving piezoelectric actuators in order to force a solid structure to deform and this vibration is called forced vibration. The forced vibration is when an alternating force or motion is applied to a mechanical system. In forced vibration, the dynamic response of the structure has the same frequency as the excitation frequency but not same magnitude. The forced vibration is normally accompanied with a transient vibration initially but the transient vibration decays with time and hence will disappear given sufficient time [49].

In ANSYS workbench, flexible dynamic analysis (also called time-history analysis) is a technique used to determine the dynamic response of a structure under the action of any general time-dependent loads. The analysis can determine the time-varying displacements, strains, stresses, and forces when an excitation force is acting on the structure [50].

## **2.7 Driving unit - piezoelectric actuator**

### **2.7.1 Piezoelectric actuator**

The piezoelectric ceramics are multi-functional devices of many applications. It can work as a generator of sufficient voltage to be used as igniters in fuel lighters, gas stoves, and other such applications. It can also work as sensors and transducers, to convert various physical parameters into electrical signals. It can also work in reverse: to convert electrical energy into vibration mechanical energy. An example is the piezoelectric ceramics used as piezoelectric actuators, converting a voltage into a precise physical displacement. The piezoelectric actuators have been widely used to generate ultrasonic vibrations [51]. In this section is explained the working principles of the piezoelectric actuator, including the piezoelectric effect, the types of actuator and the interpretation of manufacturer's data of the piezoelectric actuator [52 and 53].

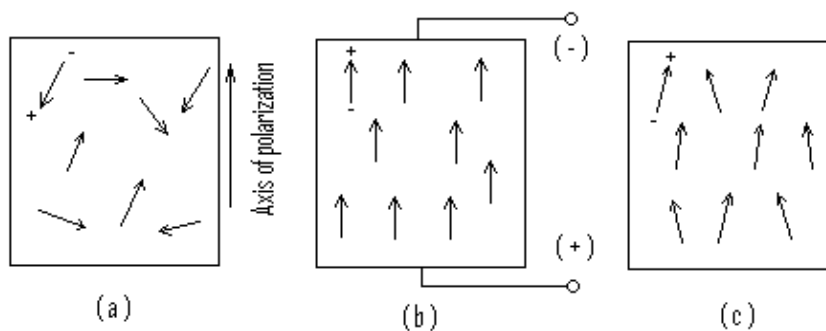


## Chapter 2 – Literature review

### 2.7.2 Piezoelectric effect

In 1880, the piezoelectric effect was discovered by two brothers, Jacques and Pierre Curie. They found out that when subjected to a mechanical force certain crystalline minerals become electrically polarized. Tension and compression generate voltages of opposite polarity, in proportion to the applied force. The converse of this relationship also is true: a voltage-generating crystal exposed to an electric field lengthens or shortens according to the polarity of the field, and in proportion to the strength of the field. These behaviours are the *piezoelectric effect* and the *inverse piezoelectric effect*, respectively [54 and 55].

An important term - *polarization axis* should be introduced, as in Figure 2.16. The polarization axis is an imaginary line that aligns with the directions of dipoles. The piezoelectric ceramics are isotropic because dipoles are randomly oriented in the piezoelectric ceramics, shown in Figure 2.16 (a), as manufactured. In order to produce the piezoelectric effect, the piezoelectric ceramics is exposed to a strong DC electric field at a temperature slightly below the Curie temperature. The dipoles can be oriented and aligned with applied DC electric field as shown in Figure 2.16 (b). But even when the electric field is removed - Figure 2.16 (c), the dipoles remain more or less in the same orientation as when the DC electric field was applied - Figure 2.16 (b). Thus the piezoelectric effect is produced through this polarization treatment. [56 and 57]



- (a) Random orientation of polar domain prior to polarization;
- (b) Polarization in DC electric field;
- (c) Remnant polarization after DC electric field removed;

## Chapter 2 – Literature review

Figure 2.16 - Polarization axis of a piezoelectric ceramic.

Figure 2.17 illustrates the working principles of the *piezoelectric effect* and the *inverse piezoelectric effect* based on those conditions. Figure 2.17 (a) shows a poling axis of a stack piezoelectric disc without applying a force or voltage. When the piezoelectric disc is compressed or stretched along the direction of polarization as shown in Figures 2.17 (b) and (c), the voltage will be produced of same polarity as the polarization axis between electrodes. Furthermore, the compression and tension can create the same magnitude of voltage but is opposite to that of the polarization axis. If a voltage is applied along the direction of the polarization as shown in Figures 2.17 (d) and (e), the length of the piezoelectric disc will lengthen or shorten and the diameter of it will become smaller or bigger, respectively. If an alternating voltage is applied, the piezoelectric disc will lengthen and shorten cyclically as shown in Figure 2.17 (f), in the same frequency as the applied frequency.

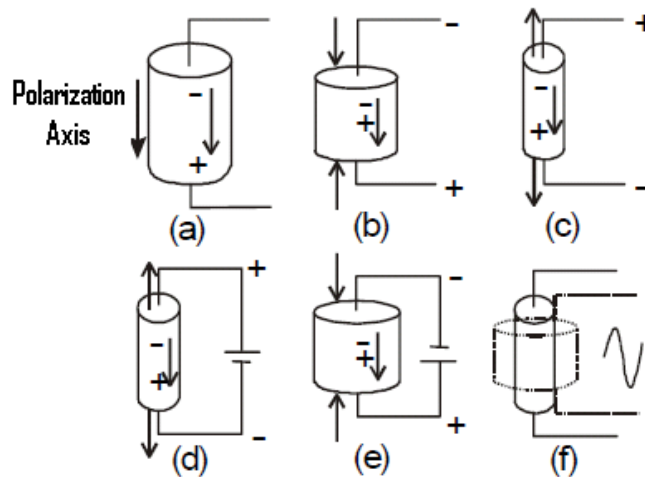


Figure 2.17 - Piezoelectric effect diagram [58].

### 2.7.3 Mathematical description for piezoelectric effect

To describe the behaviour of the piezoelectric actuator, mathematic equations are needed to model the piezoelectric effect. The piezoelectric effect is the combination between the behaviour of mechanical and electrical. The mechanical behaviour of the

## Chapter 2 – Literature review

piezoelectric actuator is described by Eq. (2.5). The strain of the piezoelectric actuator can be changed by the applied stress in terms of the compliant matrix. The electrical behaviour of the piezoelectric actuator is described by Eq. (2.6), from which the electric displacement is controlled by the production of the dielectric matrix and electric field [59].

$$(2.5)$$

$$(2.6)$$

Combining Eq. (2.5) and (2.6), the coupled equations (manufacturer's data) Eq. (2.7) and (2.8) can be used to describe the piezoelectric effect. The strain of the piezoelectric actuator can be controlled either by the mechanical term– stress and compliant matrix or by electrical term– electric displacement and piezoelectric matrix, as seen Eq. (2.7); and the electric displacement of the piezoelectric actuator can be controlled either by mechanical term - stress and transposed piezoelectric matrix or by electrical term – electrical displacement and dielectric matrix, as seen in Eq. (2.8).

$$(2.7)$$

and

$$(2.8)$$

where

= stress vector (six components  $x, y, z, yz, xz, xy$ );

= strain vector (six components  $x, y, z, yz, xz, xy$ );

= electric displacement vector (three components  $x, y, z$ );

= electric field vector (three components  $x, y, z$ );

= compliance matrix evaluated at constant electric field, i.e. short circuit;

= piezoelectric matrix relating strain/electric field;

= piezoelectric matrix relating strain/electric field (transposed);

= dielectric matrix evaluated constant stress, i.e. mechanically free.

## Chapter 2 – Literature review

The above coupled equations Eq. (2.7) and (2.8) are not only to be implemented for illustrating the piezoelectric effect but also for calculating the important parameters of the piezoelectric actuator subsequently.

### 2.7.4 Manufacturer’s data for piezoelectric actuator

All necessary manufacturer data of the purchased piezoelectric actuator are supplied. The manufacturer data can be used for calculating some basic parameters for the piezoelectric actuators, like maximum stroke length and maximum blocking force, under certain conditions. By considering the necessary parameters, the types of the piezoelectric actuators can be selected accordingly for achieving the design requirements.

To study the behaviour of the piezoelectric actuators, some piezoelectric properties are used and obtained from the manufacturer’s data sheet shown in Figure 2.18. The piezoelectric properties, or namely the piezoelectric coefficients, are described by symbols and notations. Some of the piezoelectric property symbols are listed and defined in Table 2.3 [60]. These symbols identify the piezoelectric property: electro-mechanical Coupling Coefficient, Piezoelectric Charge Constants, etc.

Table 2.3 - Piezoelectric property definitions.

Property	Definition	Units
Electro-mechanical Coupling Coefficient  k	or	–
Piezoelectric Charge Constants  d	or	meter / Volt  or Coulomb / Newton

## Chapter 2 – Literature review

Piezoelectric Voltage Constants $g$	or	Volt/Newton or meter/Coulomb
Relative Dielectric Constant $\epsilon$		–
Young's Modulus $Y$		Newton/meter <sup>2</sup>
Density $\rho$		Kg/meter <sup>3</sup>
Frequency Constant $N$	Controlling dimensions	Hz·meter

It can also be observed that the symbols are accompanied with superscript and subscript notations which describe the characteristics of a piezoelectric property, as shown in Figure 2.18. Those notations are introduced because a piezoelectric ceramic is anisotropic, piezoelectric properties are dependent on both the direction of the applied mechanical or electric force and to the directions perpendicular to the applied force. The superscripts describe external factors, like physical mounting, electrical conditions, that affect the piezoelectric property. The subscripts describe the relationship of the property to the polarization axis. The symbols and the superscript and subscript notations need to be described in orthogonal system as shown in Figure 2.19 [60]. The direction of the positive polarization is made to coincident with the Z – axis of an orthogonal system, from which the direction X, Y, or Z is represented by subscript 1, 2, or 3, respectively; and the shear is represented by the subscript 4, 5, or 6, respectively. Each piezoelectric coefficient generally consists of two subscripts, the first identifies the direction of the action and the second identifies the direction of the response. For example:  $d_{31}$ ,  $d_{32}$ , and  $k_{33}$  are described in the Table 2.4. The more description of all the other piezoelectric coefficients is given in Appendix A1.

## Chapter 2 – Literature review

### Piezoelectric Ceramics

■ Typical values (at room temp. and low signal data).

• PZT –  $\text{Pb}(\text{Zr}\cdot\text{Ti})\text{O}_3$  / The lead zirconate titanate materials ( hard ceramics ).

Material No.			C-13	C-2	C-21	C-22	C-23	C-3	C-4
Use examples.			Reso- nator Filter	Gas lighter Cleaner	Sonar Massage	Cleaner Fish sonar	Gas lighter	Flaw detector Thickness meter	
Coupling factors.	$\times 10^{-2}$	$k_p$	34	63	59	51	59	45	36
		$k_{31}$	20	37	34	29	35	26	23
		$k_{33}$	45	76	71	63	73	64	57
		$k_t$	40	52	48	45	54	49	39
		$k_{15}$	47	77	74	59	79	64	53
Frequency constants.	m · Hz	$N_p$	2600	2100	2210	2150	2210	2460	2520
		$N_{31}$	1880	1550	1630	1520	1650	1810	1840
		$N_{33}$	1910	1410	1510	1510	1480	1710	1760
		$N_t$	2230	2020	2090	2000	2040	2140	2150
		$N_{15}$	1190	880	910	930	870	1060	1100
Dielectric constants.		$\epsilon_{11}^T / \epsilon_0$	810	1970	1900	1260	1700	820	560
		$\epsilon_{33}^T / \epsilon_0$	810	1460	1400	1300	800	510	330
Piezoelectric charge constants.	$\times 10^{-12}$ m/v (c/N)	$d_{31}$	-51	-158	-131	-140	-100	-55	-39
		$d_{33}$	116	367	288	285	270	154	110
		$d_{15}$	195	692	634	392	690	381	201
Piezoelectric voltage constants.	$\times 10^{-3}$ v·m/N (m <sup>2</sup> /c)	$g_{31}$	-7.0	-12.7	-10.7	-10.2	-14.4	-12.0	-12.8
		$g_{33}$	16.0	29.2	27.2	21.5	32.8	32.4	33.7
		$g_{15}$	27.0	39.7	37.7	35.2	44.9	43.5	40.8
Yungs mdulus.	$\times 10^{10}$ N/m <sup>2</sup>	$Y_{11}^E = 1/s_{11}^E$	10.8	7.3	8.3	7.0	8.3	10.0	10.3
		$Y_{33}^E = 1/s_{33}^E$	10.8	5.3	6.4	6.4	6.1	8.2	8.7
		$Y_{55}^E = 1/s_{55}^E$	4.2	2.2	2.3	2.5	2.0	2.5	3.5
Poisson's ratio.		$\sigma$	0.30	0.30	0.29	0.34	0.26	0.28	0.29
Mechanical Q		$Q_m$	1880	1200	1400	1100	1400	1900	1700
Dissipation factor.	%	$\tan \delta$	1.4	0.25	0.30	0.20	0.27	0.20	0.35
Curie point.	°C	$T_c$	330	300	307	350	290	270	330
Density.	$\times 10^3$ kg/m <sup>3</sup>	$\rho$	7.70	7.60	7.80	7.65	7.63	7.60	7.60
Temp. coefficient.	$frT_c$ ppm/°C	-40 ~ +20 °C	-16	200	110	410	120	10	20
		+20 ~ +80 °C	-36	90	110	340	-150	-180	-170
	$C_pT_c$ ppm/°C	-40 ~ +20 °C	2000	1820	1810	1260	1500	2670	2250
		+20 ~ +80 °C	3400	4120	3630	2260	4900	5370	4360
Characteristics.			Small temp. coefficient	General high power driving			High $k_{33}$ High voltage occurrence	Low $\epsilon_{33}^E$	

Figure 2.18- Manufacturer data sheet from Fuji Ceramic Company.

## Chapter 2 – Literature review

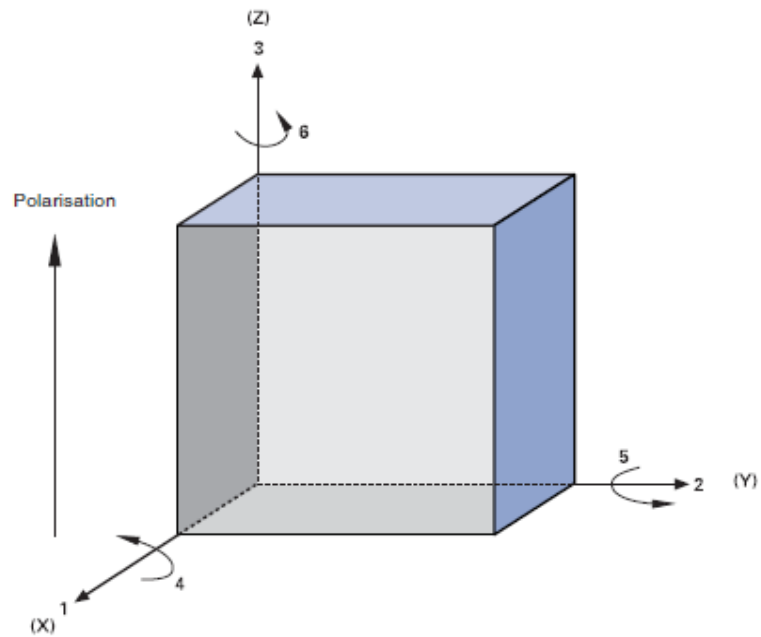


Figure 2.19 - Orthogonal system describing the properties of a piezoelectric ceramic; axis 3 is the direction of polarization [60].

Table 2.4 - Description of piezoelectric coefficients.

Piezoelectric coefficients	Descriptions
$d_{31}$	<p>First subscript 3 indicates that the electrodes are perpendicular to polarization axis 3;</p> <p>Second subscript 1 indicates that the piezoelectric induced strain, or the applied stress, is in direction 1.</p>
	<p>Superscript T indicates that all stresses on material are constant. For example: zero external forces.</p> <p>First subscript indicates the electrodes are perpendicular to axis 1;</p> <p>Second subscript indicates that permittivity for dielectric displacement in direction 1 as well.</p>

## Chapter 2 – Literature review

	<p>Superscript D indicates that the compliance is measured with electrode circuit open.</p> <p>First subscript indicates that strain or stress is in direction 1;</p> <p>Second subscript indicates that stress or strain is in direction 1.</p>
$k_{33}$	<p>First subscript indicates that the electrodes are perpendicular to axis 3;</p> <p>Second subscript indicates that the piezoelectric induced strain, or the applied stress, is in direction 3.</p>

### 2.7.5 Piezoelectric actuator types

The piezoelectric actuators can be categorized into the axial, transversal and flexional according to the type of mechanical displacement they produce. The axial actuator can accept a driving signal applied parallel to the direction in which the piezoelectric actuator element is polarized and creates a usable response in the same direction. In other words, the input signal is along Z direction and the output response is also along Z direction, so the axial actuator also is called the mode actuator, refer to Figure 2.19. The transversal actuator can accept a signal applied parallel to the direction in which the actuator element is polarized and create a useable response in the perpendicular to the direction of polarization. Or can be said that the input signal is along Z direction but the output response is along X direction, so the transversal actuator is also called the mode actuator. The flexional actuator also operating in the mode, constructed from bimorph ceramic element, produces significant large movement. [55].

The axial and transversal actuator can produce large blocking force but small movement. But the flexional actuator can produce very weak blocking force but considerable movement, so flexional actuator is commonly used as a sensor rather than an actuator.



## **Chapter 2 – Literature review**

Both the axial and transversal actuators have single layer or stack constructions. The single layer piezoelectric actuator normally is used to generate a stroke in the transversal direction [55]. For most applications, the single layer piezoelectric actuator hardly produces a usable stroke in the axial direction unless applying huge voltage (typically kilovolts) to it. The stack constructions are several piezoelectric elements connected mechanically in series and electrically in parallel. The movement of each piezoelectric element adds together to produce the total stroke length. The stack piezoelectric actuator can produce a large stroke approaching about 0.2% of the height of the total stack of elements and it also can achieve big blocking force. The maximum stroke length and the blocking force can be calculated or available from manufacturer. By understanding the capabilities of the different types of piezoelectric actuator can be useful to select for applying in the different applications. Based on the high precision feature on the stroke length, both the single layer and the stack piezoelectric actuators are widely used in the precise position devices [61 and 62], the fast tool servo (FTS) [63 and 64] in the micromachining. Moreover, they are also used for producing the active damping during machining [65].

## **2.8 Modal analysis**

### **2.8.1 Natural frequencies and mode shapes**

Modal analysis [66 and 67] can determine the theoretical vibration characteristics, in terms of natural frequencies and mode shapes, of a structure or a machine component. The natural frequencies and the mode shapes are important parameters in the design of a structure for dynamic loading conditions.

The natural frequencies are determined by the material properties (Density and Young's modulus) and the boundary conditions of the structure, so either the material or the boundary condition of the structure is changed, the natural frequencies will change.

The mode shape is a specific pattern of vibration executed by a mechanical system at a specific frequency. Different mode shapes will be associated with different natural frequencies. The experimental technique of modal analysis can discover the mode shapes and the natural frequencies [68].

## **Chapter 2 – Literature review**

### **2.8.2 Natural frequency measurement**

In the impact hammer testing experiment, the natural frequencies of the structure can be measured using either a displacement sensor or an accelerometer [69]. The difference in measurement is that the displacement sensor can measure displacement directly and the accelerometer can only obtain the displacement indirectly through two times of integration but the accuracy can be reduced. The other disadvantages of using accelerometer are that it cannot be attached onto the moving part because of the wire and its own weight can affect the natural frequency typically for light structures. But using the displacement sensor can overcome those drawbacks in such a way that it is none contacting with moving part. So the displacement is the best option for measuring film thickness in this research.

When a cyclic load with an excitation frequency is coincident with the one natural frequency of the structure, the oscillation amplitude of the structure will be much greater than exciting in other frequencies. At these resonant frequencies, even small periodic driving forces can produce large amplitude oscillations, because the system stores vibration energy. Many designs attempt to predict the natural frequencies of the structure in order to operate away from it. But this research will take advantage of using the resonance to produce larger oscillation deformation.

## **2.9 Software packages**

### **2.9.1 Pro-Engineering Wildfire 4.0**

In this research work, Pro-Engineering [70] is used for designing the structures, like the squeeze film air bearing and the guide way holder, in 3-D drawings that can also be converted into 2-D mechanical drawings for manufacturing in workshop. Moreover, the Pro-Engineering can save in the format of .STP which can be used to communicate with other software (ANSYS) for investigating and analyzing the characteristics of the structure.

## **Chapter 2 – Literature review**

### **2.9.2 ANSYS**

Finite element analysis is a computer-based numerical technique that is used to solve stress analysis, static analysis, modal analysis, fluid flow and other types of engineering problems [71]. As a general guideline, there are three stages for setting up the finite element analysis. They are:

1. Pre-processing: defining the problem.
  - Define dimensions;
  - Define element type and material properties;
  - Define mesh;
2. Solutions: assigning loads, constraints and solving.
3. Post-processing: viewing the results.

The software used for finite element analysis is ANSYS that helps in the modelling of the proposed structure for designing process and understanding the problem. In this study, ANSYS is used for modelling the modal analysis, static analysis and dynamic analysis of the squeeze film air bearing.

1. Modal analysis - To determine the natural frequencies and the mode shapes;
2. Static analysis - To calculate the static deformation of the structure by driving a piezoelectric actuator with a DC voltage;
3. Dynamic analysis - To calculate the dynamic response of the structure by driving a piezoelectric actuator by a DC offset and an AC voltage with certain frequency.

The type of finite element should be chosen correctly based on the analyses. The finite element Solid5 was chosen because:

1. It is a coupled-field element;
2. It is suitable for three dimensional (3 – D) analyses;
3. It is capable of modelling the piezoelectric actuator.

## **Chapter 2 – Literature review**

The finite element Solid 95 was chosen for modelling the behaviour of the solid structure – squeeze film bearing because:

1. It is a 20 - Node structural solid element;
2. It is suitable for three dimensional (3 – D) analyses;
3. It can tolerate irregular shapes without as much loss of accuracy;
4. It has compatible displacement shapes and well suited to model curved boundaries.

### **2.9.3 CFX**

Computational Fluid Dynamics (CFD) is a computer-based tool for simulating the behaviour of systems involving fluid flow, heat transfer, and other related physical processes. It works by solving the equations of fluid flow (in a special form) over a region of interest, with specified (known) conditions on the boundary of that region [72].

CFX, a tool for the computational fluid dynamics, is used in the research for investigating the behaviours and effects of an air film in small gaps between fixed surfaces and structures moving perpendicular to the surfaces in sufficiently high vibration frequencies. The CFX can also work out critical parameters, like oscillation amplitude and oscillation frequency, in the squeeze air film simulation.

### **2.9.4 LabVIEW**

LabVIEW is short for Laboratory Virtual Instrument Engineering Workbench, which provides a development environment based on the graphical programming language G. The LabVIEW programming environment is not only for acquiring, analyzing, and presenting data but also suitable for applications beyond measurement and automation [73 and 74]. The virtual measurement program provides a graphical interface for a user to define and control the data acquisition process to operate at various sampling rates and durations of recording as shown in Figure 2.20.

## Chapter 2 – Literature review

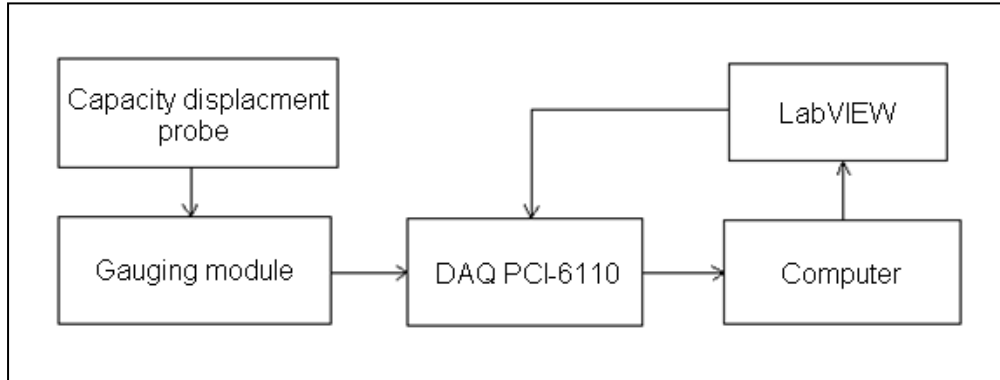


Figure 2.20 – Details of connection for transferring signals to user interface.

### 2.10 Summary

This chapter has reviewed the background of the contact and the non-contact bearings, in particular, the squeeze film bearings. It was reviewed that the development of the squeeze film bearing up to day and also pointed out the limitations of the existing squeeze film bearings. In 1964, Salbu first designed the squeeze film bearing based on the theory derived from Stefan and Reynolds. The magnetic actuator was used as the driving unit and operated in the audible range of oscillation. The main problem of this design was to induce an intolerant noise during operation. The following designs also had advantages and disadvantage. Especially, several designs and detail studies from both Stolarski and Yoshimoto really contributed the knowledge in this field. In 2006, Yoshimoto proposed a new design of the squeeze film bearing not only to overcome the noise problem but also to avoid use of the elastic hinges. But only fundamental natural frequency and mode shape had been investigated. So it has led to the questions of whether better performance can be achieved by driving a bearing at a modal frequency above the fundamental and whether the other mode shapes can also achieve the squeeze film effect, which mode shape has more superior levitation performance.

The chapter also reviewed the basic knowledge for an understanding of the squeeze film effect. It includes the ideal gas law and adiabatic process, the Reynolds equation, forced vibration, modal analysis and some detailed studies on the driving unit – piezoelectric actuators. The relevant software packages, Pro-Engineering, ANSYS and CFX are used in the design process, modelling in finite element analysis and analyzing

## **Chapter 2 – Literature review**

the critical parameters, oscillation amplitude and oscillation frequency, for the study of the squeeze air film. The LabVIEW is used to capture and filter the raw signal; moreover, it can also save data in Excel for further signal processing.

## **Chapter 3 – Single layer piezoelectric actuator calculation**

# **Chapter 3 – Single layer piezoelectric actuator calculation**

### **3.1 Introduction**

The piezoelectric ceramics as multi-functional devices can have many applications. But the main use of the piezoelectric ceramics in this research project is as an actuator. The different types of piezoelectric actuators and the working principle have been reviewed in Chapter 2. Because the levitation performance of a squeeze film bearing is largely dependent on the amplitude of the oscillation that is generated by the piezoelectric actuators, a deep understanding of the theory of the piezoelectric effect is essential to the accurate modelling of the piezoelectric actuator, its interaction with the bearing shell to which it is attached, and the coupled analysis of the bearing shell and the squeeze-film.

In this chapter, it is presented a single layer piezoelectric actuator calculation for the two parameters: the maximum stroke length and the maximum blocking force. Also described is ANSYS simulation for modelling the single layer piezoelectric actuator.

### **3.2 Single layer piezoelectric actuator calculation**

The most of applications, the displacement is produced by powering the piezoelectric actuator by an electrical signal; or if the displacement is constraint (blocked), the blocking force can be generated. The maximum blocking force can be generated by the piezoelectric actuator, which depends on its stiffness and the maximum displacement. The relationship between a blocking force and a free stroke length is shown in Figure 3.1. It can be seen that the maximum free stroke length can be obtained when the block force is zero. In other words, the piezoelectric actuator without any constraints can produce the maximum free stroke length. On the contrary, the maximum blocking force can be obtained when the free stroke is zero. In most applications, the

### Chapter 3 – Single layer piezoelectric actuator calculation

piezoelectric actuator is normally constrained though not to the full extent and so some blocking force and stroke length do exist together.

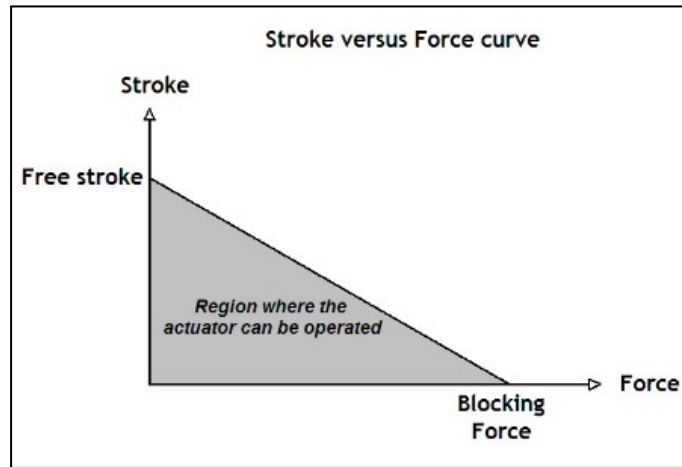


Figure 3.1 - Relationship between free stroke length and blocking force.

The single layer piezoelectric actuator selected in the study, has a length ( $l$ ) of 15 mm, a width ( $w$ ) of 5mm and a thickness ( $t$ ) of 0.5mm. The two important parameters, the maximum stroke length and maximum blocking force, can be calculated based on the dimensions of the piezoelectric actuator using the supplied manufacturer's data.

#### 3.2.1 Maximum stroke length

The maximum stroke length can be worked out using Eq. (2.7). The first term of the right hand side can be ignored because of the zero stress. So Eq. (2.7) can be simplified to

$$(3.1)$$

In Eq. (3.1), the electric field  $E$  and the strain  $S$  are defined respectively as

$$(3.2)$$

where  $V$  is the driving voltage,  $t$  is the thickness of the piezoelectric actuator,  $\Delta l$  is the increased length and  $l_0$  is the original length for the piezoelectric actuator.

By substituting Eq. (3.2) into Eq. (3.1), the maximum stroke length is



**Chapter 3 – Single layer piezoelectric actuator calculation**

(3.3)

The single layer piezoelectric actuator is the type of the transversal actuator (mode). So the maximum free stroke length should be along with the X direction rather than the other two. There are several options to increase the stroke length, which are to increase the piezoelectric constant, to increase the applied voltage, to increase the length or to decrease the thickness of the piezoelectric actuator, referred to Eq. (3.3). Some options are constrained because of the nature of the selected piezoelectric actuator, like the dimensions and the piezoelectric constant, but not of the driving voltage. In other words, the driving voltage is a relatively flexible parameter to control the stroke length; and Eq. (3.3) shows the linear relationship between the stroke length and the driving voltage. But the supplied voltage is limited by the external actuator driver and the safety issue, it is important to select a piezoelectric actuator with correct ability for the design application [75].

To position the piezoelectric actuator in the orthogonal system, in which the length is along X axis, the width is along Y axis and the thickness is along Z axis, as shown in Figure 3.2. The stroke length of the three directions in the orthogonal can be calculated using Eq. (3.3) in terms of those known values that are the piezoelectric constant  $d$ , the length  $l$  and thickness  $t$  of the piezoelectric actuator and the driving voltage  $V$ .

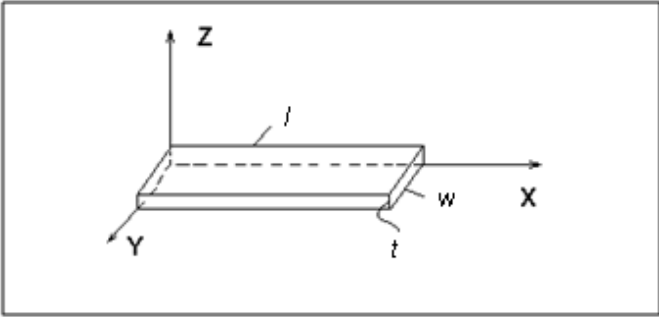


Figure 3.2 - Locate the piezoelectric actuator in the orthogonal system.

### Chapter 3 – Single layer piezoelectric actuator calculation

The piezoelectric actuator made of the material No: C – 21, the piezoelectric constant  $d_{31}$  and  $d_{33}$  are available in the manufacturer data sheet in Figure 2.17. The length ( $l$ ), the width ( $w$ ) and the thickness ( $t$ ) of the piezoelectric actuator are 15 mm, 5 mm and 0.5 mm respectively. The driving voltages of 0 V and 150 V are applied to the bottom and top surface of the piezoelectric actuator layer on the Z axis. The stroke length in the three directions,  $\Delta x$ ,  $\Delta y$ ,  $\Delta z$  are calculated and listed in Table 3.1.

Table 3.1- Stroke length in X, Y and Z directions.

Direction of stroke length	Formula	Result
		$\Delta x = 0.0015 \text{ m}$
		$\Delta y = 0.0005 \text{ m}$
		$\Delta z = 0.0075 \text{ m}$

The calculated stroke lengths are the maximum stroke length because the piezoelectric actuator is not constraint. It can be observed from Table 3.1 that the stroke length  $\Delta z$  is greater than the  $\Delta x$  and  $\Delta y$ , because the piezoelectric actuator chosen for study is the transversal type ( $d_{31}$  mode).

But in a real application, the stroke length cannot reach the maximum value because the operation condition normally involves some external forces or constraints and also be affected by the mounting manner. The other external factor, like environmental temperature and humidity, can also influence the stroke length of the piezoelectric actuator. The stroke length of the piezoelectric actuator can increase with increasing of the environmental temperature. In summary, the maximum stroke length can be considered as a method to anticipate the upper bound of the static response of a mechanical structure in the design.

### Chapter 3 – Single layer piezoelectric actuator calculation

#### 3.2.2 Maximum blocking force

The maximum blocking force is the other important parameter to be considered carefully in use of the piezoelectric actuator. The transversal type of the piezoelectric actuator can produce the most dominant block force along the transversal direction. So only the maximum blocking force along X direction is useful to be calculated. The piezoelectric actuator can be considered as a spring with a constant stiffness  $K$ ; and the maximum displacement  $X$  can be achieved without applying external force or stress. The maximum blocking of the piezoelectric actuator can be given as:

$$(3.4)$$

where  $K$  is the stiffness constant of the piezoelectric actuator,  $X$  is the maximum stroke length in the condition of the absence of the applied stress or force.

The stiffness  $K$  and the maximum stroke length  $X$  can be expressed in Eq. (3.5) and (3.6), respectively.

$$(3.5)$$

$$(3.6)$$

where  $C$  is the elastic compliance evaluated at constant electric field, the others are all mentioned already in previous sections.

Substituting Eq. (3.5) and (3.6) into (3.4) gives the maximum blocking force as

$$(3.7)$$

Both the piezoelectric constant  $d_{31}$  and the elastic compliance  $C$  are available at the manufacturer's data sheet; the  $w$  is the width of the piezoelectric actuator 5 mm; and the driving voltage is -150V. Thus the maximum block force of the studied piezoelectric actuator is:

### **Chapter 3 – Single layer piezoelectric actuator calculation**

The piezoelectric actuator has the maximum blocking force of 8.19 N when its stroke length is zero. But in the real application, the blocking force cannot reach the maximum because the piezoelectric actuator, most often, cannot be fully constrained due to the way it is mounted and the compliance of the structure. The calculation of the maximum stroke length and maximum blocking force in Excel is given in Appendix C1.

### **3.3 ANSYS simulation for calculation of single layer piezoelectric actuator**

The piezoelectric actuator can also be analyzed in ANSYS software; it can calculate not only the maximum stroke length and the maximum blocking force in the simple boundary condition, but also the static and dynamic deformation in coupled field analysis involving interaction between the piezoelectric actuator and the mechanical structure, in the complicated boundary conditions subsequently. To simulate the piezoelectric actuator in ANSYS, it is necessary to clarify some matrix conversions due to the different formats between the manufacturer data and those required by ANSYS. The constitutive relationship given by manufacturers or published data/ reports is in the form of Eq. (2.7) and (2.8). Note that both the stress vector and the strain vector consist of six elements in the form  $\{x, y, z, yz, xz, xy\}$ . Both the electric displacement vector and the electric field vector consist of three elements in the form  $\{x, y, z\}$  [76]. On the other hand, ANSYS requires data in the following form, as

$$(3.8)$$

and

$$(3.9)$$

Where

= stress vector (six elements  $x, y, z, xy, yz, xz$ );

= strain vector (six elements  $x, y, z, xy, yz, xz$ );

= electric displacement vector (three elements  $x, y, z$ );

### Chapter 3 – Single layer piezoelectric actuator calculation

= electric field vector (three elements x, y, z);

= stiffness matrix evaluated at constant electric field, i.e. short circuit;

= piezoelectric matrix relating stress/electric field;

= piezoelectric matrix relating stress/electric field (transposed);

= dielectric matrix evaluated at constant strain, i.e. mechanically clamped.

In order to convert the manufacturer's data presented in the form of Eq. (2.7) and (2.8) into ANSYS required form of Eq. (3.8) and (3.9), Eq. (2.7) needs to be based on stress rather than strain. In other words, the left hand side of Eq. (2.7) should be stress vector. The conversions are shown in the following steps:

$$(3.10)$$

$$(3.11)$$

Since Eq. (2.8) relates electric displacement to strain rather than stress, Eq. (3.11) can then be substituted back into Eq. (2.8):

$$(3.12)$$

$$(3.13)$$

Upon comparison of Eq. (3.12) and (3.13) with Eq. (3.8) and (3.9), one can obtain the relationship between manufacturing data and ANSYS – required values:

$$(3.14)$$

$$(3.15)$$

The above procedure explains the equations conversion from the manufacturer's format to ANSYS required format. Also, note that the stress vector in the form {x, y, z, xy, yz, xz} defined in ANSYS is different to the one defined in the manufacturer's. So the

### **Chapter 3 – Single layer piezoelectric actuator calculation**

following sections will explain the conversions and the commands to convert the manufacturer's data into ANSYS data for the elastic matrix, the dielectric matrix, and the piezoelectric matrix.

#### **3.3.1 Elastic matrix**

The elastic matrix specifies the stiffness matrix or the compliance matrix. The relationship between the stiffness matrix  $S^E$  and compliance matrix  $C^E$  is displayed below in the manufacturer's format or IEEE standard.

The above stiffness/compliance matrix is symmetric and based on the real conditions, thus it can be simplified to:

As mentioned before, the stress vector and the strain vector consist of six elements in the form { x, y, z, yz, xz, xy}, but the stress vector and the strain vector in the form { x, y, z, xy, yz, xz} are defined in ANSYS. It is noticed that the supplied manufacturer's matrix can be converted into ANSYS input order by switching row and column data for the shear terms as shown below:

Since the above matrix is in ANSYS input format, attention is now turned to the issue of how to use the manufacturer's data to calculate each element and to substitute them into the compliance / stiffness matrix. The elements , , and are normally supplied in the

### Chapter 3 – Single layer piezoelectric actuator calculation

manufacturer's data sheet but not the others, like  $s_{11}$ ,  $s_{12}$ ,  $s_{13}$ , and  $s_{33}$ . They can be derived from the known elements using the equations as shown in Table 3.2.

Table 3.2- Calculation for the unknown elements of the compliance/ stiffness matrix.

Unknown component	Formula	Results

To input all the elements into the compliance/stiffness matrix gives:

The **TB** commands can be used to input the anisotropic elastic matrix that includes both the compliance matrix and the stiffness matrix into ANSYS by assuming the polarization in the Z axis.

To input the compliance matrix into ANSYS, the following commands can be used:

```

s11=1.2048 E-11
s12= - 3.4940 E-12
s13= - 4.5313 E-12
s33= 1.5625 E-11
s44= 4.3478 E-11
s66 = 3.1084 E-11
    
```

### Chapter 3 – Single layer piezoelectric actuator calculation

```
tb,anel,1,1,,1           ! TBOPT = 1 for compliance input
tbdata,1,s11,s12,s13     ! Input first row
tbdata,7,s11,s13        ! Input second row
tbdata,12,s33           ! Input third row
tbdata,16,s66           ! Input fourth row
tbdata,19,s44           ! Input fifth row
tbdata,21,s44           ! Input sixth row
tblast,anel             !List inputs
```

The compliance matrix can be inverted using the fact of to find the stiffness matrix using LabVIEW, from which all the elements in the stiffness matrix can be calculated.

To input the stiffness matrix into ANSYS, the following commands can be used:

```
c11= 0.11733E+12
c12 = 0.52768E+11
c13 = 0.49393E+11
c33 = 0.92788E+11
c44 = 0.22989E+11
c66 = 0.32154E+11
tb,anel,1,1,,0           ! TBOPT = 0 for stiffness input
tbdata,1,c11,c12,c13     ! Input first row
tbdata,7,c11,c13        ! Input second row
tbdata,12,c33           ! Input third row
tbdata,16,c66           ! Input fourth row
tbdata,19,c44           ! Input fifth row
tbdata,21,c44           ! Input sixth row
tblast,anel             !List inputs
```

Finally, either the compliance matrix or the stiffness matrix in ANSYS input order is needed for single layer piezoelectric actuator simulation. Moreover, both of them can be input into ANSYS using the **TB** commands and listed using the **TBLIST** command as shown in Figure 3.3.



## Chapter 3 – Single layer piezoelectric actuator calculation

```

ANSYS TBLIST Command
File
MATERIAL INPUT USING TB,ANEL COMMANDS FOR MATERIAL NUMBER 1
Flexibility (or compliance) matrix at temperature = 0.0
0.12000E-10 0.34900E-11 0.45300E-11 0.0000 0.0000 0.0000
-0.34900E-11 0.12000E-10 0.45300E-11 0.0000 0.0000 0.0000
0.45300E-11 0.45300E-11 0.15600E-10 0.0000 0.0000 0.0000
0.0000 0.0000 0.0000 0.31100E-10 0.0000 0.0000
0.0000 0.0000 0.0000 0.0000 0.43500E-10 0.0000
0.0000 0.0000 0.0000 0.0000 0.0000 0.43500E-10
Stiffness matrix computed from flexibility matrix at temperature = 0.0
0.11733E+12 0.52768E+11 0.49393E+11 0.0000 0.0000 0.0000
0.52768E+11 0.11733E+12 0.49393E+11 0.0000 0.0000 0.0000
0.49393E+11 0.49393E+11 0.92788E+11 0.0000 0.0000 0.0000
0.0000 0.0000 0.0000 0.32154E+11 0.0000 0.0000
0.0000 0.0000 0.0000 0.0000 0.22989E+11 0.0000
0.0000 0.0000 0.0000 0.0000 0.0000 0.22989E+11
    
```

Figure 3.3 - Compliance and stiffness matrices listed in ANSYS.

### 3.3.2 Permittivity matrix

The permittivity  $\epsilon$ , or the dielectric constant, is the other coefficient required in ANSYS for the piezoelectric actuator simulation. The relative dielectric constants under constant stress, and, are given in the manufacturer’s data sheet.

To model the piezoelectric actuator in ANSYS, it needs to be inputted the relative dielectric constants under constant strain, and, because the **MP** command can only be used to input but not; and the **MP** command can be applied for all piezoelectric element types; for instance, solid 5, solid 98 and so on. The other option is to use the **TB** command and it can be used to input both and, but it can only be used for several piezoelectric element types, not including solid 5. Based on the above understanding, the only option is to use the **MP** command to input, because the element type – solid 5 is the only one that can be used for 3 – D piezoelectric actuator analysis in ANSYS.

Eq. (3.14) can be applied to convert the dielectric constant, under constant stress into the dielectric constant, under constant strain. The procedure of the calculation is shown below, as

### Chapter 3 – Single layer piezoelectric actuator calculation

The permittivity matrix has only diagonal terms and the relationship between the relative dielectric constant and the dielectric constant is shown as:

where  $\epsilon_0$  is the permittivity of free space .

So the relative dielectric constant can be calculated and it can be inputted using the **MP** command into ANSYS directly.

To input the relative dielectric constant into ANSYS, the following commands can be used:

```
K11S=856.36  
K33S=713.28  
mp,perx,1,K11S           !Permittivity (x direction)  
mp,pery,1,K11S           !Permittivity (y direction)  
mp,perz,1,K33S           !Permittivity (z direction)
```

#### 3.3.3 Piezoelectric constant matrix

The piezoelectric constant, is the last coefficient required for modelling the piezoelectric actuator in ANSYS. The manufacturer's data has, which relates mechanical strain to electric field. However, ANSYS requires, relating mechanical stress to electric field, so Eq. (3.15) can be applied for the conversion from to. Because

### Chapter 3 – Single layer piezoelectric actuator calculation

the inversed compliance matrix has already been inputted into ANSYS, ANSYS can calculate internally using the transposed piezoelectric constant. The transposed piezoelectric constant matrix is given below in the form of ANSYS required { x, y, z, xy, yz, xz}.

To input the transposed piezoelectric constant into ANSYS, the following commands can be used:

```
d31=-1.31E-10
d33=2.88E-10
d15=6.34E-10
tb,piez,1,,1                                !Define Piez. table
tbdata,1,0,0,d31,0,0,d31                    !Input Piezoelectric stress matrix
[e]
tbdata,7,0,0,d33,0,0,0
tbdata,13,0,d15,0,d15,0,0
tblast,piez
```

Finally, the piezoelectric constant can be inputted into ANSYS using the **MP** command and listed using the **TBLIST** command in Figure 3.4.

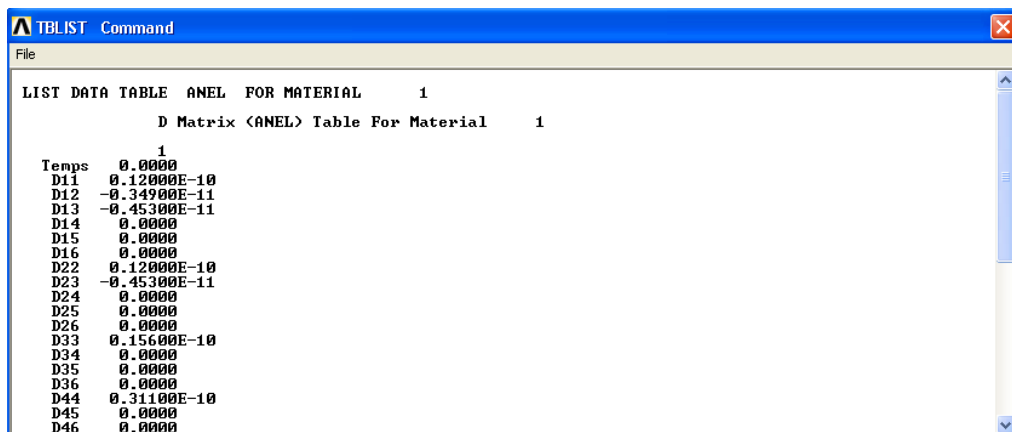


Figure 3.4 - Piezoelectric constant list in ANSYS.

## Chapter 3 – Single layer piezoelectric actuator calculation

### 3.3.4 ANSYS modelling

Using the three coefficients, namely the stiffness/compliance constant, the dielectric constant and the piezoelectric constant, the piezoelectric actuator can be analyzed and modelled in ANSYS to calculate the maximum stroke length and the maximum blocking force with 150 V and 0 V applied on the top and bottom layer of it, respectively. Furthermore, accurately modelling piezoelectric actuator can also be used for calculating the interaction between the piezoelectric actuator and the structure in the coupled field analysis subsequently.

The piezoelectric actuator is modelled and meshed in ANSYS using the commands below and shown in Figure 3.5, where the length is along the X axis, the thickness along the Y axis and the thickness along the Z axis in the coordinate system. The length is meshed 20 divisions, the width 5 divisions and the thickness 4 divisions. In ANSYS simulation, the finer and higher quality mesh provides more accurate results generally but at the expense of computational time.

```
/com  
/com -- Modeling  
/com  
block,0,15e-3,0,5e-3,0,0.5e-3 !Piezo model  
/com  
/com -- Meshing  
/com  
lesize,1,,4  
lesize,3,,4  
lesize,6,,4  
lesize,8,,4  
lesize,2,,20  
lesize,4,,20  
lesize,5,,20  
lesize,7,,20  
lesize,9,,5  
lesize,10,,5  
lesize,11,,5  
lesize,12,,5  
vsel,s,,1  
type,1  
mat,1  
mshape,0,3d !Volume mesh using Hex.
```

### Chapter 3 – Single layer piezoelectric actuator calculation

```
mshkey,1  
vmesh,1  
allsel
```

*!Mapped meshing*

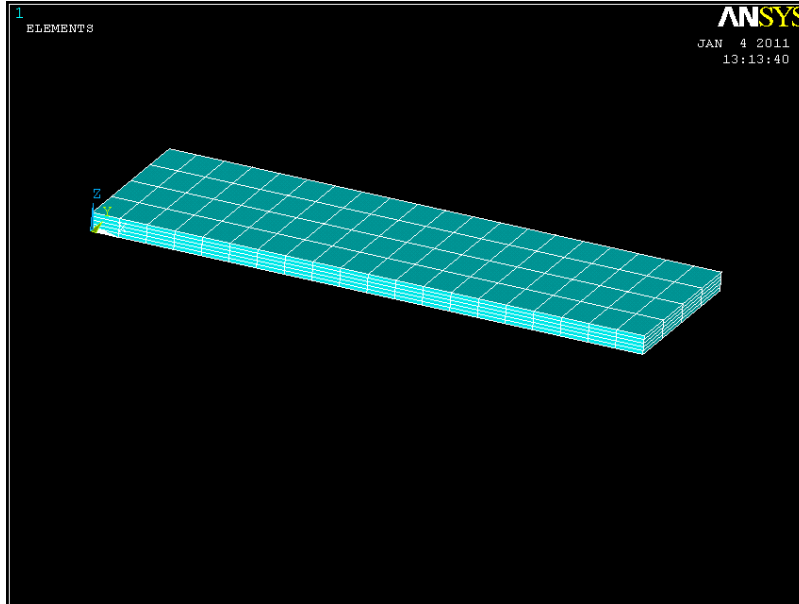


Figure 3.5 - Model of the piezoelectric actuator in ANSYS.

The boundary conditions are defined using the faces of the model of the piezoelectric actuator according to the coordinate system.

```
/com -- Boundary conditions for Piezo  
/com  
nselect,s,loc,x,0  
d,all,ux,0  
nselect,s,loc,y,0  
d,all,uy,0  
nselect,s,loc,z,0  
d,all,uz,0  
nselect,s,loc,z,0  
d,all,volt,vbot  
nselect,s,loc,z,0.5e-3  
d,all,volt,vtop  
allsel
```

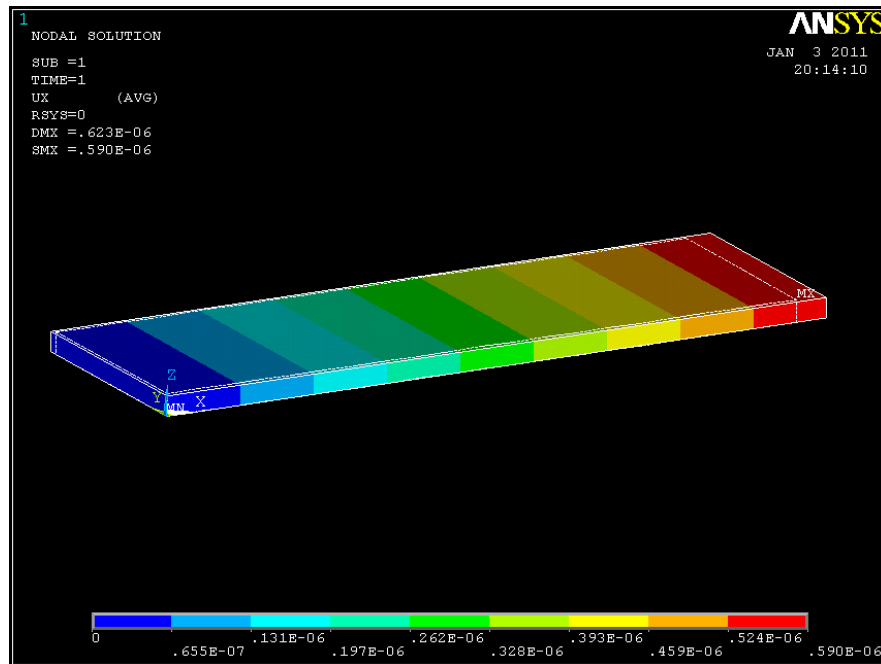
*!Fixed-free boundary conditions for all directions*

*!Apply Voltage on piezo layer*

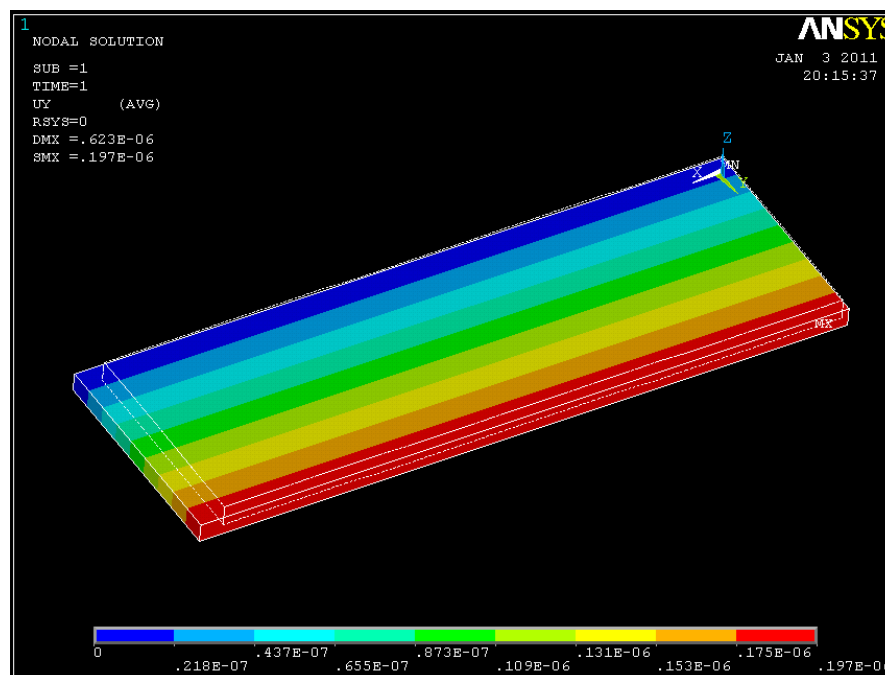
From ANSYS simulation, the results of the maximum stroke length for the piezoelectric actuator are given in Figure 3.6 where the red end of the colour spectrum denotes the maximum displacement, hence the stroke length, and where blue end of the

### Chapter 3 – Single layer piezoelectric actuator calculation

colour spectrum denotes the minimum displacement. Figure 3.6 show the maximum stroke length in the X, Y and Z directions are and , respectively. The error for the stroke length in X direction between the theoretical result and ANSYS simulation result is 0.085%.

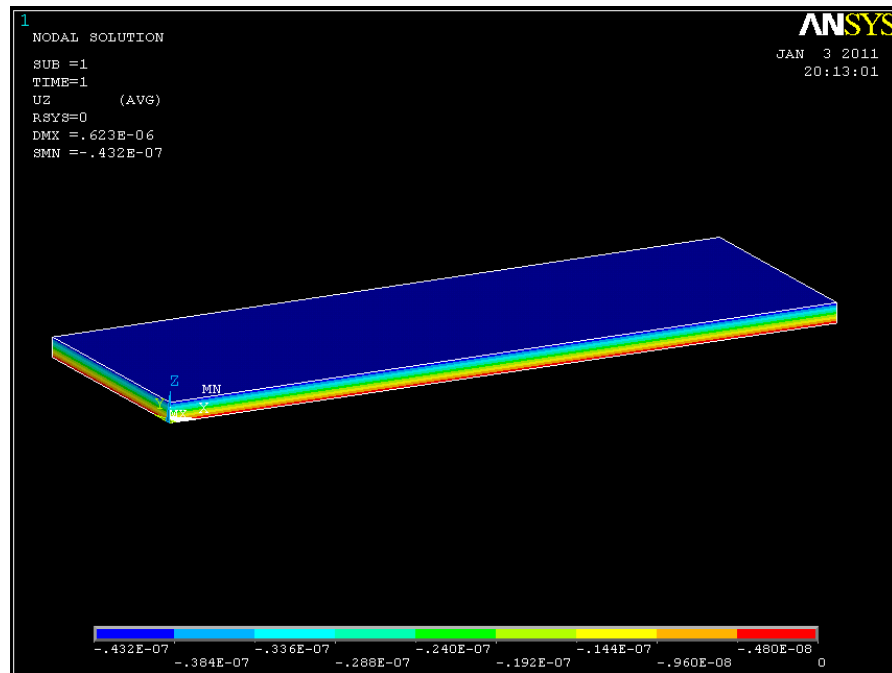


(a)



(b)

### Chapter 3 – Single layer piezoelectric actuator calculation



(c)

(a) Maximum stroke length in X direction;

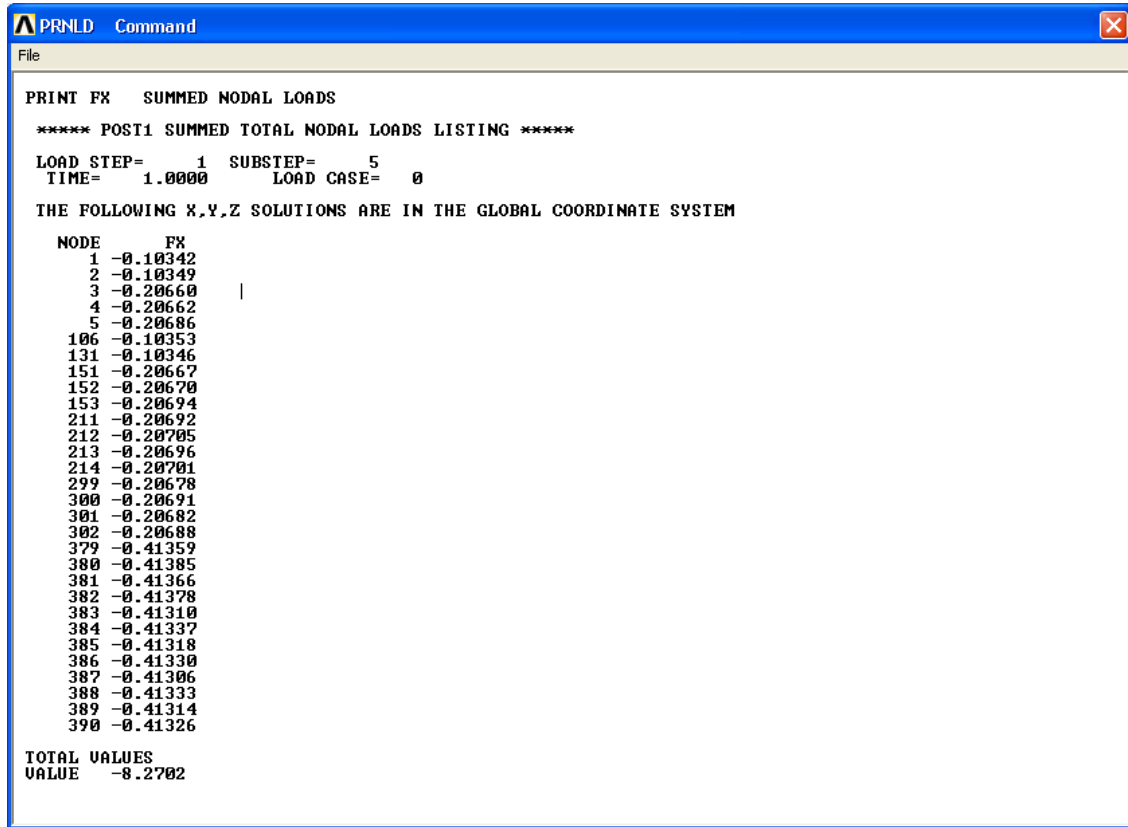
(b) Maximum stroke length in Y direction;

(c) Maximum stroke length in Z direction.

Figure 3.6 – Maximum stroke length in X, Y and Z direction with applying 150 V and 0 V on the top and bottom layer of the piezoelectric actuator.

The maximum blocking force can also be calculated by specifying that the displacements at the two end faces be zero. The maximum blocking force is 8.2702 N in ANSYS simulation shown in Figure 3.7. The error between the theoretical result and the simulation result is 0.97%.

## Chapter 3 – Single layer piezoelectric actuator calculation



```
PRNLD Command
File
PRINT FX SUMMED NODAL LOADS
***** POST1 SUMMED TOTAL NODAL LOADS LISTING *****
LOAD STEP= 1 SUBSTEP= 5
TIME= 1.0000 LOAD CASE= 0
THE FOLLOWING X,Y,Z SOLUTIONS ARE IN THE GLOBAL COORDINATE SYSTEM
NODE FX
1 -0.10342
2 -0.10349
3 -0.20660
4 -0.20662
5 -0.20686
106 -0.10353
131 -0.10346
151 -0.20667
152 -0.20670
153 -0.20694
211 -0.20692
212 -0.20705
213 -0.20696
214 -0.20701
299 -0.20678
300 -0.20691
301 -0.20682
302 -0.20688
379 -0.41359
380 -0.41385
381 -0.41366
382 -0.41378
383 -0.41310
384 -0.41337
385 -0.41318
386 -0.41330
387 -0.41306
388 -0.41333
389 -0.41314
390 -0.41326
TOTAL VALUES
VALUE -8.2702
```

Figure 3.7 – Maximum blocking force in ANSYS simulation.

ANSYS simulation of the piezoelectric actuator can model the maximum stroke length and the maximum blocking force accurately, and it is verified by the theoretical results. Such close agreement between ANSYS simulation and theoretical results increases the confidence in using ANSYS model for the subsequent coupled-field analysis where more complicated boundary conditions are expected. ANSYS Macro, which gives the programming details, to calculate the maximum stroke length and the maximum blocking of the piezoelectric actuator are given in Appendix C2.

### 3.4 Summary

In this chapter, the two important parameters, the free stroke length and the blocking force, are studied. Their values are calculated using Eqs. (3.3) and (3.7). With the



### **Chapter 3 – Single layer piezoelectric actuator calculation**

applied voltage of 0 and 150 V, the stroke length along the X direction and the blocking force were calculated to be 0.5895  $\mu\text{m}$  and 8.19 N respectively. The elastic matrix, the permittivity matrix and the piezoelectric constant matrix have to be converted into the ANSYS format from the manufacturer's data in ANSYS simulation. ANSYS simulation gives accurate results in both the stroke length and the blocking force with errors of only 0.085% and 0.97%, respectively, which can be considered acceptably small.

## **Chapter 4 – Modelling structural characteristics and squeeze film effect**

### **4.1 Introduction**

In this chapter, a coupled-field analysis is used to deal with an interaction of analyses from different engineering disciplines (physics fields). When the input of one field analysis depends on the results from another analysis, the analyses are coupled [77]. The FEA modelling is to explain the coupled-field analysis between a beam, made from Al 2024-T3, and a single layer piezoelectric actuator mounted on the top surface of the beam; it includes a modal analysis, a static analysis, a dynamic analysis, a stress analysis and a fatigue analysis. The boundary conditions for the beam are that its ends are fixed; the boundary conditions for the piezoelectric actuator are that a voltage is applied to its top and bottom layers. The modal analysis can determine the natural frequencies and the mode shapes of the structure; the static and dynamic analysis is used to work out the static and dynamic deformation respectively when the piezoelectric actuator is loaded with voltages; the stress analysis can determine the stresses on the structure due to those deformations; the fatigue analysis is to find out the life cycles of the structure before failure based on S-N curve of Al 2024-T3.

Computational Fluid Dynamics (CFD) is a computer-based tool for simulating the behaviour of systems involving fluid flow, heat transfer, and other related physical processes [72]. The theory of squeeze air film is to explain the effects of air in small gaps between two surfaces where one is moving perpendicular to the other at sufficiently high frequency. So the air remains stationary and is undergoing periodic cycles of compression and expansion. The squeeze film effect is modelled in two ways, using the ideal gas law and the CFX simulation. The ideal gas law can only be considered as a first approximation because it does not consider pressure leakage around edges. The CFX can model the squeeze air film effect more accurately because it provides a numerical solution of the Reynolds equation and the equation of the

## **Chapter 4 – Modelling structural characteristics and squeeze film effect**

motion simultaneously by considering the pressure end-leakage and the variable oscillation frequencies of the driving unit. With this improvement, some important observations were made that would form the basis of design guidelines governing squeeze air film bearings.

### **4.2 Characteristics of beam**

#### **4.2.1 Simple model analysis of a beam and boundary conditions**

Figure 4.1 shows a beam, made from the material Al 2024-T3, in the coordinate system with width of 5 mm (along Z direction), length of 45 mm (along X direction) and thickness of 2 mm (along Y direction). The beam has fix-fix support for its both ends (surfaces perpendicular to X direction). A single layer piezoelectric actuator is mounted on the top surface of the beam as a driving unit; the dimensions of it are 15 mm x 5mm x 0.5mm. The boundary conditions for the driving unit, the piezoelectric actuator, vary in the simulations, which will be introduced later in the sections.

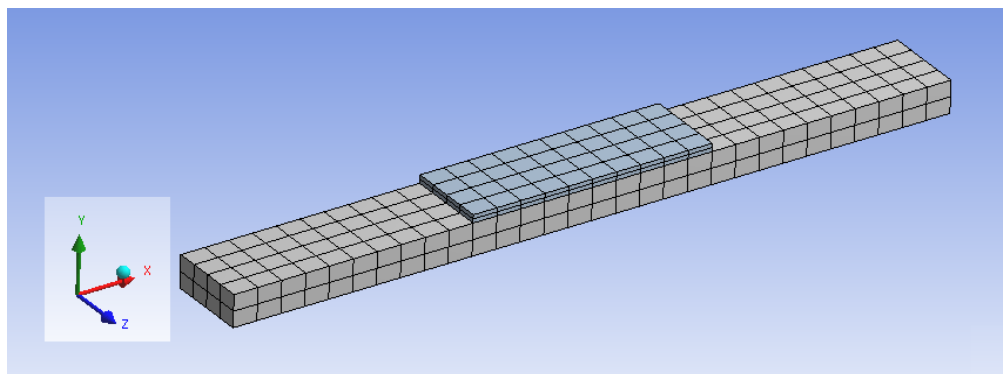


Figure 4.1- Model of rectangle beam with a single layer piezoelectric actuator mounted on top surface.

#### **4.2.2 Static analysis**

The purpose of the static analysis was to determine the static deformation of the beam when a 150 V DC voltage (0V on the bottom and 150V on the top surfaces of piezoelectric layer) was applied to single layer piezoelectric actuators. Figure 4.2 shows the result of the static analysis, from which a maximum radial deformation of

## Chapter 4 – Modelling structural characteristics and squeeze film effect

1.0441  $\mu\text{m}$  is seen to occur in the middle section of the beam, represented by a red region.

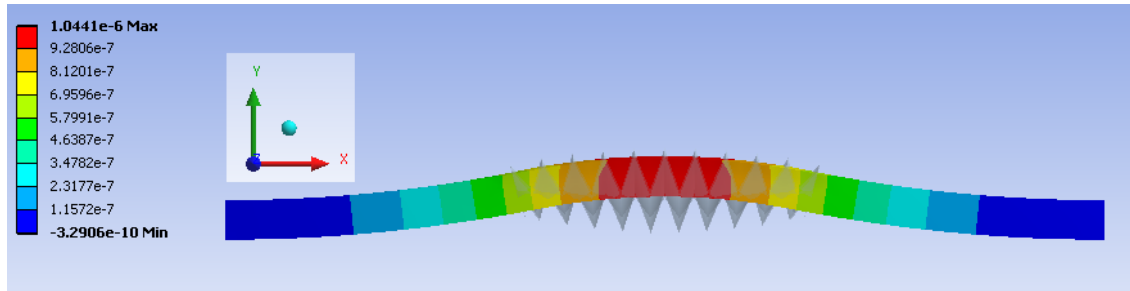
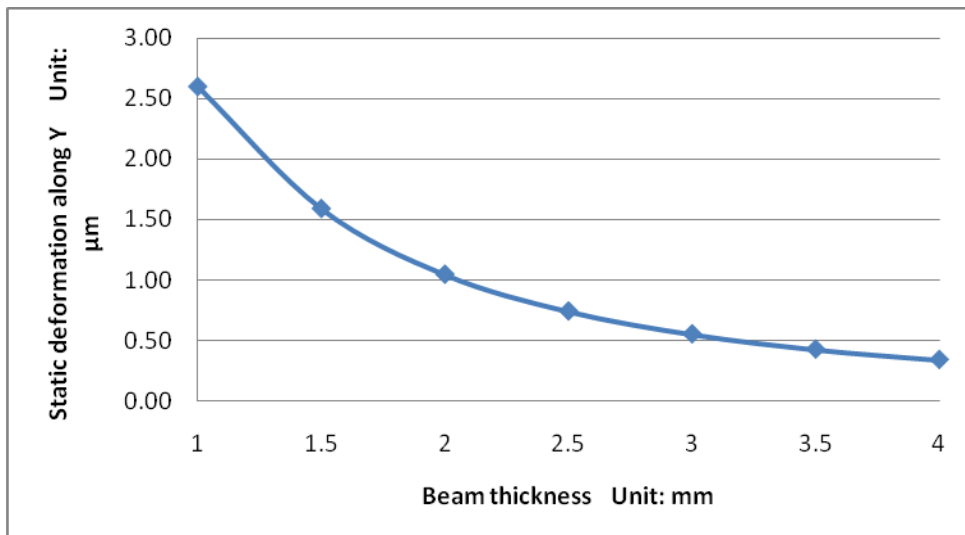


Figure 4.2- Static deformation of beam when 150 V DC was applied to the piezoelectric actuator.

When a DC voltage is applied to the piezoelectric actuator mounted on top surface of the beam, a static deformation results. A larger deformation is preferred to a small one because of the thicker squeeze air film that it creates. Evidently the deformation is a function of the beam thickness. The relationship between the thickness of the beam and the deformation in the Y direction is shown in Figure 4.3. It is observed that the beam deformation increases disproportionately as the beam thickness decreases. The static deformation of a 1 mm thick beam is about 1.7 times larger than that of 2 mm thickness; however, as thickness increases from 3 to 4 mm, the static deformation hardly changes, being around 0.2  $\mu\text{m}$ .



#### **Chapter 4 – Modelling structural characteristics and squeeze film effect**

Figure 4.3- Relationship between maximum static deformation and beam thickness.

The thickness of the beam increases, the tendency of the force also increases in an exponential fashion as shown in Figure 4.4. The force generated by the piezoelectric actuator also varies with the boundary conditions. The maximum force, 8.27 N calculated by ANSYS and 8.19 N calculated by manually, can be obtained by blocking the both ends of the piezoelectric actuator. The maximum force generated in this boundary condition that is to bond the piezoelectric actuator on the top surface of the beam, is about 4 N when beam thickness is 4 mm; and it is about 2 times as big as that of 1 mm thickness.

Figure 4.4- The force analysis for a piezoelectric actuator boned onto a beam with thickness.

The above-mentioned analysis was repeated for other driving voltages from 30 V to 150 V and Figure 4.5 shows the relationship between the maximum static deformation and the voltage input, which is observed to be linear [23]. The possible reason for explaining the linear relationship holding between the beam deformation and the applied DC voltage is because of the beam's deformation in its elastic region, and the other reason is the piezoelectric actuator expands linearly with the applied voltage.

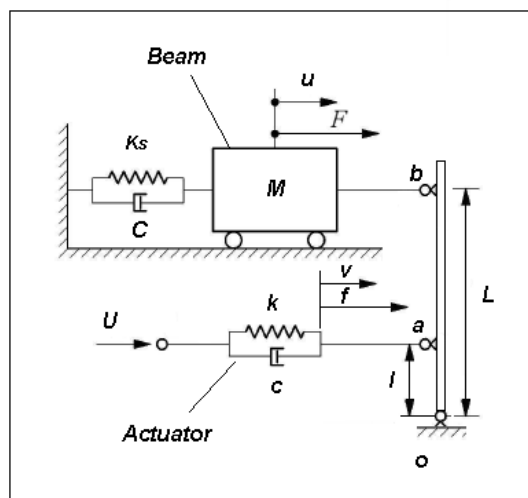
Figure 4.5 - Static deformation varies linearly with the applied DC voltage.

#### Chapter 4 – Modelling structural characteristics and squeeze film effect

The maximum stroke length of the piezoelectric actuator in its own can only achieve  $0.59 \mu\text{m}$  (chapter 3) with loading of the DC of 150 V and 0 V on its top and bottom layer respectively. According to Figure 4.3, the deformation of the beam with 2 mm thick is  $1.04 \mu\text{m}$ . It seems that the beam deformation is about 2 times as big as the maximum stroke length of the piezoelectric actuator. Figure 4.6 shows a mechanical modelling for a beam and an actuator in the coupled analysis. The mass of the beam is  $M$  and the mass of the actuator is negligible; they are connected by an infinite rigid rod fixed at pivot  $O$ . The stiffness of the beam is  $K_s$  and the material damping of it is  $C$ ; the stiffness of the actuator is  $k$  and the damping of it is  $c$ . The actuator is applied with a DC voltage of  $U$ ; it produces the stroke length  $v$  and the corresponding force  $f$ . In geometric analysis, the relationship is between the stroke length  $v$  and the deformation of the beam  $u$  as shown at below.

where  $L$  is the distance from the pivot  $O$  to  $b$  and  $l$  is the one from the pivot  $O$  to  $a$ .

It is noted that the  $L$  is longer than  $l$  in this case, which means the beam deformation  $u$  is amplified by a factor of  $\frac{L}{l}$ . It is a useful and an effective method being used in certain studies, like fast tool servo (FTS), when the maximum stroke of the existing actuator is not enough. It also explains the fact that, in terms of an amplify factor, the deformation of the beam is about 2 times as large as the maximum stroke length of the piezoelectric actuator in this coupled-field analysis.



## **Chapter 4 – Modelling structural characteristics and squeeze film effect**

Figure 4.6 – Mechanical modelling for coupled-field analysis between beam and actuator system.

In the FEA modelling process, the force of the piezoelectric actuators as it varies with the driving voltage was accurately represented. This is unlike the approximations that most other researchers, for example [23], made by assuming that a maximum blocking force of the piezoelectric actuator exists for all boundary conditions. ANSYS Macro for the above static analysis is given at Appendix C3.

### **4.2.3 Modal analysis**

Modal analysis can determine the theoretical vibration characteristics, in terms of natural frequencies and mode shapes, of a structure or a machine component. The natural frequencies and the mode shapes are important parameters in the design of a structure for dynamic loading conditions [78]. It is believed that certain mode shapes enhance the effectiveness of the squeeze film air bearings. These mode shapes have geometry that maximizes the oscillation amplitude and minimizes the pressure leakage.

Using ANSYS Workbench, the modal analysis was performed on the beam with its two ends fixed. The first four natural frequencies and the corresponding mode shapes are as shown in Figure 4.7; Mode shape 1 and 3 produce the dominant motion, represented by red colour, along Y direction when excitation frequency is 4965.5 Hz and 10440 Hz respectively; but the former is considered to be more desirable mode shape than the later because the deformation area is larger and more synchronised; moreover, mode shape 3, producing mode shape that one part moving up and the other moving down but not the middle as shown in Figure 4.7 (c), can impose the shear stress on the actuator because of the actuator mounted right in the middle of the beam, which maybe damages the brittle actuator. Mode shape 2 vibrates along Z direction and mode shape 4 just twists when excitation frequencies are 10.44 kHz and 19.84 kHz, respectively; both of them cannot be considered as a correct motion to squeeze air film.

## Chapter 4 – Modelling structural characteristics and squeeze film effect

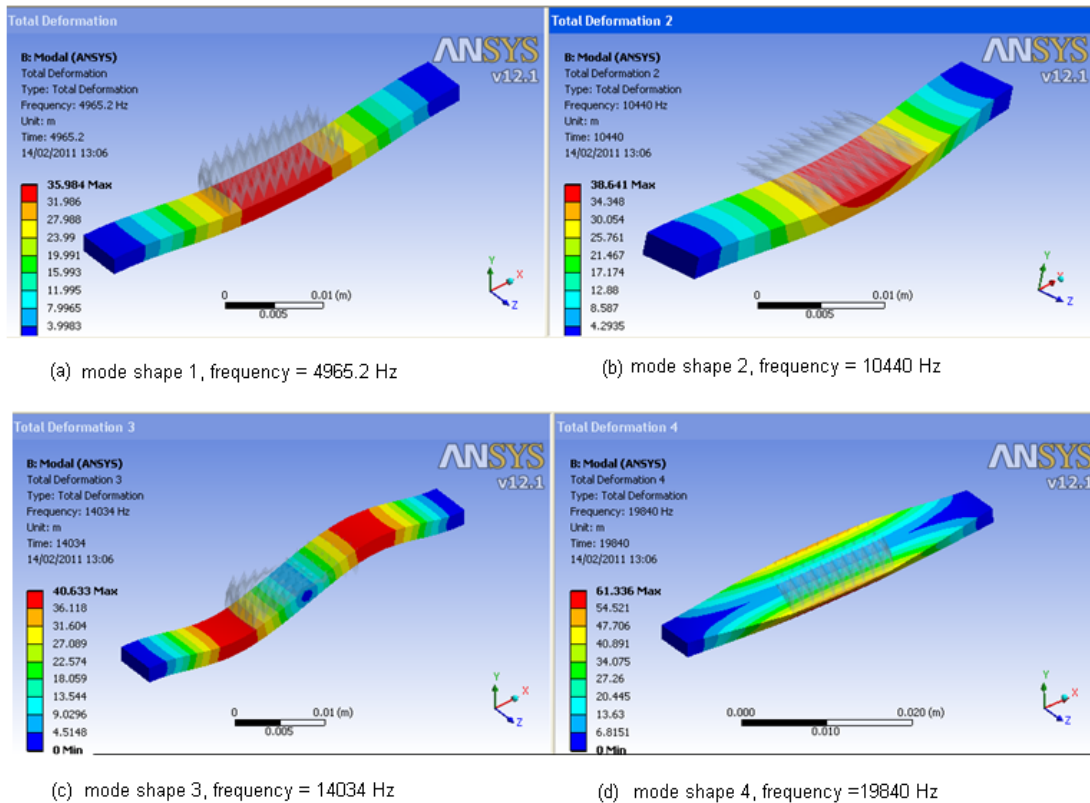


Figure 4.7- Mode shapes and natural frequencies of beam; colour red indicates maximum deformation and colour blue, no deformation (deformation no to scale).

The above four modes shapes can be obtained by driving them with the corresponding natural frequencies. The driving unit is the single layer piezoelectric actuator as mentioned in section 4.2.1. For instance, the mode shape 1 can be triggered by exciting the single layer piezoelectric actuators at 4965.2 Hz. By increasing the beam thickness from 1 mm to 4 mm, the natural frequency is seen to increase in a linear manner as shown in Figure 4.8. It is believed that the modal analysis is a critical simulation in the design of the squeeze film air bearing, because it not only shows the mode shapes but also gives the corresponding natural frequencies; both of them maybe are critical for enhancing the effectiveness of the squeeze air film in journal bearings.

Figure 4.8 – Relationship between natural frequency and beam thickness.



**Chapter 4 – Modelling structural characteristics and squeeze film effect**

**4.2.4 Dynamic analysis**

Dynamic analysis is used to determine the dynamic response of a structure under the dynamic excitation force [79]. The dynamic excitation forces are from the expansion and the compression of the piezoelectric actuators when they are loaded with an AC voltage (75V) on top of a DC offset (75V). The excitation frequency should be coincident with the fundamental natural frequencies of 4965.2 Hz for creating mode shape 1, as identified in Section 4.2.3, in order to achieve maximum dynamic response.

Figure 4.9 shows the dynamic response of the beam with thickness of 2 mm when excited at 4965.2 Hz with the AC 75 V and the DC offset 75V as occurring at the central region (shown in red) where the amplitude is 11.884  $\mu\text{m}$ . As expected the response of the beam is of the same shape as mode shape 1. By varying the beam thickness from 1 to 4mm and driving the single layer piezoelectric actuator at the fundamental natural frequency of each beam thickness, the maximum amplitude of response is seen to decrease in an exponential manner as shown in Figure 4.10, similar to that observed in the static analysis (Figure 4.3). A comparison between the two analyses is presented in Figure 4.11: the difference in magnitude is striking; for a 2-mm thick beam, the dynamic deformation is about 12 times as large as the static deformation.

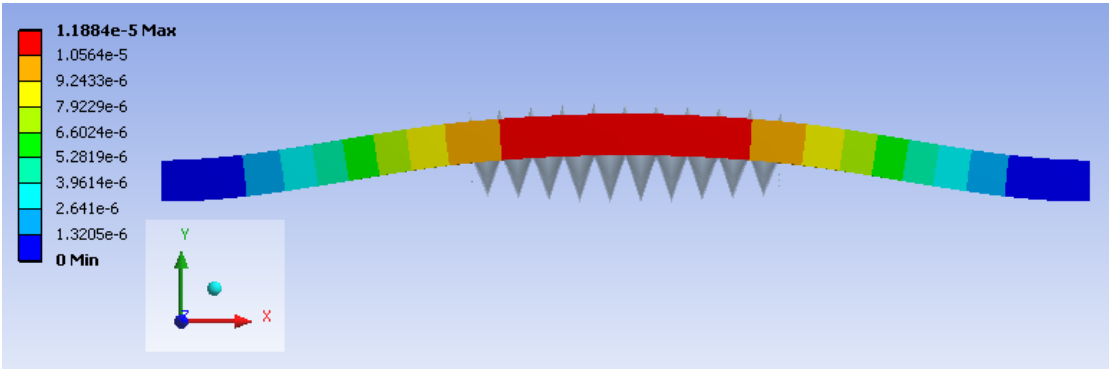


Figure 4.9 - Dynamic response of beam, thickness of 2 mm, when driven at the fundamental natural frequency of 4965.2 Hz.

## **Chapter 4 – Modelling structural characteristics and squeeze film effect**

Figure 4.10 - Dynamic deformation versus beam thickness when excited at natural frequency of beam.

Figure 4.11 - Comparison between static and dynamic beam deformations.

By varying the AC input from 45 V to 75 V but keeping the DC 75V constant, the maximum dynamic deformation is observed to increase in linear manner as shown in Figure 4.12. The dynamic deformation increases about 5  $\mu\text{m}$  when the AC is increased from 45 V to 75 V. In Figure 4.13, the DC varying from 45 V to 75 V and keeping AC 75 V constant, the dynamic deformation is also seen to increase in linear manner, but only increases about 0.2  $\mu\text{m}$  when the DC is increased from 45 V to 75 V.

Figure 4.12- Relationship between dynamic deformation and AC.

Figure 4.13- Relationship between Dynamic deformation and DC.

The dynamic response can be seen to be the other important parameter in design of the squeeze film air bearing; but bearing in mind, the big dynamic deformation may imposes strain in the driving piezoelectric actuators, which may be too high to cause them to fracture. The ANSYS Macro, for the above dynamic analysis to find out the dynamic response, is available at Appendix C4.

### **4.2.5 Stress analysis**

In ANSYS workbench, equivalent stress (also called von Mises stress) is often used in design work because it allows any arbitrary three-dimensional stress state to be represented as a single positive stress value. Equivalent stress is part of the maximum equivalent stress failure theory used to predict yielding in a ductile material. [80]

#### Chapter 4 – Modelling structural characteristics and squeeze film effect

As the deformation of the beam is expected to be at the micron level, a reasonable assumption is that the state of stress can be evaluated using linear elasticity theory. For maximum deformation 11.884  $\mu\text{m}$  of 2mm thick beam, the Von Mises stress is 14.2 MPa and located at the both fixed ends of the beam, red regions, as shown in Figure 4.14. Because the tensile yield stress of Al 2024-T3 is 345 MPa, the deformation can be considered as in elastic region because the exerted stress of 14.2 MPa is much lower than the tensile yield stress.

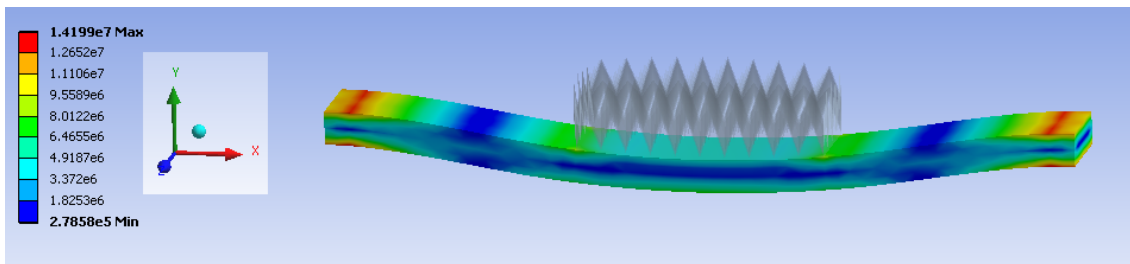


Figure 4.14 – Von-Mises stress on the beam based on maximum deformation of 11.884  $\mu\text{m}$ .

Figure 4.15 shows the relationship between the Von-Mises stress of the beam and the beam thickness. It indicates that the stress decreases with beam thickness. In the case of the beam thickness is 1 mm, the Von-Mises stress of 22.2 MPa is still much low than the tensile yield stress of 345 MPa. Figure 4.16 shows the stress on the piezoelectric actuator, it needs to be considered because maybe the resulting strain in the driving piezoelectric actuators is too high to cause them to fracture.

Figure 4.15- Von-Mises stress of beam with beam thickness.

Figure 4.16- Von-Mises stress on piezoelectric actuator with beam thickness.

## Chapter 4 – Modelling structural characteristics and squeeze film effect

### 4.2.6 Fatigue

In material science, fatigue is the progressive and localised structure damage that occurs when a material is subjected to cyclic loading. It typically happens and needs to be considered in this research to avoid structural failure due to cyclic loads. When the piezoelectric actuator is driven at certain frequency, it deforms the structure as shown in Figure 4.9 introducing stress, referred to Figure 4.14. According to Figure 4.15, the maximum Von-Mises stress is about 15 MPa with beam thickness 2mm when the piezoelectric actuator is driven at AC 75 V and DC 75 V in the fundamental natural frequency of 4965.2 Hz. The fatigue life or cycles of the structure can be predicted by using S-N curve for certain material based on the stress imposed on it, explained in the following section.

In the high-cycle fatigue situations, materials performance is commonly characterised by an *S-N* curve, also known as a *Wöhler* curve. In Figure 4.17, it is an S-N curve [81] for material of Al 2024-T3, X axis representing the logarithmic scale of cycles to failure (N) and Y axis representing the magnitude of a cyclic stress (S). The stress of 15 MPa equals to 2.176 ksi, which is below the stress that can cause the fatigue failure for the beam when loaded dynamically; that means the beam can last indefinitely without fatigue.

## Chapter 4 – Modelling structural characteristics and squeeze film effect

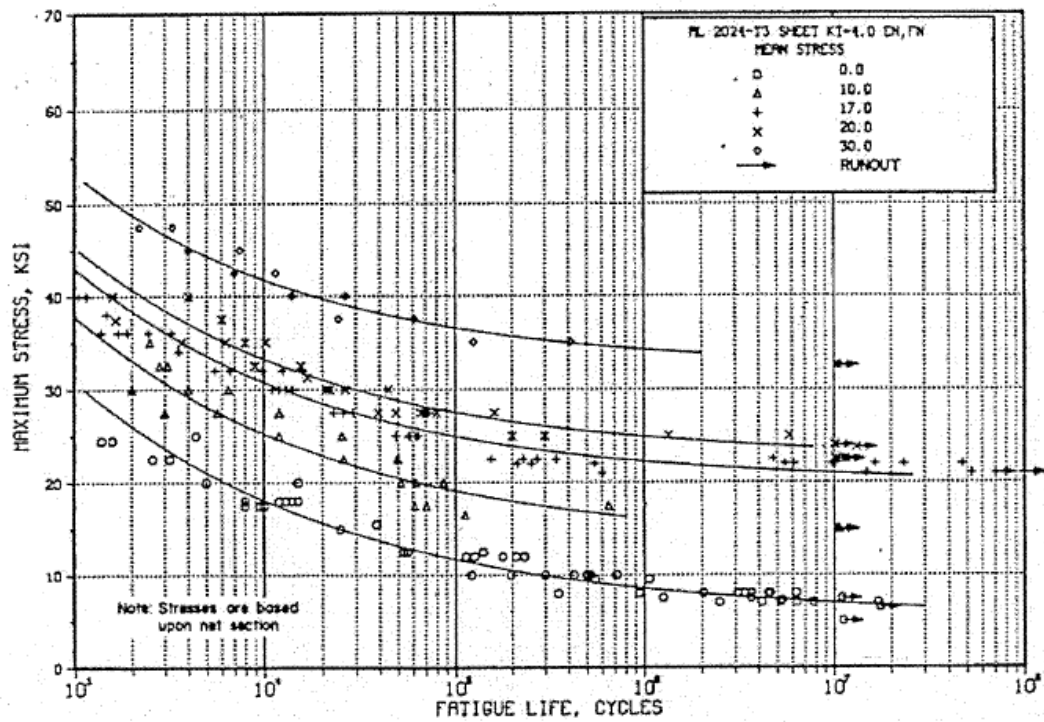


Figure 4.17 – *S-N* curve of Al 2024-T3 [81].

### 4.3 Principle of squeeze film air bearings

#### 4.3.1 Theory of squeeze air film

The theory of squeeze air film is to investigate the effects of air in small gaps between fixed surfaces and structures moving perpendicular to the surfaces in sufficiently high vibration frequencies. So the air therefore remains stationary and is undergoing periodic cycles of compression and expansion. The asymmetrical pressure field and load-carrying capacity can be generated in terms of such rapidly repeated squeeze motion. Moreover, the asymmetrical pressure can be described by the ideal gas law as the first approximation without considering the pressure end-leakage. The more accurate model is to solve the Reynolds equation and the equation of the motion simultaneously to investigate the levitation performance based on the variable input parameters, the oscillation frequency and amplitude, with considering pressure end leakage.

## Chapter 4 – Modelling structural characteristics and squeeze film effect

### 4.3.2 Ideal gas law

Consider two parallel plates of infinite lateral dimensions separated by a gap of  $h_0$ ; one of the plates oscillates sinusoidal normal to the other at a frequency  $\omega$  with an amplitude  $a$ . If the oscillating frequency is very high and the gap very small, then edge leakage of air is insignificant and in addition the process can be regarded as adiabatic. Thus

$$pV^\gamma = K ,$$

where  $p$  is the pressure,  $V$  the volume,  $\gamma$  the adiabatic constant equal to 1.4 for air, and  $K$  the constant.

Suppose the moving plate is at the initial distance of  $h_0$  from the stationary plate, at which the air pressure in the squeeze film is ambient, denoted as  $p_0$ , then

$$p_0 V_0^\gamma = K \quad (4.1)$$

At time  $t$ , the plate moves to  $h = h_0 + a \sin(\omega t)$  at which the pressure in the air film has changed ( $p+p_0$ ), where  $p$  is the gauge pressure; thus the equation of state becomes

$$(p + p_0)V^\gamma = K \quad (4.2)$$

Dividing Eq. (4.1) by Eq. (4.2) and rearranging to obtain the pressure ratio as

$$\frac{p}{p_0} = \left( \frac{V}{V_0} \right)^{-\gamma} - 1 \quad (4.3)$$

Since the volume is proportional to the gap height, Eq. (4.3) can be rewritten in terms of the ratio of gap heights, as

$$\frac{p}{p_0} = \left( \frac{h}{h_0} \right)^{-\gamma} - 1 \quad (4.4)$$

The plate moves sinusoidally such that the gap height at time  $t$  is governed by  $h = h_0 + a \sin(\omega t)$ , which on substitution into Eq.(4.4) gives

## Chapter 4 – Modelling structural characteristics and squeeze film effect

$$\frac{p}{p_0} = \left( \frac{h_0 + a \sin(\omega t)}{h_0} \right)^{-\gamma} - 1 \quad (4.5)$$

Introducing the non-dimensional parameters to Eq. (4.5), namely the amplitude ratio

$$\varepsilon = \frac{a}{h_0}, \text{ and the time ratio } \tau = \frac{t}{T}, \text{ where } T \text{ is the period of oscillation related to the}$$

angular frequency  $\omega$  by  $T = \frac{2\pi}{\omega}$ , Eq. (4.5) can be simplified to

$$\frac{p}{p_0} = (1 + \varepsilon \sin(2\pi\tau))^{-\gamma} - 1 \quad (4.6)$$

It is possible to show that the mean pressure ratio over a cycle of oscillation is positive, which means that the squeeze film exerts a lifting force on the plate thus causing it to float. The proof is given below.

Using Binomial expansion, the pressure ratio, Eq. (4.6), can be represented by the infinite series

$$p_r = \frac{p}{p_0} = \sum_{n=1}^{\infty} \frac{-\gamma(-\gamma-1)K(-\gamma-n+1)}{n!} \varepsilon^n \sin^n(2\pi\tau) \quad (4.7)$$

The coefficients of the terms in this series are successively  $-\gamma$ ,  $-\gamma(-\gamma-1)$ ,  $-\gamma(-\gamma-1)(-\gamma-2)$ , etc. Since  $\gamma$  is positive, the sign of the coefficient alternates: negative when  $n$  is odd and positive when  $n$  is even.

The mean pressure ratio  $\overline{p_r}$  is obtained by integrating, with respect to  $\tau$ , the series (4.7) term by term over the non-dimensional time interval  $\tau = [0, 1]$ . In mathematical terms,

$$\overline{p_r} = \sum_{n=1}^{\infty} \frac{-\gamma(-\gamma-1)K(-\gamma-n+1)}{n!} \varepsilon^n \int_0^1 \sin^n(2\pi\tau) d\tau \quad (4.8)$$

For odd powers of  $\sin^n(2\pi\tau)$ , that is, when  $n = 2m+1$ , ( $m = 0, 1, 2, \dots$ )

#### Chapter 4 – Modelling structural characteristics and squeeze film effect

$$\int_0^1 \sin^{2m+1}(2\pi\tau) d\tau = 0 \quad (4.9)$$

For even powers, that is, when  $n = 2m$ ,

$$\int_0^1 \sin^{2m}(2\pi\tau) d\tau = \frac{1.3.5L (2m-3)(2m-1)}{2.4.6L (2m-2)2m} \quad (4.10)$$

Substituting Eqs. (4.9) and (4.10) into (4.8) gives the mean pressure ratio as

$$\bar{p}_r = \sum_{m=1}^{\infty} \frac{-\gamma(-\gamma-1)K(-\gamma-2m+1)}{2m!} \times \frac{1.3.5L (2m-3)(2m-1)}{2.4.6L (2m-2)2m} \times \epsilon^{2m} \quad (4.11)$$

The series (4.11) contains only even power terms, and so is positive, thus confirming the existing of a levitation force in the squeeze film whose gap oscillates at high frequency in a sinusoidal manner.

Furthermore, since each term in Eq. (4.11) is positive, the factor

$$\frac{-\gamma(-\gamma-1)L(-\gamma-2m+1)}{2m} \quad \text{can be replaced by} \quad \frac{\gamma(\gamma+1)L(\gamma+2m-1)}{2m}, \quad \text{and Eq. (4.11)}$$

can be re-written as

$$\bar{p}_r = \sum_{m=1}^{\infty} \frac{\gamma(\gamma+1)K(\gamma+2m-1)}{2m!} \times \frac{1.3.5L (2m-3)(2m-1)}{2.4.6L (2m-2)2m} \times \epsilon^{2m} \quad (4.11a)$$

The theoretical mean pressure ratio can be calculated using Eq. (4.11a) or by performing numerical integration on Eq. (4.6). However, it would be helpful to be able to use a simpler formula for estimating the mean pressure ratio. The following derivation shows the formula.

In Eq. (4.11a), the coefficient of the first term of the series is  $C_1 = \frac{\gamma(\gamma+1)}{2!} \times \frac{1}{2}$ ; and for

$$\gamma = 1.4 \quad C_1 = 0.840$$

Similarly the coefficient for the  $m^{\text{th}}$  term is given by

$$C_m = \frac{\gamma(\gamma+1)L(\gamma+2m-1)}{2m} \times \frac{1.3.5L (2m-3)(2m-1)}{2.4.6L (2m-2)2m},$$



#### Chapter 4 – Modelling structural characteristics and squeeze film effect

and of the  $(m+1)^{\text{th}}$  term by

$$C_{m+1} = \frac{\gamma(\gamma+1)L(\gamma+2m-1)(\gamma+2m)(\gamma+2m+1)}{(2m+2)!} \times \frac{1.3.5L(2m-3)(2m-1)(2m+1)}{2.4.6L(2m-2)(2m)(2m+2)}$$

The ratio of the two coefficients, after simplifying, is

$$\frac{C_{m+1}}{C_m} = \frac{(2m+\gamma)(2m+\gamma+1)}{(2m+2)^2}$$

For  $\gamma = 1.4$ ,  $\frac{C_{m+1}}{C_m} < 1$  for all positive integer values of  $m$ . In addition, since  $\varepsilon^2 \leq 1$ , the series (4.11a) converges. The largest coefficient is  $C_1$ , whose value is 0.840, as calculated earlier; other coefficients have values that are smaller than  $C_1$ .

This suggests another infinite series which defines the upper bound mean pressure

ratio; this series is  $\bar{p}_{ru} = \sum_{m=1}^{\infty} C_m \varepsilon^{2m}$  and is a geometric series whose sum is

$$\bar{p}_{ru} = \frac{0.840 \varepsilon^2}{1 - \varepsilon^2} \quad (4.12)$$

Figure 4.18 shows the relationship between the mean pressure ratio and amplitude ratio  $\varepsilon$  based on Eq. (4.12) as the approximate solution.

Figure 4.18 - Mean pressure ratio versus amplitude ratio –approximate solution Eq. (4.12).

Eq. (4.6) can be used to plot the asymmetrical pressure curve in one period, as the exact solution, based on two parameters, and; they are given at below for plotting one period with 0.05 intervals of asymmetrical pressure curve also shown in Figure 4.19.

In Figure 4.19, it shows the top area greater than the bottom one, which means the mean pressure is always positive value, moreover, bigger than the ambient pressure ratio 0 Pa. The mean pressure ratio is the levitation pressure for separating two metal

#### Chapter 4 – Modelling structural characteristics and squeeze film effect

surfaces. The mean pressure ratio can be calculated using numerical integration - trapezoidal rule in terms of  $\omega$  as below.

Mean pressure ratio:

Figure 4.19 - Asymmetrical pressure curve with two input parameters and

Figure 4.20 shows the relationship between the pressure ratio and amplitude ratio when applying numerical integration to Eq. (4.6) over the non-dimensional time period  $\tau = [0, 1]$  with  $\gamma=1.4$  and  $\varepsilon=0.1$  to  $0.7$  in  $0.1$  increments, the corresponding values of the mean pressure ratio were obtained. It is noted that as the amplitude ratio increases the pressure ratio increases in an exponential manner. By place the exact solution calculated by Eq. (4.6) and the approximate solution calculated by Eq. (4.12) side by side as shown in Figure 4.21, two solutions are quite close to each other but the approximate solution is always bigger than the exact one, it is noted that up to an amplitude ratio  $\varepsilon$  of  $0.4$ , the error in the mean pressure ratio  $\overline{P_r}$  is less than about  $1.3\%$ .

Figure 4.20 - Relationship between mean pressure ratio and amplitude ratio.

Figure 4.21 - Mean pressure ratio versus amplitude ratio – exact solution Eq.(4.7)  
versus approximate solution Eq.(4.12).

Using the ideal gas law in the studying of the squeeze air film effect can only describe the relationship between the oscillation amplitude and the mean pressure as shown in Figure 4.21, with limitations of without considering the pressure end-leakage and assuming infinite high of the oscillation frequency. Obviously, it does not hold true in

#### **Chapter 4 – Modelling structural characteristics and squeeze film effect**

real situations. In the following section 4.3.3, the Reynolds equation and the equation of motion will be applied and solved simultaneously in the CFX modelling of oscillation flat plate, in order to find out some critical parameters in the design of squeeze film air bearing by considering the pressure end-leakage, the oscillation frequencies and amplitude.

### **4.3.3 CFX**

#### 4.3.3.1 Pressure profile

Consider an air film that is squeezed between two flat plates having relative sinusoidal motion of frequency  $\omega$  at amplitude  $e$ , in the direction of the film thickness, as shown in Figure 4.22(a). The pressure at a point in the air film is governed by the Reynolds equation,

$$(4.13)$$

Eq. (4.13) is given in a non-dimensional form.  $X$ ,  $Y$  and  $Z$  are the coordinates of a point in the air film expressed as a fraction of its length, width and thickness respectively;  $p$  is the ratio of the instantaneous pressure to the initial pressure;  $H$  the ratio of the instantaneous to the initial film thickness;  $\sigma$  the squeeze number; and  $\tau$  the non-dimensional time obtained as the product of the angular frequency of oscillation  $\omega$  and time  $t$ .

The squeeze number is defined as where  $\mu$  is the dynamic viscosity and  $L$  the length of the air film.

The instantaneous film thickness  $h = h_0 + e \sin(\tau)$  and hence the instantaneous film thickness ratio, being  $h/h_0$ , is given by.

#### 4.3.3.2 Numerical calculation of the dynamics of the top plate

To understand the floating characteristics of the top plate based on the theory of squeeze air film, the Reynolds equation and the equation of motion needs to be solved

#### **Chapter 4 – Modelling structural characteristics and squeeze film effect**

simultaneously by using numerical calculation [82 and 83]. The non-dimensional Reynolds equation can be simplified into the two dimensions by assuming the pressure is constant throughout Y direction.

The equation of motion for the top plate can be derived based on the Newton's Second Law [84]. The forces acting on the top plate contain the weight of its self and the levitation force generated by the squeeze air film action, so the equation of motion of the top plate is given at below.

$$(4.14)$$

Where  $m_{Top}$  is the mass of the top plate;  $vel_{Top}$  is the velocity of the top plate in the Y coordinate direction;  $F_L$  is the levitation force acting on the top of plate.

The time derivative of the top plate can be discretized as shown at below.

$$(4.15)$$

And the further discretized is necessary to find out the new displacement of the top plate.

$$(4.16)$$

Finally, the new displacement of the top plate, Eq. (4.17) can be obtained by substituting the Eq. (4.15) and Eq. (4.16) into Eq. (4.14) as given at below.

$$(4.17)$$

The floating characteristics of the model of oscillating plates can be analyzed based on the Reynolds equation and the equation of motion in terms of the defined boundary conditions. Eq. (4.14) to (4.17) programmed using CFX Common Language (CCL) is available at Appendix C5.

#### 4.3.3.3 Simple model of oscillating plates and boundary conditions

The simple model considered is the one as shown in Figure 4.22(a), with dimensions of the plates and the initial air film thickness as indicated. The bottom plate was given a

#### Chapter 4 – Modelling structural characteristics and squeeze film effect

sinusoidal motion whilst the top plate, of mass  $6.24 \times 10^{-3}$  kg, responded also with a sinusoidal motion. The air film, as shown in Figure 4.22(b), is assumed to have no leakage around the three sides of its edges, namely the left, front and back sides; but there is leakage from the right side. Such assumptions are justified by the following considerations:

1. The left side is on the plane of symmetry of the complete air film. In other words, what is shown in Figure 4.22(b) is only the right half and hence there is no sideways flow of air across the symmetry plane.
2. The front and back sides is also symmetrical, which means the plate is infinite along Z direction.
3. The right side, however, is exposed to the atmosphere and pressure end-leakage is expected.

The computation was performed with CFX instead of home-built programming codes to save time.

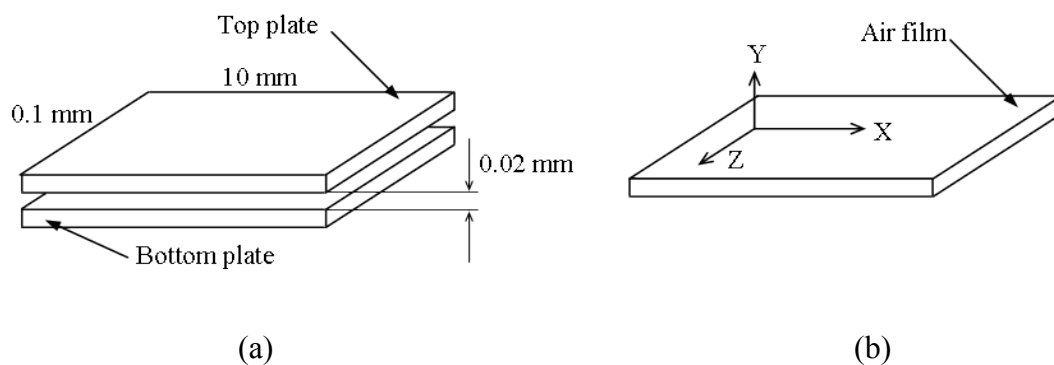


Figure 4.22-(a) Dimensions of the plates and the air film thickness; and (b) the air film in the rectangular coordinate system used.

#### 4.3.3.4 Calculation results

Figure 4.23 shows the relationship between the minimum air film thickness and the oscillation frequency of the bottom plate (oscillates amplitude of  $1 \mu\text{m}$ ). It is observed

#### **Chapter 4 – Modelling structural characteristics and squeeze film effect**

that the air film thickness at first increases with oscillation frequency but it reaches a constant value beyond around 15 kHz.

Figure 4.23 - Air film thicknesses versus excitation frequency of bottom plate  
(oscillation amplitude of 1  $\mu\text{m}$ ).

Figure 4.24 shows the relationship between the air film thickness and the oscillation amplitude with the oscillation frequency of the bottom plate kept at 10 kHz. It is noted that as the oscillation amplitude increases the air film thickness increases in an exponential fashion. The second order polynomial trend-line pretty fits with the CFX simulation result as indicated by R – squared value of 0.9999. The polynomial equation is also displayed in Figure 4.24, which can be used to predict the air film thickness based on the variable oscillation amplitude.

Figure 4.24 - Air film thickness versus oscillation amplitude of bottom plate (oscillation frequency at 10 kHz).

The relationship between the air film stiffness and the oscillation amplitude is shown in Figure 4.25. The air film stiffness is calculated by the weight of the top plate over the air film thickness as shown in the Eq. (4.18). Both parameters are known as the weight of the top plate of Kg and the air film thickness of showing in Figure 4.24. Figure 4.25 shows that the air film stiffness decreases from  $\text{N}/\mu\text{m}$  to  $\text{N}/\mu\text{m}$  with a polynomial manner when the oscillation amplitude increases from 1  $\mu\text{m}$  to 5 $\mu\text{m}$ . The second order polynomial trend-line fits the CFX simulation results well as the R – squared value reaches 0.9999. Because the air film thickness increases in terms of increasing the oscillation amplitude, as a result the air film stiffness decreased based on the Eq. (4.18). The polynomial equation is also indicated in Figure 4.25, which can be used to predict

#### **Chapter 4 – Modelling structural characteristics and squeeze film effect**

the air film stiffness by varying the oscillation amplitude. The air film stiffness shown in Figure 4.26 in terms of various the oscillation frequencies can also be calculated using Eq. (4.18) based on the weight of the top plat ( kg) and the air film thickness in Figure 4.23.

$$(4.18)$$

The air film stiffness can also be calculated out by varying the length of left side (length along Z direction shown in Figure 4.22) based on the above two driving conditions which are the oscillation amplitude and the oscillation frequency. For instance, the length of left side increases to 60 mm and keep the length of the frontal and back side constant to be 10 mm, with driving condition of the oscillation amplitude 2 $\mu$ m and the oscillation frequency of 10 kHz; the air film stiffness will be 3.12 N/ $\mu$ m. Moreover, the air film stiffness has to be chosen to be in such a way that cannot be weak because it could cause the instability and cannot be too rigid as well because it could increase the friction.

Figure 4.25 – Air film stiffness versus oscillation amplitude.

Figure 4.26 – Air film stiffness versus oscillation frequency.

#### **Chapter 4 – Modelling structural characteristics and squeeze film effect**

Figure 4.27 shows the steady-state pressure distribution of the air film over a period of oscillation along the x-axis (Figure 4.22(b)) from the left edge ( $x = 0$  mm) to the right edge ( $x = 10$  mm) where the air film interfaces with the atmosphere whose pressure ratio  $P$  is 1. There are nine pressure profile curves shown and they represent the pressure at different time instants in the cycle of oscillation. It is noted that the mean pressure ratio in the film at any distance is above unity; thus an up-thrust is created to levitate the top plate. The same conclusion was drawn by the authors in their paper using the theory of the ideal gas law [85]. By considering the pressure end-leakage issue is around and at edges but not in the middle part, according to Figure 4.27. So the ideal mode shape of the structure should provide the largest deformation as close as possible to its centre in order to minimize the pressure end-leakage and therefore to maximize the squeeze film effect.

Figure 4.27 – Steady-state pressure distribution in the x-direction (Figure 4.22(b)) of air film in a period of oscillation of bottom plate in frequency of 10 kHz.

Figure 4.28 shows the pressure distribution along length of plate at three excitation frequency levels. It can be seen that the pressure ratio is minimum at the center ( $x=0$ mm) with the excitation frequency of 10 kHz among three excitation conditions. The reason is due to the fact that the pressure is inversely portion to the air film thickness. Moreover, it can also be observed that the pressure keeps constant along the



#### **Chapter 4 – Modelling structural characteristics and squeeze film effect**

length with the high excitation frequency 10 kHz; for the low excitation frequency 1 kHz, the pressure increases gradually and reaches the maximum at the center.

Figure 4.28 – Pressure distribution in the x - direction (Figure. 22(b)) at three levels of excitation frequencies in the steady-state position.

Figure 4.29 shows the transition to the final equilibrium position of the top plate from the initial film thickness of 20  $\mu\text{m}$  at the two oscillation frequencies of the bottom plate, namely 1 kHz and 10 kHz. The observation from Figure 4.23 that the air film thickness increases with oscillation frequency below 15 kHz is seen also to hold true here. In addition, at higher oscillation frequency of the bottom plate the response of the top plate shows greater stability, with no residual oscillation, achieved at around 0.037s.

Figure 4.29 - Transition to equilibrium position of top plate for two excitation frequencies of bottom plate at 1 kHz and 10 kHz.

Figure 4.30 shows air flow velocity between the plates during compressive movement, the bottom plate moving close to the other. In order to clearly observe the air film, it is divided into three parts which are the left end, the middle part and the right end, because of the length of air film much greater than the thickness. It is noted that the air flowing velocity hardly moves horizontally, as shown that all the arrows point vertically, along the length of the plate in the left end, in terms of the symmetrical boundary condition of the left side. In the middle part of the air film, the air starts

## Chapter 4 – Modelling structural characteristics and squeeze film effect

moving horizontally with considerably low speed during compressive movement of the top plate. For the right end, the air flows towards to the right direction (apart from the a layer of air next to the top and bottom walls; their velocities are zero) with the maximum velocity of 1.38 m/s because of the boundary condition is set to be open to the atmosphere.

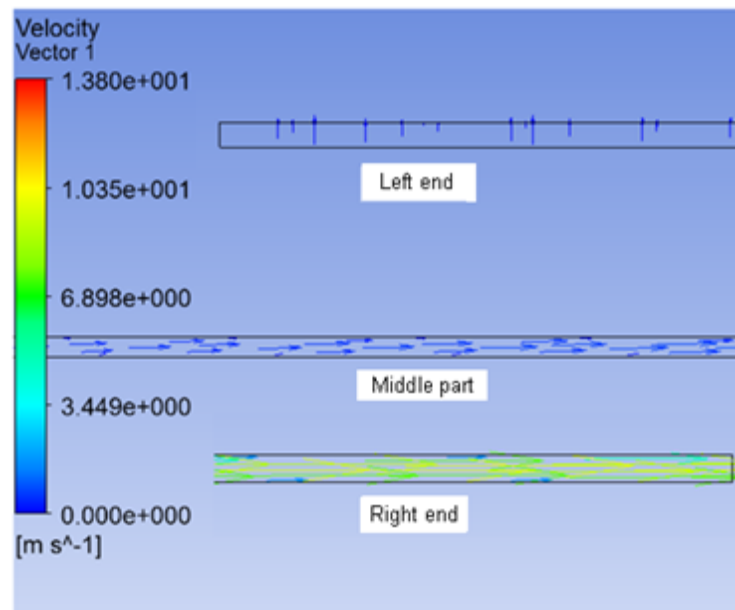


Figure 4.30 – Air flow velocity between plates during compressive movement.

## 4.4 Discussion

### 4.4.1 Discussion in characteristics of beam

In section 4.2 the beam was first studied as the simplest model in order to identify important characteristics of the squeeze air film and parameters that would better inform subsequent design activity, leading to the design of a squeeze film air journal bearing.

The static analysis shows the relationship between the maximum deformation and the beam thickness as shown in Figure 4.3; and also shows the force generated by piezoelectric actuator changes in an exponential manner with beam thickness, Figure 4.4. According to the above two Figures, when the beam thickness is 2 mm, the beam can deform about 1  $\mu\text{m}$  and the force generated by piezoelectric actuator can be about 3

#### **Chapter 4 – Modelling structural characteristics and squeeze film effect**

N, as the single layer piezoelectric actuator driven at 150 V and 0 V on the top and bottom layer respectively.

The modal analysis is to determine vibration characteristics, in terms of the natural frequencies and the mode shapes of the beam, in certain boundary conditions. Figure 4.7 shows the first four natural frequencies and mode shapes, for instance, the 1<sup>st</sup> mode shape has the natural frequency of 4965.2 Hz. By considering those mode shapes, only the 1<sup>st</sup> mode shape is the most effective in terms of producing the squeeze motion in such way that one surface oscillating perpendicular to the other. Furthermore, the modal analysis can be seen as a starting point in the study of the dynamic response of the beam to a general excitation.

In the dynamic analysis, Figure 4.9 shows the dynamic deformation of 11.884  $\mu\text{m}$  for the beam thickness of 2 mm when the piezoelectric actuator is loaded with the DC 75 V and the AC 75 V. The relationship between the beam thickness and the dynamic deformation, in Figure 4.10, shows the exponential manner of decreasing with beam thickness. By comparing the static deformation and the dynamic deformation is shown in Figure 4.12: the difference in magnitude is striking; for a 2-mm thick plate, the dynamic deformation is about 9 times as large as the static deformation. In Figure 4.12, it shows that by varying AC from 45 V to 75V and keeping DC of 75 V constant, the deformation increases from 6.89  $\mu\text{m}$  to 11.88  $\mu\text{m}$ . But by increasing the DC from 45 V to 75 V and keeping the AC of 75 V constant, Figure 4.13 shows the deformation only increases from 11.64  $\mu\text{m}$  to 11.88  $\mu\text{m}$ ; it is not as significant as increasing the AC.

Both the stress analysis and the fatigue analysis are for monitoring the conditions of the beam when it is in the dynamic loading. It makes sure that the stress on the piezoelectric actuator cannot be too high to fracture it and the stress on the structure cannot be too high to issue the fatigue and beyond the tensile stress of the material used.

## **Chapter 4 – Modelling structural characteristics and squeeze film effect**

### **4.4.2 Discussion in principle of squeeze film air bearing**

The model of an air film between two flat plates using the ideal gas law assuming adiabatic process proves theoretically the existence of a mean positive pressure and that this pressure increases as the amplitude ratio, Figure 4.21. It does not, however, attempt to model the pressure leakage on the edges the squeeze film air bearing. Often, it is argued that when the plates oscillate at a very high frequency, the leakage effect can be ignored and the adiabatic process holds true.

On the issue of the mean pressure, according to Figure 4.21 higher mean pressure is achieved by higher amplitude ratio, which means that the structure must be such designed that the bearing surface can have large displacement. The proposed design allows this to happen with relative ease.

The model of the simple oscillating plate to squeeze air film is to demonstrate the levitation phenomena in terms of the squeeze film action in the CFX simulation (Figure 4.22), from which not only considers the pressure end –leakage round and at edges but also considers the variable input excitation frequency in prediction the air film thickness, but both of them don't be considered in the ideal gas law. So the squeeze film effect can be described more accurate and realistic using the CFX simulation based on the Reynolds equation.

Figures 4.23, 4.24, 4.25, 4.26, 4.27 and 4.29 highlight some findings for the design of squeeze air film bearings. Specifically:

1. According to Figure 4.23, to ensure a greater film thickness, the oscillation frequency imposed on the air film should be high, preferably above 15 kHz because the end leakage becomes insignificant.
2. Figure 4.24 points to the fact that the greater the oscillation amplitude of the air film, the greater is its air film thickness.
3. According to Figure 4.25 and 4.26, the air film stiffness decreases with increasing the air film thickness. By varying the length of the sides the air film stiffness can still be

#### **Chapter 4 – Modelling structural characteristics and squeeze film effect**

calculated. Moreover, the air film stiffness has to be chosen from a certain range to avoid the issue of the instability and excessive friction.

4. According to Figure 4.27, it suggests that in order to minimize the pressure end-leakage, the ideal mode shape of the structure should be deformed in as such way that the middle part has a larger deformation rather than the both ends.

5. Figure 4.29 suggests that with a greater oscillation frequency of the air film, the top plate reaches its stable equilibrium position much more quickly. Furthermore, in its steady-state position, the top plate being excited at the frequency of 10 kHz was much less oscillatory than when it was excited at the frequency of 1 kHz.

Using above five findings, it helps for designing the squeeze film air bearing in such way that more practical and stable in next chapter. It is also believed that certain mode shapes enhance the effectiveness of the squeeze air film in journal bearings. These mode shapes have geometry that maximizes the oscillation amplitude and minimizes the pressure end-leakage around and at edges.

#### **4.5 Summery**

This chapter models a simple structure of the beam fixed at its both ends in ANSYS workbench and also models the oscillation of plates using the ideal gas law and the Reynolds equation.

In the coupled analysis between the piezoelectric actuator and the structure, the simple beam fixed both ends is induced here as a starting point to make sure that ANSYS programmes works before moving to a complicate structure like a squeeze film air bearing. The other advantage of using the beam is that the number of the mesh is relatively less than the complicated ones, which can reduce the computation time significantly. The static, modal and dynamic analyses are implemented to determine the deformations and vibration mode shape when the piezoelectric actuator drives in certain conditions. The stress and fatigue analyses are studied to help the structure within safe operation range, which means below the tensile stress of the material of Al 2024 - T3 and not to be too high to issue the fatigue problem. From the above analyses,

#### **Chapter 4 – Modelling structural characteristics and squeeze film effect**

the behaviour of the proposed squeeze film air journal bearing can be determined, like the amplitude of the static and the dynamic deformation, the vibration mode shape and also the vibration frequency; moreover, these results will maybe considered as the important parameters in the squeeze film effect.

The model of the oscillation plate using the ideal gas law fins out the relationship between the pressure and the oscillation amplitude shown in Figure 4.21. But is has the limitation such as without considering the pressure end-leakage at and around the edges and assuming the oscillation frequency to be infinity. But those limitations can be overcome by solving the Reynolds equation and the equation of the motion simultaneously in the CFX modelling, from which creates five findings in the design of the squeeze film air bearing as talked in the discussion. Those findings are going to be applied in next chapter for designing the squeeze film air journal bearing.

## **Chapter 5 - Design of squeeze film air bearing and its experiments**

### **5.1 Introduction**

The chapter is to describe design of the squeeze film air journal bearing, experiments design and experimental set-up. The five findings, from the CFX simulation in Chapter 4, are used to design the squeeze film air journal bearing. For the experiments design, it is to discuss the purposes and procedure for the dynamic response experiment and the load-carrying capacity experiment. The last part of the chapter is to describe the electrical inputs, mechanical structure, the measurement instrument and the LabVIEW user interface.

### **5.2 Squeeze film air bearings system and process for testing and modelling**

A new type of bearing, a squeeze film air bearing, to separate two metal surfaces: 1) without using the external pressurized air is studied; 2) without suffering wear during the start-up period and shutdown; 3) and without using potentially contaminating lubricant as discussed in Chapter 2. In Chapter 4, the dynamic characteristics of the beam were modelled in terms of its mode shapes, natural frequencies and dynamic deformations in the FEA modal analysis and coupled-field analysis; the static, stress, and fatigue analyses were also studied. In addition, the squeeze film effect was also modelled in two ways: the ideal gas law (Section 4.3.2) and the CFX simulation (Section 4.3.3). Therefore, in order to validate those results of the FEA modelling and the CFX simulation, a physical prototype needs to be built.

Figure 5.1 shows the squeeze film air bearing system and the process for the testing and modelling. The CAD model is shown on the upper left corner and the physical prototype is on the upper right side in this diagram.

### Chapter 5 – Design of squeeze film air bearing and its experiments

In the dynamic response experiments, the dynamic characteristics of the proposed bearings will be tested using the input variables of 1) the excitation frequencies, 2) the AC voltages, 3) the mode shapes, and 4) the materials, as shown in the bottom left corner in Figure 5.1. The proposed bearing is modelled in the FEA to find out its natural frequencies, mode shapes and dynamic deformations. In the load-carrying capacity experiments, the bearing is inserted into the guide way, set up as a cantilever as shown at upper right in Figure 5.1. A mass was hung onto a wire attached to bearing shell. This experiment can be used to explain: 1) the relationship between the air film thickness and the load; and 2) the air film thickness under various driving conditions, such as the oscillation frequency and amplitude. In the CFX modelling, simulation results can also be provided for both the maximum load-carrying capacity and the corresponding air film thickness under the various driving conditions.

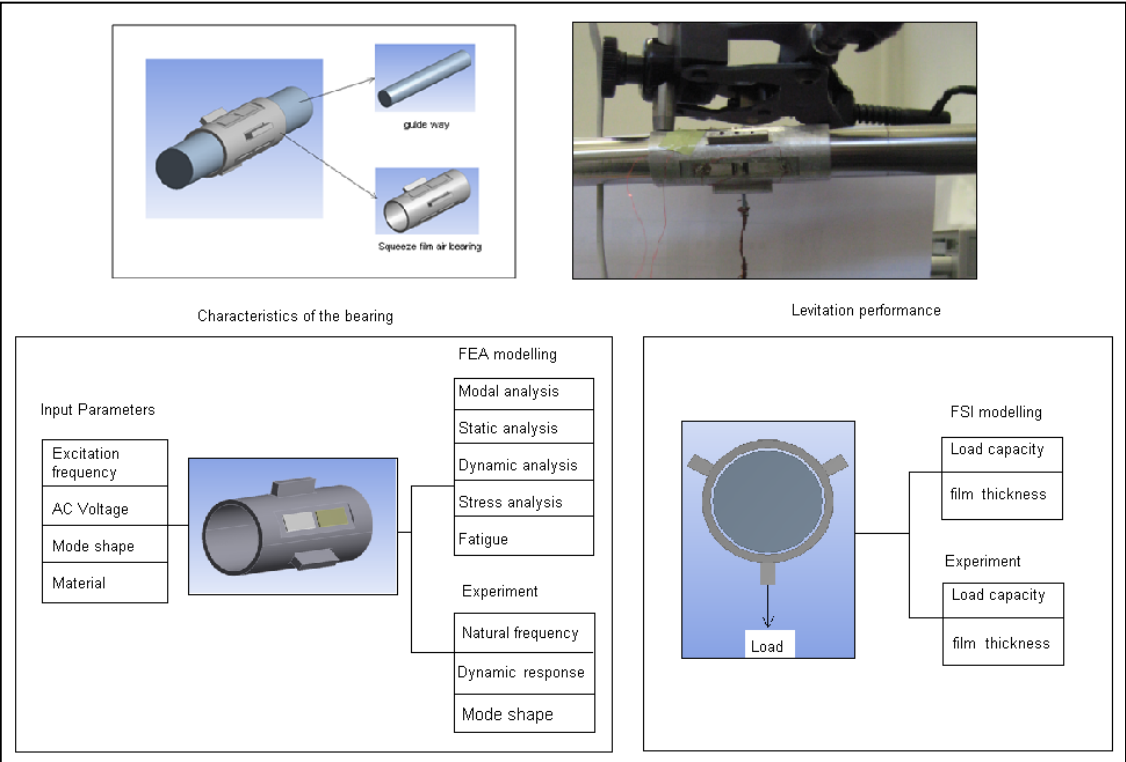


Figure 5.1 - Squeeze film air bearing system and the processes for testing and modelling.



## **Chapter 5 – Design of squeeze film air bearing and its experiments**

### **5.3 Design of the proposed squeeze film air journal bearing**

In Chapter 4, the five findings were made from the CFX simulation. Those findings would guide the design of squeeze film bearings [86]. They are repeated below:

1. To ensure a greater film thickness, the oscillation frequency imposed on the air film should be high, preferably above 15 kHz because the end leakage becomes insignificant (Figure 4.23).
2. The greater the oscillation amplitude of the air film, the greater is its film thickness (Figure 4.24).
3. The stiffness of an air film is inversely proportional to its thickness (Figure 4.25 and 4.26).
4. When a vibrating beam has maximum oscillation in the middle rather than at its ends, there is minimum pressure end-leakage (Figure 4.27).
5. The higher the frequency of oscillation, the more quickly the loading beam settles down to its final position with zero residual oscillation (Figure 4.29).

Using these five findings, a design of the squeeze film air journal bearing, as shown in Figure 5.2, is proposed. This bearing is in the shape of a hollow round tube with three longitudinal flats milled equi-spaced around the circumference. Using an odd numbers of flats around the bearing shell ensures that there is at least one active – that is, vibrating – bearing shell, the squeezing action of which is opposite to the line of action of the loading. Three flats are preferred to five flats because of the larger static and dynamic deformation that can be produced under the same driving condition. During excitation with a piezoelectric actuator mounted on the flat, the segment of the bearing tube in between the two fins vibrates. The fins, in effect act as supports. The smaller the number of fins, the longer the distance between supports and hence the greater the vibration amplitude at the bearing tube segment. Furthermore, it is also cheaper to manufacture a bearing tube with fewer flats.

## **Chapter 5 – Design of squeeze film air bearing and its experiments**

According to the CFX model, the air film thickness increases in an exponential manner with the oscillation amplitude (Figure 4.24). But if the maximum dynamic deformation was the only design criterion, then the thinner of the tube wall the better. However, the natural frequency drops as the thickness of the tube wall decreases (Figure 4.8); and the low natural frequency cannot effectively minimize the pressure leakage, which can affect the air film thickness (Figure 4.23). In addition, the flat surfaces were milled on the outside face of the tube for mounting the piezoelectric actuators. The piezoelectric actuator also needs to be considered because it is made of a brittle material that can be fractured if the resulting strain is too high. From the above considerations, the thickness of the tube wall was chosen to be 2 mm for this study.

Two piezoelectric actuators are mounted length-wise on each flat and they are driven simultaneously by an AC voltage with a DC offset. The material and geometry of the tube are such chosen that at least one modal frequency exists which is above 15 kHz (Finding 1) and has a desirable mode shape that has maximum oscillation in the middle rather than at its edges (Finding 4). In order to mount the driving unit, namely the piezoelectric actuator, on the tube for producing greater oscillation amplitude, three flat surfaces were milled on the outer face of the tube 120° apart as shown in Figure 5.2.

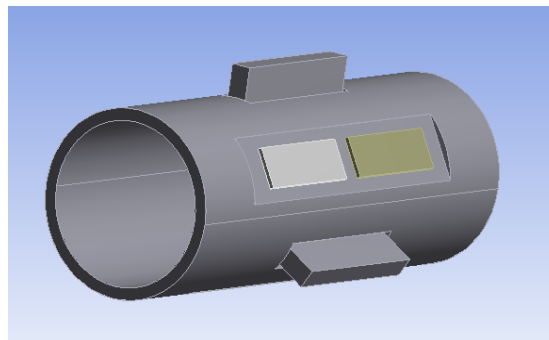
The modal shape of choice should be one that produces purely a radial deformation of the tube wall without the tube experiencing any torsion and bending. Therefore the only possible modal shape for the design should be that the tube wall has a ‘pinching’ action. When the pinching action is highly magnified, the ‘pinched’ tube, when viewed normal to its end, gives a triangular appearance (Figure 6.4). To encourage the tube to distort into a ‘triangle’, three external fins are added, which in effect partitions the tube into three 120° sectors. The fins do not cover the whole length of the tube but are foreshortened. This is to make sure that it can achieve the bigger deformation when the piezoelectric actuator is driven in both static and dynamic conditions. But the natural frequency needs to be higher than 15 kHz to minimize the end leakage in the longitudinal direction (Finding 1).

At the desired mode as described above, at the mid-third section of the tube the part of the wall between the fins flexes in a radial direction whilst simultaneously the fins also

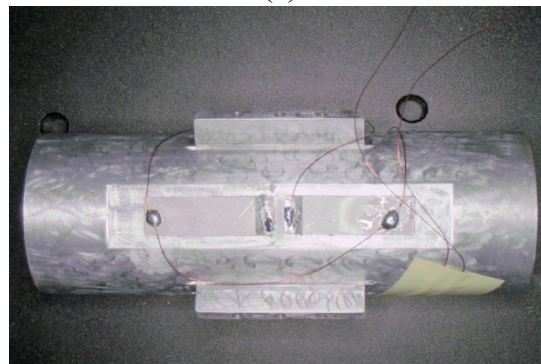
## Chapter 5 – Design of squeeze film air bearing and its experiments

move bodily in a radial direction. The two motions are 180 degree out of phase with each other (Figure 6.4(a)).

Based on the above design ideas in terms of the five findings, the final design is created, which is shown in Figure 5.2. Such bearings of identical geometry were made with different materials: one is Al 2024-T3 (namely Al bearing), and the other is Cu 101-C (namely Cu bearing). In this design, the bearing's inner diameter is 20.02 mm, its length 60mm and thickness 2 mm. Three fins, each 20 mm long, are positioned 120° apart on the outer circumference of the bearing tube; they are designed to provide a desirable modal shape of a triangular cross-section when excited by the piezoelectric actuators. This enables the air gap underneath the actuators to behave effectively as a squeeze air film. The engineering drawings of the proposed bearing are given in Appendix B1.



(a)



(b)

(a) CAD model; (b) Physical prototype in aluminium;

Figure 5.2 - The bearing with six single layer piezoelectric actuators mounted on three milled flat surfaces.

## **Chapter 5 – Design of squeeze film air bearing and its experiments**

### **5.4 Experiments design**

In Chapter 4, the FEA model of the beam fixed at its both ends was developed to calculate out the static and dynamic deformation when the driving unit, the piezoelectric actuator, was powered at the DC 75 V for the static analysis and at the DC 75 V and AC 75 V for the dynamic analysis. Similarly, the journal bearing can be analysed by the FEA simulation. Results obtained from the simulation need to be validated by experiments. In the CFX model, the X-axis (Figure 4.22(b) in Chapter 4) of the plate is aligned with the longitudinal axis of the bearing tube, the Y-axis with the radial axis, and the Z - axis with the tangential axis to the circumference. Since air is very light compared to other fluids, when the air in the squeeze film is forced to flow round a curvature, hence changing its direction, the radial force required to make this happen is negligibly small. For this reason, the curvature of the bearing plates is not an influencing variable in the study of the fluid dynamics and they can be assumed flat without much loss of accuracy. Leakage is only significant in the longitudinal directions (both positive and negative directions of the x-axis) but otherwise virtually non-existent in the radial (Y - axis) or tangential (Z - axis) direction. So CFX model of the oscillation plate presented in Chapter 4 mainly holds for the proposed geometry of squeeze film air bearing. In this section, the experiments will be described. They are divided into two types: one is to measure the dynamic deformation and the other is the air film thickness from which the load-carrying capacity can be estimated.

The dynamic response experiment is to determine the modal shapes and modal frequencies of the journal bearing and its dynamic deformation when excited. The levitation performance of the journal bearing at the desirable modes in respect of the film thickness and load-carrying capacity also need to be investigated mainly in this study. Therefore, the experimental set-up should be designed to be focusing on finding the two parameters: 1) Film thickness and 2) Load-carrying capacity.

#### **5.4.1 Experiment for dynamic characteristics**

Figure 5.3 shows a schematic diagram of the experimental set-up for the dynamic response experiment. It includes a signal generator, an actuator driver and an actuator

## Chapter 5 – Design of squeeze film air bearing and its experiments

monitor unit, an oscilloscope, a capacitive displacement sensor, a data acquisition card, and a computer. The function of each instrument is described in Table 5.1 with the flow sequence referred to Figure 5.3.

Table 5.1 - Function description of instrumentation.

<b>Instrumentation</b>	<b>Function description</b>
Signal generator	It is capable of producing a sinusoidal wave with a maximum voltage of 5 V and variable frequency up to 100 kHz for working with the actuator driver.
Actuator driver	It is to amplify the input signal that from signal generator 15 times. The actuator driver can also apply a Dc offset.
Actuator monitor unit	It is to monitor and display the DC offset.
Oscilloscope	It is to read and display the AC and DC signal that are for driving the piezoelectric actuator.
Piezoelectric actuator	It is used to generate a motion with certain frequency to deform the bearing.
Capacitive displacement sensor	It is used to measure the mode shapes, the resonance frequency, the dynamic response and film thickness.
Data acquisition card	It is to convert analogue waveforms into digital values for processing, such as filtering a raw signal.
LabVIEW	It is to display and save the signal.

Figure 5.3 also shows how to validate the dynamic characteristics of the proposed squeeze film air bearing based on the driving input signal and signal output measurements. The purposes of the experiment are:

## Chapter 5 – Design of squeeze film air bearing and its experiments

1. To validate the desired mode shapes (predicted from FEA modelling);
2. To validate the natural frequencies (predicted from FEA modelling) at desired mode shapes;
3. To validate the dynamic deformation (predicted from the coupled-field analysis) at desired Mode shapes;
4. To validate the dynamic deformation (predicted from the coupled field analysis) at different levels of the AC voltage;
5. To validate the dynamic deformation (predicted from the coupled field analysis) of the bearings made of two materials, Al 2024-T3 and Cu - C101;
6. To determine the repeatability of the dynamic deformation (purely from experiment).

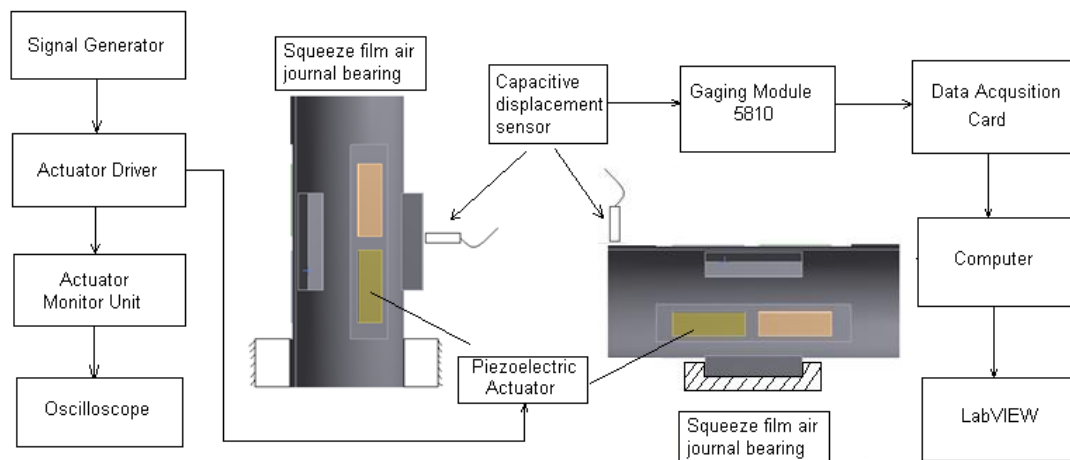


Figure 5.3 - Schematics of the experimental set-up for measuring the dynamic response of the squeeze film air bearing.

In Figure 5.3, it can be seen that both the bearing and the capacitive displacement sensor are fixed at different regions due to different mode shapes. For the dynamic response measurement of the proposed bearings at different mode shapes, the bearings need to be fixed at the region where have none movement that can be predicted from FEA modal analysis. For instance, the bearing shell is fixed at the bottom of one edge

## **Chapter 5 – Design of squeeze film air bearing and its experiments**

vertically and the sensor is fixed to measure the dynamic deformation of the fin, refer to left diagram of Figure 5.3. The capacitive displacement sensor is the tool for measuring the dynamic deformation of the bearing without any contacts.

This dynamic response experiment can be used to validate not only for the natural frequency and mode shapes of the proposed bearing but also for its dynamic deformation. By varying the AC voltage at three levels, namely 55 V, 65 V and 75 V, the bearing should achieve the maximum dynamic response at the AC 75 V as predicted by the FEA modelling. This point can also be validated from the dynamic response experiment.

The experimental procedure for measuring the dynamic response of Al bearing is listed as:

1. To hold the bearing tube, Figure 5.3, at the nodes (points of zero displacement; details in Chapter 6) identified from the FEA modal analysis and to set up the displacement sensor to measure the maximum dynamic deformation also predicted from the modal analysis;
2. To set the coupling mode in the voltage input setup of the data acquisition card to be “AC” so that only the dynamic, rather than static, response is measured;
3. To excite the piezoelectric actuator on the flats of the bearing at and around the natural frequency, identified from the FEA modal analysis, with a DC offset of 75V and a 75V AC at a particular driving frequency; and to record the dynamic deformation over 10 cycles of oscillation;
4. To estimate the average and the standard error (that is, standard deviation of the average) of the displacement amplitude over the 10 cycles;
5. To repeat Steps 3 and 4 for other driving frequencies;

## Chapter 5 – Design of squeeze film air bearing and its experiments

6. To repeat Steps 1 to 5 for Cu bearing.

### 5.4.2 Experiment for load-carrying capacity

Figure 5.4 shows the schematic diagram of the experimental set-up for the load-carrying capacity experiment. The set up is almost identical to that for the dynamic response experiment presented in Section 5.4.1. The only additional component is the guide way shown in Figure 5.4, which is a round rod. The air film thickness created by the squeeze film action between the guide way and the squeeze film air bearing itself can also be measured directly by the capacitive displacement sensor.

The purposes of this experiment are:

1. To determine the relationship between the load-carrying capacity and the air film thickness;
2. To determine the air film thickness with load at both desired mode shapes;
3. To determine the air film thickness with load at various excitation frequencies;
4. To determine the air film thickness at three levels of the AC voltage;
5. To determine the air film thickness at bearings made from different materials, Al 2024-T3 and Cu - C101.

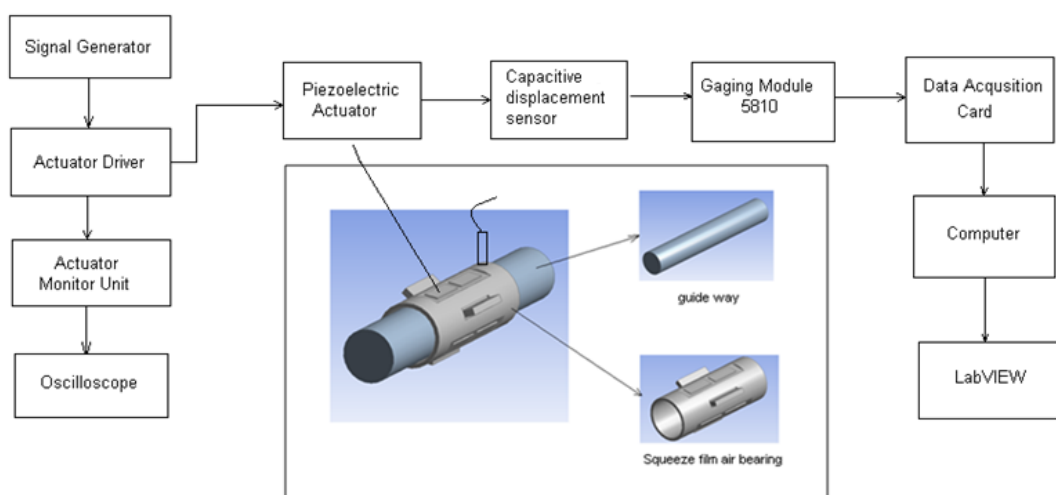


Figure 5.4- Schematics of the experimental set-up for measuring the air film thickness between the squeeze film air bearing and the guide way.



## **Chapter 5 – Design of squeeze film air bearing and its experiments**

In the load-carrying capacity experiments, AI bearing will be exciting at and around the natural frequency of the certain mode shapes to find out the relationship between the air film thickness and the load.

The experimental procedure for measuring the air film of AI bearing is as follows:

1. To clean the surface of guide way (a round ground rod) and the interior surface of the bearing tube before inserting the bearing tube onto the guide way.
2. With the tube hanging on the guide way, to mount the capacitive displacement sensor vertically above the tube with a nominal gap between them; then to 'zero' the displacement reading of the sensor, which serves as is the measurement datum.
3. To set the coupling mode to "DC" in the voltage input setup of the data acquisition card.
4. To excite the bearing at a frequency that gives the greatest oscillation amplitude with the same input voltage as that of the dynamic response; the bearing will now levitate above the guide way and the upward displacement, which is picked up by the sensor, is the instantaneous air film thickness.
5. To record the displacement signal over 10 cycles of oscillation.
6. To take an average of the valley values of the 10 cycles to give the averaged minimum air film thickness. If the average is above zero, then the bearing has been floating.



## Chapter 5 – Design of squeeze film air bearing and its experiments

### 5.5.2 Actuator driver and actuator monitor unit

The actuator driver ENP-1-1U (Echo Electronics) and the actuator monitor unit ENP-50U (Echo Electronics) are shown in Figure 5.6. The signal generator is connected to the actuator driver. The function of the actuator driver is to amplify the AC sinusoidal signal with amplitude of 3.6 V, 4.3 V and 5 V from the signal generator to be 55 V, 65 V and 75 V, respectively. In other words, the amplification of the actuator driver is 15 times.



Figure 5.6 - Actuator driver ENP-1-1U (Echo Electronics) and actuator monitor unit ENP-50U (Echo Electronics).

### 5.5.3 Oscilloscope

The oscilloscope HM 604 [87] shown in Figure 5.7 is to display the amplified AC signal with a DC offset. The oscilloscope HM 604 is capable of measuring a signal with frequency up to 600 MHz.

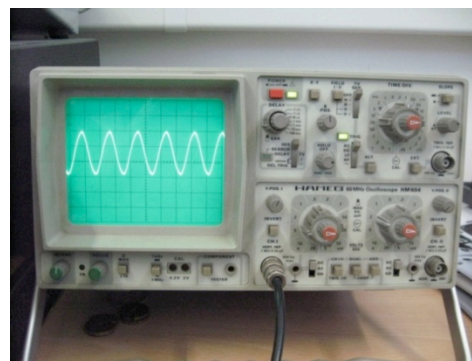


Figure 5.7- Oscilloscope HM604 (HAMEG).

## Chapter 5 – Design of squeeze film air bearing and its experiments

### 5.5.4 Piezoelectric actuator

The piezoelectric actuator C -21 used here is single layer piezoelectric actuator that has the dimensions with the length of 15 mm, the width of 5 mm and the thickness of 0.5 mm, as shown in Figure 5.8.

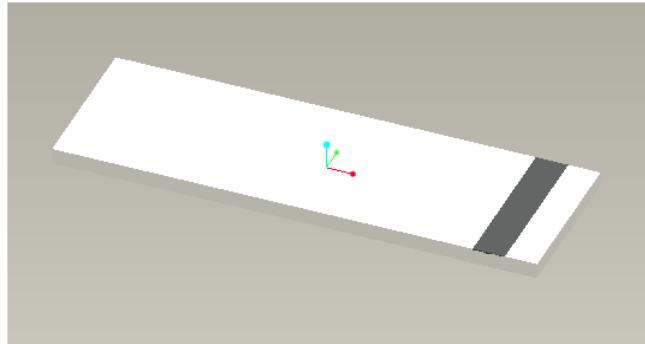


Figure 5.8- CAD model for single layer piezoelectric actuator.

The basic principle of the piezoelectric effect is that when a voltage is applied on the top and the bottom surfaces of a piezoelectric actuator, it changes its dimensions. Moreover, the relationship between input voltage and movement is linear. The top and bottom surfaces of the piezoelectric actuator shown in Figure 5.8 are coated with silver material where are used to apply the voltage onto it. When the actuator is mounted on the structure, there is no room to weld a wire to the bottom electrode for applying the voltage. But the problem was solved by manufacturers by extending the bottom surface all the way up to the top surface. It can be observed that there are two surfaces on the top separated by a black strip in Figure5.8; the larger area is the electrode for the top surface, the other one is the electrode for the bottom surface. The function of the black strip is to isolate the two electrodes avoiding the short circuit when loaded input voltage.

The single layer piezoelectric actuator needs to be bonded onto a structure by using adhesives - *3M's DP 460 Epoxy*. The steps to bond them are given below [88].

1. To clean the bonded surface of the structure using *acetone*;

## Chapter 5 – Design of squeeze film air bearing and its experiments

2. To put the adhesives uniformly to the surface of the structure;
3. To use cello-tape as a longer handle to adjust the actuator in the position;
4. To put into a 50° to 60°C oven about 2 hours with a reasonable weight on top.
5. To check the connection of the electric circuit using a *multimeter* before powering the actuator.

It is important that the piezoelectric actuator should, under no circumstances, be pressed too hard against the structure in an attempt to create a good bond. This can often result in a ‘dry’ bond where the adhesive is completely expelled such that a short circuit occurs between the bottom electrode of the actuator and the structure. The structure becomes live when the actuator is powered and can give a nasty shock if the structure is accidentally touched. Applying too much force during bonding can also risk fracturing the actuator.

The function of the single layer piezoelectric actuator here is to produce the sinusoidal motion with a certain frequency in order to deform the bearing in a desired mode shape. Some important manufacturer’s data of the single layer piezoelectric actuator are extracted from Figure 2.18 and listed in Table 5.3.

Table 5.3 – Parameters of single layer piezoelectric actuator.

<b>PZT – pb(Zr·Ti)O<sub>3</sub> / The lead zirconate titanate materials (hard ceramics).</b>	
<b>Material No</b>	<b>C -21</b>
<b>Coupling factors</b>	$k_p = 59$
	$k_{31} = 34$
	$k_{33} = 71$
	$k_t = 48$
	$k_{15} = 74$
X10 <sup>-2</sup>	

## Chapter 5 – Design of squeeze film air bearing and its experiments

<b>Dielectric constants</b>	1900 1400
<b>Piezoelectric charge constants</b>  X 10 <sup>-12</sup>	d <sub>31</sub> = -131 d <sub>33</sub> = 288 d <sub>15</sub> =634
<b>Young's modulus</b>  X10 <sup>10</sup>	8.3 6.4 2.3

### 5.5.5 Squeeze film air journal bearing

Figure 5.9 shows a physical prototype of the proposed squeeze film air journal bearing with the BNC connection box input to the piezoelectric actuator. The squeeze film air bearing has three longitudinal flats on the circumference 120° apart. On each flat surface were bonded two single layer piezoelectric actuators, Figure 5.9. The six actuators are connected in very thin copper wires in parallel. Using the thin copper wires is because the weight of it can be ignored to avoid influencing the floating performance. The external circuit for powering the actuators is connected with the actuator driver in BNC cable.

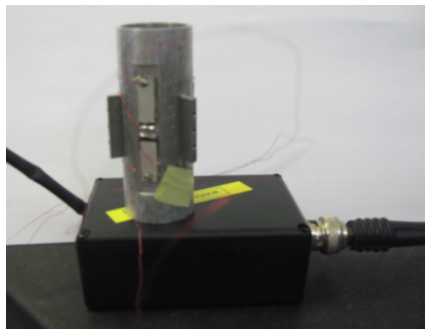


Figure 5.9 - Physical prototype of the proposed squeeze film air journal bearing with the BNC connection box input to the piezoelectric actuator.

Two bearings are made from material Al 2024-T3 and Cu C-101 have the exactly same dimensions (Details is given in Section 5.3). The dimensions are checked using the

## Chapter 5 – Design of squeeze film air bearing and its experiments

Coordinate Measurement Machine. The material properties of the two bearings are listed in Table 5.4.

Table 5.4 – Material properties of bearings.

Materials of bearing	Al 2024 - T3	Cu - C101
Young's modulus	73.1 GPa	117 GPa
Density	2780 Kg/m <sup>3</sup>	8910 Kg/m <sup>3</sup>
Poisson's Ratio	0.33	0.29
Fatigue Strength	0.138 GPa	0.117 GPa
Mass of bearing	0.0185 Kg	0.0575Kg

### 5.5.6 Guide way and guide way holder

The guide way, made from the material of the standard steel, is a round rod fixed at one end and free at the other with an overhang of 130mm; the short overhang is desired to avoid sagging due to its own weight. The diameter of the round rod is 19.99 mm (measured from CMM) and the surface roughness is only several nano-meters (measured from Zygo).

The guide way holder is also made of the steel and fixed on a heavy granite table mounted in such a way as to minimize the vibration transmitted from the ground. The guide way only was fixed at one end rather than both. The Engineering drawings for both the guide way and the guide way holder are presented in Appendices B2 and B3.

## 5.6 Signal-pickups

### 5.6.1 Capacitive displacement sensor

To measure vibration, a capacitive displacement probe (MicroSense 5501) and a gauging modulus (MicroSense 5810) shown in Figure 5.10, was used. The probe can measure a gap with the range of  $\pm 100$   $\mu\text{m}$  and with resolution of  $\pm 49.69$  nm. The measurement frequency is up to 7.703 MHz. In Figure 5.10, the probe is connected with the amplifier and the other BNC connection is for the signal output.

## Chapter 5 – Design of squeeze film air bearing and its experiments



Figure 5.10 - Capacitive displacement probe (MicroSense 5501) and gauging modulud (MicroSense 5810).

### 5.6.2 Data acquisition card

Data acquisition is the process of sampling signals that measure real world physical conditions such as vibration, and converting the resulting samples into digital numeric values, that can be manipulated by a computer. The function of the data acquisition card is to convert analogue waveforms into digital values for processing. The DAQ PCI-6110 is shown in Figure 5.11. The functions, specifications and operation coupling mode of DAQ PCI - 6110 are listed below.

#### •Signal recording

The signal detected from the capacitive displacement sensor was recorded on the DAQ card simultaneously with sampling frequency 300 kHz. The sampling frequency 300 kHz was chosen to make sure 10 samplings per cycle in order to capture a high frequency signal. Then the signal is converted into a digital format that can not only be stored in the PC but also be processed and analysed later on.

#### •Specifications of DAQ PCI – 6110

Four 12-bit input resolution channels, simultaneously sampled analogue-to-digital (A/D) input channels with scalable input limits and adjustable sampling rates up to 5 M samples/s; and also has two 16-bits analogue output resolution channels with samples



## Chapter 5 – Design of squeeze film air bearing and its experiments

rates 4 M samples/s for single channel. The DAQ PCI – 6110 has the high resolution input with enough input channels and the high sampling rates, which is suitable for capturing signal at both dynamic deformation and film thickness measurement [89]

•Operation coupling mode: AC and DC

The DAQ PCI-6110 also can select the coupling mode to be AC or DC in the voltage input setup. AC or DC coupling configure analogue inputs for AC or DC coupling on a per-channel basis. AC coupling removes the DC offset for applications only analyzing signals in the frequency domain. Some applications like measuring the dynamic response of the proposed bearing only need to measure the AC, so the DC offset can be removed. But some applications like measuring the mean film thickness between the bearing and the guide way need to measure both the AC and the DC offset.

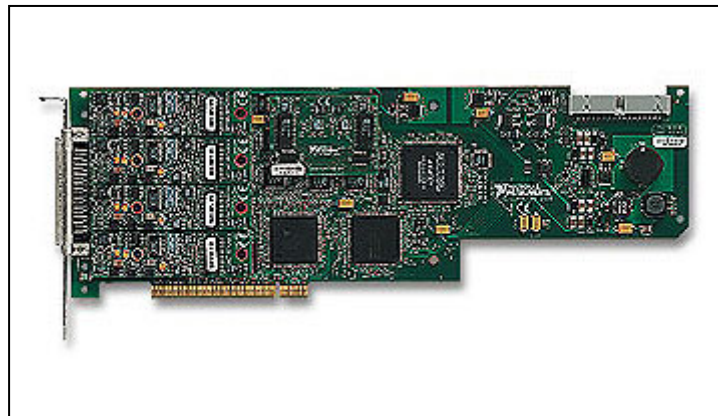


Figure 5.11- Data acquisition card PCI – 6110 from National Instrument [89].

### 5.6.3 LabVIEW user interface

Figure 5.12 shows the LabVIEW user interface in measuring the dynamic response of the squeeze film air bearing. The three graphs show the raw signal for amplitude response of the bearing, and the saw signal can be filtered to produce clearer signal in second graph. The third graph is the frequency response of the filtered signal. The amplitude response, oscillation amplitude in the second graph, was converted into the unit of  $\mu\text{m}$  from the voltage measured from the capacitive displacement sensor programmed in the block diagram panel. The conversion used is 1V to 10  $\mu\text{m}$ . The

## Chapter 5 – Design of squeeze film air bearing and its experiments

button “Save” and “Stop” is to save data in Excel and is to terminate running program.

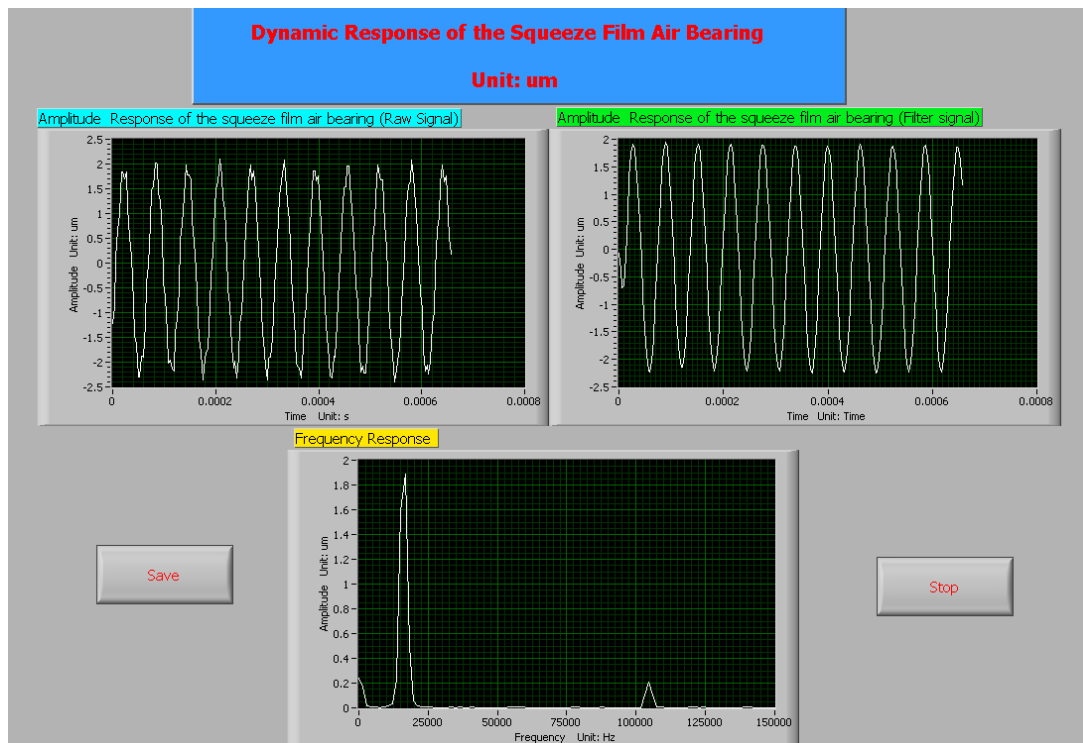


Figure 5.12- User interface for measuring the dynamic response of squeeze film air bearing.

### 5.7 Summery

The squeeze film air bearing system and process for the testing and modelling have been discussed in Section 2. The function of instrumentation is described in Table 1; and connections for instrumentation follows signal flow path shown in Figure 5.3.

Based on the five findings obtained from CFX simulation in Chapter 4, two journal squeeze air film bearings of identical geometry (Figure 5.1), one made from Al 2024 – T3 and the other Cu – 101C, were designed and built.

The design of the experiments and procedures used were presented in Section 5.4. The single layer piezoelectric actuators, driven by the actuator driver and bonded on the flat surface of the bearing, are used as the vibration source to deform the bearing as shown in Figure 5.2. For the proposed journal bearing, its mode shapes, natural frequencies,

### **Chapter 5 – Design of squeeze film air bearing and its experiments**

and dynamic deformations can be measured in Figure 5.3. The film thickness also can be measured in Figure 5.4. These experiments can be used to validate the theoretical results from FEA modelling. They were also used to determine the load-carrying capacity from the CFX simulation.

To measure the dynamic deformation of the squeeze film air bearing and the film thickness, the capacitive displacement sensor is used. The DAQ PCI-6110 is used to convert the analogue signal into the digital format. The LabVIEW user interface is used to collect the signals in the dynamic response and load-carrying capacity experiments.

## **Chapter 6 – Experimental and theoretical results of proposed squeeze film air journal bearing**

# **Chapter 6 - Experimental and theoretical results of proposed squeeze film air journal bearing**

### **6.1 Introduction**

This chapter is divided into two parts. Firstly, to study of the characteristics of the proposed squeeze film air journal bearing, it includes investigations on the static analysis, the modal analysis and the dynamic analysis on the bearings that made from the different materials, one is Al 2024 – T3 and the other is Cu – C101. Secondly, the load-carrying capacity experiments are also investigated for the two bearings based on the squeeze film effect.

In the static analysis, the static deformation of both bearings are analyzed and compared when the driving units, single layer piezoelectric actuators, are loaded with a DC of 75 V. Two normal mode shapes for both Al bearing and Cu bearing, the 13<sup>th</sup> and 23<sup>rd</sup>, at the respective frequencies of 16.368 kHz and 25.637 kHz for the former, at the respective frequencies of 12.315 and 18.709 kHz for the other, were analyzed theoretically and verified experimentally; furthermore, both of mode shapes were identified for further investigation by experiments with respect to the squeeze film thickness and its load-carrying capacity. The dynamic analysis gives the dynamic deformations at Mode 13 and 23 for the both bearings when the piezoelectric actuators are powered at a 75 V AC with a 75 V DC offset and the driving frequency coincided with the modal frequency of them.

In the load-carrying capacity experiments, Al bearing was excited at and around the natural frequency of Mode 13 and that of Mode 23 in order to find out the air film thickness. Particularly at Mode 13, the air film thickness was obtained by driving the piezoelectric actuators in the variable AC voltages that have three levels 55 V, 65 V and 75 V. By knowing the air film thickness at the both Mode shapes for Al bearing, therefore the comparison is laid out to find out the superior Mode shape. When it comes

## **Chapter 6 – Experimental and theoretical results of proposed squeeze film air journal bearing**

to Cu bearing, the experiment will only focus on the Mode 13 and the AC driving voltage of 75 V because both driving conditions suggested from doing Al bearing experiment can produce better levitation performance. The comparison for the air film thickness is also laid out between Al bearing and Cu bearing in order to find out a superior material in terms of the levitation performance for designing squeeze film bearing.

### **6.2 Theoretical and experimental results of characteristics of squeeze film air journal bearing**

#### **6.2.1 Material properties of proposed squeeze film air journal bearings**

The two proposed squeeze film air journal bearings, one made from Al 2024 –T3 and from Cu – C101, have the same structural geometries; but different the material properties as is listed in Table 5.4. In ANSYS simulations, the material properties (Young's modulus, Poisson's ratio and Density of material) need to be written into ANSYS Macro for ANSYS software recognizing structure's material for all the analyses. The following sections will be studying the static analysis, the modal analysis and the dynamic analysis. The stress and fatigue analyses are exclusive because both of them were proven to be safe for a small deformation in squeeze film bearing as results suggested in Chapter 4.

#### **6.2.2 Static analysis - computer modelling and simulation**

The purpose of the static analysis was to determine the static deformation of the sleeve bearing when a DC voltage (0V on the bottom and 75V on the top surfaces of piezoelectric layer) was applied to the six single layer piezoelectric actuators. Figure 6.1 shows the result of the analysis, from which a maximum radial deformation of 0.124  $\mu\text{m}$  for the sleeve bearing made from Al 2024-T3 (Al bearing) is seen to occur in the middle section, represented by the red colour. The spikes occur at outside face of the bearing is because of the deformation of the piezoelectric actuator; and the deformation is exaggerated for clear view.

## Chapter 6 – Experimental and theoretical results of proposed squeeze film air journal bearing

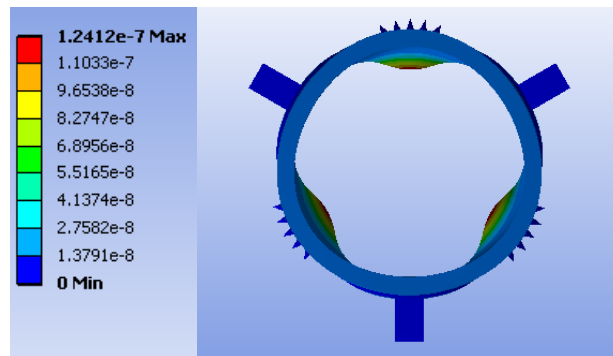


Figure 6.1 - Static deformation of the bearing when a 75V DC voltage was applied to the six actuators. (Deformation no to scale)

The above-mentioned analysis was repeated for other driving DC voltages and Figure 6.2 shows the relationship between the maximum static deformation and the voltage input, which is observed to be linear [23]. When the same driving condition is applied to the sleeve bearing made of Cu - C101 (Cu bearing), the comparison of the static deformation between Cu bearing (red colour line) and Al bearing (blue colour line) is shown in Figure 6.3. Moreover, it is observed that the static deformation of Cu bearing is less than that of the Al bearing; for instance, the maximum radial deformation for the Cu bearing is  $0.104 \mu\text{m}$  with applied 75 DC voltages, but with the same DC voltage Al bearing can have static deform of  $0.124 \mu\text{m}$ . The ANSYS Macros for the static deformation analysis is available at Appendix C3.

Figure 6.2 - Static deformation varies linearly with the applied DC voltage.

Figure 6.3 - Comparison of the static deformation between Al bearing and Cu bearing with the various DC voltages.

## **Chapter 6 – Experimental and theoretical results of proposed squeeze film air journal bearing**

In the FEA modelling process, the force of the piezoelectric actuators as it varies with the driving voltage was accurately represented. This is unlike the approximations that most other researchers, for example [23], made by assuming that a maximum blocking force exists for all boundary conditions.

### **6.2.3 Modal analysis**

Modal analysis can determine the theoretical vibration characteristics, in terms of natural frequencies and mode shapes, of a structure or a machine component. The natural frequencies and the mode shapes are important parameters in the design of a structure for dynamic loading conditions. It is believed that certain mode shapes enhance the effectiveness of the squeeze air film in journal bearings. These mode shapes have geometry that maximizes the amplitude ratio  $\varepsilon$  and minimizes the end leakage.

From the FEA modal analysis, two candidate mode shapes were identified to have the desired geometry, namely the 13<sup>th</sup> and the 23<sup>rd</sup> modes at the respective natural frequencies of 16.368 kHz and 25.637 kHz for Al bearing and natural frequency of 12.315 kHz and 18.409 kHz for Cu bearing. The mode shapes are shown in Figure 6.4 where the red end of the colour spectrum denotes greater deformation. It is observed that:

1. Both modes produce flexing of the shell on the sleeve between pairs of fins which remain in the same angular orientation during the vibration; both mode shapes are triangular.
2. At Mode 13, the outer edges of the round sleeve do not appear to deform much while the middle section deforms noticeably.
3. At Mode 23, the outer edges of the round sleeve deform noticeably while the middle section deforms not as much.

## Chapter 6 – Experimental and theoretical results of proposed squeeze film air journal bearing

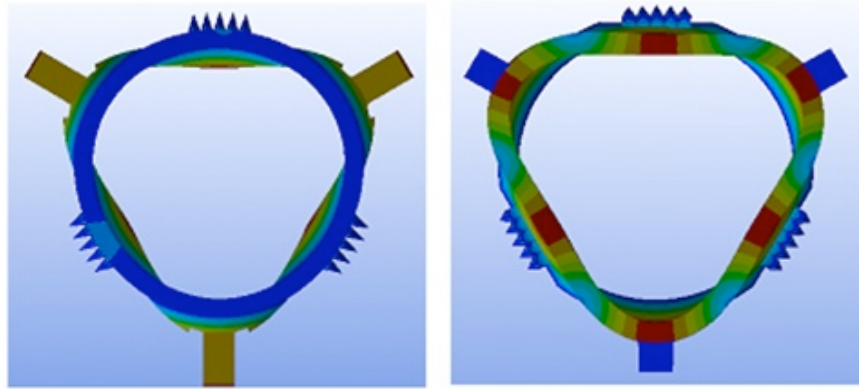


Figure 6.4 - a) Left - mode shape 13; b) right - mode shape 23.

To create these mode shapes all six piezoelectric actuators need to be driven in synchronisation at the natural frequency of the mode shape. For instance, the mode shape 13 for Al bearing can be obtained by driving the piezoelectric actuator at natural frequency of 16.368 kHz.

The experiment was fulfilled by using the capacitive displacement sensor to measure the maximum dynamic deformations in the radial direction and the corresponding natural frequencies at and around the natural frequencies suggested by the FEA modal modelling. The comparison for the natural frequencies between the theory and experiment for Al bearing and Cu bearing are listed in Table 6.1. It can be observed that the natural frequency of Al bearing is about 1.33 times and 1.37 times as large as that of Cu bearing for Mode 13 and for Mode 23, respectively. The analytical solution of natural frequencies for a cantilever beam is described in Eq. (6.1). The equation is applicable as an approximation for the two proposed bearings because the flat can be seen as fixed supporter and middle body can be considered as the beam. By considering the two bearings have same geometries, which means  $I$ ,  $L$ ,  $A$  can be cancelled; moreover, the both of them driven at same Mode 13 so  $\lambda$  can also be dropped out. Based on the above cancellation, the natural frequency ratio for Cu bearing and Al bearing can be expressed as Eq. (6.2). Both Young's modulus and density for Al bearing and Cu bearing were given in Table 5.4. So the natural frequency ratio of them is calculated to be 1.415 driven at Mode 13 using the analytical solution. The natural frequency ratio can be worked out to be 1.329 based on the results (Table 6.1) from the



**Chapter 6 – Experimental and theoretical results of proposed squeeze film air journal bearing**

FEA modal analysis. The natural frequency ratio can also be worked out to be 1.339 based on the experimental results as indicated in Table 6.1. The difference of natural frequency ratio between the FEA and experimental results is 0.773%. The other modal frequencies of Al bearing are given at Appendix A5.

Table 6.1 – Comparison between experimental and theoretical results in natural frequencies for Al bearing and Cu bearing.

	<b>Material used for bearing</b>	<b>Al bearing</b>	<b>Cu bearing</b>
<b>Mode shape 13</b>	<b>Theoretical</b>	16.368 kHz	12.315 kHz
	<b>Experimental</b>	16.320 kHz	12.184 kHz
<b>Mode shape 23</b>	<b>Theoretical</b>	25.637 kHz	18.709 kHz
	<b>Experimental</b>	25.322 kHz	18.459 kHz

$$f \tag{6.1}$$

where,  $Y$  is Young’s modulus,  $\rho$  is density,  $A$  is cross section area,  $I$  is second moment of area,  $L$  is the length of the beam and  $\alpha$  is mode coefficient.

Theoretical solution: Natural frequency ratio = 1.415 (6.2)

Experimental solution: Natural frequency ratio = 1.339

**6.2.4 Dynamic analysis**

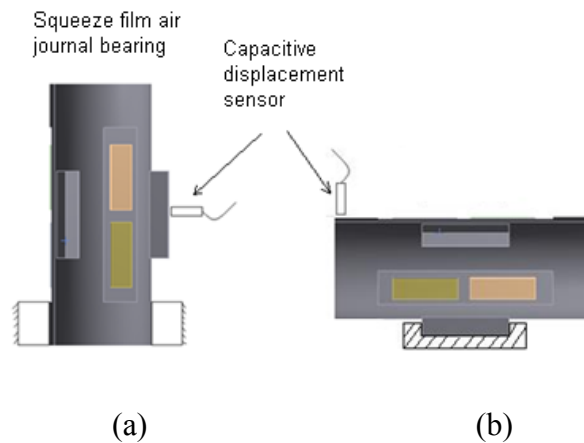
6.2.4.1 Dynamic analysis for Mode 13 and 23 of Al bearing

The dynamic excitation forces are created by the expansion and the compression of the piezoelectric actuators when they are loaded with an AC voltage (75V) on top of a DC offset (75V). The excitation frequency should be coincident with one of the natural frequencies for either Mode 13 or 23, as identified in Section 6.2.3 for achieving the maximum dynamic response.

A dynamic response experiment was performed to validate the bearing’s natural frequencies and mode shapes at Modes 13 and 23 for both Al bearing and Cu bearing. For measuring Mode 13, the bearing was placed on a horizontal flat surface, as shown in Figure 6.5 (a), and was supported at two positions (line contacts) near to the bottom

## Chapter 6 – Experimental and theoretical results of proposed squeeze film air journal bearing

edge. These points of contact were chosen to coincide with the nodal points (of no displacement) of the bearing; those nodal points were determined by the FEA modal modelling. The displacement of a fin was measured with the non-contacting capacitive displacement sensor, also shown in Figure 6.5 (a). In order to validate Mode 13 as same as that suggested by the FEA modal modelling, the capacitive displacement sensor needs to be used for measuring the other two fins; through experiments the movement of three fins are validated to be similar. The dynamic deformation of Mode13 for Al bearing is shown in Figure 6.6.



(a) for Mode 13; and (b) for Mode 23

Figure 6.5 - Set-up for the dynamic deformation measurement.

Figure 6.6 - Dynamic deformation on the fin of the Al bearing at Mode 13 versus the excitation frequency for the three levels of AC input; the error bars represent  $\pm 2$  standard errors

Figure 6.6 shows the dynamic deformation of a point on the fin of Al bearing as measured by the capacitive displacement sensor. Measurements were made 10 times and it is the average that is shown on the graph; the corresponding error bar represents  $\pm 2$  standard errors. The narrow extent of the error bars suggests good measurement repeatability and high precision of the dynamic deformation obtained. The measurement data are available at Appendix A2.

## **Chapter 6 – Experimental and theoretical results of proposed squeeze film air journal bearing**

To correctly locate the natural frequency at Mode 13, the actuators were driven to excite the bearing over a range of frequencies from 16.28 kHz to 16.55 kHz at three different levels of AC voltage, namely 75V, 65V and 55V. The natural frequency for Mode 13, from Figure 6.6, is 16.320 kHz at which the dynamic deformation on the fin is the greatest, for example, at 75V AC, the dynamic deformation is 2.88  $\mu\text{m}$ ; at 65 V AC, the dynamic deformation is 2.27  $\mu\text{m}$ ; at 55V AC, the dynamic deformation is 1.88  $\mu\text{m}$ . The dynamic deformation decreases by reducing the AC voltage. The trend agrees with the FEA modelling for the simple beam in Chapter 4.

The dynamic deformation was measured at the AC of 75 V and the DC of 75 V using LabVIEW software as shown in Figure 6.7. In the LabVIEW data acquisition program, the sampling is 200 points and sample rate is 300 kHz, so the display time is only 0.00066 s. The driving frequency is 16.320 kHz, so the numbers of cycles displayed in Figure 6.7 is 10.7 and each cycle contains about 18 points. The sampling rate is required to be high for capturing the maximum peak of each cycle. The dynamic deformations at 55 V AC and 65 V AC measured by LabVIEW are available at Appendix A3.

Since the 75V AC gives the greatest dynamic deformation, which in turn produces the greatest mean pressure ratio as suggested by the CFX modelling and the ideal gas law modelling (Chapter 4). This validated driving condition is going to be used for driving the bearings subsequently in the load-carrying capacity experiments.

## Chapter 6 – Experimental and theoretical results of proposed squeeze film air journal bearing

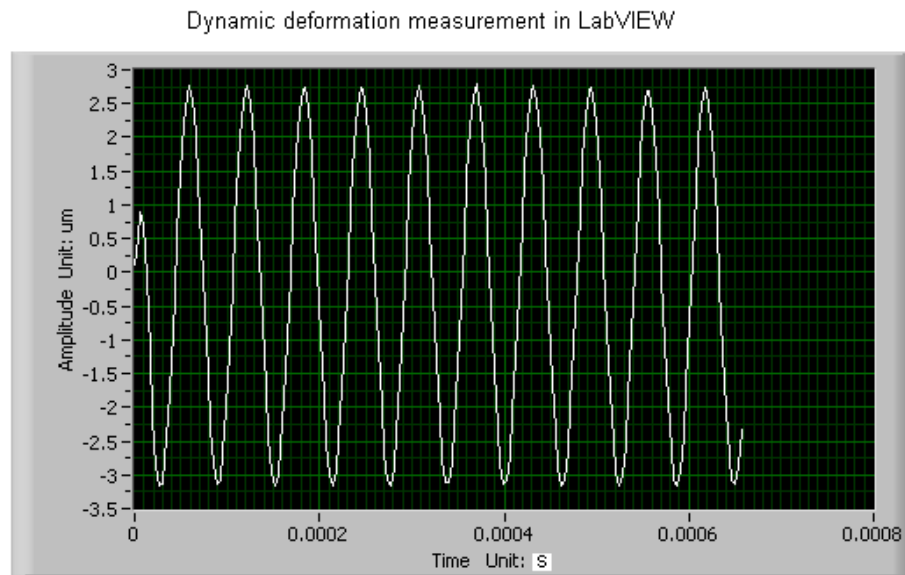


Figure 6.7 – Dynamic deformation measurement using LabVIEW software.

The experiment was repeated for Mode 23 of Al bearing. The measurement point, in this case, was near the end of the sleeve where the deformation is observed to be significant, Figure 6.4 (b). So the position of the capacitive displacement sensor should be placed near to the edge of the sleeve to measure the dynamic deformation as shown in Figure 6.5 (b). The results are shown in Figure 6.8. It is noted that the natural frequency for Mode 23 is 25.310 kHz and the maximum dynamic deformation is 1.94  $\mu\text{m}$  at 75 V AC.

Figure 6.8 - Dynamic deformation at the edge of Al bearing at Mode 23 versus the excitation frequency for the three levels of AC input.

Figure 6.9 shows the dynamic deformation of Al bearing in the FEA dynamic response modelling for Mode 13. The piezoelectric actuator is driven by the 75V DC offset and the 75V AC at the excitation frequency of 16.368 kHz. It can be observed from Figure 6.9 that, according to the theory of forced vibration, the transient vibration happens initially but it decays quickly; the forced vibration starts from 0.55 ms and the maximum dynamic deformation of that is about 3.22  $\mu\text{m}$ . Mode shape 23 is also

## Chapter 6 – Experimental and theoretical results of proposed squeeze film air journal bearing

studied in the FEA dynamic response modelling by driving the piezoelectric actuator in the frequency of 25.637 kHz. The maximum dynamic deformation is about 2.08  $\mu\text{m}$ .

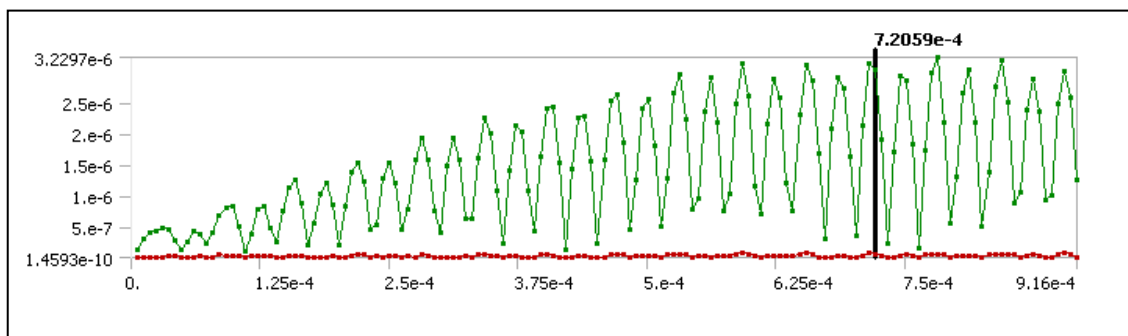
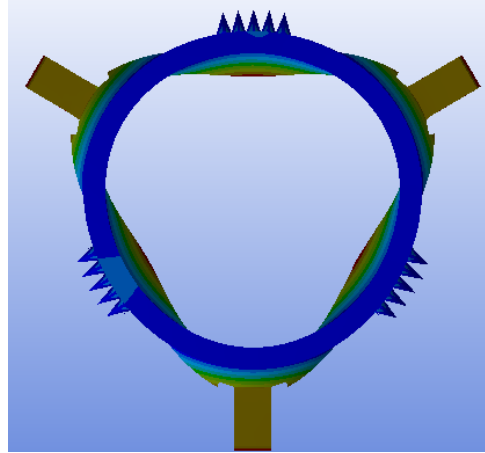


Figure 6.9 – FEA dynamic modelling for dynamic deformation of mode shape 13. (Horizontal axis is time, unit: s; and vertical axis is dynamic deformation, unit: m)

From the FEA model, the theoretical dynamic deformation at the measurement point was also obtained for the different driving conditions. Figure 6.10 shows the comparison between the theoretical and experimental dynamic deformation at Mode 13. The deviation between the theoretical and experimental results is 0.33  $\mu\text{m}$  at 75 V and is 0.02  $\mu\text{m}$  at 55 V. Figure 6.11 shows the comparison between the theoretical and experimental dynamic deformation at Mode 23. The deviation between the theoretical and experimental results is 0.14  $\mu\text{m}$  at 75 V and 0.18  $\mu\text{m}$  at 55 V.

By comparing Mode 13 and Mode 23 in Figure 6.12, the former has larger dynamic deformation than the latter in the same driving conditions. For instance, Mode 13 in experimental result gives the dynamic deformation of 2.88  $\mu\text{m}$  at 75 V and Mode 23 in

## **Chapter 6 – Experimental and theoretical results of proposed squeeze film air journal bearing**

experimental result only gives that of  $1.94\ \mu\text{m}$ . Furthermore, the maximum deformation regions of Mode 13 and 23 are different; Mode 13 has the maximum deformation on the three fins, but Mode 23 has that on the edges of the sleeve. Both of these differences, the dynamic deformation and the deformation region, maybe affect the levitation performance of the squeeze film air journal bearing.

Figure 6.10 - Comparison between theoretical and experimental dynamic deformation at Mode 13 for Al bearing (DC = 75V and variable AC).

Figure 6.11- Comparison between theoretical and experimental dynamic deformation at Mode 23 for Al bearing (DC = 75V and variable AC).

Figure 6.12 – Comparison between Mode 13 and Mode 23 for Al bearing (DC = 75V and variable AC)

### 6.2.4.2 Dynamic analysis for Mode 13 and 23 of Cu bearing

The same test was repeated for obtaining the dynamic deformation of Cu bearing. In order to accurately locate the natural frequency at Mode 13, the piezoelectric actuator were driven to excite the bearing over a range of frequency from 11.90 kHz to 12.35 kHz at three different levels of AC voltage and constant DC of 75 V as shown in Figure 6.13. It can be observed that the maximum dynamic deformation is  $2.41\ \mu\text{m}$  with

## **Chapter 6 – Experimental and theoretical results of proposed squeeze film air journal bearing**

excitation frequency of 12.184 kHz at AC 75 V. The mode shape 23 also can be obtained with driving the piezoelectric actuator in the excitation frequency of 18.459 kHz as shown in Figure 6.14, from which the maximum dynamic deformation is 1.68  $\mu\text{m}$  at AC 75 V.

Figure 6.13 - Dynamic deformation on the fin of Cu bearing at Mode 13 versus the excitation frequency for the three levels of AC input.

Figure 6.14 - Dynamic deformation on the fin of Cu bearing at Mode 23 versus the excitation frequency for the three levels of AC input.

Figure 6.15 and Figure 6.16 show the comparison between the theoretical and experimental dynamic deformation at Mode 13 and 23, respectively. The deviation between the theoretical and experimental results at Mode 13 is 0.05  $\mu\text{m}$  at AC 75 V and at Mode 23 is 0.02  $\mu\text{m}$  at AC 75 V. The position of the capacitive displacement sensor was located in the positions according to Figure 6.5(a) and 6.5 (b) for Mode 13 and 23 respectively. Furthermore, the dynamic deformation displayed in the LabVIEW program, similar to Figure 6.7, for Cu bearing is available at Appendix A4.

Figure 6.15 - Comparison between theoretical and experimental dynamic deformation at Mode 13 for Cu bearing (DC = 75V and variable AC).

Figure 6.16- Comparison between theoretical and experimental dynamic deformation at Mode 23 for Cu bearing (DC = 75V and variable AC).

## **Chapter 6 – Experimental and theoretical results of proposed squeeze film air journal bearing**

### **6.2.4.3 Comparison study in the dynamic response between Al bearing and Cu bearing**

Figure 6.17 and Figure 6.18 show the comparison between the theoretical and experimental dynamic deformation of Al bearing and Cu bearing at Mode 13 and Mode 23. It can be observed from both figures that the experimental dynamic deformation of Al bearing is greater than Cu bearing has at all the AC voltage. The theoretical results in the FEA modelling also show that Al bearing has the greater dynamic deformation than that of Cu bearing at all the AC voltages 55 V, 65 V and 75 V.

According to the CFX modelling, from which points that the greater oscillation amplitude the thicker air film thickness can be obtained. By taking into account the above finding, Al bearing should give superior levitation performance than that of Cu - C101 relied on the greater dynamic deformation. The assumption can be validated experimentally in the following sections by load-carrying capacity experiments.

Figure 6.17 - Comparison between the theory and the experiment of dynamic deformation for Al bearing and Cu bearing at Mode 13 (DC = 75V and variable AC).

Figure 6.18 - Comparison between the theory and the experiment of dynamic deformation for Al bearing and Cu bearing at Mode 23 (DC = 75V and variable AC).

## **6.3 Load-carrying capacity experiments**

### **6.3.1 Experiment description**

In the load-carrying capacity experiments, the squeeze film air journal bearing was inserted into the round guide way, set up as a cantilever, as shown in Figure 6.19. A mass was hung onto a wire attached to a fin of the bearing and the bearing was excited at a number of frequencies near a particular mode. Using the measurement from the



## Chapter 6 – Experimental and theoretical results of proposed squeeze film air journal bearing

capacitive displacement sensor, it is possible to calculate the instantaneous film thickness in the vertical plane of the bearing. The minimum value was then computed from the instantaneous film thickness over a number of oscillations, typically a thousand. The procedure was then repeated for other masses.

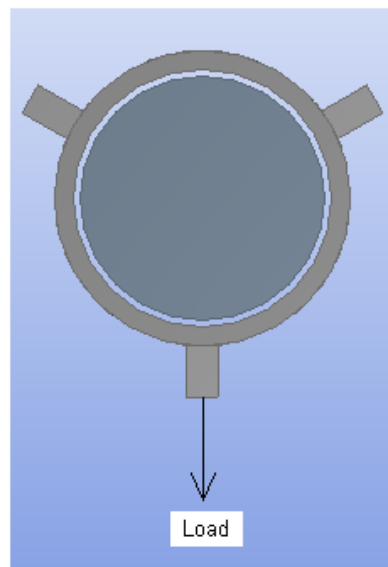


Figure 6.19 - Direction of loading by hanging masses.

### 6.3.2 Load-carrying capacity experiments on Al bearing at Mode 13 and 23

For Al bearing at Mode 13, Figure 6.20 shows the relationship between the air film thickness and load at four different excitation frequencies at and around the natural frequency of Mode 13. At the natural frequency of 16.320 kHz, the air film thickness is greater than those at other frequencies below a load of about 2 N. From this experiment, it proves the point derived in the CFX modelling that the greater oscillation amplitude can give the greater air film. Because when the excitation frequency is

## **Chapter 6 – Experimental and theoretical results of proposed squeeze film air journal bearing**

coincident with the bearing's natural frequency, it produces the bigger dynamic deformation than the other excitation frequency has. However, when the load is increased beyond 2.5 N, its film thickness becomes about the same as those at other frequencies. An explanation could be that with increasing load through adding mass, the natural frequency of the bearing/mass system shifts away from its original value and so the bearing is no longer being excited at its true natural frequency.

Figure 6.20 - Air film thickness of bearing versus load at four excitation frequencies around Mode 13 of Al bearing.

Figure 6.21 shows the relationship between the air film stiffness and load steps. The initial load is 1.14 N at load step 1 and each step increases load of 0.50 N for Al bearing driven at Mode 13 with the AC 75V and DC 75V. The air film stiffness can be calculated by using increased weights divided decreased film thicknesses. It can be observed that the initial air film stiffness is very small only around 0.3 N/ $\mu\text{m}$  up to load step 2. When it is in the load step 3 and 4, the stiffness is increased to about 0.7 N/ $\mu\text{m}$  and 1.2 N/ $\mu\text{m}$  respectively.

Figure 6.21 – Air film stiffness versus load steps for Al bearing driven at Mode 13 with AC 75 V and DC 75 V.

Figure 6.22 shows the relationship between the air film thickness and load when Al bearing is excited around the natural frequency 16.320 kHz at three levels of the AC voltage 75 V, 65 V and 55 V. The air film thickness driven at AC 75 V can be observed from Figure 6.22, which is greater than the other two have. Moreover, the air film thickness is nearly zero when the load is beyond 2N driven at AC 65V and 55V. This is because of the AC 75 V produces larger oscillation amplitude than the others. In order to achieve the greater film thickness, the AC 75V is chosen for the rest analysis.

## **Chapter 6 – Experimental and theoretical results of proposed squeeze film air journal bearing**

Figure 6.22 - Air film thickness driven in the variable AC, namely, 55 V, 65 V and 75 V.

Figure 6.23 shows the relationship between the air film thickness and load at four different excitation frequencies at and around the natural frequency of Mode 23. At the natural frequency of 25.322 kHz, the air film thickness is also greater in the range of loads experimented. It also proves the point discovered from the CFX simulation.

Figure 6.23 - Air film thickness of bearing versus load at four excitation frequencies around Mode 23 of Al bearing.

When the air film thickness at Mode 13 and Mode 23 are placed side by side, the difference in values is striking, showing that Mode 13 is a far superior mode in terms of load-carrying capacity. The comparison is made in Figure 6.24 where the bearing was excited at the natural frequency of Mode 13 and Mode 23. When the bearing is loaded at 1.64 N, the air film thickness of Mode 13 is about 6.5 times as large as that of Mode 23. By considering the fact that Mode 13 is a far superior mode in terms of load-carrying capacity than that of Mode 23 has. The following study in Cu bearing will only focus on load-carrying experiment at Mode 13.

Figure 6.24 - Comparison between Mode 13 and Mode 23 in the load-carrying capacity.

## **Chapter 6 – Experimental and theoretical results of proposed squeeze film air journal bearing**

Because of the effect of the added mass on the natural frequency of the bearing, if the excitation frequency was to remain a constant, then the bearing might not be always excited in the particular mode at the exact natural frequency. However, if the excitation frequency was changed to make sure that it was in tune with the natural frequency, the air film thickness might turn out to be greater. When the squeeze film bearing was loaded up to 2 N, the excitation frequency was changed from 16.320 kHz to 16.980 kHz. Figure 6.25 compares two sets of results obtained, one with frequency adjustment and the other without.

Figure 6.25 - Effect of mass loading on the natural frequency of the bearing, affecting the air film thickness and hence the load-carrying capacity.

### **6.3.3 Load-carrying capacity experiments on Cu bearing at Mode 13**

Figure 6.26 shows the relationship between the air film thickness and load at three different excitation frequencies at and around the natural frequency of Cu bearing. At the natural frequency of 12.184 kHz, the air film thickness is also greater than the others driving at 11.906 kHz and 12.156 kHz.

Figure 6.26- Floating test based on the variable excitation frequencies for copper squeeze film air bearing.

When the air film thickness for Al bearing and Cu bearing are placed side by side, the difference in values is striking, showing that Al bearing is a far better than Cu bearing in terms of the load-carrying capacity. The comparison is made in Figure 6.27 where the bearing was excited at the natural frequency of Al bearing and Cu bearing. It can be observed that the air film thickness of Al bearing is about three times as large as Cu bearing has with load around 1.55 N. By increasing load up to 2 N, the air film thickness of Al bearing is about two times as large as that of Cu bearing. It proves that

## **Chapter 6 – Experimental and theoretical results of proposed squeeze film air journal bearing**

the bearing made from the Al produces a better levitation performance than that made from the Cu.

Figure 6.27 - Comparison between Al bearing and Cu bearing in the load-carrying capacity.

### **6.3.4 CFX simulation validations**

#### **6.3.4.1 Air film thickness and oscillation amplitude**

According to the second finding (in Chapter 4) the air squeeze film thickness increases with the amplitude of oscillation of the shell. Experiments were conducted to validate this assertion. Figure 6.28 shows the relationship between the air film thickness and the oscillation amplitude at three load levels. The loading was implemented by attaching a weight to the journal bearing and three loads were studied, namely 1.14 N, 1.64 N and 2.14 N. These loads were hung on the bottom fin – see Figure 6.19 – such that there was a squeeze air film at the top and another pair symmetrically disposed at  $120^\circ$  on either side. In Figure 6.28, it can be seen that the minimum film thickness increases in an exponential fashion with increasing oscillation amplitude for all three different loads.

Figure 6.28 – Air film thickness versus oscillation amplitude at three load levels.

#### **6.3.4.2 Comparison between experimental and theoretical air film thickness**

With the journal bearing loaded as described in Section 6.3.1 corresponding to the orientation of the three squeeze films as shown in Figure 6.19, an approximate simulation CFX model was formulated and analysed. Three simplifying assumptions were made:

## **Chapter 6 – Experimental and theoretical results of proposed squeeze film air journal bearing**

1. As the surrounding sleeve is loaded, the squeeze film at the top has a thickness which is much smaller than that at the other two squeeze film situated towards the bottom (Figure 6.19), such that the levitation force created is solely due to the top squeeze film;
2. The top squeeze film is flat and there is no leakage along circumferential direction but leakage along bearing's length-wise direction when in operation; and
3. The upper plate of the top squeeze film translates bodily up and down with no deformation (rigid body).

The CFX simulation modelled an air film which was 30mm long, 0.1 mm wide and 0.03 mm thick using the same set of boundary conditions as that described in Section 4.3.3.3. The sliced air film in the CFX simulation only has width of 0.1 mm, which 40 times less than the deformable area of the bearings shell along circumferential direction in order to make sure that the boundary conditions for the front and back sides (Figure 4.22) can be applied as symmetrical. The length of air film is 30 mm, which is half length of the bearing shell to make sure that the boundary condition of the left side can be applied as symmetrical. The air film thickness of 0.03mm is the total gap clearance between the guide way and the inner surface of the bearing shell. Since the bearing shell of the top squeeze film did not oscillate as a rigid body but rather flexed itself at Mode 13 natural frequency, the average amplitude of oscillation of 1.31  $\mu\text{m}$  was used in the simulation. This average was obtained by measuring the modal shape of the bearing shell at the top squeeze film with the bearing driven at Mode 13 natural frequency of 16.320 kHz and then taking an arithmetical average from these measurements.

Figure 6.29 shows the results from the simulation as compared to those obtained from the experiment for different loadings. There is a broad agreement between the two in terms of the trend and of the values of the air film thickness, with better fit towards the higher loading. It is summarized that the better fit could be due to the fact that the first assumption becomes more correct as the loading increases. The agreement between the

## **Chapter 6 – Experimental and theoretical results of proposed squeeze film air journal bearing**

theoretical and experimental results serves, in some way, to validate the CFX simulation results, from which the five findings were derived.

Figure 6.29 – Comparison of theoretical and experimental for air film thickness.

### 6.3.4.3 Comparison between experimental and theoretical air film stiffness

Figure 6.30 shows the comparison between the experimental and theoretical air film stiffness. As the thickness of the air film decreases, the air film stiffness increases with an exponential manner. Initially, the air film stiffness is very low because the thick air film is formed with light loading by the squeeze film effect. As keep increasing the loading, the air film thickness gets decreased as result the air film stiffness increased. The air film stiffness can be infinite based on the theory but the optimal stiffness is necessary to be considered to avoid instability and to avoid excessive friction.

Figure 6.30 – Comparison between experimental and theoretical air film stiffness.

## **6.4 Discussion**

On the issue of the end leakage, driving Al bearing at its natural frequency particularly at higher modes is beneficial because the natural frequency tends to be high. The design described in the paper was operated at Mode 13 and 23 at the natural frequencies of 16.368 kHz and 25.637 kHz respectively. This compares favourably with the designs by

## **Chapter 6 – Experimental and theoretical results of proposed squeeze film air journal bearing**

Stolarski [23] and by Yoshimoto [21], both driving their designs at a frequency lower than or at the fundamental frequency. For Cu bearing, the natural frequency for Mode 13 and 23 are 12.184 kHz and 18.459 kHz, respectively.

Between Mode 13 and Mode 23, Mode 13 has superior performance for Al bearing. This is because of its lower end-leakage due to the deformable geometry: the sleeve has the maximum deformation in the middle section of itself under the actuators are made to flex thus creating a squeeze air film. The ring of stagnant air film at both ends of the squeeze film minimises the leakage effect.

In the FEA modelling of the bearing, the piezoelectric actuators are accurately represented as a unit that expands and contracts with the driving voltage. In addition, the interaction with sleeve as the actuator moves is also accounted for by including the material properties of the two parts. Consequently the analysis is more accurate.

According to Figure 6.3, the static analysis shows the linear relationship between the input DC voltage and the deformation on Al bearing and Cu bearing. Moreover, Al bearing can produce bigger static deformation than Cu bearing has when both of them are loaded in same driving condition (DC 75 V). The linear relationship between input DC voltage and the deformation was also obtained by Stolarski.

Given the same driving condition, the dynamic response is much bigger than the static response for the both of bearings. In particular for Al bearing, when it is driven at the Mode 13 natural frequency the maximum displacement at the fin is roughly 3  $\mu\text{m}$ . However, when excitation frequency drifts from the natural frequency, the amplitude falls, Figure 6.6. The same conclusion can be drawn for Mode 23. The similar result was also obtained by Yoshimoto [28], who observed vibration amplitudes of about 1.5  $\mu\text{m}$  at the excitation frequency of 23.7 kHz and at 70V AC.

Figure 6.30 shows the air film stiffness of the proposed Al bearing driven at Mode 13 (AC 75V and DC 75V). Initially, the air film stiffness is less rigid that could induce the issue of instability during operation. Furthermore, the air film stiffness cannot be too rigid; otherwise, it could induce excessive friction during operation as well.



## **Chapter 6 – Experimental and theoretical results of proposed squeeze film air journal bearing**

Given the different driving conditions for AC at 55 V, 65 V and 75 V, the bigger air film thickness can be obtained when AC is 75V in Figure 6.22. The bigger air film thickness can also be obtained when the excitation frequency is coincident with the natural frequency of Mode 13 for both, Al bearing and Cu bearing than the excitation frequency is coincident with the natural frequency of Mode 23. However, when the air film thickness for Al bearing and Cu bearing are placed side by side, the strike difference can be observed in Figure 6.27. The two reasons for that: firstly, the dynamic deformation of Al bearing is bigger than that of Cu bearing when excited in Mode 13, Figure 6.17; secondly, Al bearing at the natural frequency of Mode 13 is much higher than Cu bearing has, according to Table 6.1. The above two explanations are based on the results of the CFX modelling.

### **6.5 Summery**

The characteristics of the proposed squeeze film air journal bearings are analyzed theoretically and experimentally in this chapter. The load-carrying capacity experiments also fulfilled for the both bearings to find out the relationship between the air film thickness and the load in terms of excitation frequency at and around their natural frequency of Mode shapes.

The findings in this chapter are summarized as follows:

1. Two normal modes, at the 13<sup>th</sup> and 23<sup>rd</sup>, of both Al bearing and Cu bearing were identified to have the desired geometry of the modal shape, namely that of a triangle. The corresponding theoretical natural frequencies were found to be 16.368 kHz and 25.637 kHz for Al bearing and 12.315 kHz and 18.709 kHz for Cu bearing at Mode 13 and Mode 23, respectively. The results are confirmed also by experiments.
2. From the FEA analysis, the maximum radial static deformation of Al bearing when driven at 75 V DC was observed to be 0.124  $\mu\text{m}$ . In the same driving condition, the static radial deformation of Cu bearing is 0.104  $\mu\text{m}$  less than Al bearing has.

## **Chapter 6 – Experimental and theoretical results of proposed squeeze film air journal bearing**

3. When Al bearing was driven at 75V AC with 75V DC offset, the dynamic deformation was 2.88  $\mu\text{m}$  (Figure 6.6) and 1.98  $\mu\text{m}$  (Figure 6.8) for Modes 13 and 23 respectively. The measurements were highly repeatable as is evident from the small extent of the error bars in Figure 6.6. When Cu bearing was driven at same condition, the dynamic deformation is 2.41  $\mu\text{m}$  (Figure 6.13) and 1.68  $\mu\text{m}$  (Figure 6.14) at Mode 13 and 23 respectively.

4. For Al bearing, between Mode 13 and 23, Mode 13 has superior performance in the Load-carrying experiments. This is because of its lower end-leakage due to the deformation in the middle at Mode 13 rather than that of around edges at Mode 23.

5. The load-carrying experiments also show that when Al bearing driven at AC 75 V can produce the bigger air film thickness than the driven at both AC 65 V and 55 V, according to Figure 6.22.

6. By comparing the air film thickness between the bearings driven at the natural frequency of Mode 13 with the AC 75 V and the DC 75 V, Al bearing has superior levitation performance than Cu bearing as shown in Figure 6.27. The two reasons for that are: first, Al bearing at natural frequency of Mode 13 is greater than Cu bearing has, which can reduce pressure end-leakage of the squeeze-air film; second, the dynamic deformation of Al bearing is larger than that of Cu bearing at the same driving voltage.

7. By comparing the air film thickness and the air film stiffness for Al bearing between the experimental and theoretical results, both of them show a broad agreement.

## **Chapter 7 – Fluid solid interaction (FSI) in coupled- field analysis for squeeze film effect**

### **Chapter 7 – Fluid solid interaction (FSI) in coupled- field analysis for squeeze film effect**

#### **7.1 Introduction**

A coupled-field analysis (also called Multiphysics) is a combination of analyses from different engineering disciplines (physics fields) that interact to solve a global engineering problem; hence, the coupled-field analysis is often referred as a Multiphysics analysis. When the input of one field analysis depends on the results from another, the analyses are coupled [90 and 91].

The coupled-field analysis involved is a two-way coupling for a piezoelectric analysis in Chapter 4; it handles the interaction between the solid structure (squeeze film bearing) and the electric fields (voltage): typically it solves the static and dynamic deformation of the structure due to applied voltage to piezoelectric actuators. Moreover, the dynamic deformation of the structure depends not only on the magnitude of the applied voltage but also on its excitation frequency.

The other coupled-field analysis is to study a fluid solid interaction (FSI) problem because thin film effects are important not only for microstructures but also for macrostructures. Presence of such fluids may add mass, stiffness and damping, which change the structural mechanics of the system. But for light-weight, easily compressible fluid such as a gas does not add appreciable mass, but they can add stiffness to the structure at certain operation conditions [92 and 93]. In this study, the dynamic behaviour of the structure can be influenced by involving a thin layer of air film between the levitated object and the structure itself during the squeeze film action. The fluid solid interaction (FSI) in the squeeze film effect will be studied in the following sections.

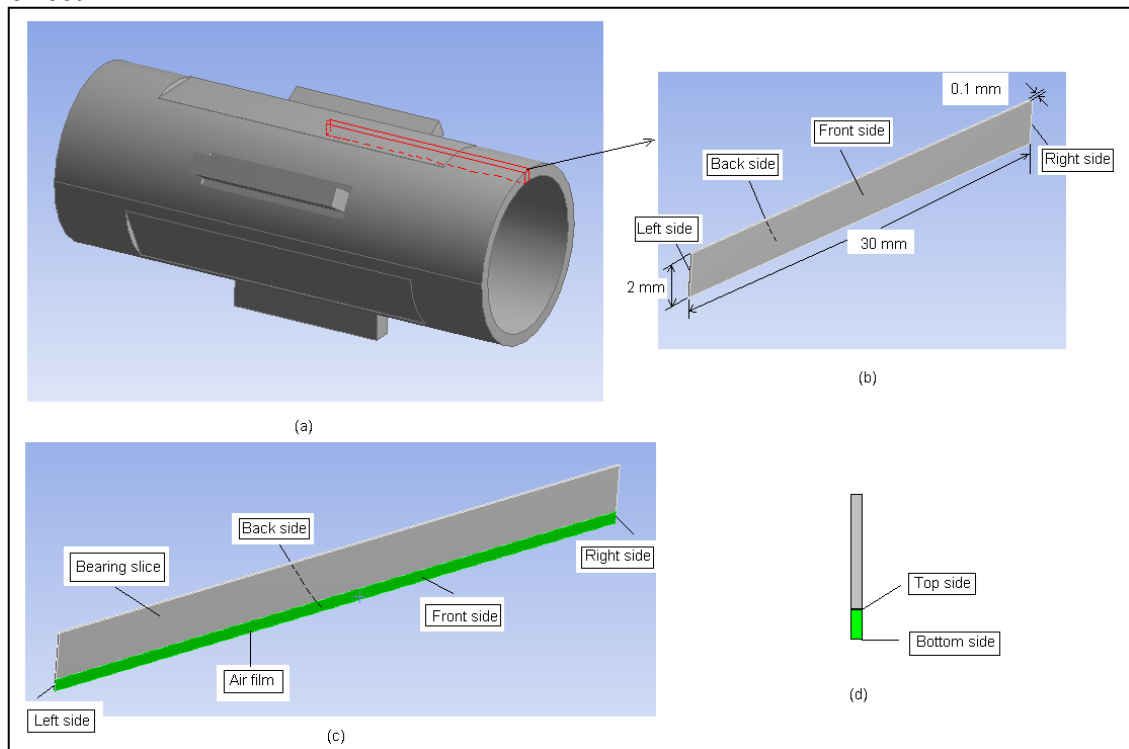
## **Chapter 7 – Fluid solid interaction (FSI) in coupled- field analysis for squeeze film effect**

### **7.2 Fluid solid interaction (FSI)**

Squeeze film analysis simulates the effects of fluid in small gaps between fixed surfaces and structures moving perpendicular to the surfaces. Depending on the operating frequencies, the fluid can add stiffness or damping or both to the system. At lower frequencies, the fluid can escape before it is compressed. Therefore, the fluid only adds damping to the system. At high frequencies, the fluid compresses before it can escape. Therefore, the fluid adds both stiffness and damping to the system but the stiffness is more dominant than the other at the high frequency excitation [94]. Moreover, the squeeze film effect tends to be prevalent at high frequency at which a mean pressure about the ambient is created, resulting in a levitation force. So the air film at high frequency oscillation needs to be considered and analyzed to see how it affects the dynamic behaviour of the squeeze film bearing during a rapid squeeze film action.

In the FSI analysis, it is not necessary to assume that the bearing slice is a rigid body, as was assumed for the CFX simulation. Figure 7.1 shows a bearing slice with its surfaces labelled and dimensioned (Figure 7.1(b)) from the whole squeeze film air journal bearing (Figure 7.1(a)); the fluid solid interaction system (Figure 7.1(c)) shows an air film beneath the bearing slice. In the FSI analysis, a single layer piezoelectric actuator is mounted on the top of the bearing slice; moreover, it is driven at certain frequency to produce the desired mode shapes.

## Chapter 7 – Fluid solid interaction (FSI) in coupled- field analysis for squeeze film effect



(a) Squeeze film air journal bearing;

(b) Bearing slice;

(c) Fluid solid interaction system; (air film thickness not to scale)

(d) Section view of fluid solid interaction system;

Figure 7.1 – Bearing slice from whole squeeze film air journal bearing.

In the coupled-field analysis, the single layer piezoelectric actuator is mounted on the top of the bearing slice. The piezoelectric actuator is driven at 75 V AC at a frequency of 16.32 kHz with a 75 V DC offset. The boundary conditions of the bearing slice is defined as (refer to Figure 7.1 (b)):

1) The left side of the bearing slice is fixed;

2) The right side is applied as symmetrical; and that

3) The front and back sides are considered to be symmetrical as well.

## Chapter 7 – Fluid solid interaction (FSI) in coupled- field analysis for squeeze film effect

Figure 7.2 shows the coupled-field analysis result. It can be seen that a maximum dynamic deformation of 2.91  $\mu\text{m}$  occurs in the region indicated in red. In contrast, the blue region indicates no movement. In this case, it is more complicated than the CFX modelling of the two flat plates (Chapter 6) where the bottom one is considered a rigid body and oscillates perpendicularly to the top plate at a certain frequency. In the FSI analysis, the bearing slice is modelled more realistically as a flexible body that can deform dynamically. This means that the bearing slice moves the different amount of distance in the vertical direction, referred to Figure 7.2. It is believed to be the more realistic and hence accurate way for analyzing the squeeze film effect because it considers not only the pressure end-leakage around edges, but also the flexibility of the structure that can vibrate at a certain mode shape.

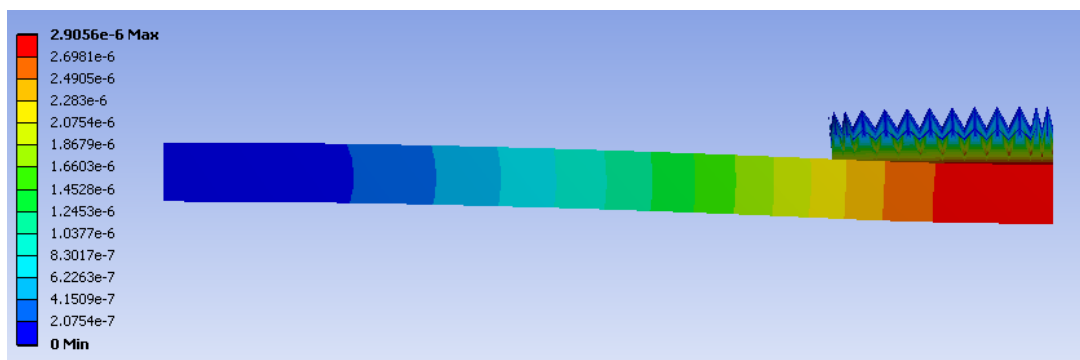


Figure 7.2 – The dynamic deformation of bearing slice.

### 7.2.1 FSI analysis at Mode 13

For the squeeze film bearing at Mode 13, as observed from the modal analysis reported in Chapter 6, only the middle region of the bearing shell is deformed rather than the two edges. The coupled-field analysis for the FSI modelled an air film underneath the bearing slice (Figure 7.1 (c) and (d)). The dynamic deformation of the bearing slice is investigated with consideration of the air film at Mode 13. The boundary conditions of the air film are given below:

- 1) The right side is on the plane of symmetry of the complete air film;
- 2) The left side is open, exposed to the atmosphere and pressure end-leakage is expected.

## **Chapter 7 – Fluid solid interaction (FSI) in coupled- field analysis for squeeze film effect**

3) The front and back sides is also symmetrical;

4) The top side is defined as a fluid solid interface;

5) The bottom side is considered as a rigid Wall;

Figure 7.3 shows the relationship between the oscillation frequency and the dynamic deformation at the point which is on the right side (Figure 7.1 (b)) when the bearing slice vibrates close to the air film with a thickness of 5  $\mu\text{m}$ . It can be seen that the dynamic deformation of the bearing slice is reduced from 2.91  $\mu\text{m}$  without considering the air film (Figure 7.2) to 1.90  $\mu\text{m}$  when considering the air film (Figure 7.3) at the oscillation frequency of 16.32 kHz. In addition, it can also be observed that the dynamic deformation decreases with the oscillation frequency; even at low frequency of 0.1 kHz the micron level of gap clearance provides a damping effect that influences the dynamic deformation slightly. In Chapter 4, Finding 1, from CFX simulation, concludes that the higher oscillation frequency can create the bigger air film thickness within a certain range of the oscillation frequency. In that case, it was assumed that the fluid force had a negligible effect on the deformation during high frequency squeeze action. But in this study, it is observed that the fluid force does affect the dynamic deformation especially at high frequency. This contradiction needs to be considered in the modelling of the squeeze film bearing. The coupled-field analysis for FSI does point to the fact that the fluid forces in the squeeze air film can affect the dynamic deformation of the structure at some mode shapes such as Mode 13.

Figure 7.3 – Dynamic deformation versus oscillation frequency of bearing slice at air film thickness of 5  $\mu\text{m}$ .

Figure 7.4 shows the relationship between the air film thickness and the dynamic deformation of the bearing slice at Mode 13. It can be seen that the dynamic deformation of the bearing slice increases with the air film thickness in a logarithmic

## **Chapter 7 – Fluid solid interaction (FSI) in coupled- field analysis for squeeze film effect**

manner. For example, even at the gap clearance of 40  $\mu\text{m}$ , there is still damping present, enough to reduce the dynamic deformation of the bearing slice by 0.06  $\mu\text{m}$ .

Figure 7.4–Dynamic deformation of bearing slice versus gap clearance.

### **7.2.2 FSI analysis at Mode 23**

For the squeeze film bearing at Mode 23, the bearing shell deforms at and round edges at the frequency of 25.322 kHz but not in the middle region. Therefore, the boundary conditions of the air film in the CFX simulation need to be defined to reflect this, as (refer to Figure 7.1(c)):

- 1) The left side is on the plane of symmetry of the complete air film;
- 2) The right side is open, exposed to the atmosphere and pressure end-leakage is expected.
- 3) The front and back sides is also symmetrical;
- 4) The top side is defined as a fluid solid interface;
- 5) The bottom side is considered as Wall;

The above boundary conditions are used in the FSI analysis to see how the fluid force affects the dynamic deformation of the bearing slice at Mode 23. Figure 7.5 shows the dynamic deformation at 9 locations which is from the right middle of the bearing slice to the furthest point which is 3 mm away from right side edge, referred to Figure 7.6, at three levels of gap clearance. It can be observed that the dynamic deformation is hardly affected by decreasing gap clearance; and it even hardly decreases compared to the dynamic deformation of 2.91  $\mu\text{m}$  for the bearing slice in the absence of an air film. Based on the above observations, it can be concluded that the fluid force hardly affects



### Chapter 7 – Fluid solid interaction (FSI) in coupled- field analysis for squeeze film effect

the dynamic deformation of the bearing slice at Mode 23; and at the three micron levels of gap clearance, very little damping effect is shown for the bearing slice oscillating at Mode 23. The reason for this is due to the presence of pressure end-leakage at and around edges.

Figure 7.5 – Dynamic deformation of bearing slice along the length at three levels of gap clearance, 10  $\mu\text{m}$ , 20  $\mu\text{m}$  and 30  $\mu\text{m}$ .

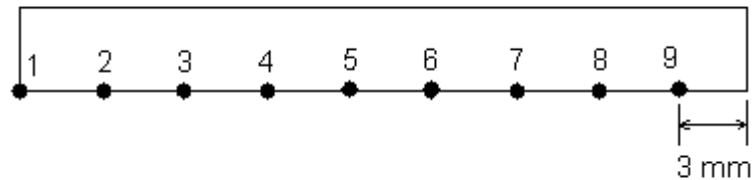


Figure 7.6 – Monitoring points along the length-wise of the bearing slice.

The coupled-field analysis procedure for FSI is shown in Figure 7.7. In it, the coupling effect is represented by the data transfer of total mesh displacement and total force function between the solid domain and the fluid domain. Detailed procedure on how to generate each of the files ( .inp --- .def ----- .cdb ----- .dat) for FSI analysis is given at Appendix D1.

**Chapter 7 – Fluid solid interaction (FSI) in coupled- field analysis for squeeze film effect**

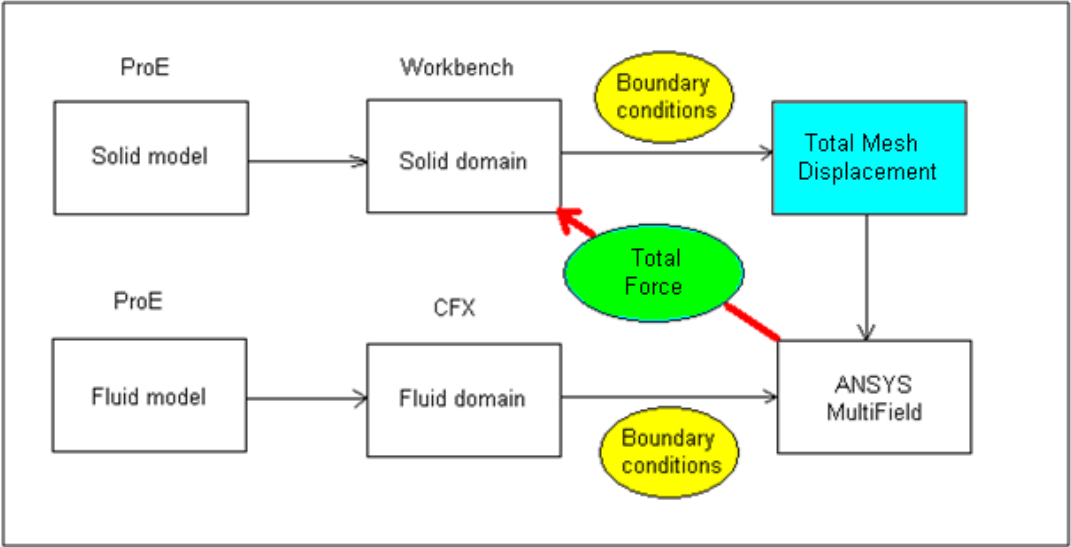


Figure 7.7 – Diagram of fluid solid interaction.

**7.3 Conclusion**

The coupled-field analysis for FSI is studied at Modes 13 and 23. From the analysis, it can be concluded that the fluid force can influence the dynamic deformation of the bearing slice, especially at high oscillation frequency, more at Mode 13 than at Mode 23 due to the relatively high pressure end-leakage in the latter. The dynamic deformation of the bearing slice increases with the gap clearance in a logarithmic manner at Mode 13 (Figure 7.4). Furthermore, the micron levels of gap clearance provide a damping effect on the dynamic deformation of the bearing slice at both Mode 13 and 23, though much less dominant.

## Chapter 8 – Conclusions and recommendations for further work

# Chapter 8 – Conclusions and recommendations for further work

This chapter presents conclusions drawn from the research and investigation reported in earlier chapters, highlights the contributions to knowledge, and recommends further areas of research that need to be conducted in the field of squeeze film bearings.

### **8.1 Conclusions**

Based on the theoretical simulation results in Chapter 3 and 4 and the experimental results in Chapter 6 and 7, the following conclusions can be drawn:

1. Two Modes, at the 13<sup>th</sup> and 23<sup>rd</sup>, of both the Al bearing and Cu bearing were identified to have the desired modal shape geometry, namely that resembling a triangle when the deflection is highly magnified. The theoretical natural frequencies were found to be 16.368 kHz and 25.637 kHz for Al bearing and 12.315 kHz and 18.709 kHz for Cu bearing at Mode 13 and Mode 23, respectively (Chapter 6.2.3). The results are confirmed also by experiments.
2. From the FEA analysis, the maximum radial static deformation of Al bearing when driven at 75 V DC was observed to be 0.124  $\mu\text{m}$ . In the same driving condition, the static radial deformation of the Cu bearing is 0.104  $\mu\text{m}$  being less than that of the Al bearing (Chapter 6.2.2).
3. When Al bearing was driven at 75V AC with a 75V DC offset, the dynamic deformation was 2.88  $\mu\text{m}$  for Mode 13 (Figure 6.6) and 1.98  $\mu\text{m}$  for Mode 23 (Figure 6.8) (Chapter 6.2.4.1). The measurements were highly repeatable as is evident from the small extent of the error bars in Figure 6.6. When the Cu bearing was driven in the same condition, the dynamic deformation is 2.41  $\mu\text{m}$  (Figure 6.13) and 1.68  $\mu\text{m}$  (Figure 6.14) at Mode 13 and 23 respectively (Chapter 6.2.4.2).

## **Chapter 8 – Conclusions and recommendations for further work**

4. For Al bearing, between Mode 13 and 23, the former has a superior performance in the load-carrying capacity experiments (Figure 6.24). This is because of its lower end-leakage due to the deformation in the middle at Mode 13 rather than that occurring around the outer edges at Mode 23.

5. The load-carrying capacity experiments also show that Al bearing driven at AC 75 V can produce bigger air film thickness than when driven at either AC 65 V or 55 V, according to Figure 6.22.

6. By comparing the air film thickness between the bearings driven at the natural frequency of Mode 13 with the AC 75 V and the DC 75 V, it is observed that Al bearing has a superior levitation performance than Cu bearing (Figure 6.27). There are two reasons for that. First, Al bearing at natural frequency of Mode 13 is greater than Cu bearing has, which can reduce pressure end-leakage of the squeeze-air film; second, the dynamic deformation of Al bearing is larger than that of the Cu bearing.

7. For Al bearing, there is a broad agreement between the theoretical and experimental air film thickness and stiffness (Figure 6.30).

8. From the FSI analysis, it can be concluded that at high frequencies the fluid force is significant enough to affect the dynamic deformation of the bearing slice for Mode 13 during the rapid squeeze film action (Figure 7.3); but this is not the case for Mode 23 (Figure 7.5). It is also found that the micron gap clearance produces a damping effect that influences the dynamic deformation slightly for both Modes 13 and 23.

### **8.2 Contributions to knowledge**

The research has led to the following contributions to knowledge. It includes the dynamic characteristics of bearing, bearing material, location for mounting single layer piezoelectric actuator and fluid solid interaction for analyzing squeeze film effect.

## **Chapter 8 – Conclusions and recommendations for further work**

### **8.2.1 Dynamic characteristics of bearing**

The dynamics of the squeeze film air journal bearing should be considered following the below findings in order to produce a larger film thickness or greater load-carrying capacity.

1. The oscillation frequency should be at least 15 kHz to ensure a greater film thickness and to reduce end leakage;
2. The operating frequency should be set to coincide with one of natural frequencies of the squeeze film air bearing in order to produce greater oscillation amplitude. Two operation frequencies are 16.320 kHz and 25.322 kHz for Al bearing and 12.184 kHz and 18.459 kHz for Cu bearing;
3. Not all mode shapes are suitable for generating the same level of levitation performance. The desirable mode shape should be such that there is minimum end leakage, thus giving a maximum levitation force. In the load-carrying capacity experiment, it is found that Mode 13 can produce better levitation performance than Mode 23;
4. The oscillation amplitude should be large enough to ensure a greater air film thickness. It is found that as the oscillation amplitude increases the air film thickness increases in an exponential manner;
5. The oscillation frequency should be high enough to ensure that the bearing reaches its stable equilibrium position in a short time. The higher the oscillation frequency the smaller is the bearing shell response amplitude about its equilibrium position.

### **8.2.2 Bearing material**

The material for the bearing is also an important factor that can affect the levitation performance. It is believed that the same geometry made by certain material can produce a larger deformation than others with the same load. In this research, the bearing made from Al gives a larger static and dynamic deformation than the bearing

## **Chapter 8 – Conclusions and recommendations for further work**

made from Cu. Because of the different static and dynamic deformation, it leads to the different levitation performance. In the load-carrying capacity experiment, it is proven that Al bearing has a superior levitation performance than Cu bearing. Moreover, Al bearing has relatively low mass than Cu bearing due to the different density. This research also has proved that Al bearing can carry a heavier load than Cu bearing.

### **8.2.3 Location for mounting single layer piezoelectric actuator**

The location for mounting the single layer piezoelectric actuator is important because it can influence the deformation of the bearing shell, particularly when the range of actuator force considered is low. In this study, the three flat surfaces were milled outside the bearing shell for mounting the piezoelectric actuator to deform the bearing shell directly. This arrangement can produce the dynamic deformation: for Al bearing, 2.88  $\mu\text{m}$  and 1.94  $\mu\text{m}$  at Mode 13 and 23, respectively; and for Cu bearing, 2.41  $\mu\text{m}$  and 1.61  $\mu\text{m}$  at Mode 13 and 23, respectively.

### **8.2.4 Coupled-field analysis between piezoelectric actuator and solid structure**

The single layer piezoelectric actuator was modelled to calculate two important parameters, the maximum stroke length and the maximum blocking force, as a starting point leading to the subsequent study. In the coupled-field analysis, both the piezoelectric actuators and the solid structure were modelled with the realistic boundary conditions; especially for the piezoelectric actuator, it was modelled without assuming that the maximum blocking force exists for all boundary conditions. Furthermore, the realistic boundary conditions are the key leading to accurate simulation results.

### **8.2.5 Fluid solid interaction for analyzing squeeze film effect**

At the micron levels of the gap clearance, the fluid film can influence the stiffness and damping in the dynamic deformation of the bearing shell of a certain mode shape at the

## **Chapter 8 – Conclusions and recommendations for further work**

high operation frequency. So the oscillation frequency needs to be chosen not only to minimise the pressure end-leakage but also to keep the oscillation amplitude high. The fluid solid interaction analysis has determined that the dynamic deformation of Al bearing shell is reduced by 1.01  $\mu\text{m}$  at Mode 13 when the air film thickness is 5  $\mu\text{m}$ ; and the dynamic deformation of Al bearing shell is only reduced by 0.24  $\mu\text{m}$  at Mode 23 when the air film thickness is 10  $\mu\text{m}$ .

### **8.3 Recommendations for future work**

While having solved a number of important issues, the research has led to a host of questions that have yet to be answered. These lead to the following recommendations for future work:

1. To optimize the existing design based on the findings in the beginning of this chapter. Implementing these findings in designing a squeeze film bearing often leads to compromises. For example, the finding suggests that high oscillation amplitude in the bearing shell is desirable. This can be achieved by making the shell thinner. But a thinner shell can lower the modal frequency and this is in conflict with the other finding that the excitation frequency has to be high to avoid end leakage. The bearing design is therefore an act of optimisation. It will be interesting to establish what combinations of design parameters will produce the optimal design.
2. To improve the driving unit. The piezoelectric actuator is made from brittle material that could be fractured if the structure deformation is too big. Instead of using the piezoelectric actuator, a new type of material, the Macro Fibre Composite (MFC), could be a better driving unit due to its higher flexibility [95].
3. To use the acoustic emission to detect the onset of physical contact between the journal and the bearing. In the load-carry capacity experiment, the surface finish of both surfaces that enclose the very thin squeeze film can be crucial to the levitation. With increasing loading, the two surfaces will start touching each other at a certain load

## **Chapter 8 – Conclusions and recommendations for further work**

and local deformation on the surfaces may occur. Whilst the capacitive displacement sensor is capable of measuring displacement down to nanometre level, it is not sensitive enough to detect the onset of physical contact. By contrast, the acoustic emission [96], may be a more effective and obvious method.

4. To validate the theoretical results on how the dynamic deformation of the squeeze film bearing is affected at the micro gap clearances at both low frequency and high frequency operation conditions.



## References

## References

- [1] Tonphong, K. 'Bearing Condition Monitoring using Acoustic Emission and Vibration – The Systems Approach –'. PhD Thesis, Brunel University, September 2002.
- [2] Salbu, E. (1964) 'Compressible squeeze films and squeeze bearings', ASME.Journal of Basic Engineering, 86, pp.355-366.
- [3] Jonathan, W. (2003) *An Introduction to Mechanical Engineering*. Xian: Xian Jiaotong University Press.
- [4] New way precision (2003) Air bearing application and design guide. Available at: [www.newwayprecision.com](http://www.newwayprecision.com) [Accessed 5th January 2010].
- [5] Venkatesh, V. C. and Izman, S. (2007) *Precision Engineering*. USA: Tata McGraw-Hill.
- [6] Westwind Air Bearings (2007) Air Bearing Technology, Available at: <http://www.westwind-airbearings.com/AirBearing/documents/AirBearingTechnologybriefv2.pdf> [Accessed 25th March 2009].
- [7] Grassam, N. S. (1964) *Gas lubricated bearings*. UK: R.J.Acford Ltd.
- [8] Liquid lubrication (2008). Available at: [www.roymech.co.uk/Useful\\_Tables/Tribology/Liquid\\_Lubrication.htm](http://www.roymech.co.uk/Useful_Tables/Tribology/Liquid_Lubrication.htm) [Accessed 23rd January 2010].
- [9] British Petroleum Company. (1969) *Lubrication theory and its application*. UK: Harrison and Sons Limited High Wycombe press.
- [10] Society of Tribologists and Lubrication Engineers (2008) Basics of Lubrication, Available at: <http://www.stle.org/resources/lubelearn/lubrication/default.aspx> [Accessed 26th September 2010].
- [11] Abdel-Rahman, G. M. (2007) 'Studying fluid squeeze characteristics for aerostatic journal bearing', Journal of Physica B, 403, pp. 2390-2393.

## References

- [12] Klimenkov, Y.S. (2008) 'Improving the Operation of Aerostatic Bearings', Journal of Russian Engineering Research, 28, pp.14-19.
- [13] Guo, Z. L., Hirano, T. and Kirk, R.G. (2005) 'Application of CFD analysis for rotating machinery – Part1: Hydrodynamic, hydrostatic bearings and squeeze film damper', Journal of Engineering for Gas Turbines and Power, 127(10), pp.445-451.
- [14] Moore, D. F. (1964) 'A review of squeeze films', Journal of WEAR, 8, pp. 245-263.
- [15] Emmerich, C. L. "Piezoelectric oscillating bearing", US patent No.3351393, November 1967.
- [16] Warnock, L. F. "Dynamic gas film supported inertial instrument", US patent No. 3339421, September 1967.
- [17] Farron, T. B. R., John R. "Squeeze film bearings", US patent No.3471205, October 1969.
- [18] Caruso, M. B., Scranton, R. A. "Long Tube Bender Element Squeeze Bearing", US patent No.4593956, October 1986.
- [19] Scranton, R. A. "Planar and cylindrical oscillating pneumatodynamic bearings", US patent No. 4666315, May 1987.
- [20] Yoshimoto, S. and Anno, Y. (1993) 'Rectangular squeeze-film gas bearing using a piezoelectric actuator – application to a linear motion guide', International Journal of JSME, 27(3), pp.259-263.
- [21] Yoshimoto, S., Anno, Y., Sato, Y. and Hamanaka, K. (1995) 'Floating characteristics of squeeze-film gas bearing with elastic hinges for linear motion guide', International Journal of JSME, 60(11), pp. 2109-2115.
- [22] Stolarski, T.A. and Chai, W. (2006) 'Self-levitation sliding air contact', International Journal of Mechanical Sciences, 48 (1), pp.601-620.

## References

- [23] Stolarski, T.A. and Woolliscroft, S.P. (2007) 'Performance of a self-lifting linear air contact', *Journal of Mechanical Engineering Science*, 221, pp.1103-1115.
- [24] Stolarski, T.A. (2006) 'Self-lifting contacts: from physical fundamentals to practical application', *International Journal of Mechanical Engineering Science*, 220 (C), pp.1211-1218.
- [25] Stolarski, T.A. and Woolliscroft, C.I. (2007) 'Near Field Acoustic Levitation Sliding Constant', *Journal of Applied Mechanics*, 74(4), pp.816-820.
- [26] Stolarski, T.A. and Chai, W. (2006) 'Load-carrying capacity generation in squeeze film action', *International Journal of Mechanical Sciences*, 48 (3), pp.736-741.
- [27] Stolarski, T.A. (2009) 'Numerical modelling and experimental verification of compressible squeeze film pressure', *Journal of Tribology International*, 43, pp. 356-360.
- [28] Yoshimoto, S., Kobayashi, H. and Miyatake, M. (2006) 'Floating characteristics of a squeeze –film bearing for a linear motion guide using ultrasonic vibration', *Journal of Tribology International*, 40 (5), pp.503-511.
- [29] Ono, Y., Yoshimoto, S. and Miyatake, M. (2009) 'Impulse-Load dynamics of squeeze film gas bearings for a linear motion guide', *Journal of Tribology*, 131(10), pp. 1-6.
- [30] Ha, D.N., Stolarski, T.A. and Yoshimoto, S. (2004) 'An aerodynamic bearing with adjustable geometry and self-lifting capacity. Part 1: self-lift capacity by squeeze film', *Journal of Engineering Tribology*, 219(J), pp.33-39.
- [31] Stolarski, T.A. (2011) 'Running Characteristics of Aerodynamic Bearing with Self-Lifting Capability at Low Rotational Speed', *Journal of Advanced in Tribology*, 2011, pp.1-10.
- [32] Zhao, S. and Wallaschek, J.: Design and modelling of a novel squeeze film journal bearing, in: *Proceedings of the 2009 IEEE International Conference on Mechatronics and Automation*, Changchun, China, 9-12 August 2009, 1054-1059, 2009.

## References

- [33] Moreno, E., Acevedo, P. and Fuentes, M.: Design and Construction of a Bolt-Clamped Langevin Transducer, in: Proceedings of the 2<sup>nd</sup> International Conference on Electrical and Electronics Engineering (ICEEE) and XI Conference on Electrical Engineering (CIE2005), Mexico City, Mexico, 7-9 September 2005, 393-396, 2005.
- [34] Young, H.D. and Freedman, R. A. (1996) *University Physics*. 9th edn. USA: Addison – Wesley Publishing Company press.
- [35] Memorial University of Newfoundland, Isothermal and Adiabatic Processes, Available at: <http://www.physics.mun.ca/~cdeacon/labs/2053/adiabatic.pdf> [Accessed 24th May 2010].
- [36] Miranda, E. N. (2002) ‘Adiabatic reversible compression: a molecular view’, *European Journal of Physics*, 23, pp.389-393.
- [37] Gross, W.A. (1962) *Gas Film Lubrication*. New York: John Wiley and Sons.
- [38] Stolarski, T.A. and Chai, W. (2008) ‘Inertia effect in squeeze film air contact’, *Journal of Tribology International*, 41, pp.716-723.
- [39] Cameron, A. (1976) *Basic Lubrication Theory*. 2nd edn. UK: Ellis Horwood Limited.
- [40] Bao, M. H., Yang, H. and Sun, Y.C., et al. (2003) ‘Modified Reynolds’ equation and analytical analysis of squeeze – film air damping of perforated structures’, *Journal of Micromechanics and Microengineering*, 13, pp.795-800.
- [41] Ashok, K. P. and Rudra, P. (2007) ‘Effect of flexural modes on squeeze film damping in MEMS cantilever resonators’, *Journal of Micromechanics and Microengineering*, 17, pp.2475-2484.
- [42] Young, J.Y. ‘Squeeze–film Damping for MEMS Structures’. Master Dissertation, Massachusetts Institute of Technology, 1998.
- [43] Mehner, J.E., Doetzel, W. and Schauwecker, B., et al. (2003) Reduced Order Modeling of Fluid Structural Interactions in MEMS Based on Modal Projection Techniques. Available at: <http://www.fem-ware.de/latestarticles/trans2003.pdf> [Accessed 25th January 2010].
- [44] Bao, M.H. and Yang, H. (2007) ‘Squeeze film air damping in MEMS’, *Journal of Sensors and Actuator A PHYSICAL*, 136, pp.3-27.

## References

- [45] Bao, M.H., Yang, H. and Sun, Y, C., et al. (2003) ‘Squeeze – film air damping of thick hole – plate’, *Journal of Sensors and Actuators A PHYSICAL*, 108, pp.212-217.
- [46] Ostergaard, D. and Mehner, J. (2003) Using a Heat Transfer Analogy to Solve for Squeeze Film Damping and Stiffness Coefficients in MEMS Structure. Available at: [http://www.jigsaw.com/scid8376611/dale\\_ostergaard.xhtml](http://www.jigsaw.com/scid8376611/dale_ostergaard.xhtml) [Accessed 21st May 2010].
- [47] Minikes, A. and Bucher, I. (2002) ‘Coupled dynamics of a squeeze – film levitated mass and a vibrating piezoelectric disc: numerical analysis and experimental study’, *Journal of Sound and Vibration*, 263, pp.241-268.
- [48] Ibrahim, R. ‘Vibration Assisted Machining: Modelling, Simulation, Optimization, Control and Applications’. PhD Thesis, Brunel University, 2010.
- [49] Rao, S.S. (1995) *Mechanical Vibrations*. 3rd edn. USA: Addison – Wesley.
- [50] Dadkhah, F. and Zecher, J. (2007) *ANSYS Workbench™ Software Tutorial with Multimedia CD Release*. ANSYS Inc: Schroff Development Corporation.
- [51] Veidt, M., Liu, T.R. and Kitipornchai, S. (2001) ‘Flexural waves transmitted by rectangular piezoceramic transducers’, *Journal of Smart Material and Structure*, 10, pp. 681-688.
- [52] Kandagal, S. B. (2009) ‘Piezoceramic (PZT) patch Impulse hammer for modal analysis’, *India Journal of Science and Technology*, 2, pp.1-4.
- [53] Freyer, B. H., Theron, N. J. and Heyns, P. S. (2007) ‘Simulation of Tool Vibration Control in Turning - Using a self-Sensing Actuator’, *Journal of Vibration and Control*, 14(7), pp.999-1019.
- [54] Piezoelectric materials (2007). Available at: <http://www.piezomaterials.com/> [Accessed 19th October 2009].
- [55] APC International Ltd. (2002) *Piezoelectric Ceramics: Principles and Applications*. USA: APC International Ltd.
- [56] Introduction to Piezoelectric actuator, Available at: <http://www.piezo.com/tech2intropiezotrans.html> [Accessed 25th October 2009].
- [57] Physik Instrument. (2004) ‘Fundamentals of Piezoelectricity and Piezo Actuators’, Available at: [http://www.physikinstrumente.com/tutorial/4\\_15.html](http://www.physikinstrumente.com/tutorial/4_15.html) [Accessed 1st January 2010].
- [58] PZT application manual, Available at: <http://www.aurelienr.com/electronique/piezo/piezo.pdf> [Accessed 28th March 2009].

## References

- [59] Bernard, J. (1974) *Piezoelectric ceramics*. 2<sup>nd</sup> edn. UK: Academic Press.
- [60]PI, Available at: [http://www.piceramic.de/pdf/PIC\\_Catalog\\_Piezoelectric\\_Ceramic\\_Actuators\\_Custom\\_Piezo\\_Assemblies\\_c.pdf](http://www.piceramic.de/pdf/PIC_Catalog_Piezoelectric_Ceramic_Actuators_Custom_Piezo_Assemblies_c.pdf) [Accessed 18th May 2009].
- [61] Pozzi, M. and King, T. (2001) 'Piezoelectric Actuators in Micropositioning', *Journal of Engineer Science and Education*, 10, pp. 31-36.
- [62]Letty, R.L., Barillot, F. and Fabbro, H., et al.: Miniature Piezo Mechanisms for Optical and Space Applications, in: 9th International Conference on New Actuators, Bremen,Germany,14-16 June 2004, 177-180, 2004.
- [63] Cheng, K. (2008) *Machine Dynamics, Fundamental, Applications and Practices*. Springer Series in Advance Manufacturing, London: Springer Verlag.
- [64] Olivier, S.A., Pages, C.P. and Thomas, M.(2009) 'Servo piezo tool SPT400MML for the fast and precise machining of free forms', *International Journal of Advanced Manufacturing Technology*, 47, pp.903-910.
- [65] Zhang, Y.M. and Sims, N.D. (2005) 'Milling workpiece chatter avoidance using piezoelectric active damping: a feasibility study', *Journal of Smart Material and Structure*, 14, pp.65-70.
- [66] Hermans, L. and Auweraer, V. D. H. (2002) 'Modal testing and analysis of structures under operational conditions: industrial applications', *Journal of Mechanical Systems and Signal Processing*, 13(2), pp.193-216.
- [67] Avitabile, P. (2000) Experimental Modal Analysis. Available at: [http://macl.caeds.eng.umsl.edu/umlspace/s&v\\_Jan2001\\_Modal\\_Analysis.PDF](http://macl.caeds.eng.umsl.edu/umlspace/s&v_Jan2001_Modal_Analysis.PDF) [Accessed 17th March 2009].
- [68] Weck, M. (1984) *Handbook of Machine Tools*. UK: A Wiley Heyden.
- [69] Lee, S.W., Mayor, R. and Ni, J. (2006) 'Dynamic Analysis of a Mesoscale Machine Tool', *Journal of Manufacturing Science and Engineering*, 128, pp.194-203.
- [70] PTC. Available at: <http://www.ptc.com/products/proe/wildfire4/> [Access 21st May 2011].
- [71] Stolarski, T.A., Nakasone, Y. and Yoshimoto, S. (2006) *Engineering Analysis with Ansys software*. UK: Elsevier.
- [72] ANSYS inc. (2009) ANSYS CFX-Pre User's Guide. Available at: <http://www.ansys.com> [Accessed 25th May 2010].

## References

- [73] Bishop, R.H. (2006) *LabVIEW 7 Express*. Prentice Hall: Perason
- [74] Bitter, R. (2006) *LabView: Advanced Programming Techniques*. 2<sup>nd</sup> edn. Taylor & Francis: CRC Press.
- [75] Zhou, H.X., Henson, B. and Bell, A. (2001) Linear Piezo-Actuator and its Applications. Available at: <http://zhouhx.tripod.com/piezopaper.pdf> [Accessed 29th November 2009].
- [76] Imaoka, S. (1999) Conversion of Piezoelectric Material Data. Available at: <http://www.csi-ansys.com> [Accessed 25th November 2009].
- [77] ANSYS, n.d. (2005) ANSYS Coupled-Field Analysis Guide. Available at: <http://steflikk6.cs.binghamton.edu/~nano/nanotube/documents/guide.pdf> [Accessed 27th October 2010]
- [78] Ibrahim, R., Cheng, K., Bateman, R., Wang, C. and Au, J. (2010) ‘Design and analysis of a desktop micro-machine for vibration-assisted micromachining’. Proceedings of the IMechE, Part B: Journal of Engineering Manufacture. (In press)
- [79] Reaves, M.C. and Horta, L. (2001) Test Case for Modelling and Validation of Structures with Piezoelectric Actuators. Available at: [http://femci.gsfc.nasa.gov/workshop/2000/presentations/09\\_1430\\_Horta.pdf](http://femci.gsfc.nasa.gov/workshop/2000/presentations/09_1430_Horta.pdf) [Accessed 20th August 2010].
- [80] Hartog, J.P. (1949) *Strength of Materials*. USA: Constable and Company Ltd.
- [81] Kim, D. and Pechaud, L. (2001) Improved Methodology for the Prediction of the Empennage Maneuver in-flight Loads of a General Aviation Aircraft Using Neural Networks. Available at: <http://www.tc.faa.gov/its/worldpac/techrpt/ar01-80.pdf> [Accessed 22nd August 2010].
- [82] Houcque, David. ‘Ordinary Differential Equation (ODE)’. School of Engineering and Applied Science, University of Northwestern, UK, pp.1-12.
- [83] Newton Raphson Method. Available at: <http://personal.maths.surrey.ac.uk/st/S.Gourley/NewtonRaphson.pdf> [Accessed 20th August 2010].
- [84] Hibbeler, R.C. (2010) *Engineering Mechanics: Statics*. 12<sup>nd</sup> edn. Prentice Hall: Perason.
- [85] Wang, C. and Au, Y. H. J.: Levitation Characteristics of a Squeeze Film Air Journal Bearing at its Normal Modes, Journal of Advanced Manufacturing Technology [submitted in Jan 2011].

## References

- [86] Wang, C. and Au, Y. H. J. (2011) ‘Study of design parameters for squeeze film air journal bearing – excitation frequency and amplitude’, *Journal of Mechanical Sciences*, 2, pp.147-155.
- [87] HAMEG, Available at: <http://sziget.mine.nu/~tAB/muszer/Oscilloscope/Hameg/HM604.PDF> [Accessed 10th May 2011].
- [88] Smart material (2010) Macro fibre composite – MFC. Available at: <http://www.smart-material.com/Datasheets.html> [Accessed 12nd May 2011].
- [89] National Instrument, Available at: <http://sine.ni.com/nips/cds/view/p/lang/en/nid/11888#> [Accessed 2nd May 2011].
- [90] Scampoli, S. (2008) ‘Multiphysics in Action’, *ANSYS Advantage*, 2, pp1-7.
- [91] Kjellgren, P. and Hyvarnen, J. (1998) ‘An Arbitrary Lagrangian – Eulerian finite element method’. *Journal of Computational Mechanics*, 21, pp. 81-90.
- [92] Moosrainer, M. (2009) ‘Analyzing Vibration with Acoustic– Structural Coupling’, *ANSYS advantage*, ANSYS Inc.
- [93] Gullman, S. J., Nielsen, K. K. and Hansen, L.V.: *DES and FSI for Industrial Applications*, Proceedings of 4th National Conference on Computational Mechanics, Copenhagen, Denmark, 2007, 7–24, 2007.
- [94] Stephan, D.A.H. and Daniel. J.R.: *Coupling plate deformation, electrostatic actuator and squeeze film damping in a FEM model of a Micro switch*, Proceedings of International Conference on Computational method for coupled problems in Science and Engineering, Barcelona, Spain, 2009.
- [95] Smart materials for a smart word MFC sensors & actuators energy harvesting systems piezo powering and instrumentation engineering services. Available at: [www.smart-material.com](http://www.smart-material.com) [Accessed 20th January 2011].
- [96] Wang, C. and Au, Y. H. J.: *Guided Wave Mode Dispersion of Transient Acoustic Emission on Copper Pipes – Its Visualization and Application to Source Location*, *Journal of ultrasonics*. [Submitted in August, 2010]



## References

## **Appendices**

## **Appendices**

## **Appendices**

### **Appendix A**

#### **Piezoelectric coefficient description and measurement data for squeeze film bearings**

##### **A1 – Description on Piezoelectric coefficient**

## Appendices

Piezoelectric coefficients	Descriptions
$d_{33}$	<p>First subscript 3 indicates that the electrodes are perpendicular to polarization axis 3;</p> <p>Second subscript 3 indicates that the piezoelectric induced strain, or the applied stress, is in direction 3.</p>
$d_{15}$	<p>First subscript 1 indicates that the electrodes are perpendicular to axis 1;</p> <p>Second subscript 5 indicates that the shear strain about axis 2 per unit electric field applied in direction 1.</p>
	Permittivity for dielectric displacement and electric field in direction 3 (parallel to direction in which ceramic element is polarized), under constant strain.
	<p>Superscript D indicates that the compliance is measured with electrode circuit open.</p> <p>First subscript indicates that strain or stress is in direction 3;</p> <p>Second subscript indicates that stress or strain is in direction 3.</p>
$k_{31}$	<p>First subscript indicates that the electrodes are perpendicular to axis 3;</p> <p>Second subscript indicates that the piezoelectric induced strain, or the applied stress, is in direction 1.</p>
$k_t$	Factor for electric field in direction 3 and vibrations in direction 3 (thin disk, surface dimensions large relative to thickness; $k_t < k_{33}$ ).

### A – 2 Measurement of dynamic deformation at Mode 13

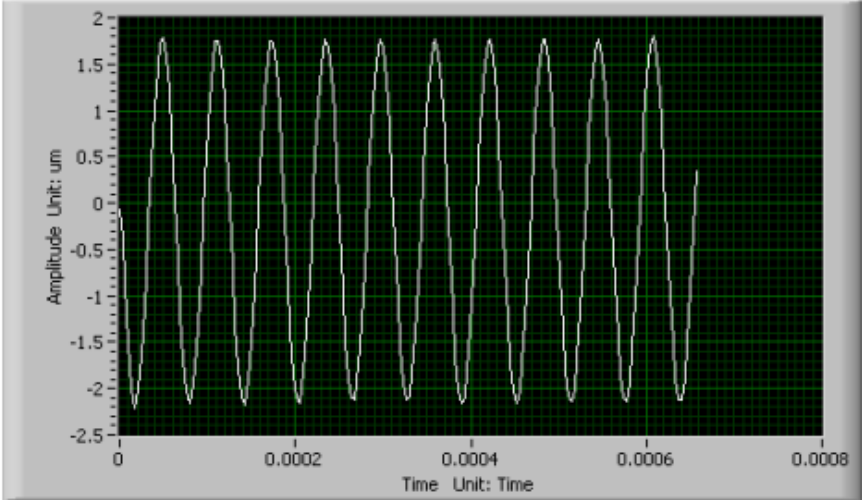
## Appendices

Forced Vibration (Al)		Unit: um																			
Frequency = 16.286KHz		Frequency = 16.320 KHz				Frequency = 16.371 KHz				Frequency = 16.455KHz				Frequency = 16.463KHz				Frequency = 16.554 KHz			
AC = 75V	AC = 65 V	AC = 55V	AC = 75V	AC = 65 V	AC = 55V	AC = 75V	AC = 65 V	AC = 55V	AC = 75V	AC = 65 V	AC = 55V	AC = 75V	AC = 65 V	AC = 55V	AC = 75V	AC = 65 V	AC = 55V	AC = 75V	AC = 65 V	AC = 55V	
2.63	2.089	1.856	2.861	2.25	1.908	2.406	1.893	1.626	1.861	1.555	1.295	1.767	1.471	1.237	1.418	1.202	0.968				
2.644	2.138	1.807	2.89	2.285	1.895	2.437	1.89	1.6	1.85	1.542	1.296	1.82	1.486	1.268	1.41	1.225	0.956				
2.661	2.164	1.854	2.884	2.238	1.851	2.445	1.833	1.543	1.8	1.555	1.359	1.76	1.444	1.246	1.43	1.231	0.933				
2.63	2.122	1.789	2.896	2.286	1.883	2.44	1.844	1.569	1.826	1.586	1.301	1.81	1.491	1.247	1.418	1.225	0.918				
2.64	2.117	1.834	2.87	2.28	1.851	2.43	1.875	1.597	1.8	1.572	1.287	1.793	1.461	1.256	1.347	1.225	0.914				
2.633	2.147	1.801	2.897	2.299	1.877	2.444	1.88	1.598	1.87	1.549	1.294	1.791	1.475	1.274	1.4	1.214	0.97				
2.674	2.174	1.8	2.872	2.286	1.857	2.457	1.836	1.573	1.806	1.55	1.299	1.814	1.5	1.28	1.427	1.202	0.928				
2.623	2.114	1.8	2.888	2.283	1.916	2.449	1.841	1.545	1.836	1.551	1.313	1.814	1.502	1.258	1.436	1.201	0.97				
2.62	2.131	1.792	2.898	2.261	1.903	2.418	1.883	1.544	1.811	1.545	1.31	1.82	1.53	1.209	1.419	1.222	0.958				
2.634	2.188	1.83	2.869	2.285	1.884	2.477	1.9	1.578	1.852	1.59	1.324	1.834	1.474	1.226	1.352	1.222	0.958				
Mean	2.6389	2.1384	1.8163	2.8825	2.2753	1.8825	1.8675	1.5773	1.8312	1.5595	1.3078	1.8023	1.4834	1.2501	1.4057	1.2169	0.9473				
Standard dev	0.016046	0.028765	0.023846	0.012777	0.018155	0.022398	0.024703	0.026684	0.024939	0.016182	0.019914	0.022834	0.022857	0.020859	0.029702	0.010737	0.020756				
2 Standard dev	0.032093	0.057531	0.047691	0.025554	0.03631	0.044795	0.049406	0.053367	0.049878	0.032364	0.039828	0.045669	0.045714	0.041718	0.059404	0.021475	0.041512				

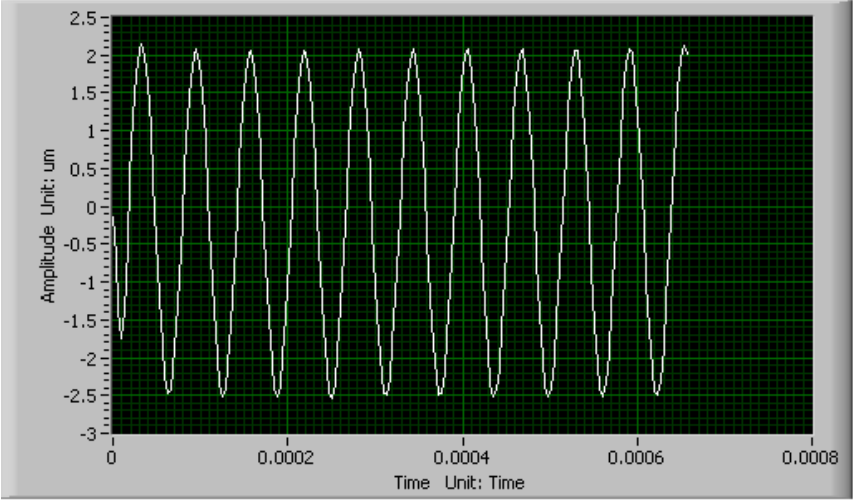
**A3 – Data measurement for dynamic response driven at AC of 55V and 65V for AL bearing**

**Appendices**

Amplitude Response of the squeeze film air bearing



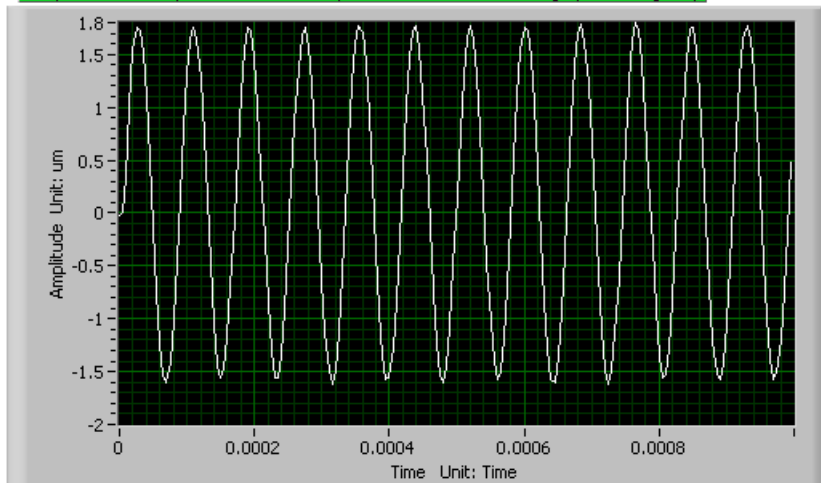
Amplitude Response of the squeeze film air bearing



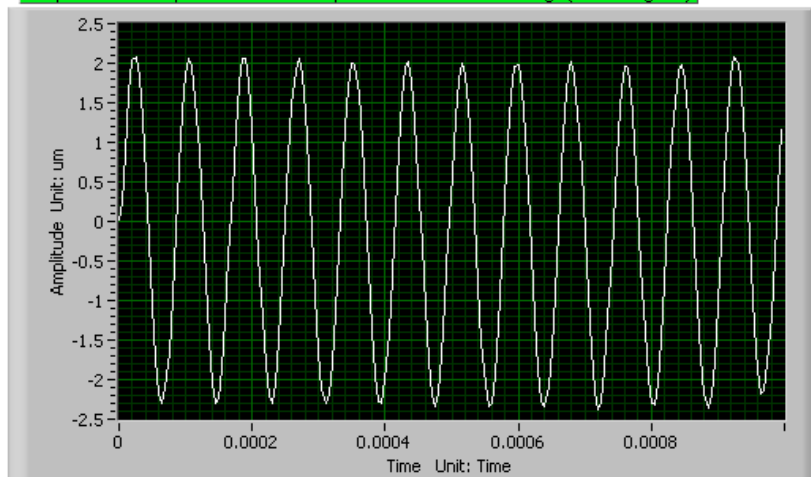
**A4 - Data measurement for dynamic response driven at AC of 55V and 65V for AL bearing**

## Appendices

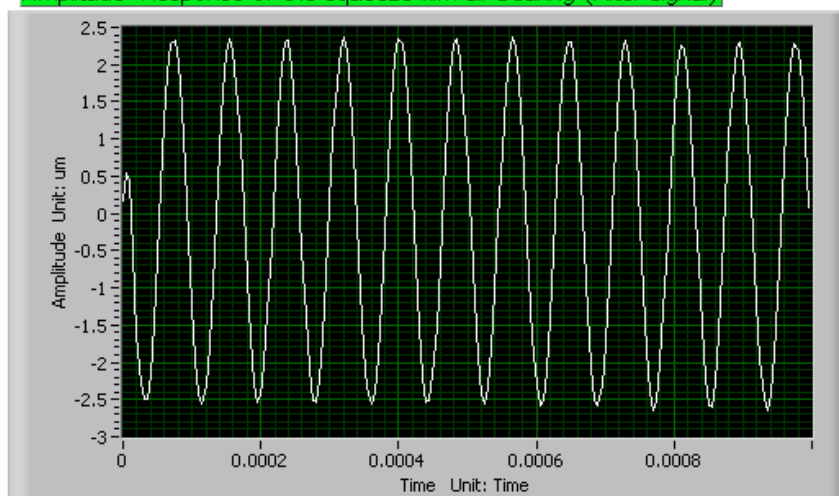
Amplitude Response of the squeeze film air bearing (Filter signal)



Amplitude Response of the squeeze film air bearing (Filter signal)



Amplitude Response of the squeeze film air bearing (Filter signal)



## A5 – Other modal frequencies of the squeeze film bearing

## Appendices

Mode shape	Natural frequency
7	7103.1 Hz
8	7115.6 Hz
9	8594.6 Hz
10	8597.4 Hz
11	14511 Hz
12	14515 Hz
13	16368 Hz
14	20594 Hz
15	22339 Hz
16	23027 Hz
17	23199 Hz
18	23230 Hz
19	24674 Hz
20	25510 Hz
21	25525 Hz
22	25591 Hz
23	25637 Hz
24	29091 Hz
25	29224 Hz

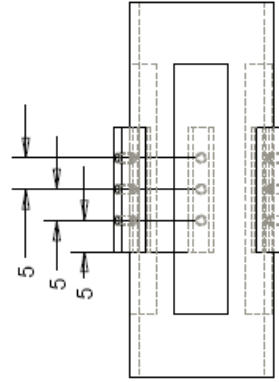
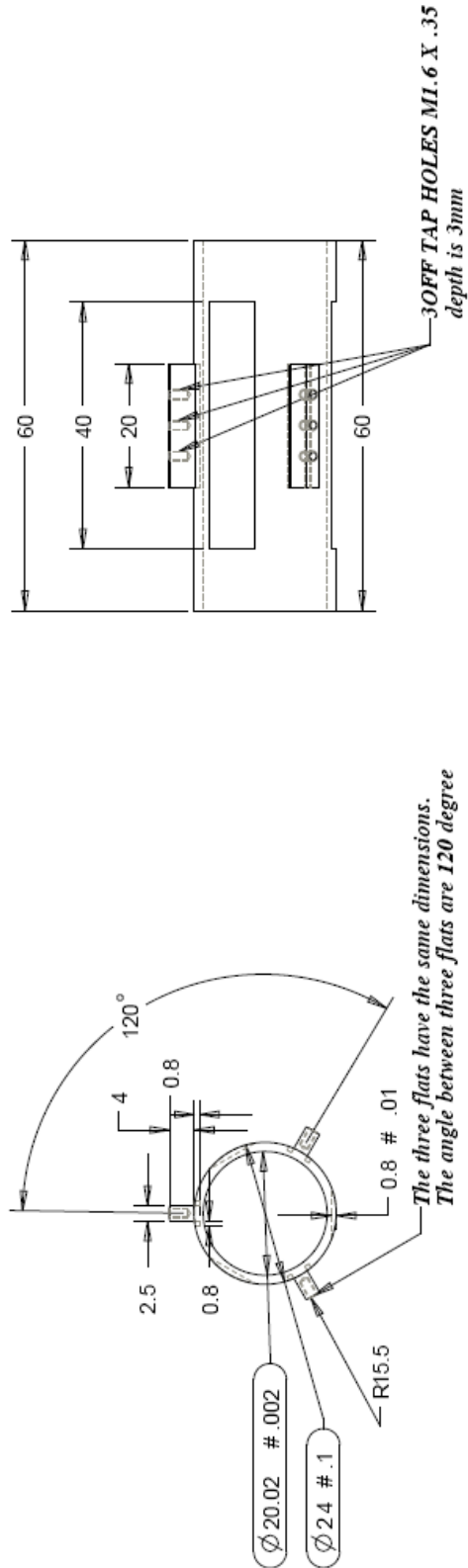


**Appendices**

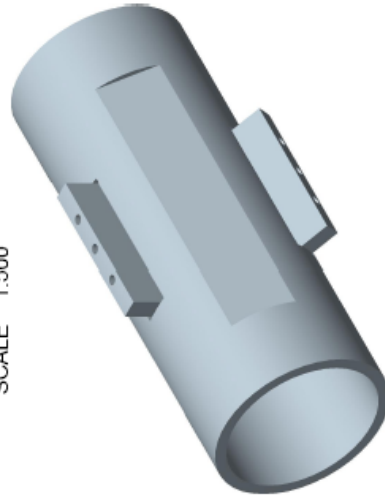
**Appendix B**  
**Engineering drawings**

**B1 - Squeeze film air journal bearing**

**Squeeze film air bearing Unit: mm**



SCALE 1.500

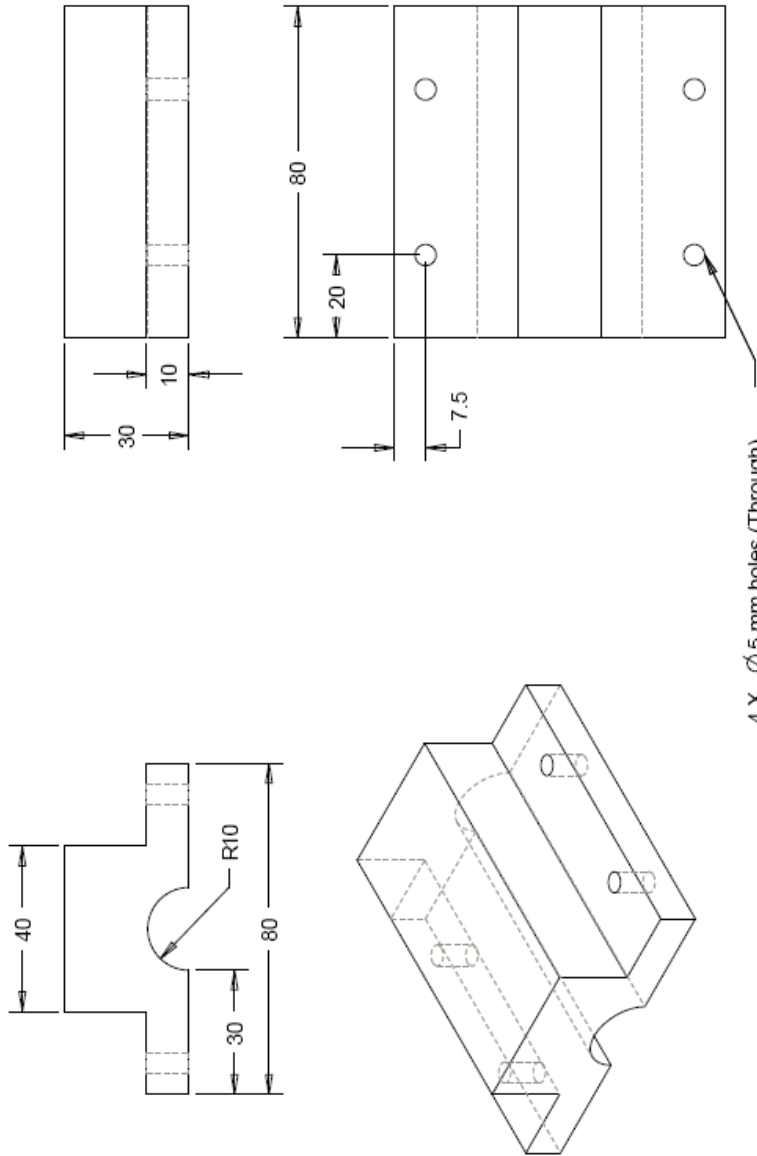


SCALE 2.000

**B2 - Bearing block**

AMEE Brunel University Uxbridge Middlesex UB8 3PH	Copyright information	Part Name : P2T holder	Drawing No:
Author By: /	Checked By: /	Approved By: /	Released By: /
Drawn By: /	Revised By: /	Revised By: /	Revised By: /
Scale: 1:1	Material: /	Part No: /	Rev: /

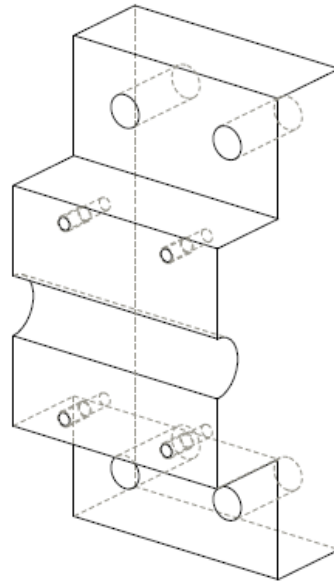
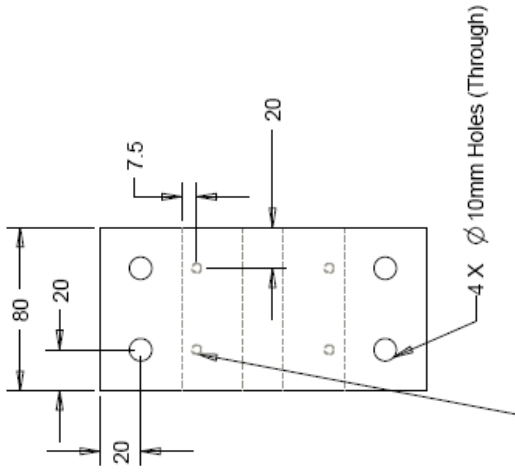
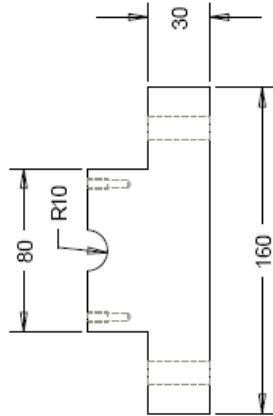
**Bearing Block (upper)**      **Unit: mm**



4 X  $\varnothing 5$  mm holes (Through)

AMEE Brunel University Uxbridge Middlesex UB8 3PH				Material: <b>Steel</b>		Part Name : Bearing Block_1		Drawing No:	
DESIGNED BY:	CHECKED BY:	DRAWN BY:	APPROVED BY:	PART NO:	CASE NO:	DATE:	QUANTITY:	Part Number: 1	
								Date: 2006/09	

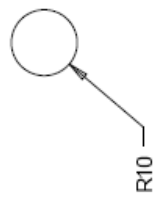
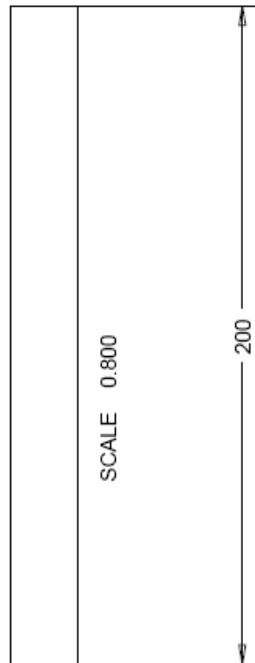
**Bearing Block 2** Unit:mm



SCALE 0.800

AMEE Brunel University Uxbridge Middlesex UB8 3PH		Material: Steel		Part number: 2 Part Name: Bearing block 2		Drawing No:	
Design Date:	Drawn Date:	Checked Date:	Approved Date:	Project Name:	Page No:	Revision No:	Drawing No:

# Appendices



AMEE Brunel University Uxbridge Middlesex UB8 3PH		 Copyright Information		Drawn by ROBIN	Checked by	Produced by Machine	Project Name Part Name : Shaft	Scale 1:1	Region File Date	Assembly Drawing No.
--	--	---	--	----------------------	---------------	---------------------------	--------------------------------------	--------------	------------------------	-------------------------

## **Appendices**

### **Appendix C**

#### **Piezoelectric actuator calculation and computer programs**

##### **C 1 – Maximum stroke length and maximum blocking force calculation in Excel**

## Appendices

	B	C	D	E	F	G	H	I	J	K	L
1	C 21										
2		<b>1. Relative permittivity</b>									
3		$\kappa_{11}^r$	1900								
4		$\kappa_{33}^r$	1400				<b>verifications</b>				
5							V=	-150	volt		
6		TB,DPER,1,,,1					t	5.00E-04	m		
7		TB,DATA,1,K11T,K11T,K33T					L=	1.50E-02	m		
8		TBLIST					B	5.00E-03	m		
9											
10		<b>2. Piezo electric matrix</b>					Ez=	300000	volt/m	E=-V/h	
11		d31	-1.31E-10	m/v			strains				
12		d33	2.88E-10				ex=	-3.93E-05	UX=	-5.8950E-07	
13		d15	6.34E-10				ey=	-3.93E-05	UY=	-1.9650E-07	
14							ez=	8.64E-05	UZ=	4.3200E-08	
15		TB,PIZE,1,,,1									
16		TB,DATA,1,0,0,d31,0,0,d31									
17		TB,DATA,7,0,0,d33,0,0,0									
18		TB,DATA,13,0,d15,0,d15,0,0									
19											
20		<b>3. Compliance matrix</b>									
21		Y11E	8.30E+10	N/m^2							
22		Y22E	8.30E+10		Y22=Y11		assumptions:				
23		Y33E	6.40E+10				$\sigma_{xy} = \sigma_{xz} = 0.29$		for s12E and s13E		
24		Y55E	2.30E+10		Y55E=Gyz=Gxz						
25		poisson	0.29								
26											
27		s11E	1.20E-11			Ex	8.30E+10				
28		s12E	-3.49E-12			Ey	8.30E+10				
29		s13E	-4.53E-12			Ez	6.40E+10				
30		s33E	1.56E-11			nuxy	2.90E-01				
31		s55E	4.35E-11			nuxz	2.90E-01				
32		s44E	4.35E-11			nuyz	2.90E-01				
33		s66E	3.11E-11			Gxy	3.22E+10				
34						Gyz	2.30E+10				
35						Gxz	2.30E+10				

C2 – ANSYS Macro for single layer piezoelectric actuator simulation

FINI

## Appendices

/CLEAR

/com \*\* =====

/com \*\*

/com \*\* Piezo-fsi 3D layered / ANSYS master file

/com \*\*

/com \*\* =====

vtop = 150

!Voltage applied to the top of the PZT layer

vbot = 0

!Voltage applied to the bottom of the PZT layer

seltol,1e-6

!Selection tolerance

/prep7

/com

/com -- Element types

/com

et,1,solid5,3 ! Hexaedral Coupled-Field Solid

et,2,solid95 ! 3-D 20-Node Structural

/com -- Material matrices for PZT C-12 (polar axis along Z-axis): ANSYS input

/com

/com [s11E s12E s13E 0 0 0] [0 0 d31] [K11T 0 0]

/com [0 s11E s13E 0 0 0] [0 0 d31] [ K11T 0 ]

/com [0 0 s33E 0 0 0] [0 0 d33] [ K33T ]

/com [0 0 0 s66E 0 0] [0 0 0]

/com [0 0 0 0 s44E 0] [0 d15 0]

/com [0 0 0 0 0 s44E] [d15 0 0]

s11=1.20E-11

s12=-3.49E-12

s13=-4.53E-12

s33=1.56E-11

s44=4.35E-11

s66=3.11E-11

tb,anel,1,1,,1

!Define structural table

tbddata,1,s11,s12,s13

!Input elastic stiffness matrix [c]

tbddata,7,s11,s13

tbddata,12,s33

tbddata,16,s66

tbddata,19,s44

tbddata,21,s44



## Appendices

tblist,anel

d31=-1.31E-10

d33=2.88E-10

d15=6.34E-10

tb, piez, 1,, 1

tbdata, 1, 0, 0, d31, 0, 0, d31

tbdata, 7, 0, 0, d33, 0, 0, 0

tbdata, 13, 0, d15, 0, d15, 0, 0

!Define Piez. table

!Input Piezoelectric stress matrix [e]

tblist, piez

!K11T=1900

!K33T=1400

!TB, DPER, 1,, 1

!TBDATA, 1, K11T, K11T, K33T

! solid5 can't accept permittivity by TB

! this TB is used to find K11S and K33S

! from K11T and K33T by TBLISTING

!tblist, dper

K11S=856.36

K33S=713.28

mp, perx, 1, K11S

mp, pery, 1, K11S

mp, perz, 1, K33S

mp, dens, 1, 7800

!Permittivity (x direction)

!Permittivity (y direction)

!Permittivity (z direction)

!Density

/com

/com -- Modeling

/com

block, 0, 15e-3, 0, 5e-3, 0, 0.5e-3

!Piezo model

/vup,, z

/view,, 0, -1, 0

/replot

/com

/com -- Meshing

/com

lesize, 1,, 4

lesize, 3,, 4

lesize, 6,, 4

lesize, 8,, 4

lesize, 2,, 20

lesize, 4,, 20

lesize, 5,, 20

## Appendices

```
lesize,7,,,20  
lesize,9,,,5  
lesize,10,,,5  
lesize,11,,,5
```

```
lesize,12,,,5
```

```
vsel,s,,,1
```

```
type,1
```

```
mat,1
```

```
mshape,0,3d
```

```
!Volume mesh using Hex.
```

```
mshkey,1
```

```
!Mapped meshing
```

```
vmesh,1
```

```
allsel
```

```
/com
```

```
/com -- Boundary conditions for Piezo
```

```
/com
```

```
nset,s,loc,x,0
```

```
d,all,ux,0
```

```
nset,s,loc,y,0
```

```
d,all,uy,0
```

```
nset,s,loc,z,0
```

```
d,all,uz,0
```

```
nset,s,loc,z,0
```

```
d,all,volt,vbot
```

```
nset,s,loc,z,0.5e-3
```

```
d,all,volt,vtop
```

```
allsel
```

```
/solu
```

```
antype,static
```

```
outres,all,all
```

```
time,1
```

```
deltim,0.2,0.2,1
```

```
solve
```

```
finish
```

## C3 - ANSYS Macro for static coupled-field analysis

```
seltol,1e-6
```

```
!Selection tolerance
```

## Appendices

```
/prep7
/com
/com -- get the highest et and mat numbers
/com

*get,et_max,etyp,0,num,max

*get,mat_max,mat,0,num,max
et1=et_max+1
et2=et_max+2
mat1=mat_max+1
mat2=mat_max+2

/com ** =====
/com **
/com ** Piezo-fsi 3D layered / ANSYS master file
/com **
/com ** =====
!/config,nres,5000
Ksolu=0                ! 0=static
vtop = -75             ! Voltage applied to the top of the PZT layer
vbot = 0               ! Voltage applied to the bottom of the PZT layer

vamp=75
vavg=0

seltol,1e-6           ! Selection tolerance
/units,SI

/prep7
/com
/com -- Element types
/com
et,et1,solid5,3        ! Hexahedral Coupled-Field Solid
et,et2,solid95        ! 3-D 20-Node Structural

/com -- Material matrices for Fuji PZT C-12 (polar axis along Z-axis): ANSYS input
/com
/com [s11E s12E s13E 0 0 0] [0 0 d31] [K11T 0 0]
/com [0 s11E s13E 0 0 0] [0 0 d31] [ K11T 0 ]
/com [0 0 s33E 0 0 0] [0 0 d33] [ K33T ]
/com [0 0 0 s66E 0 0] [0 0 0 ]
/com [0 0 0 0 s44E 0] [0 d15 0 ]
/com [0 0 0 0 0 s44E] [d15 0 0 ]
```

## Appendices

s11=1.20E-11

s12=-3.49E-12

s13=-4.53E-12

s33=1.56E-11

s44=4.35E-11

s66=3.11E-11

tb,anel,mat1,1,,1

tbdata,1,s11,s12,s13

!Input elastic stiffness matrix [c]

tbdata,7,s11,s13

tbdata,12,s33

tbdata,16,s66

tbdata,19,s44

tbdata,21,s44

tblist,anel

d31=-1.31E-10

d33=2.88E-10

d15=6.34E-10

tb,piez,mat1,,,1

!Define Piez. Table

tbdata,1,0,0,d31,0,0,d31

!Input Piezoelectric stress matrix [e]

tbdata,7,0,0,d33,0,0,0

tbdata,13,0,d15,0,d15,0,0

tblist,piez

!K11T=1900

! solid5 can't accept permittivity by TB

!K33T=1400

! This TB is used to find K11S and K33S

!TB,DPER,1,,,1

! From K11T and K33T by TBLISTING

!TBDATA,1,K11T,K11T,K33T

!tblist,dper

K11S=856.36

! solid5 can't accept permittivity by TB

K33S=713.28

mp,perx,mat1,K11S

!Permittivity (x direction)

mp,pery,mat1,K11S

!Permittivity (y direction)

mp,perz,mat1,K33S

!Permittivity (z direction)

mp,dens,mat1,7800

!Density

/com

/com -- Material properties for aluminium

## Appendices

/com

mp,ex,mat2,75E9

!Young modulus

mp,prxy,mat2,0.3

!Poisson coefficient

mp,dens,mat2,2700

!Density

/com-----

/com changes

/com-----

/prep7

cmsel,s,PZT1,elem

allsel,below,elem

emid,remove,all

emodif,all,type,et1

emodif,all,mat,mat1

emodif,all,esys,12

cmsel,s,PZT2,elem

allsel,below,elem

emid,remove,all

emodif,all,type,et1

emodif,all,mat,mat1

emodif,all,esys,13

cmsel,s,PZT3,elem

allsel,below,elem

emid,remove,all

emodif,all,type,et1

emodif,all,mat,mat1

emodif,all,esys,14

cmsel,s,PZT4,elem

allsel,below,elem

emid,remove,all

emodif,all,type,et1

emodif,all,mat,mat1

emodif,all,esys,15

cmsel,s,PZT5,elem

allsel,below,elem

emid,remove,all

emodif,all,type,et1

emodif,all,mat,mat1

emodif,all,esys,16

## Appendices

```
cmsel,s,PZT6,elem  
allsel,below,elem  
emid,remove,all  
emodif,all,type,et1  
emodif,all,mat,mat1  
emodif,all,esys,17
```

```
cmsel,s,PZT1,elem  
cmsel,a,PZT2,elem  
cmsel,a,PZT3,elem  
cmsel,a,PZT4,elem  
cmsel,a,PZT5,elem  
cmsel,a,PZT6,elem  
esel,inve  
allsel,below,elem  
cm,bearing,elem  
emodif,all,type,et2  
emodif,all,mat,mat2
```

```
etdele,1,et_max  
mpdele,all,1,mat_max
```

```
esel,all
```

```
numcmp,mat  
numcmp,type
```

```
/com  
/com -- sinusoidal load  
/com
```

```
*if,Ksolu,eq,1,then  
freq=1000*0.5      !Hz  
T0=1/freq  
NT0=20  
NTP=180  
DT=1/NTP  
PI=ACOS(-1)  
*DIM,VTB,TABLE,(NT0*NTP+1),,,TIME  
*DO,K1,1,NT0  
*DO,K2,1,NTP  
I=(K1-1)*NTP+K2  
TK=(I-1)*DT  
VTB(I,0)=TK*T0  
VTB(I,1)=-((Vamp)*SIN(2*PI*TK)+Vavg)
```

## Appendices

\*ENDDO

\*ENDDO

I=I+1

TK=(I-1)\*DT

VTB(I,0)=TK\*T0

VTB(I,1)=-((Vamp)\*SIN(2\*PI\*TK)+Vavg)

\*vplot,VTB(1,0),VTB(1,1)

\*endif

/com

/com -- Boundary conditions for Piezo

/com

csys,12

cmsel,s,PZT1,elem

allsel,below,elem

nselect,r,loc,z,0.5e-3

\*if,Ksolu,eq,1,then

d,all,volt,%VTB%

\*elseif,Ksolu,eq,0,then

d,all,volt,vtop

\*endif

allsel,below,elem

nselect,r,loc,z,0

d,all,volt,vbot

csys,13

cmsel,s,PZT2,elem

allsel,below,elem

nselect,r,loc,z,0.5e-3

\*if,Ksolu,eq,1,then

d,all,volt,%VTB%

\*elseif,Ksolu,eq,0,then

d,all,volt,vtop

\*endif

allsel,below,elem

nselect,r,loc,z,0

d,all,volt,vbot

csys,14

cmsel,s,PZT3,elem

allsel,below,elem

## Appendices

```
nselect,r,loc,z,0.5e-3
*if,Ksolve,eq,1,then
d,all,volt,%VTB%
*elseif,Ksolve,eq,0,then
d,all,volt,vtop
*endif
```

```
allselect,below,elem
nselect,r,loc,z,0
d,all,volt,vbot
```

```
csys,15
cmselect,s,PZT4,elem
allselect,below,elem
nselect,r,loc,z,0.5e-3
*if,Ksolve,eq,1,then
d,all,volt,%VTB%
*elseif,Ksolve,eq,0,then
d,all,volt,vtop
*endif
allselect,below,elem
nselect,r,loc,z,0
d,all,volt,vbot
```

```
csys,16
cmselect,s,PZT5,elem
allselect,below,elem
nselect,r,loc,z,0.5e-3
*if,Ksolve,eq,1,then

d,all,volt,%VTB%
*elseif,Ksolve,eq,0,then
d,all,volt,vtop
*endif
```

```
allselect,below,elem
nselect,r,loc,z,0
d,all,volt,vbot
```

```
csys,17
cmselect,s,PZT6,elem
allselect,below,elem
nselect,r,loc,z,0.5e-3
*if,Ksolve,eq,1,then
d,all,volt,%VTB%
```



## Appendices

```
*elseif,Ksolu,eq,0,then  
d,all,volt,vtop  
*endif
```

```
allsel,below,elem  
nset,r,loc,z,0  
d,all,volt,vbot  
allsel  
finish  
/solu
```

### C4- ANSYS Macro for dynamic coupled field analysis

```
seltol,1e-6 !Selection tolerance  
/prep7  
/com  
/com -- get the highest et and mat numbers  
/com  
  
*get,et_max,etyp,0,num,max  
*get,mat_max,mat,0,num,max  
et1=et_max+1  
et2=et_max+2  
mat1=mat_max+1  
mat2=mat_max+2  
  
/com ** =====  
/com **  
/com ** Piezo-fsi 3D layered / ANSYS master file  
/com **  
/com ** =====  
!/config,nres,5000  
Ksolu=0  
  
vtop = -75 !Voltage applied to the top of the PZT layer  
vbot = 0 !Voltage applied to the bottom of the PZT layer  
  
vamp=75  
vavg=0  
  
seltol,1e-6 !Selection tolerance  
/units,SI  
  
/prep7
```

## Appendices

```
/com
/com -- Element types
/com
et,et1,solid5,3          ! Hexahedral Coupled-Field Solid
et,et2,solid95          ! 3-D 20-Node Structural

/com -- Material matrices for Fuji PZT C-12 (polar axis along Z-axis): ANSYS input
/com
/com [s11E s12E s13E 0 0 0] [0 0 d31] [K11T 0 0]
/com [0 s11E s13E 0 0 0] [0 0 d31] [ K11T 0 ]
/com [0 0 s33E 0 0 0] [0 0 d33] [      K33T ]
/com [0 0 0 s66E 0 0] [0 0 0 ]
/com [0 0 0 0 s44E 0] [0 d15 0 ]
/com [0 0 0 0 0 s44E] [d15 0 0 ]

s11=1.20E-11
s12=-3.49E-12
s13=-4.53E-12
s33=1.56E-11
s44=4.35E-11
s66=3.11E-11

tb,anel,mat1,1,,1      !Define structural table
tbdata,1,s11,s12,s13   !Input elastic stiffness matrix [c]
tbdata,7,s11,s13
tbdata,12,s33
tbdata,16,s66
tbdata,19,s44
tbdata,21,s44

tblast,anel

d31=-1.31E-10
d33=2.88E-10
d15=6.34E-10

tb,piez,mat1,,,1      !Define Piez. Table
tbdata,1,0,0,d31,0,0,d31 !Input Piezoelectric stress matrix [e]
tbdata,7,0,0,d33,0,0,0

tbdata,13,0,d15,0,d15,0,0

tblast,piez

!K11T=1900
```

## Appendices

```
!K33T=1400 ! This TB is used to find K11S and K33S
!TB,DPER,1,,1 ! From K11T and K33T by TBLISTING
!TBDATA,1,K11T,K11T,K33T
```

```
!tblast,dper
```

```
K11S=856.36
K33S=713.28
mp,perx,mat1,K11S !Permittivity (x direction)
mp,pery,mat1,K11S !Permittivity (y direction)
mp,perz,mat1,K33S !Permittivity (z direction)
mp,dens,mat1,7800 !Density
```

```
/com
```

```
/com -- Material properties for aluminium
```

```
/com
```

```
mp,ex,mat2,75E9 !Young modulus
mp,prxy,mat2,0.3 !Poisson coefficient
mp,dens,mat2,2700 !Density
```

```
/com-----
```

```
/com changes
```

```
/com-----
```

```
/prep7
```

```
cmsel,s,PZT1,elem
allsel,below,elem
emid,remove,all
emodif,all,type,et1
emodif,all,mat,mat1
emodif,all,esys,12
```

```
cmsel,s,PZT2,elem
allsel,below,elem
emid,remove,all
emodif,all,type,et1
emodif,all,mat,mat1
emodif,all,esys,13
```

```
cmsel,s,PZT3,elem
allsel,below,elem
emid,remove,all
emodif,all,type,et1
emodif,all,mat,mat1
emodif,all,esys,14
```

## Appendices

cmsel,s,PZT4,elem  
allsel,below,elem  
emid,remove,all  
emodif,all,type,et1  
emodif,all,mat,mat1  
emodif,all,esys,15

cmsel,s,PZT5,elem  
allsel,below,elem  
emid,remove,all  
emodif,all,type,et1  
emodif,all,mat,mat1  
emodif,all,esys,16

cmsel,s,PZT6,elem  
allsel,below,elem  
emid,remove,all  
emodif,all,type,et1  
emodif,all,mat,mat1  
emodif,all,esys,17

cmsel,s,PZT1,elem  
cmsel,a,PZT2,elem  
cmsel,a,PZT3,elem  
cmsel,a,PZT4,elem  
cmsel,a,PZT5,elem  
cmsel,a,PZT6,elem  
esel,inve  
allsel,below,elem  
cm,bearing,elem  
emodif,all,type,et2  
emodif,all,mat,mat2  
etdele,1,et\_max  
mpdele,all,1,mat\_max

esel,all

numcmp,mat  
numcmp,type

/com  
/com -- sinusoidal load  
/com

\*if,Ksolu,eq,1,then

## Appendices

freq=1000\*0.5 !Hz

T0=1/freq

NT0=20

NTP=180

DT=1/NTP

PI=ACOS(-1)

\*DIM,VTB,TABLE,(NT0\*NTP+1),,,TIME

\*DO,K1,1,NT0

\*DO,K2,1,NTP

I=(K1-1)\*NTP+K2

TK=(I-1)\*DT

VTB(I,0)=TK\*T0

VTB(I,1)=-((Vamp)\*SIN(2\*PI\*TK)+Vavg)

\*ENDDO

\*ENDDO

I=I+1

TK=(I-1)\*DT

VTB(I,0)=TK\*T0

VTB(I,1)=-((Vamp)\*SIN(2\*PI\*TK)+Vavg)

\*vplot,VTB(1,0),VTB(1,1)

\*endif

/com

/com -- Boundary conditions for Piezo

/com

csys,12

cmsel,s,PZT1,elem

allsel,below,elem

nselect,r,loc,z,0.5e-3

\*if,Ksolve,eq,1,then

d,all,volt,%VTB%

\*elseif,Ksolve,eq,0,then

d,all,volt,vtop

\*endif

allsel,below,elem

nselect,r,loc,z,0

d,all,volt,vbot

csys,13

cmsel,s,PZT2,elem

allsel,below,elem

nselect,r,loc,z,0.5e-3

## Appendices

```
*if,Ksolu,eq,1,then  
d,all,volt,%VTB%  
*elseif,Ksolu,eq,0,then  
d,all,volt,vtop  
*endif
```

```
allsel,below,elem
```

```
nselect,r,loc,z,0  
d,all,volt,vbot
```

```
csys,14  
cselect,s,PZT3,elem  
allsel,below,elem  
nselect,r,loc,z,0.5e-3  
*if,Ksolu,eq,1,then  
d,all,volt,%VTB%  
*elseif,Ksolu,eq,0,then  
d,all,volt,vtop  
*endif
```

```
allsel,below,elem  
nselect,r,loc,z,0  
d,all,volt,vbot
```

```
csys,15  
cselect,s,PZT4,elem  
allsel,below,elem  
nselect,r,loc,z,0.5e-3  
*if,Ksolu,eq,1,then  
d,all,volt,%VTB%  
*elseif,Ksolu,eq,0,then  
d,all,volt,vtop  
*endif
```

```
allsel,below,elem  
nselect,r,loc,z,0  
d,all,volt,vbot  
csys,16  
cselect,s,PZT5,elem  
allsel,below,elem  
nselect,r,loc,z,0.5e-3  
*if,Ksolu,eq,1,then  
d,all,volt,%VTB%  
*elseif,Ksolu,eq,0,then
```

## Appendices

```
d,all,volt,vtop  
*endif
```

```
allsel,below,elem  
nset,r,loc,z,0  
d,all,volt,vbot
```

```
csys,17  
cmsgel,s,PZT6,elem  
allsel,below,elem  
nset,r,loc,z,0.5e-3
```

```
*if,Ksolu,eq,1,then  
d,all,volt,%VTB%  
*elseif,Ksolu,eq,0,then  
d,all,volt,vtop  
*endif
```

```
allsel,below,elem  
nset,r,loc,z,0  
d,all,volt,vbot  
allsel  
finish  
/solu
```

## C5 - CFX – CEL expressions for fluid dynamics

LIBRARY:

CEL:

EXPRESSIONS:

$FFlow = force\_y()@Top$

$dBallNew = FFlow*tStep^2/mBall+(dBallOld+velBallOld*tStep -g0*tStep^2)$

$dBallOld = areaAve(Total\ Mesh\ Displacement\ y)@Top$

$freq0 = 14000 [s^{-1}]$

$g0 = 9.8 [m\ s^{-2}]$

$mBall = 6.2429e-4 [kg]$

## Appendices

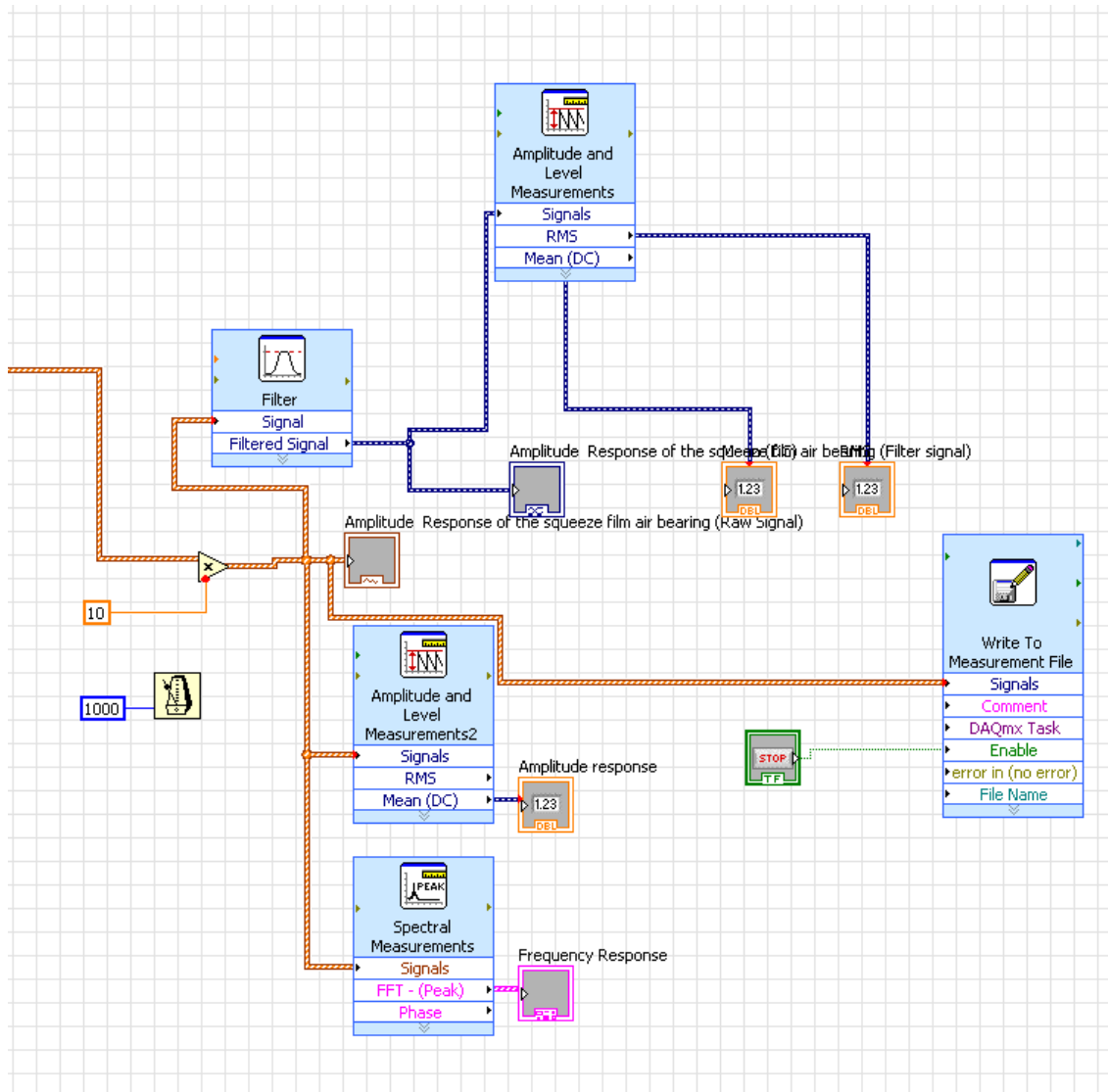
$t_{Step} = 7.15e-6$  [s]

$u_{y0} = 1.e-6$  [m]

$u_{yt} = u_{y0} * \sin(2 * \pi * freq_0 * t)$

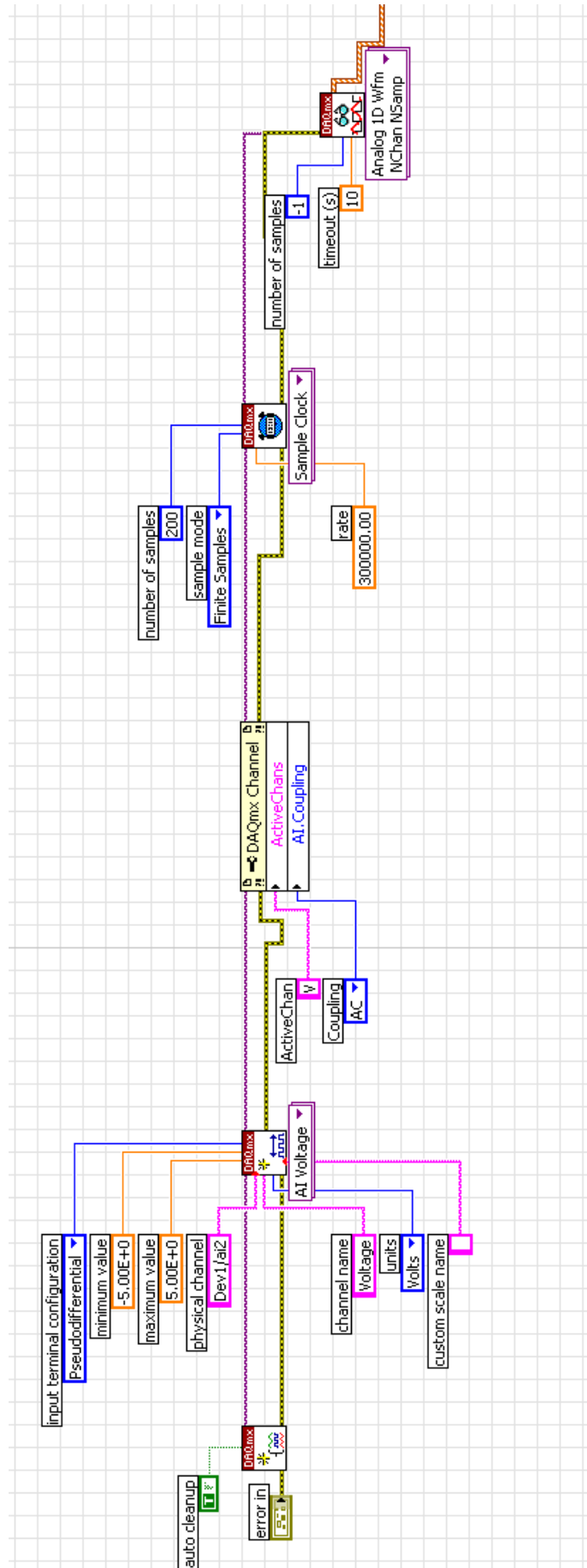
$vel_{BallOld} = \text{areaAve}(\text{Mesh Velocity } v) @ \text{Top}$

## C6 -LabVIEW for signal acquisitions and signal processing





# Appendices



## **Appendices**

### **Appendix D** **Coupled - field for FSI analysis**

## Appendices

### D 1 - Coupled filed for FSI analysis

In coupled-field for fluid solid analysis (FSI), there are necessary files ( inp --- .def  
----- .cdb ----- .dat) in the study generated by the variable software as shown at below.

**Workbench ----- .inp**

**CFX ----- .def**

**ANSYS batch ----- .cdb**

**ANSYS ----- .dat**

To write an ANSYS input field ( .inp):

- (1) Highlight the Solution object folder in the tree.
- (2) From the Main Menu, choose Tools> Write ANSYS Input File....
- (3) In the Save As dialog box, specify a location and name for the input file.

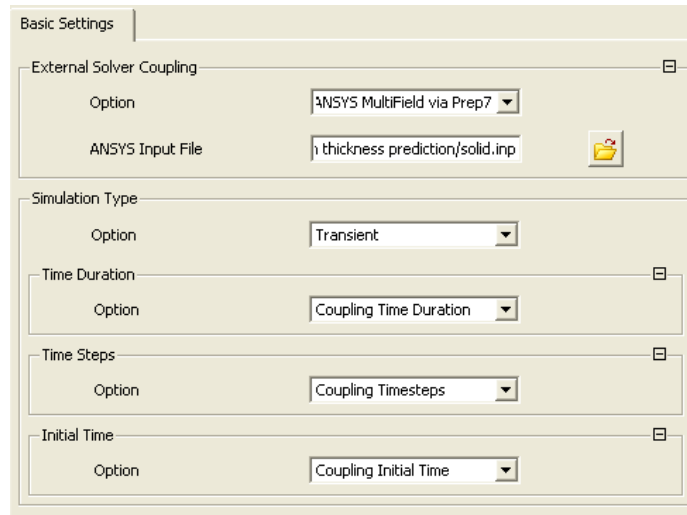
In workbench, it is better not use any kind of mesh tool, like only use Hex or Tet mesh a structure. The reason for that is because the multi- elements are brought in. For instance, **solid 186 or 187**, and **surface ----**. Those elements may not be suitable for the coupled – field studying. So it needs to program in Workbench as shown at below.

```
seltol,1e-6                               !Selection tolerance
/prep7
/com
/com -- get the highest et and mat numbers
/com
*get,et_max,et,0,num,max
et1=et_max+1
et,et1,solid95 ! 3-D 20-Node Structural
/com
/com -- Material properties for aluminium
/com
mp,ex,mat1,75E9                             !Young modulus
mp,prxy,mat1,0.3                             !Poisson coefficient
mp,dens,mat1,2700                             !Density
etdele,et_max
mpdele,all,mat_max
esel,all
numcmp,mat
```

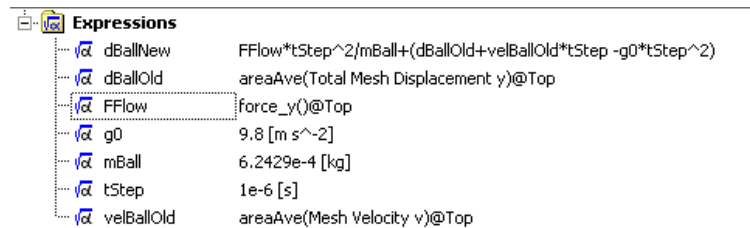
**Appendices**  
*numcmp,type*  
*allsel*  
*finish*

*/solu*

The above step will create an ANSYS input **.inp** file. Without modifying anything but inputting into the CFX software is for generating **.def** . The basic set-ups are like below.



In CFX, the boundary conditions of the fluid domain need to be set to be Open, Interface and Symmetry. You also need to program to add your own Code in **CCL**. Those codes include the weight of the structure and also the partial differential equations and so on as shown.



The **.inp** file is also for creating a **.cdb** file. But before processing in ANSYS batch, some modifications is necessary. Firstly, some commands in **.inp** needs to be deleted from **line 1** up to **/prep 7**. Secondly, the command (**cdwrite, db, file name, cdb**) need to be added at the end of the line before **finish**. After that modification **.inp** file is ready to input into ANSYS batch running.

## **Appendices**

The .cdb will be generated in the directory. The **.cdb** includes the model, the boundary conditions, the loadings and the fluid solid interface. When **.cdb** input into ANSYS, the solid model, material properties, element types and boundary conditions can be display.

The next step is to turn on the **MF**X/**CF**X function for creating **.dat**.

*\* make sure the name used for Interface in CFX is same as that in ANSYS.*

The last step is to turn on the MF

X - ANSYS/**CF**X in simulation environment to input **.dat** in ANSYS RUN and **.def** in **CF**X RUN.

For the post – processing, it can be in both ANSYS and **CF**X.

## **Appendices**

### **Appendix E**

#### **List of publications arising from this research**

## Appendices

### **Guided Wave Mode Dispersion of Transient Acoustic Emission on Copper Pipes – Its Visualization and Application to Source Location**

Chao Wang, Y H Joe Au,

*Advanced Manufacturing and Enterprise Engineering,*

*School of Engineering and Design, Brunel University, United Kingdom.*

Corresponding author: Y J Joe Au, Advanced Manufacturing and Enterprise Engineering, School of Engineering and Design, Brunel University, Uxbridge, Middlesex UB8 3PH, United Kingdom. Telephone: +44 1895 274000, E-mail: [joe.au@brunel.ac.uk](mailto:joe.au@brunel.ac.uk)

#### **Abstract**

In this paper is presented an improved method for locating a transient acoustic emission (AE) source on a pipeline with two broad-band AE sensors. Using Short Time Fourier Transform (STFT), the method identifies a flexural wave mode, F(1,1), in the two AE signals detected, notes its respective arrival times at different frequencies, and determines the location of the AE source based on the arrival times. Due to velocity dispersion, the arrival time of the wave mode varies with frequency. The method has three main advantages: that the wave speed is not required in the calculation, that it is insensitive to threshold setting for arrival time estimation, and that, at least in theory, the accuracy of the source location can be made as high as desired. The paper first demonstrates, by way of an experiment, the inadequacy of threshold-crossing as a method for identifying the first arrival time of the AE wave. The paper then presents the theory of the proposed method and of the estimated error inherent in the theory and an explanation on how the error can be reduced. The method is then verified experimentally using results obtained from a 3-m long copper pipe of 22 mm diameter.

#### **Keywords:**

## **Appendices**

Acoustic Emission (AE); Short-Time Fourier Transform (STFT); velocity dispersion curves; guided transient elastic waves; source location.

### **1. Introduction**

Pipeline leakage detection is an important issue in the pipeline transportation industry. The leakage not only affects the normal operation but also wastes resources, pollutes the environment, and threatens the health and safety of operators [1-4]. Because of the serious nature of failure consequences in some applications, it is necessary to develop robust systems to monitor pipeline condition and to locate the source of a leak accurately.

Jiao et al [2] reported that the methods for detecting and locating leaks can be into two categories: direct and indirect. The direct methods include the cable method, and the gas method. The indirect methods include Acoustic Emission (AE), negative pressure testing, mass/volume balance and flow/pressure change testing.

Pipeline degradation that results in a leak manifests itself in loss of material in the pipe and AE is created whenever loss of material occurs. AE is a transient elastic wave generated by the rapid release of energy within a material due to relief of stress [5]. A typical artificial AE source is one produced by pencil lead break where a 0.5 mm pencil lead is pressed against a surface until fracture occurs on the pencil lead. This type of source creates a transient signal.

In the conventional source location method on a pipeline with a two-sensor array, both the AE arrival times of the source signal and the wave speed are needed for calculating the position of the source relative to the sensors. Evidently the accuracy of the exercise depends on the accuracy of the values used for the arrival times and the wave speed. Whilst the arrival times are measured, the wave speed is often taken from a materials handbook.

Shehadeh, Steel and Reuben [6] examined the role of arrival time estimation in the source location method and used the techniques of wavelet transform, cross-correlation, filtering and thresholding to obtain arrival times for various modes of an AE transient generated with the pencil lead break. The advantage of wavelet decomposition is that it provides a clearer insight into the signal in terms of its components so that a more realistic threshold can be set, leading to more accurate arrival time estimation. However, as will be seen in this paper, threshold setting is an influential parameter that affects arrival time estimation. It is therefore important that its influence should be kept small or eliminated altogether.



## Appendices

Taking the wave speed from a materials handbook can be fraught with problems. The

wave speed is typically calculated using the formula  $\sqrt{\frac{E(1-\nu)}{\rho(1+\nu)(1-2\nu)}}$  where E is the modulus of elasticity,  $\rho$  the density and  $\nu$  the Poisson ratio. The problem is that the value of E given in the materials handbook varies over a range. Thus, for example, the value of E for copper can be from 110 GPa to 130 GPa and this results in a percentage difference in speed relative to the latter of about 8%. The temperature can also affect the wave speed because it changes the density of a material, though its effect is far less than that of E; a 10°C temperature increase results in just under 0.03% drop in wave speed.

Since wave speeds in metal are high, typically in thousands of metres per second, a high sampling frequency for recording a wave is required in order to capture the essential features of the wave. In fact, the sampling interval, being the inverse of the sampling frequency, determines the resolution of the source location; the lower the sampling frequency, the larger the sampling interval and the coarser the location resolution.

The inability to set the ‘correct’ threshold and to know accurately the wave speed plagues the arrival-time method. This paper describes a source location method which does not require the knowledge of wave speed and the precise setting of threshold.

## 2. Cylindrical Guided Wave Modes

Wave modes that propagate in a pipe must have particle displacements that are either uniform about the circumference or change smoothly, typically harmonically, around the circumference. If the former, the wave modes are known as axi-symmetric modes; if the latter, they are axi-asymmetric. Axi-symmetric wave modes can be further classified as longitudinal and torsional. Axi-asymmetric wave modes are known as the flexural wave modes. These three wave modes are as shown in Figure 1. The fundamental longitudinal wave mode, L(0,1), has no circumferential displacement, some radial displacement (due to the Poisson ratio effect), but almost all displacements occur in the axial direction. The fundamental torsional wave mode, T(0,1), has purely circumferential displacement. The fundamental flexural wave mode, F(1,1), has mainly radial and circumferential displacements but hardly any axial displacement [8].

## **Appendices**

The AE sensors used in this paper were designed to pick up radial displacements on the pipe and so were sensitive to the flexural and longitudinal wave modes. The pencil lead break produces a strong flexural wave mode, which may be accompanied with a much weaker longitudinal wave mode due to the axial friction sliding of the pencil lead tip on the pipe.

For a copper pipe of 11 mm outer and 10 mm inner radii, taking the elastic modulus of copper as 110 GPa, density of 8920 kg.m<sup>-3</sup> and Poisson ratio of 0.33, the group wave speed was calculated to be 4265 m/s. The theoretical group speeds for the three wave modes F(1,1), F(1,2) and L(0,1), were then calculated using the Pcdisp MATLAB function [9] in the frequency range 0 to 1000 kHz. The resulting dispersion curves are as shown in Figure 2. It is noted that the flexural wave modes, F(1,1) and F(1,2) and the longitudinal wave mode, L(0,1) show great dispersion at low frequencies and that they all converge to the speed of the torsional wave, T(0,1), that is 2615 m/s, at high frequencies.

### **3. Limitation of Time-of-flight Method in Determining Wave Speed**

#### **3.1 Equipment and instrumentation**

For the experiment to determine the wave speed using the time-of-flight method in order to highlight its inaccuracy and inadequacy, the set up as explained below was used.

Two miniature AE sensors were chosen for AE measurement. These were the PAC model PICO broadband sensors with an operating frequency up to about 1 MHz. Each AE sensor was connected to a PAC pre-amplifier set to provide a gain of 60 dB and a band-pass filter with lower and upper cut-off frequencies of 20 kHz and at 1 MHz respectively. Both preamplifiers were powered by a 28 volt DC supply.

The AE signal output from the preamplifier was acquired into a PC via an A/D converter (NI, BNC-6110) controlled by a bespoke program written in LabVIEW. The sampling frequency was 1 MHz and the size of the sample was 3000 points. The signal flow is as shown in Figure 3.

The two sensors, Sensor 1 and Sensor 2 from left to right along the pipe, were attached to the surface of a continuous copper pipe, as shown in Figure 4, at a distance of 2.88 m. The pipe had the outer and inner diameters of 22 mm and 20 mm respectively and a length of 3 m. The pipe was supported at regular intervals on wooden blocks to ensure as little wave reflection as possible occurring at the wood/copper interface.

## Appendices

### 3.2 Inadequacy of threshold setting

An artificial AE source produced with a 0.5-mm diameter pencil lead was created at a point on the pipe 1.35 m from the left-hand sensor, Sensor 1. AE time-signals recorded in LabVIEW for the two sensors are as shown in Figure 5. A pre-trigger time of 1000 samples, that is 1 millisecond, on Sensor 1 and a threshold level of 1V was used in order to avoid false triggering by noise in the signal.

By setting a threshold at the various voltage levels of 0.5 V to 4.5 V in 0.5 V increments, the time at which the signal first crossed the threshold was recorded. If the Sensor 1 signal crosses the threshold at  $t_1$  and Sensor 2 signal at  $t_2$ , the AE wave speed,  $v$ , can be calculated from

$$v = \frac{l_2 - l_1}{t_2 - t_1},$$

where  $l_1$  and  $l_2$  are the respective source distances from Sensors 1 and 2.

Figure 6 shows the variation of wave speed at different threshold levels. As the threshold level increased the wave speed determined decreased but eventually settled down to the constant speed of about 160 m/s beyond the threshold level of 3 V. This constant speed compares favourably to the theoretical longitudinal L(0,1) wave mode speed of 180 m/s at just under 65 kHz - see Figure 2.

## 4. Short-Time-Fourier Transform and Wave Modes

The Short-Time-Fourier-Transform (STFT) method is a signal processing method which decomposes a signal into constituent frequency components locally as it varies with time. The result is often viewed in a time-frequency-density three-dimensional representation where the x-, y- and z-axes denote the time, frequency and energy density of the signal. Alternatively a two-dimensional colour map is used where the energy density is represented by a colour chosen from a colour spectrum. The STFT is a suitable signal processing method to use when the signal to be analyzed changes over time; the artificial AE signal, being of a transient nature, described in this paper was analyzed with the STFT method.

A program written in LabVIEW was used to obtain the STFT for the two sensor signals presented in Figures 5 and 6 and their time-frequency representation is as shown in

## Appendices

Figures 7 and 8. In these diagrams, the vertical axes represent frequency from 0 to 1000 times 333 Hz or 333 kHz.

Superimposed on the STFT diagrams are the theoretical dispersion curves for the wave modes, F(1,1) in blue, F(1,2) in red and L(0,1) in yellow. The presence of these wave modes is evident. In particular, the theoretical and measured arrival times of F(1,1) matched well but less so for L(0,1). It was also noticed in Figure 7 that ahead of the main F(1,1) wave mode profile there was a shadowy weaker profile of a similar shape. This could be due to the pencil lead fracture occurring as two quick successive fracture events. However, this phenomenon is not as clearly observed in Figure 8.

## 5. Source Location with Two Sensors

### 5.1 Theory of the new method

In Figure 9, two sensors  $S_1$  and  $S_2$  at a distance of  $L$  are attached to the pipe. An AE source,  $S$ , is at distances  $l_1$  and  $l_2$  from  $S_1$  and  $S_2$  respectively. Referring to Figure 10, let the pre-trigger time be  $\tau$  and the time measured from the triggering instant for the AE source to travel to  $S_1$  and  $S_2$  be  $t_1(f)$  and  $t_2(f)$ . If the AE wave mode travels at the speed of  $v(f)$ , then

$$l_1 = v(f)[t_1(f) - \tau_0] \quad (1)$$

$$l_2 = v(f)[t_2(f) - \tau_0] \quad (2)$$

where  $\tau_0$  is the interval between the instant at which the recording is started and the instant at which the AE is generated (see Figure 10).

Dividing Equations (2) by (1), and noting that  $L = l_1 + l_2$ ,

$$\frac{L}{l_1} - 1 = \frac{t_2(f) - \tau_0}{t_1(f) - \tau_0}$$

Rearranging to obtain the  $S_1$ -to- $S$  distance

$$l_1 = \frac{L}{1 + \frac{t_2(f) - \tau_0}{t_1(f) - \tau_0}} \quad (3)$$

## Appendices

Equation (3) holds for a range of frequencies of a particular wave mode, for example, F(1,1), and, in theory, the same value of  $l_1$  should be returned every time. Thus,

$$\frac{t_2(f) - \tau_0}{t_1(f) - \tau_0} = m \quad (4)$$

where  $m$  is a constant.

Rearranging Equation (4) to give

$$t_2(f) = mt_1(f) + (1 - m)\tau_0 \quad (5)$$

Equation (5) is a linear equation with slope  $m$  and intercept  $(1 - m)\tau_0$ .

The  $S$ -to- $S_I$  distance as given in Equation (3) can be expressed in terms of the slope  $m$  as

$$l_1 = \frac{L}{1 + m} \quad (6)$$

Substituting Equation (6) into Equation (1) to obtain the AE wave speed

$$v(f) = \frac{L}{t_1(f) + t_2(f)} \quad (7)$$

For a source  $S$  upstream of sensors  $S_I$  and  $S_2$ , then  $L = l_2 - l_1$  and following the same derivation procedure as that described above, the  $S$  to  $S_I$  distance is obtained as

$$l_1 = \frac{L}{m - 1} \quad (8)$$

And the AE speed is

$$v(f) = \frac{L}{t_2(f) - t_1(f)} \quad (9)$$

By noting Equations (1) and (2) and the expression for  $m$  as in Equation (4), the slope  $m$  of the fitted straight line can be seen to be

$$m = \frac{l_2}{l_1} \quad (10)$$

So if  $m$  is greater than unity, the source  $S$  is closer to  $S_2$  than to  $S_I$  and vice versa.

## Appendices

### 5.2. Errors estimation of the new method

From Equations (6) and (8), the accuracy of the estimated  $l_1$  depends on how accurately the slope  $m$  can be determined, which, in turn, depends on the accuracy of the coordinates  $(t_1(f), t_2(f))$ . Let  $T_1(f) = t_1(f) - \tau_0$  and  $T_2(f) = t_2(f) - \tau_0$ , then Equation (4) becomes

$$m = \frac{T_2}{T_1}, \text{ and the relative error can be shown to be}$$

$$\frac{\Delta m}{m} = -\frac{\Delta T_1}{T_1} + \frac{\Delta T_2}{T_2}, \text{ from which}$$

$$\left| \frac{\Delta m}{m} \right| = \left| \frac{\Delta T_1}{T_1} \right| + \left| \frac{\Delta T_2}{T_2} \right| = \frac{|\Delta T_1|}{T_1} + \frac{|\Delta T_2|}{T_2}$$

where  $\Delta m$ ,  $\Delta T_1$  and  $\Delta T_2$  are the errors in  $m$ ,  $T_1$  and  $T_2$  respectively. The maximum absolute time errors  $|\Delta T_1|$  and  $|\Delta T_2|$  are equal to the sampling interval, say  $|\Delta T|$ , so that

$$\left| \frac{\Delta m}{m} \right| = |\Delta T| \left( \frac{T_1 + T_2}{T_1 T_2} \right)^{\frac{1}{2}}$$

Since  $T_1 = l_1/v$ ,  $T_2 = l_2/v$  and  $T = L/v$ , and define  $r = l_1/L$  hence  $(1-r) = l_2/L$ , then the above expression can be simplified to

$$\left| \frac{\Delta m}{m} \right| = \left( \frac{1}{r(1-r)} \right)^{\frac{1}{2}} \frac{|\Delta T|}{T} \quad (11)$$

The relative error of the slope  $|\Delta m/m|$  reaches a minimum when  $r = 1/2$  at which the coefficient in Equation (11)  $f(r) = 1/r(1-r) = 4$ ; at other values of  $r$ , the coefficient  $f(r)$  is greater than 4 and will tend to infinity as  $r \rightarrow 0$  or  $r \rightarrow 1$ . The change of the coefficient with respect to  $r$  is as shown in Figure 11.

## Appendices

In summary, when an AE source is at mid-span between the two AE sensors, the relative error in the time ratio  $m = T_2/T_1$  is the minimum but it is still 4 times that of the time measurement error  $|\Delta T|/T$ , which can be considered rather high, worse still if the source is near either of the sensors. But if  $m$  is taken to be the slope of the straight line in Equation (5),  $m$  in effect is the average of the time ratio  $T_2/T_1$ . If there are  $n$  of these ratios, the resulting error will be reduced to  $1/\sqrt{n}$  of that of a single ratio. In theory, the relative error  $|\Delta m/m|$  can be made infinitely small and hence the estimates for  $l_1$  and  $l_2$  infinitely accurate through repeated trials.

### 5.3 Procedure

In summary, in order to obtain the location of an AE source, take the following steps.

1. Plot a graph of  $t_2(f)$  versus  $t_1(f)$ , fit a linear regression line, then compute the slope  $m$  and intercept  $(m-1)\tau_0$ .
2. Assuming the source is in between the sensors, compute the source location and the wave speed using Equations (6) and (7).
3. Assuming the source is outside the span covered by the two sensors, compute the source location using Equations (8) and (9).
4. Compare the speed values obtained from Steps 2 and 3 with the theoretical values

obtained from the formula  $vel = \sqrt{\frac{E(1-\nu)}{\rho(1+\nu)(1-2\nu)}}$ ; choose the corresponding source location value whose experimental wave speed is closest to the theoretical wave speed.

As an illustration of the steps described above, the outline of the F(1,1) wave mode in Figures 7 and 8 were measured in terms of the arrival time at a number of common frequencies. The results were then used to plot the graph in Step 1, which is as shown in Figure 11.

The slope of the regression line was found to be  $m = 1.122$ . Assuming the source is between the sensors, then the  $S_1$ -to- $S$  distance  $l_1 = 2.88 / (1+1.122) = 1.357$  m, and the corresponding group wave speed was 2013 m/s. Given the fact that the  $S_1$ -to- $S$  distance was 1.35 m, the relative percentage error is 0.5%.

## 6. Results

## Appendices

Five more tests were conducted at various locations of the pencil-lead break source. The measured results are shown in table 1. The five actual source locations are displayed in the second row and the estimated locations over 8 trials were tabulated below them. The last three rows show values for the mean, standard error and three times the standard error at each source location.

Trial no.	Actual Location from the left-hand sensor				
	25	50	75	100	125
1	22.66	43.30	75.0	94.76	120.55
2	22.73	43.82	75.5	96.75	123.28
3	24.32	44.39	80.2	97.31	124.82
4	28.97	49.30	81.5	97.38	129.40
5	27.24	48.73	81.2	97.31	127.30
6	23.80	48.37	80.2	96.90	126.00
7	23.50	43.78	76.8	96.00	124.26
8	22.70	43.67	72.1	93.14	123.43
Mean	24.49	45.67	77.8	96.19	124.88
Std error	0.83	0.93	5	0.54	0.96
3xSE	2.50	2.78	3.65	1.61	2.87

Table-1- Source location estimation on the copper pipe – all locations in cm, span between sensors being 288 cm.

Figure 13 shows the comparison between the actual and estimated locations of the five sources. It is noted that the actual and estimated locations compare well.

## 7. Conclusions

In this paper, it has been shown that the proposed method can determine the location of an AE transient source without prior knowledge of the wave speed, giving a level of accuracy superior to that achieved by the conventional time-of-flight method. As an added bonus of the method, the wave speed is also determined in the process.



## Appendices

In theory, the source location estimation error as embodied in the relative slope error  $|\Delta m/m|$  is at least, four times as large as the relative arrival time error  $|\Delta T/T|$ . However, this can be reduced by increasing the number,  $n$ , of the measured coordinates used for plotting the arrival-time graph: the source location estimation error is proportional to  $1/\sqrt{n}$ .

## Acknowledgement

The authors would like to thank Mr Abraham Gaber, a Master's student in AMEE, Brunel University, who performed the experiments on source location estimation and provided the data to which the proposed theory was applied.

## References

- [1] Brunone, B. (1999), 'Transient test-based technique for leak detection in outfall pipes', *Water Resources Planning and Management*, 125 (5), pp.302-306.
- [2] Jiao, Y., Yang, Q., Li, G. and Zhang, J. (2006), 'Acoustic Emission Source Identification Technique for Buried Gas Pipeline Leak', *Control, Automation, Robotics and Vision, ICARCV '06* pg 1.
- [3] Zhang, S. Q. and Jin, S. J. (2006), 'Crucial technologies of oil-transporting pipe leak detection and location based on wavelet and chaos', *Measurement Science and Technology*, 17, pp. 572–577.
- [4] Yaqing, T., Dongqiang, Q. and Du, Z. (2003), 'A Revised Statistical Deduction Approach to Pipeline Leak Detection', *IEEE Instrumentation and Measurement Technology Conference Proceedings: held in Vail, Colorado, USA, 20-22 May 2003*. IEEE Conference Publications Management Group, pp. 1639-1642.
- [5] Kaewkongka, T. and Lim, J. (2007), 'Statistical estimated parameter for pipeline condition monitoring using acoustic emission', *IEEE Instrumentation and Measurement Technology Conference Proceedings: held in Warsaw, Poland, 1-3 May 2007*. IEEE Conference Publications Management Group, pp.1-3.
- [6] Shehadeh, M., Steel, J. and Reuben, R. (2006), 'Acoustic emission source location for steel pipe and pipeline applications: the role of arrival time estimation', Part E: *Journal of Process Mechanical Engineering, Proceedings of IMechE.*, May 2006, pp. 121-133.
- [7] TWI Ltd (2006), Long range ultrasonic inspection technology. Available at: [http://www.twi.co.uk/content/lrut\\_overview.html](http://www.twi.co.uk/content/lrut_overview.html) [Accessed 22nd July 2010].
- [8] Catton, P. P. (2008), *The Use of Ultrasonic Guided Waves for the In Situ Inspection of Industrial Pipelines for Corrosion Damage*, PhD thesis, Brunel University.
- [9] Pcdisp (2009), *A Matlab program for calculating Velocity Dispersion*, PhD Research at CSIC. Available at: <http://www.iai.csic.es/users/fseco/pcdisp/pcdisp.htm> [Accessed 22nd July 2010].

## Appendices

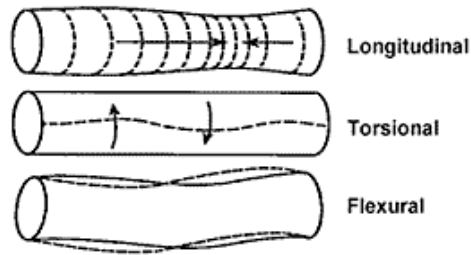


Figure 1 - The guided wave modes in a pipe [7].

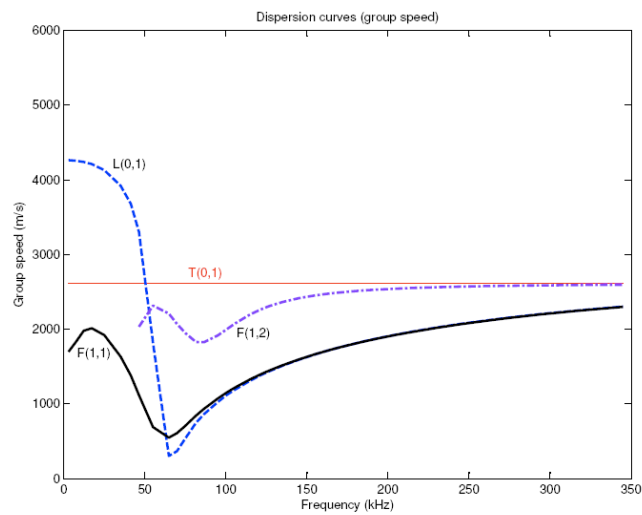


Figure 2 – Calculated group speed/frequency dispersion curve using the MATLAB function Pcdisp [8].

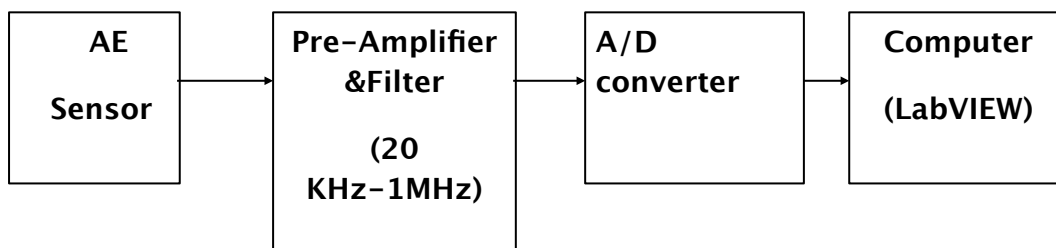


Figure 3 – AE signal-flow diagram

## Appendices

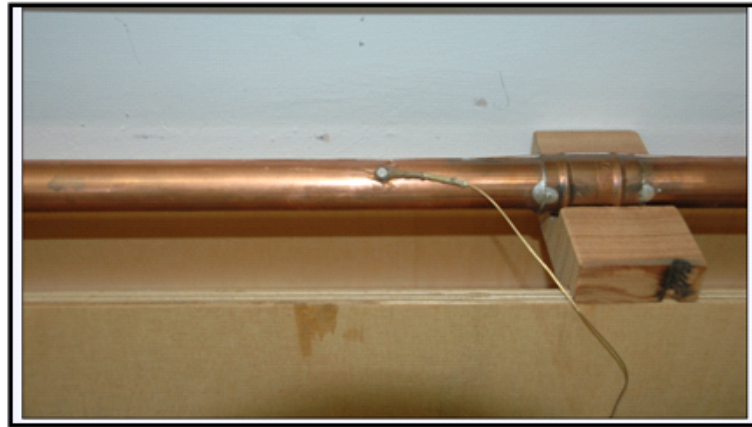
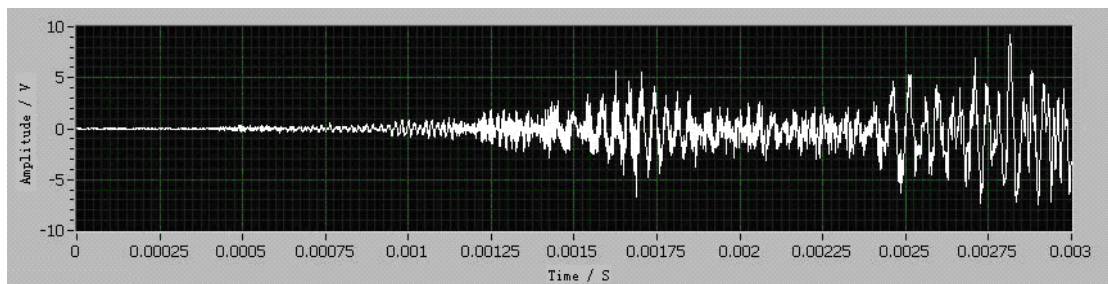
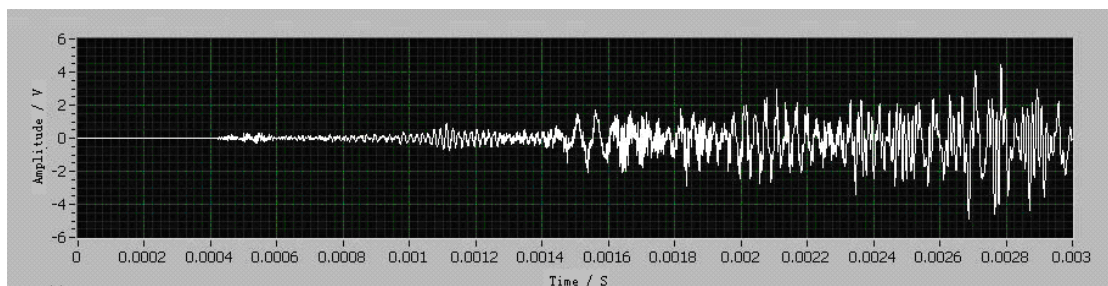


Figure 4 - Acoustic emission sensor attached to the copper pipe.



Sensor 1 – Left-hand end



Sensor 2 – Right-hand end

Figure 5 – AE time-signals for the two sensors

## Appendices

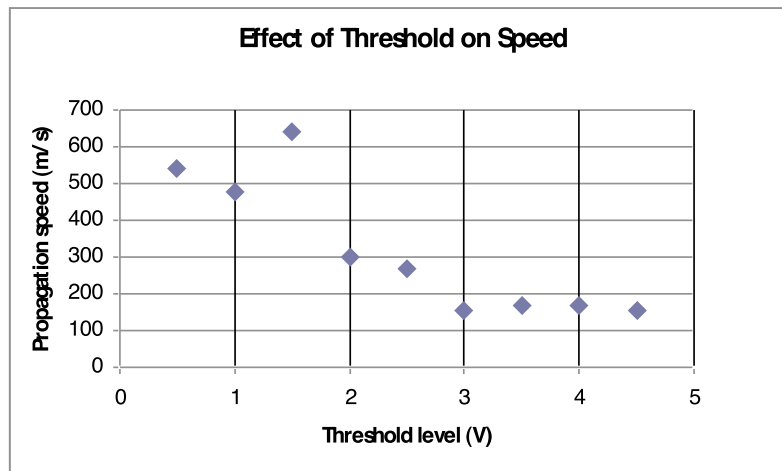


Figure 6 – Effect of threshold level on propagation speed.

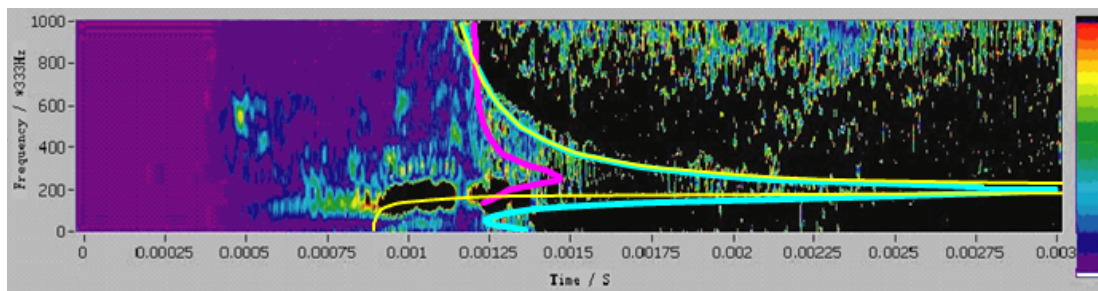
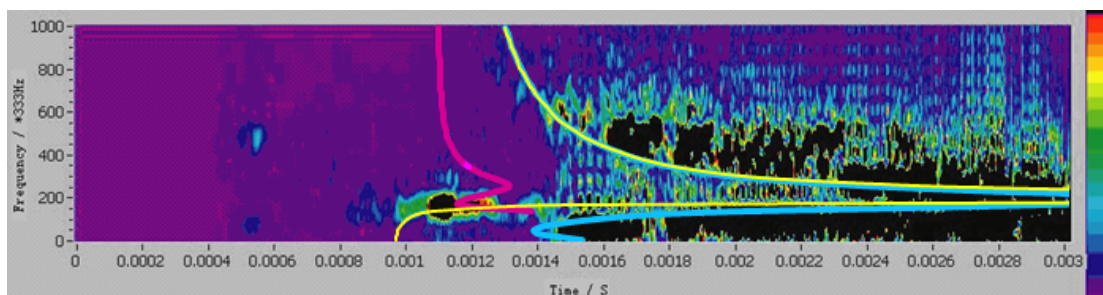


Figure 7 – STFT of Sensor 1 (left) signal.



Appendices

Figure 8 – STFT of Sensor 2 (right) signal.

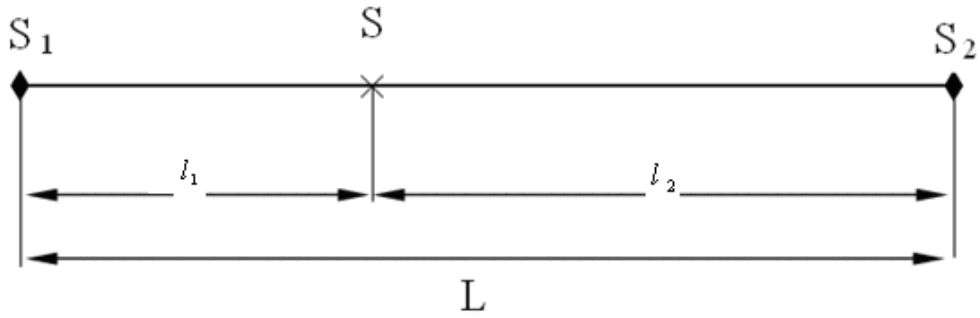


Figure 9 – Schematic diagram of sensors  $S_1$  and  $S_2$  on a pipe with a source  $S$ .

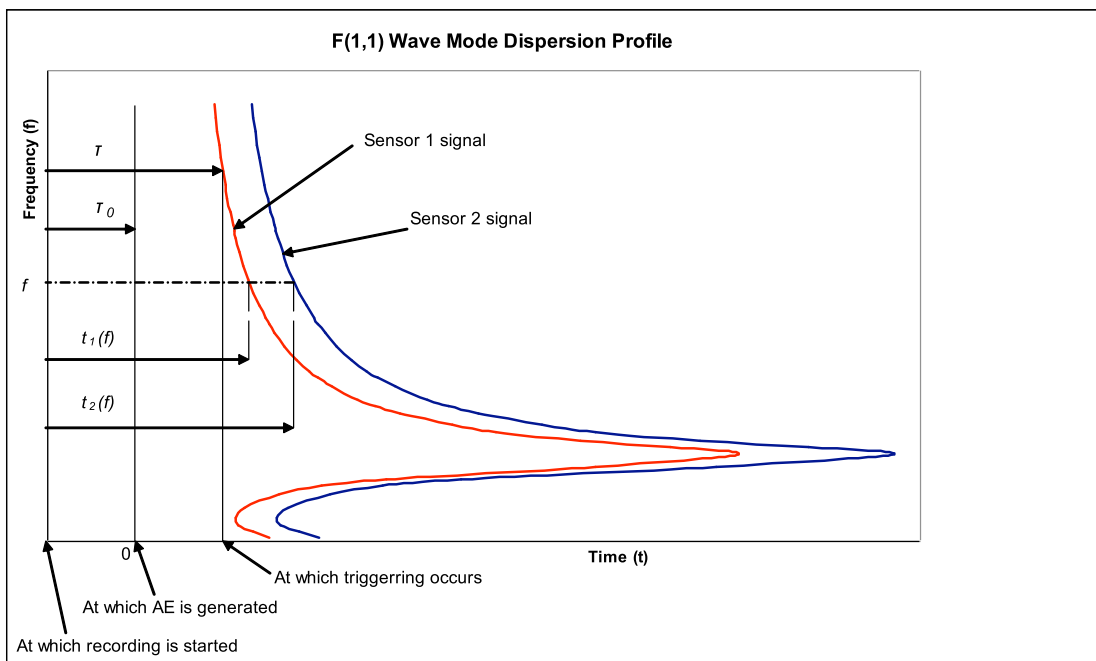


Figure 10 – Schematic graph showing the wave mode arrival times  $t_1(f)$  and  $t_2(f)$  and the pre-trigger time  $\tau$ .

## Appendices

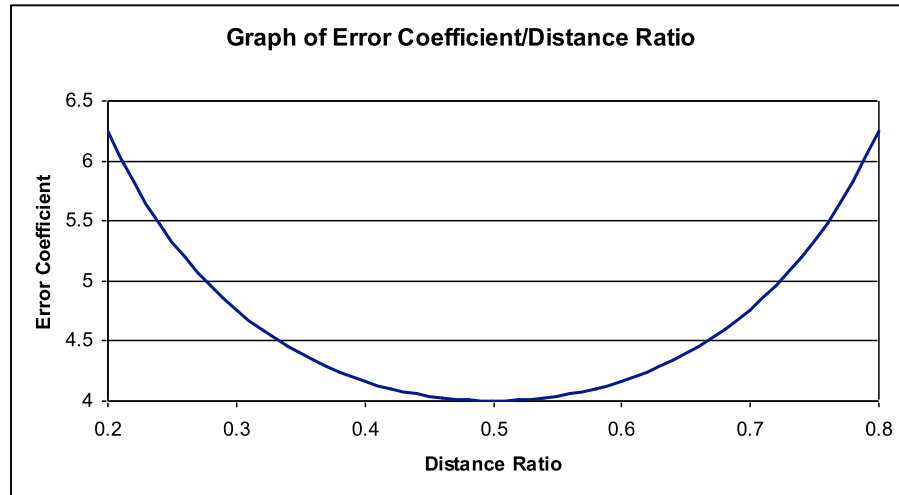


Figure 11 – Graph of error coefficient  $f(r)$  versus distance ratio  $r$ .

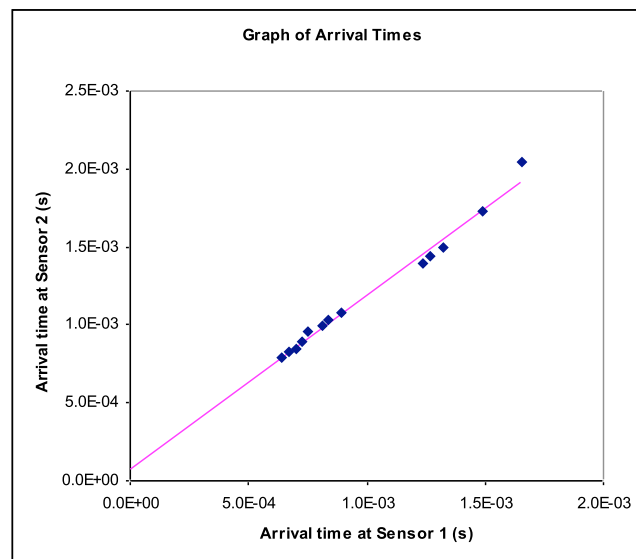


Figure 12 – Arrival Time Graph of  $t_2(f)$  versus  $t_1(f)$  with data points, shown as ‘◆’, and the regression line.

## Appendices

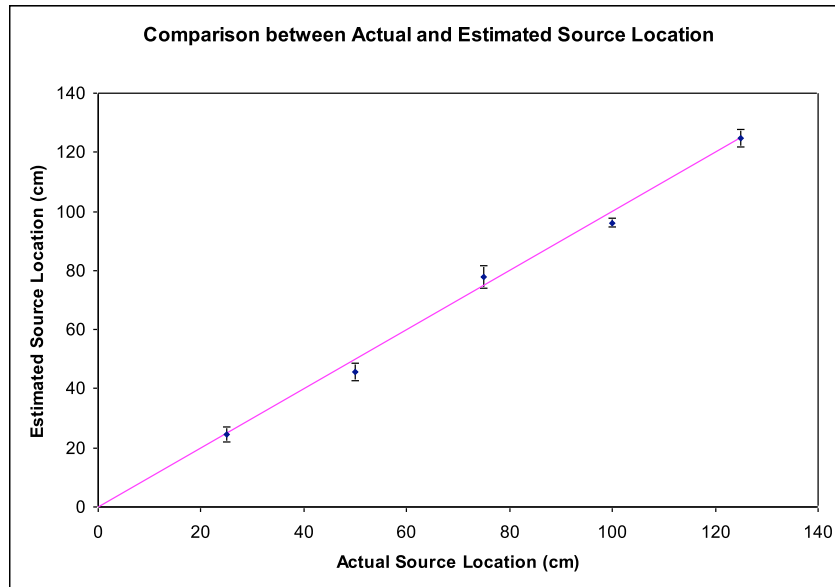


Figure 13 – Comparison between actual and estimated values of source location – the vertical error bar represents 3 times standard errors.

## Appendices

### Levitation Characteristics of a Squeeze Film Air Journal Bearing at its Normal Modes

Chao Wang and Y H Joe Au\*

Advanced Manufacturing and Enterprise Engineering, School of Engineering and Design, Brunel University, UK

\* Corresponding author: Joe.Au@brunel.ac.uk

#### Abstract

A tubular squeeze-film journal bearing was designed such that it flexed its shell at its normal modes producing a triangular modal shape. The shell motion was created by a single-layer piezoelectric actuator powered at 75V AC with a 75V DC offset and the driving frequency coincided with the modal frequency of the bearing. The paper provided a theory that shows the existence of a positive pressure in a squeeze-film responsible for the levitation phenomenon. The various modes of vibration of the tubular bearing, made from aluminium AL2024-T3, were obtained from a finite-element model implemented in ANSYS. Two normal modes, the 13<sup>th</sup> and 23<sup>rd</sup>, at the respective frequencies of 16.4 and 25.6 kHz, were identified for further investigation by experiments with respect to the squeeze-film thickness and its load-carrying capacity. While the bearing at both modes could cause levitation, the 13<sup>th</sup> mode had a greater load-carrying capacity because its modal shape produced a much lower end-leakage.

**Keywords:** *Single layer piezoelectric actuator, squeeze film air bearing, mode shape, natural frequency, elastic hinge.*

#### 1. Introduction

In modern-day engineering, it is necessary to have bearings that can operate with high precision motion, low friction and wear, generating very little heat in an oil-free condition [1]. In this respect, aerostatic and aero-dynamic bearings have been developed and they can meet the requirements, except for the fact that ancillary



## **Appendices**

equipment is needed for their satisfactory operation. The equipment typically consists of air compressors and hoses, all of which take up space and are not very portable, which is a significant obstacle to miniaturization of machine tools for micro- or nano-machining. To consider the above requirements and the limitations of the existing bearing arrangement, the principle of squeeze-film action may be the only possible way to separate two metal surfaces by a thin air film.

The general theory of the operation of squeeze film type bearings has been documented by, for example, Salbu [2] who provided a basic account of the principle of squeeze film bearing. Since its publication, a variety of bearing designs based on this principle had been proposed and used. The squeeze film action was created using a piezoelectric actuator; some of the ideas had even been patented in the US [3, 4, 5 and 6].

The design of the squeeze-film air bearing created by Yoshimoto [7] in 1993 involved a counterweight and two stack piezoelectric actuators. The disadvantages of such a design are that the counterweight adds to the load and the stack actuators are more expensive than their single-layer counterparts, not to mention the higher power consumption. Yoshimoto [7] and Storlaski [8 and 9] produced designs that used what are called ‘elastic hinges’ – in order to create localised reduction in stiffness – resulting in a greater deformation and hence a greater variation of the squeeze-film thickness. But designing elastic hinges is a complex matter and they cost more to manufacture. All the designs reported in [7, 8 and 9] excited the bearings at frequencies below that of their fundamental. In 2006, Yoshimoto [10] reported the research on a newer design in which the bearing was driven by two piezoelectric actuators at the fundamental frequency, at 23.7 kHz, of the bearing. When driven at this frequency the oscillating amplitude of the bearing plate was significantly increased and, being ultrasonic, the bearing was quiet in operation. Yoshimoto’s work has led to the question of whether better performance can be achieved by driving a bearing at a modal frequency above the fundamental. This paper attempts to explore such a possibility.

The purposes of work reported in this paper are:

1. To develop a model that affirms the existence of positive pressure developed in a squeeze-film air bearing and to produce an approximate working formula for estimating the pressure;
2. To develop a finite-element model for a single layer piezoelectric actuator that incorporates realistic boundary conditions;
3. To develop a finite-element model for the squeeze-film air bearing to study its modal shapes at various normal modes and to identify desirable modes for acceptable bearing performance;

## Appendices

4. To determine by experiments the levitation performance of the squeeze-film air bearing at the desirable modes in respect of the air-film thickness and load-carrying capacity.

### 2. Principle of squeeze film air bearings

Consider two parallel plates of infinite lateral dimensions separated by a gap of  $h_0$ ; one of the plates oscillates sinusoidal normal to the other at a frequency  $\omega$  with an amplitude  $a$ . If the oscillating frequency is very high and the gap very small, then edge leakage of air is insignificant and in addition the process can be regarded as adiabatic. Thus

$$pV^\gamma = K,$$

where  $p$  is the pressure,  $V$  the volume,  $\gamma$  the adiabatic constant equal to 1.4 for air, and  $K$  the constant.

Suppose the moving plate is at the initial distance of  $h_0$  from the stationary plate, at which the air pressure in the squeeze film is ambient, denoted as  $p_0$ , then

$$p_0 V_0^\gamma = K \quad (1)$$

At time  $t$ , the plate moves to  $h = h_0 + a \sin(\omega t)$  at which the pressure in the air film has changed ( $p+p_0$ ), where  $p$  is the gauge pressure; thus the equation of state becomes

$$(p + p_0)V^\gamma = K \quad (2)$$

Dividing Eq.(1) by Eq.(2) and rearranging to obtain the pressure ratio as

$$\frac{p}{p_0} = \left( \frac{V}{V_0} \right)^{-\gamma} - 1 \quad (3)$$

Since the volume is proportional to the gap height, Eq.(3) can be rewritten in terms of the ratio of gap heights, as

$$\frac{p}{p_0} = \left( \frac{h}{h_0} \right)^{-\gamma} - 1 \quad (4)$$

The plate moves sinusoidally such that the gap height at time  $t$  is governed by  $h = h_0 + a \sin(\omega t)$ , which on substitution into Eq.(4) gives

## Appendices

$$\frac{p}{p_0} = \left( \frac{h_0 + a \sin(\omega t)}{h_0} \right)^{-\gamma} - 1 \quad (5)$$

Introducing the non-dimensional parameters to Eq.(5), namely the amplitude ratio

$$\varepsilon = \frac{a}{h_0}, \text{ and the time ratio } \tau = \frac{t}{T}, \text{ where } T \text{ is the period of oscillation related to the}$$

$$\text{angular frequency } \omega \text{ by } T = \frac{2\pi}{\omega}, \text{ Eq.(5) can be simplified to}$$

$$\frac{P}{P_0} = (1 + \varepsilon \sin(2\pi\tau))^{-\gamma} - 1 \quad (6)$$

It is possible to show that the mean pressure ratio over a cycle of oscillation is positive, which means that the squeeze film exerts a lifting force on the plate thus causing it to float. The proof is given below.

Using Binomial expansion, the pressure ratio, Eq.(6), can be represented by the infinite series

$$p_r = \frac{P}{P_0} = \sum_{n=1}^{\infty} \frac{-\gamma(-\gamma-1)K(-\gamma-n+1)}{n!} \varepsilon^n \sin^n(2\pi\tau) \quad (7)$$

The coefficients of the terms in this series are successively  $-\gamma$ ,  $-\gamma(-\gamma-1)$ ,  $-\gamma(-\gamma-1)(-\gamma-2)$ , etc. Since  $\gamma$  is positive, the sign of the coefficient alternates: negative when  $n$  is odd and positive when  $n$  is even.

The mean pressure ratio  $\overline{P_r}$  is obtained by integrating, with respect to  $\tau$ , the series (7) term by term over the non-dimensional time interval  $\tau = [0, 1]$ . In mathematical terms,

$$\overline{P_r} = \sum_{n=1}^{\infty} \frac{-\gamma(-\gamma-1)K(-\gamma-n+1)}{n!} \varepsilon^n \int_0^1 \sin^n(2\pi\tau) d\tau \quad (8)$$

For odd powers of  $\sin^n(2\pi\tau)$ , that is, when  $n = 2m+1$ , ( $m = 0, 1, 2, \dots$ )

$$\int_0^1 \sin^{2m+1}(2\pi\tau) d\tau = 0 \quad (9)$$

## Appendices

For even powers, that is, when  $n = 2m$ ,

$$\int_0^1 \sin^{2m}(2\pi\tau) d\tau = \frac{1.3.5L (2m-3)(2m-1)}{2.4.6L (2m-2)2m} \quad (10)$$

Substituting Eqs.(9) and (10) into (8) gives the mean pressure ratio as

$$\bar{p}_r = \sum_{m=1}^{\infty} \frac{-\gamma(-\gamma-1)K(-\gamma-2m+1)}{2m!} \times \frac{1.3.5L (2m-3)(2m-1)}{2.4.6L (2m-2)2m} \times e^{-2m} \quad (11)$$

The series (11) contains only even power terms, and so is positive, thus confirming the existing of a levitation force in the squeeze film whose gap oscillates at high frequency in a sinusoidal manner.

Furthermore, since each term in Eq.(11) is positive, the factor

$$\frac{-\gamma(-\gamma-1)L(-\gamma-2m+1)}{2m} \quad \text{can be replaced by} \quad \frac{\gamma(\gamma+1)L(\gamma+2m-1)}{2m}, \quad \text{and Eq.(11) can be re-written as}$$

$$\bar{p}_r = \sum_{m=1}^{\infty} \frac{\gamma(\gamma+1)K(\gamma+2m-1)}{2m!} \times \frac{1.3.5L (2m-3)(2m-1)}{2.4.6L (2m-2)2m} \times e^{-2m} \quad (11a)$$

The theoretical mean pressure ratio can be calculated using Eq.(11a) or by performing numerical integration on Eq.(6). However, it would be helpful to be able to use a simpler formula for estimating the mean pressure ratio. The following derivation shows the formula.

$$\text{In Eq.(11a), the coefficient of the first term of the series is } C_1 = \frac{\gamma(\gamma+1)}{2!} \times \frac{1}{2}; \text{ and for } \gamma = 1.4 \quad C_1 = 0.840$$

Similarly the coefficient for the  $m^{\text{th}}$  term is given by

$$C_m = \frac{\gamma(\gamma+1)L(\gamma+2m-1)}{2m} \times \frac{1.3.5L (2m-3)(2m-1)}{2.4.6L (2m-2)2m}$$

and of the  $(m+1)^{\text{th}}$  term by

$$C_{m+1} = \frac{\gamma(\gamma+1)L(\gamma+2m-1)(\gamma+2m)(\gamma+2m+1)}{(2m+2)!} \times \frac{1.3.5L (2m-3)(2m-1)(2m+1)}{2.4.6L (2m-2)(2m)(2m+2)}$$

## Appendices

The ratio of the two coefficients, after simplifying, is

$$\frac{C_{m+1}}{C_m} = \frac{(2m + \gamma)(2m + \gamma + 1)}{(2m + 2)^2}$$

For  $\gamma = 1.4$ ,  $\frac{C_{m+1}}{C_m} < 1$  for all positive integer values of  $m$ . In addition, since  $\varepsilon^2 \leq 1$ , the series (11a) converges. The largest coefficient is  $C_1$ , whose value is 0.840, as calculated earlier; other coefficients have values that are smaller than  $C_1$ .

This suggests another infinite series which defines the upper bound mean pressure

ratio; this series is  $\bar{p}_{ru} = \sum_{m=1}^{\infty} C_m \varepsilon^{2m}$  and is a geometric series whose sum is

$$\bar{p}_{ru} = \frac{0.840 \varepsilon^2}{1 - \varepsilon^2} \quad (12)$$

Alternatively, applying numerical integration to Eq.(6) over the non-dimensional time period  $\tau=[0,1]$  with  $\gamma=1.4$  and  $\varepsilon=0.1$  to  $0.7$  in  $0.1$  increments, the corresponding values of the mean pressure ratio  $\bar{p}_r$  were obtained. The relationship between  $\bar{p}_r$  and  $\varepsilon$  is as shown in Fig 1. Also shown on the graph is the upper bound mean pressure ratio  $\bar{p}_{ru}$  calculated from Eq.(12). It is noted that up to an amplitude ratio  $\varepsilon$  of  $0.4$ , the error in the mean pressure ratio  $\bar{p}_r$  is less than about  $1.3\%$ .

## Appendices

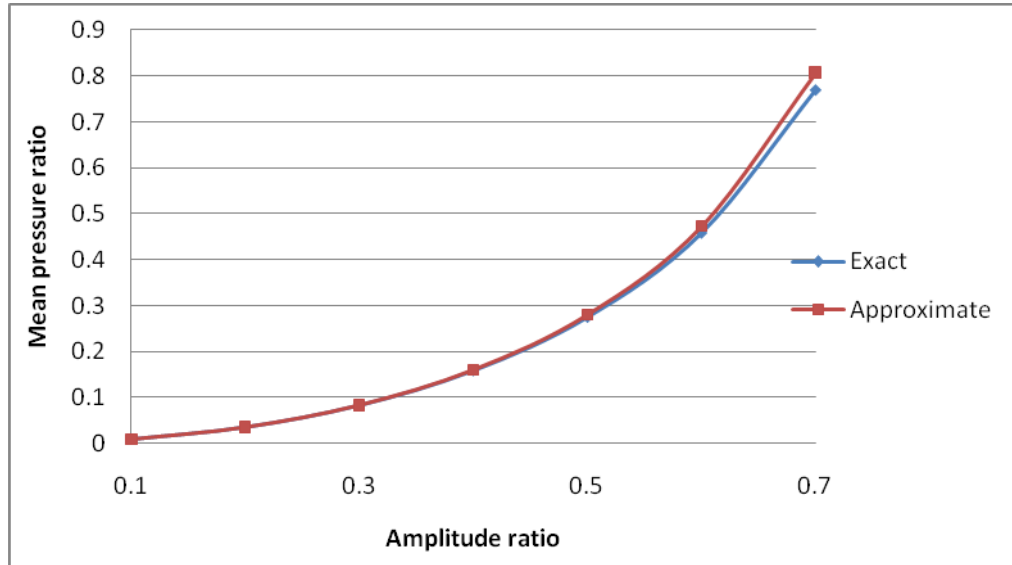


Fig.1. Mean pressure ratio versus amplitude ratio – exact solution Eq.(7) versus approximate solution Eq.(12).

### 3. Modelling of the proposed squeeze film air bearing

#### 3.1 Configuration of the bearing

## Appendices

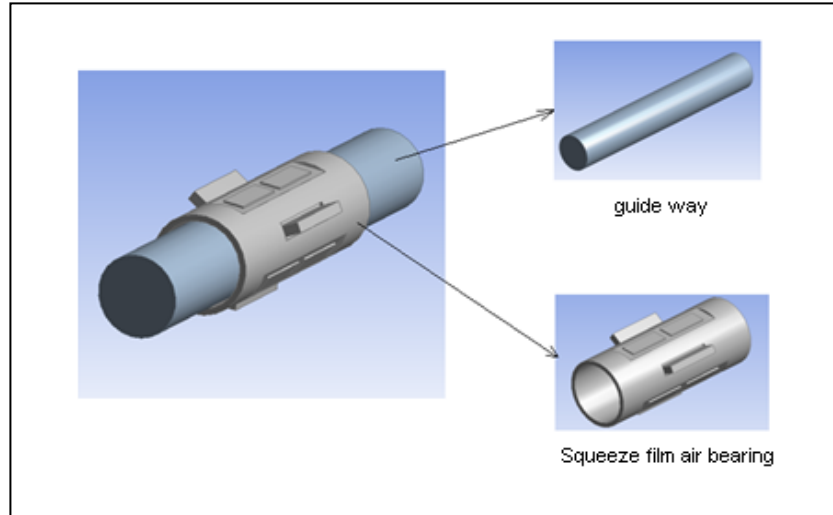


Fig. 2. Squeeze air film bearing and its components: a guide way, a bearing and six piezoelectric actuators bonded to the three flat surfaces

Fig 2 shows a squeeze film air bearing. It consists of a guide way and a squeeze film air bearing with three longitudinal flats on the circumference  $120^\circ$  apart. On each flat surface were bonded two single layer piezoelectric actuators, Figure 2.

The guide way is a round rod fixed at one end and free at the other with an overhang of 130mm; the short overhang is desired to avoid sagging due to its own weight. The diameter of the round rod is 19.99 mm and the surface was ground finished. The bearing, made from the material AL2024-T3, has a diameter of 20.02 mm, a length of 60mm and a thickness of 2mm. Three fins, each 20 mm long, are positioned  $120^\circ$  apart on the outer circumference of the bearing; they are designed to provide a desirable modal shape of a triangular cross-section when excited by the actuators. This enables the air gap underneath the actuators to behave effectively as a squeeze air film.

The design does not rely on complex elastic hinges to provide local flexibility, as used by other researchers [7, 8, 9], in order to achieve greater deflection of elements. Being a simpler design, its manufacturing cost is much lower and the bearing can be adequately driven by a single-layer piezoelectric actuator (0.5 mm thick) with little power to provide the sinusoidal squeeze film motion [10]. Furthermore, the simple geometry of the design makes for subsequent simpler finite-element analysis.

### 3.2 Experimental set-up

## Appendices

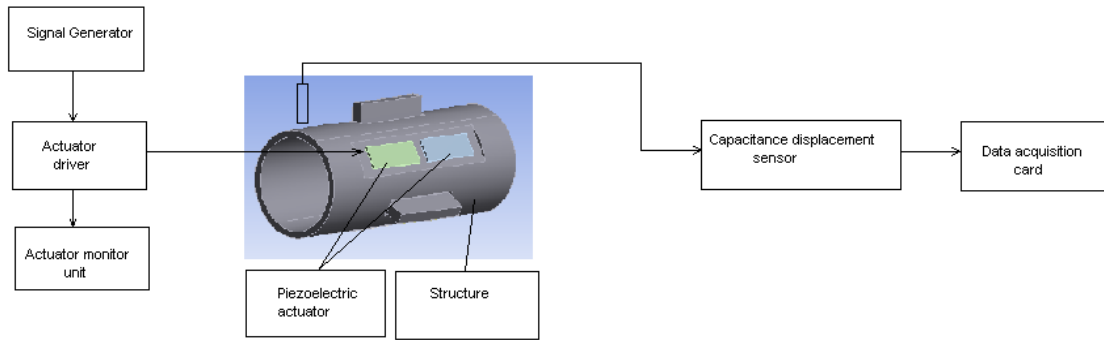


Fig.3. Schematics of the experimental set-up

Fig 3 shows a schematic diagram of the experimental set-up. The items of equipment used were:

1. A signal generator – 0 to 15 V peak-to-peak and 0 to 100 kHz (S J Electronics)
2. An actuator driver – ENP-1-1U (Echo Electronics)
3. An actuator driver monitor – ENP-50U (Echo Electronics)
4. A capacitance displacement sensor and a gauging module – MicroSense 6810; measurement bandwidth up to 100 kHz; measurement ranges from 20  $\mu\text{m}$  to 2 mm; resolution 0.25 nm rms at 5 kHz over 50  $\mu\text{m}$  measurement range (Ixthus)
5. A data acquisition card – PXI 6110 (National Instruments)

The signal generator created a sinusoidal wave which was amplified by the actuator driver and shaped by the actuator monitor to provide an excitation signal, with a 75V DC offset and a 75V peak-to-zero AC sinusoid. This excitation signal was used to drive the single layer piezoelectric actuators. The vibration response of the structure caused by the actuators was measured by the capacitance displacement sensor, whose output was sampled into a PC via the data acquisition card controlled by a LabVIEW program.

### 3.3 Modal analysis

Modal analysis can determine the theoretical vibration characteristics, in terms of natural frequencies and mode shapes, of a structure or a machine component. The natural frequencies and the mode shapes are important parameters in the design of a structure for dynamic loading conditions. It is believed that certain mode shapes enhance the effectiveness of the squeeze air film in journal bearings. These mode shapes have geometry that maximizes the amplitude ratio  $\varepsilon$  and minimizes the end leakage.



## Appendices

From the FEA modal modelling, two candidate mode shapes were identified to have the desired geometry, namely the 13<sup>th</sup> and the 23<sup>th</sup> modes at the respective natural frequencies of 16.368 kHz and 25.637 kHz. The mode shapes are shown in Fig 4 where the red end of the colour spectrum denotes greater deformation. It is observed that:

1. Both modes produce flexing of the shell on the sleeve between pairs of fins which remain in the same angular orientation during the vibration; both mode shapes are triangular.
2. At mode 13, the outer edges of the round sleeve do not appear to deform much while the middle section deforms noticeably.
3. At mode 23, the outer edges of the round sleeve deform noticeably while the middle section deforms not as much.

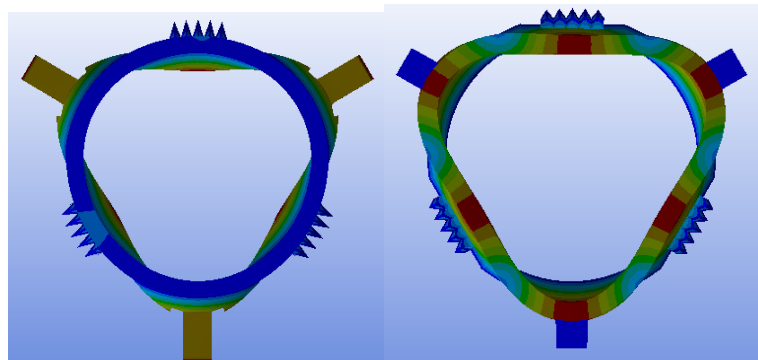


Fig. 4. a) Left - mode shape 13 (16.368 kHz); b) right - mode shape 23 (25.637 kHz)

To create these mode shapes all six piezoelectric actuators need to be driven in synchronisation at the natural frequency of the mode shape.

## 3.4 Static and dynamic analysis

### 3.4.1 Static analysis – computer modelling and simulation

The purpose of the static analysis was to determine the static deformation of the sleeve bearing when a 75 V DC voltage (0V on the bottom and 75V on the top surfaces of piezoelectric layer) was applied to the six single-layer piezoelectric actuators. Fig 5 shows the result of the analysis, from which a maximum radial deformation of 0.124  $\mu\text{m}$  is seen to occur in the middle section of the sleeve.

## Appendices

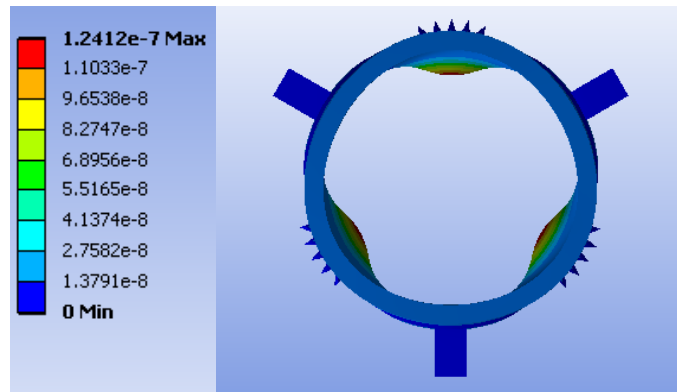


Fig. 5. Static deformation of the bearing when a 75V DC voltage was applied to the six actuators.

The above-mentioned analysis was repeated for other driving voltages and Fig 6 shows the relationship between the maximum static deformation and the voltage input, which is observed to be linear [9].

In the FEA modelling process, the force of the piezoelectric actuators as it varies with the driving voltage was accurately represented. This is unlike the approximations that most other researchers, for example [9], made by assuming that a maximum blocking force exists for all boundary conditions.

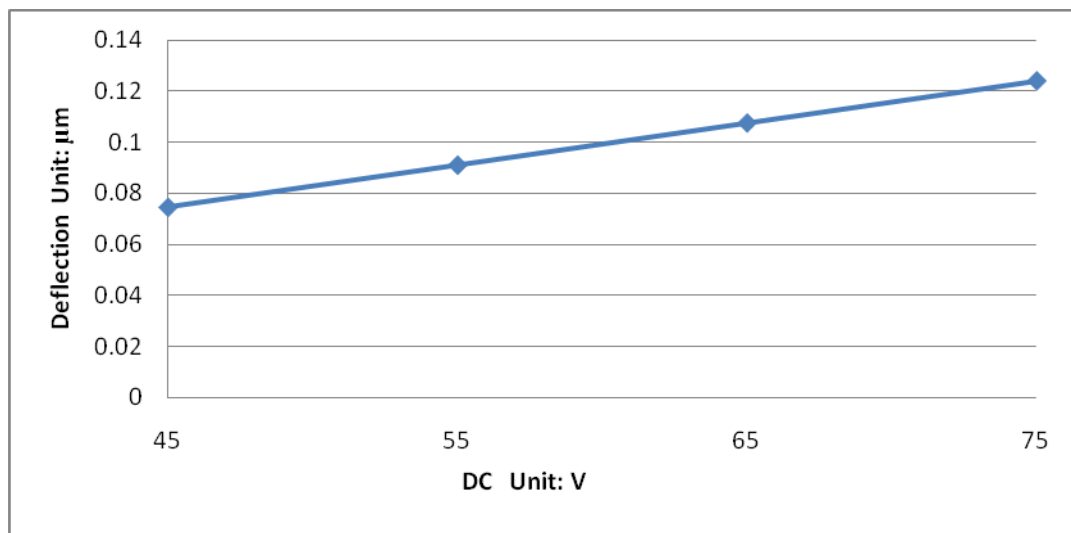


Fig. 6. Static deformation varies linearly with the applied DC voltage

### 3.4.2 Dynamic analysis

## Appendices

Dynamic analysis is used to determine the dynamic response of a structure under the dynamic excitation force. The dynamic excitation forces are from the expansion and the compression of the piezoelectric actuators when they are loaded with an AC voltage (75V) on top of a DC offset (75V). The excitation frequency should be coincident with one of the natural frequencies for either mode 13 or 23, as identified in Section 3.3, in order to achieve maximum dynamic response.

A dynamic experiment was performed to verify the bearing's natural frequencies and mode shapes at modes 13 and 23. The bearing was placed on a horizontal flat surface, as shown in Fig 7, and was supported at two positions near the bottom edge. These points of contact were chosen to coincide with the nodal points (of no displacement) of the bearing. The displacement of a fin was measured with the non-contacting capacitance displacement sensor, also shown in Fig 7.

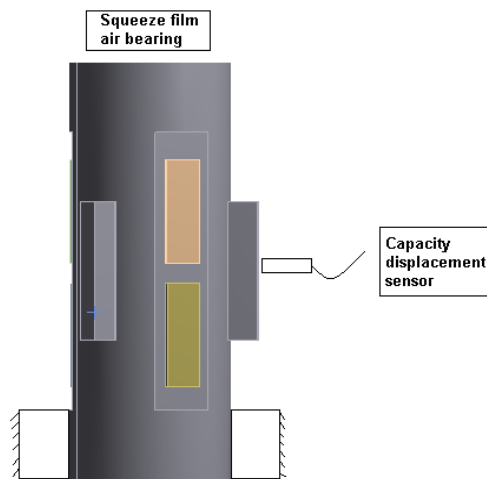
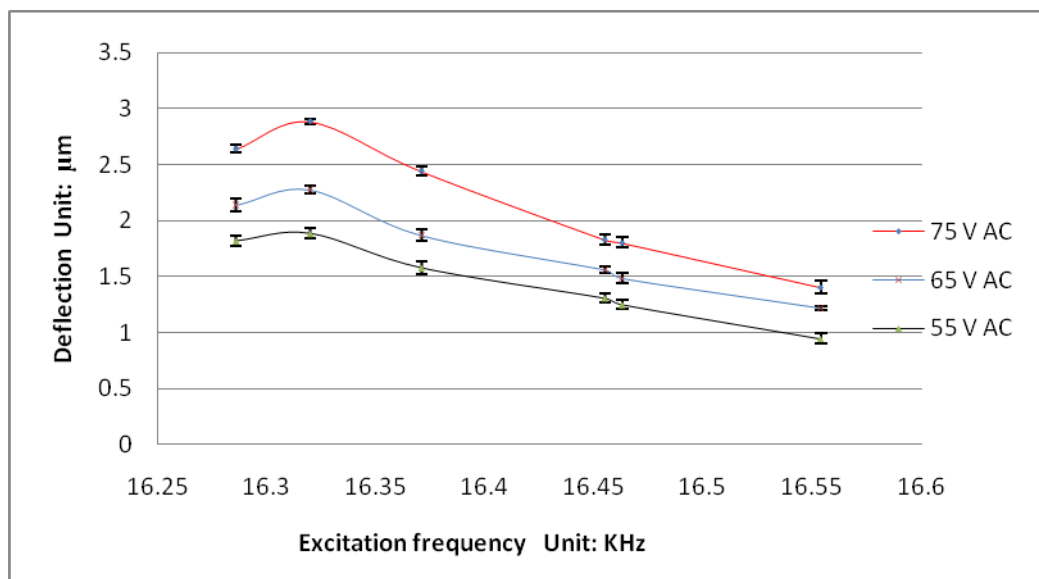


Fig. 7. Set-up for the dynamic response measurement



## Appendices

Fig. 8. Displacement amplitude on the fin of the bearing at Mode 13 versus the excitation frequency for the three levels of AC input; the error bars represent  $\pm 2$  standard errors

Fig. 8 shows the vibration amplitude of a point on the fin of the bearing as measured by the non-contacting displacement sensor. Measurements were made 10 times and it is the average that is shown on the graph; the corresponding error bar represents  $\pm 2$  standard errors. The narrow extent of the error bars suggests good measurement repeatability and high precision of the displacement amplitude obtained.

To correctly locate the natural frequency, the actuators were driven to excite the bearing over a range of frequencies from 16.28 kHz to 16.55 kHz at three different levels of AC voltage, namely 75V, 65V and 55V. The natural frequency for Mode 13, from Fig. 8, is 16.32 kHz at which the displacement amplitude on the fin is the greatest, for example, at 75V AC, the displacement is 2.88  $\mu\text{m}$ . Since the 75V AC gives the greatest displacement amplitude, which in turn produces the greatest mean pressure ratio, Fig. 1, this condition was going to be used for driving the bearing subsequently.

The experiment was repeated for Mode 23. The measurement point, in this case, was near the end of the sleeve where the deformation is observed to be significant, Fig 4b. The results are shown in Fig 9. It is noted that the natural frequency for Mode 23 is 25.31 kHz

Fig.9. Displacement amplitude on the fin of the bearing at Mode 23 versus the excitation frequency for the three levels of AC input.

From the FEA model, the theoretical displacement amplitude at the measurement point was also obtained for the different driving conditions. Fig 10 and Fig 11 show the comparison between the theoretical and experimental displacement amplitude at Mode 13 and Mode 23 respectively.

Fig. 10. Comparison between theoretical and experimental displacement amplitude at Mode 13 (DC = 75V and variable AC).

## Appendices

Fig. 11. Comparison between theoretical and experimental displacement amplitude at Mode 23 (DC = 75V and variable AC).

### 4. Load-carrying capacity experiments

In these experiments, the bearing was inserted into the round guide way, set up as a cantilever, as shown in Fig 12. A mass was hung onto a wire attached to a fin of the bearing and the bearing was excited at a number of frequencies near a particular mode.

Using the measurement from the displacement sensor, it is possible to calculate the instantaneous film thickness in the vertical plane of the bearing. The mean value was then computed from the instantaneous film thickness over a number of oscillations, typically a thousand. The procedure was then repeated for other masses.

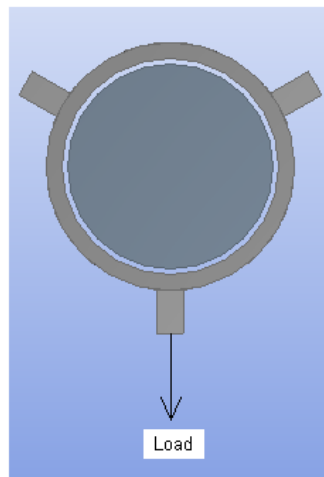


Fig. 12. Direction of loading by hanging masses

For Mode 13, Fig 13 shows the relationship between the mean film thickness and load at four different excitation frequencies at and around the natural frequency of Mode 13. At the natural frequency 16.32 kHz, the mean film thickness is greater than those at other frequencies below a load of about 2 N. However, when the load is increased beyond 2.5 N, its film thickness becomes about the same as those at other frequencies.

## **Appendices**

An explanation could be that with increasing load through adding mass, the natural frequency of the bearing/mass system shifts away from its original value and so the bearing is no longer being excited at its true natural frequency.

Fig 14 shows the relationship between the mean film thickness and load at four different excitation frequencies at and around the natural frequency of Mode 23. At the natural frequency of 25.21 kHz, the mean film thickness is also greater in the range of loads experimented.

Fig. 13. Mean film thickness of bearing versus load at four excitation frequencies around Mode 13

Fig. 14. Mean film thickness of bearing versus load at four excitation frequencies around Mode 23

When the mean film thickness at Mode 13 and Mode 23 are placed side by side, the difference in values is striking, showing that Mode 13 is a far superior mode in terms of load carrying capacity. The comparison is made in Fig 15 where the bearing was excited at the natural frequency of Mode 13 and Mode 23.

Fig. 15. Comparison between Mode 13 and Mode 23 in the load-carrying capacity.

Because of the effect of the added mass on the natural frequency of the bearing, if the excitation frequency was to remain a constant, then the bearing might not be always excited in the particular mode at the exact natural frequency. However, if the excitation frequency was changed to make sure that it was in tune with the natural frequency, the mean film thickness might turn out to be greater. Fig 16 compares two sets of results obtained, one with frequency adjustment and the other without.

## Appendices

Fig.16. Effect of mass loading on the natural frequency of the bearing, affecting the mean film thickness and hence the load carrying capacity.

### 5. Discussion

The model of an air film between two flat plates using the ideal gas law assuming adiabatic process proves theoretically the existence of a mean positive pressure and that this pressure increases as the amplitude ratio, Fig 1. It does not, however, attempt to model the pressure leakage on the edges the squeeze film air bearing. Often, it is argued that when the plates oscillate at a very high frequency, the leakage effect can be ignored and the adiabatic process holds true.

On the issue of the end leakage, driving the bearing at its natural frequency particularly at higher modes is beneficial because the natural frequency tends to be high. The design described in the paper was operated at Mode 13 and Mode 23 at the natural frequencies of 16.368 kHz and 25.637 kHz respectively. This compares favourably with the designs by Stolarski [9] and by Yoshimoto [7], both driving their designs at a frequency lower than or at the fundamental frequency.

On the issue of the mean pressure, according to Fig 1 higher mean pressure is achieved by higher amplitude ratio, which means that the structure must be such designed that the bearing surface can have large displacement. The proposed design allows this to happen with relative ease.

Between Mode 13 and Mode 23, Mode 13 has superior performance. This is because of its lower end-leakage due to the deflection geometry: both ends of the sleeve hardly deform while the shell in the middle section of the sleeve under the actuators are made

## Appendices

to flex thus creating a squeeze film. The ring of stagnant air film at both ends of the squeeze film minimises the leakage effect.

In the FEA modelling of the bearing sleeve, the piezoelectric actuators are accurately represented as a unit that expands and contracts with the driving voltage. In addition, the interaction with sleeve as the actuator moves is also accounted for by including the material properties of the two parts. Consequently the analysis is more accurate.

The static analysis shows the linear relationship between the input DC voltage and the deformation on the bearing. The same result was also obtained by Stolarski [9].

Given the same driving condition, the dynamic response is much bigger than the static response. In particular, when driven at the Mode 13 natural frequency the maximum displacement at the fin is roughly  $3\ \mu\text{m}$ . However, when excitation frequency drifts from the natural frequency, the amplitude falls, Fig 8. The same conclusion can be drawn for Mode 23. The similar result was also obtained by Yoshimoto [10], who observed vibration amplitudes of about  $1.5\ \mu\text{m}$  at the excitation frequency of 23.7 KHz and at 70V AC.

## 6. Conclusion

The advantage of a squeeze-film air bearing system is its compactness because it does not require an externally pressurized air supply system. The advantage of the tubular squeeze-film air bearing, as reported in this paper, is its simple design, not involving any elastic hinges, which can be difficult to manufacture.

The findings from this research are summarized as follows:

1. The theory developed from using the ideal gas law shows the existence of a positive pressure in the tubular squeeze-film air bearing that causes levitation.
2. The positive pressure at any amplitude ratio can be estimated using the approximate formula, Eq.(12), with an error of less than about 1.3% up to the amplitude ratio of 0.4.
3. Two normal modes, at the 13<sup>th</sup> and 23<sup>rd</sup>, of the bearing were identified to have the desired geometry of the modal shape, namely that of a triangle. The corresponding theoretical natural frequencies were found to be 16.37 KHz and 25.64 KHz, a result confirmed also by experiments.
4. From the FEA analysis, the maximum radial deformation of the bearing when driven at 75 V DC was observed to be  $0.124\ \mu\text{m}$ .
5. When the bearing was driven at 75V AC with 75V DC offset, the displacement response was  $2.88\ \mu\text{m}$  (Fig. 8) and  $1.98\ \mu\text{m}$  (Fig. 9) for modes 13 and 23 respectively. The measurements were highly repeatable as is evident from the small extent of the error bars in Fig 8.



## Appendices

6. The load-carrying experiments show that when driven at the natural frequency in either mode 13 or 23, the squeeze-air film was the thickest. However, comparing between the two modes, mode 13 has superior levitation performance than mode 23 (Fig. 15) because the former has a modal shape (Fig. 4a) that reduces end-leakage of the squeeze-air film.

## Reference

- [1] Stolarski, T.A. and Chai, W. (2006) 'Load-carrying capacity generation in squeeze film action', *International Journal of Mechanical Sciences*, 48 (3) PP.736-741.
- [2] Salbu, E. (1964) 'Compressible squeeze films and squeeze bearings', *Journal of Basic Engineering*, 86, PP.355-366.
- [3] C. L. Emmerich, "Piezoelectric oscillating bearing," *US patent No.3351393*, no. 3351393, November 1967.
- [4] L. F. Warnock Jr., "Dynamic gas film supported inertial instrument," *US patent No. 3339421*, no. 3339421, September 1967.
- [5] N. Scranton, Robert A. (South Salem, "Planar and cylindrical oscillating pneumatodynamic bearings," *US patent No. 4666315*, no. 4666315, May 1987.
- [6] T. B. R. Farron, John R., "Squeeze film bearings," *US patent No.3471205*, no. 3471205, October 1969.
- [7] Yoshimoto, S., Anno, Y., Sato, Y and Hamanaka, K. (1995) 'Floating characteristics of squeeze-film gas bearing with elastic hinges for linear motion guide', *International Journal of JSME*, 60(11) PP. 2109-2115.
- [8] Stolarski, T.A. and Chai, W. (2006) 'Self-levitation sliding air contact', *International Journal of Mechanical Sciences*, 48 (1) PP.601-620.
- [9] Stolarski, T.A. and Woolliscroft, S.P. (2007) 'Performance of a self-lifting linear air contact', *Journal of Mechanical Engineering Science*, 221, PP.1103-1115.
- [10] Yoshimoto, S., Kobayashi, H. and Miyatake, M. (2006) 'Floating characteristics of a squeeze –film bearing for a linear motion guide using ultrasonic vibration', *Journal of Tribology International*, 40 (5) PP.503-511.

## Appendices

### Study of design parameters for squeeze film air journal bearing – excitation frequency and amplitude

Chao Wang and Y H Joe Au\*

Advanced Manufacturing and Enterprise Engineering, School of Engineering and Design, Brunel University, UK

\* Corresponding author: [Joe.Au@brunel.ac.uk](mailto:Joe.Au@brunel.ac.uk)

#### Abstract

The paper presents a design of squeeze film air journal bearing based on the design rules derived from CFX and FEA simulation study of an air film in between two flat plates, one of which was driven in a sinusoidal manner. The rules are that the oscillation frequency should be at least 15 kHz and that the oscillation amplitude be as large as possible to ensure a greater film thickness and to allow the bearing to reach its stable equilibrium quickly. The proposed journal bearing is made from AL2024-T3, of 20.02 mm outer diameter, 600 mm length and 2 mm thickness. Three 20-mm long fins are on the outer surface of the bearing tube and are spaced 120° apart; three longitudinal flats are milled equi-spaced between the fins and two piezoelectric actuators are mounted lengthwise on each flat. Such a design produces a modal shape on the bearing tube which resembles a triangle. When excited in this mode at the frequency of 16.4 kHz, and a voltage of 75V AC with 75V DC offset acting on the piezoelectric actuators, the air gap underneath of the bearing tube behaves as a squeeze air film with a response amplitude of 3.22 μm. The three design rules were validated by experiments.

**Keywords:** *Single layer piezoelectric actuator, design of squeeze film air journal bearing, mode shape, natural frequency.*

#### 1. Introduction

Precision engineering dictates that bearings used in machine tools must be capable of producing high precision motion with low friction and wear and generating very little heat in an oil-free condition [1]. Whilst aerostatic and aero-dynamic bearings can meet these requirements, they do come with bulky ancillary equipment, such as air

## Appendices

compressors and hoses, and hence not very portable. A search for better bearings was an activity that has exercised the minds of many researchers.

To study the bearing behaviour of a thin air film between two surfaces, the Reynolds equation is used. Stolarski [1] identified three mechanisms from the equation that would show a pressure-generating phenomenon, which gives the bearing its load-carrying capability. The first refers to the 'physical wedge' as is found in hydrodynamic bearings where the fluid flows through a wedge; the second requires the two surfaces to contract or expand in-plane in order to create a variable velocity on the bearing surfaces; the third requires that the two bearing surfaces move normal to each other with an oscillating velocity and is known as the 'squeeze film' effect. Stolarski [1] asserted that the pressure generated by the hydrodynamic and squeeze film effects is of a similar order of magnitude and hence the justification for exploring the latter in the design of a new type of bearing. Squeeze film bearings have the significant advantage due to the fact that they do not require air compressors and connecting hoses; the equipment needed for generating the squeeze film action is far smaller and it can be miniaturised to the extent that it becomes a single package with the bearing.

In the design investigated by Stolarski [2] and Yashimoto [3], the squeeze film air bearings, made from Aluminium, used elastic hinges to ensure easy flexing of the bearing plates when driven at and around the fundamental frequency of a few KHz by stack piezoelectric actuators. The presence of the elastic hinges helps increase the dynamic response resulting in a thicker air film but because of the intricate machining required, the manufacturing cost increased. In addition, the driving frequency, being of a few kHz, is within the sensitive audible range, which can cause annoyance. In 2006, Yashimoto [4 and 5] proposed another design of bearing that was driven at ultrasonic frequency with single-layer piezoelectric actuators to avoid problem of audible noise during operation. The use of the single-layer piezoelectric actuators can reduce the power consumed.

The purposes of work reported in this paper are:

1. To develop a model that affirms the existence of positive pressure developed in a squeeze-film air bearing;
2. To develop a finite-element model for a single layer piezoelectric actuator that uses realistic boundary conditions;
3. To design a journal squeeze film air bearing using the design rules derived from the modelling of the squeeze air film.

## Appendices

### 2. Theory of Squeeze Air Film for flat plates

#### 2.1 Pressure profile

Consider an air film that is squeezed between two flat plates having relative sinusoidal motion of frequency  $\omega$  at amplitude  $e$ , in the direction of the film thickness, as shown in Fig. 1(a). The pressure at a point in the air film is governed by the Reynolds equation,

$$(1)$$

Equation (1) is given in a non-dimensional form [6].  $X$ ,  $Y$  and  $Z$  are the coordinates of a point in the air film expressed as a fraction of its length, width and thickness respectively;  $p$  is the ratio of the instantaneous pressure to the initial pressure;  $H$  the ratio of the instantaneous to the initial film thickness;  $\sigma$  the squeeze number; and  $\tau$  the non-dimensional time obtained as the product of the angular frequency of oscillation  $\omega$  and time  $t$ .

The squeeze number is defined as where  $\mu$  is the dynamic viscosity and  $L$  the length of the air film.

The instantaneous film thickness  $h = h_0 + e \sin(\tau)$  and hence the instantaneous film thickness ratio, being  $h/h_0$ , is given by.

#### 2.2 Equation of motion of flat plates

If now the bottom plate is given a sinusoidal motion normal to its surface while the top plate is supported by the air film, the top plate will be caused to move in a manner governed by the Newton's Second Law, namely

$$m \frac{dv}{dt} = F_L - mg \quad (2)$$

In Eq. (2),  $m$  and  $v$  are the respective mass and velocity of the top plate,  $F_L$  is the levitation force exerted by the air film and  $mg$  is the weight force of the top plate.

Equation (1) computes the pressure profile of the air film between the two plates. From the pressure profile is obtained the force of levitation  $F_L$ . The corresponding value of velocity  $v$  can then be found from Eq. (2), from which the displacement of the top plate is calculated by integration. This displacement, together with the sinusoidal motion of the bottom plate, changes the air film thickness  $h$  and hence the thickness ratio  $H$ . This, in turn changes the pressure profile as computed from Eq. (1). By repeating the afore-

## Appendices

mentioned calculation procedure over time, it is possible to determine the corresponding displacement response of the top plate.

### 2.3 Simple model of oscillating plates and boundary conditions

The simple model considered is the one as shown in Fig. 1(a), with dimensions of the plates and the initial air film thickness as indicated. The bottom plate was given a sinusoidal motion whilst the top plate, of mass  $6.24 \times 10^{-4}$  kg, responded also with a sinusoidal motion. The air film, as shown in Fig. 1(b), is assumed to have no leakage around the three sides of its edges, namely the left, front and back sides; but there is leakage from the right side. Such assumptions are justified by the following considerations:

1. The left side is on the plane of symmetry of the complete air film. In other words, what is shown in Fig. 1(b) is only the right half and hence there is no sideways flow of air across the symmetry plane.
2. The front and back sides do not have air flow across them because of the symmetrical arrangement of the three pairs of bearing plates in the proposed journal bearing design – see Fig. 13 – and the synchronised driving of them.
3. The right side, however, is exposed to the atmosphere and leakage is expected.

The computation was performed with CFX [7] instead of home-built programming codes [2] to save time.

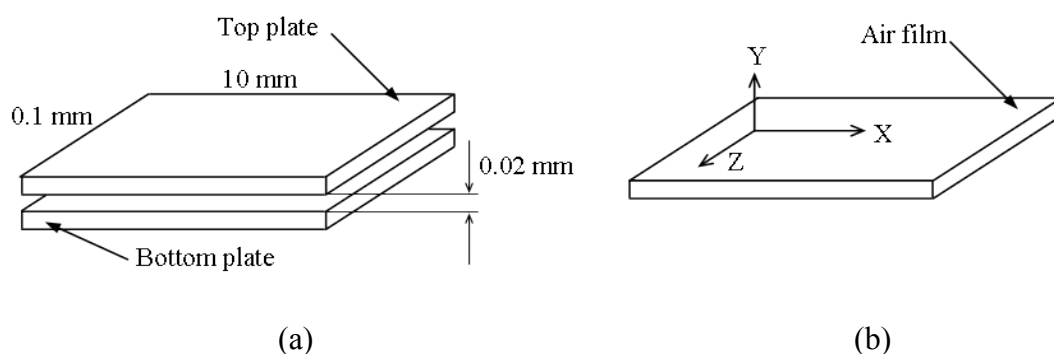


Figure 1 – (a) Dimensions of the plates and the air film thickness; and (b) the air film in the rectangular coordinate system used.

### 2.4 Calculation results

## Appendices

Figure 2 shows the relationship between the air film thickness and the oscillation frequency of the bottom plate. It is observed that the mean air film thickness at first increases with oscillation frequency but it reaches a constant value beyond around 15 kHz.

Figure 2 - Mean air film thicknesses versus excitation frequency of bottom plate

Figure 3 shows the relationship between the mean air film thickness and the oscillation amplitude with the oscillation frequency of the bottom plate kept at 10 KHz. It is noted that as the oscillation amplitude increases the mean air film thickness increases in an exponential fashion.

Figure 3 - Mean film thickness versus oscillation amplitude of bottom plate (oscillation frequency at 10 kHz)

Figure 4 shows the steady-state pressure distribution of the air film over a period of oscillation along the x-axis (Fig. 2(b)) from the left edge ( $x = 0$  mm) to the right edge ( $x = 10$  mm) where the air film interfaces with the atmosphere whose pressure ratio  $P$  is 1. There are 9 pressure profile curves shown and they represent the pressure at different time instants in the cycle of oscillation such that the time interval between successive points, for example P1 and P2, is constant, being  $12.5 \mu\text{s}$ . It is noted that the mean pressure ratio in the film at any distance is above unity; thus an up-thrust is created to levitate the top plate. The same conclusion was drawn by the authors in their paper using the theory of ideal gas law [8].

Figure 4 – Steady-state pressure distribution in the x-direction (Fig. 2(b)) of air film in a period of oscillation of bottom plate in frequency of 10 KHz

Figure 5 shows the transition to the final equilibrium position of the top plate from the initial film thickness of  $20 \mu\text{m}$  at the two oscillation frequencies of the bottom plate, namely 1 kHz and 10 kHz. The observation from Fig. 3 that the mean film thickness increases with oscillation frequency below 15 kHz is seen also to hold true here. In addition, at higher oscillation frequency of the bottom plate the response of the top plate shows greater stability, with no residual oscillation, achieved at around 0.037s.

## Appendices

Figure 5 - Transition to equilibrium position of top plate for two excitation frequencies of bottom plate at 1 kHz and 10 kHz

### 3. Design of the proposed squeeze film air bearing

Figures 2, 3 and 5 highlight some rules for the design of squeeze air film bearings. Specifically:

1. According to Fig.2, to ensure a greater film thickness, the oscillation frequency imposed on the air film should be high, preferably above 15 kHz because the end leakage becomes insignificant.
2. Figure 3 points to the fact that the greater the oscillation amplitude of the air film, the greater is its mean thickness.
3. Figure 5 suggests that with a greater oscillation frequency of the air film, the bearing reaches its stable equilibrium position much more quickly.

Using these three design rules, a design of the squeeze film air journal bearing [9 and 10], as shown in Fig. 13, is proposed. This bearing is in the shape of a hollow round tube with three longitudinal flats milled equi-spaced around the circumference. Two piezoelectric actuators are mounted length-wise on each flat and they are driven simultaneously by an AC voltage with a DC offset. The material and geometry of the tube are such chosen that at least one modal frequency exists which is above 15 kHz and has a desirable modal shape.

With such a design, the x-axis (Fig. 1(b)) of the bearing plate is aligned with the longitudinal axis of the bearing tube, the y-axis with the radial axis, and the z-axis with the tangential axis to the circumference. Since the film thickness is very small in relation to the width or length of the bearing, the bearing plate can be assumed to be

## Appendices

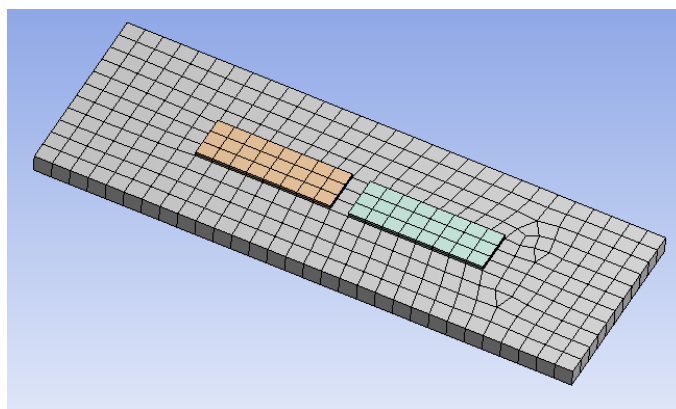
flat. Leakage is only significant in the longitudinal directions (both positive and negative directions of the x-axis) but otherwise virtually non-existent in the radial (y-axis) or tangential (z-axis) direction. To first approximation the model presented in Section 2 holds.

The modal shape of choice should be one that produces purely a radial deformation of the tube wall without the tube experiencing any torsion. Therefore the only possible modal shape for the design as shown in Fig. 13 has to be a triangle similar to Fig. 14. To encourage the tube to distort into a triangle, three external fins are added, which in effect partitions the tube into three  $120^\circ$  sectors. The fins do not cover the whole length of the tube but are foreshortened. This is to make sure that both ends of the tube do not deform or at least not as much as the inner sections of the tube; consequently the end leakage in the longitudinal direction can be further minimised.

At the desired mode as described above, the three fins can be imagined to have only radial motion and the tube wall between any consecutive pair of fins flexes about the fins as its end supports. Its static and dynamic behaviour is modelled in the next section.

### 3.1 Modal analysis

Figure 6 shows a flat plate with a width of 21 mm (equal to the circumferential width of the tube between two consecutive fins), length of 60 mm (the length of the tube) and thickness of 2 mm (the thickness of the tube). The plate has a built-in support along the two 60-mm edges. Two single-layer piezoelectric actuators are mounted on the top surface of the plate as a driving unit; the dimensions of the single-layer piezoelectric actuator are 15 mm x 5 mm x 0.5 mm.





## Appendices

Figure 6 - Model of rectangular plate with two single-layer piezoelectric actuators mounted on top surface

Using ANSYS Workbench, a modal analysis was performed on the flat rectangular plate. The first four natural frequencies and the corresponding mode shapes are as shown in Fig. 7. Mode shape 1, obtained by exciting the two single-layer piezoelectric actuators at 23606 Hz [4], gives the most desirable mode shape feature. This is because the maximum deformation region occurs right at the centre of the plate, resulting in minimum leakage at the two opposite 21-mm edges. In addition, the excitation frequency, being higher than 15 kHz, is also conducive to reducing end leakage according to Fig.2.

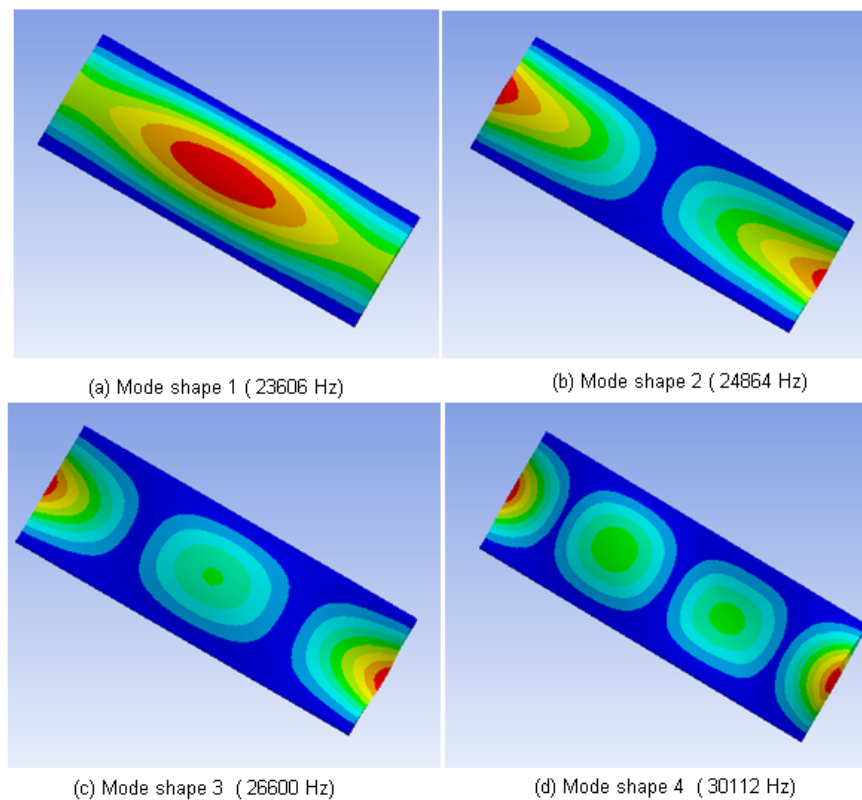


Figure 7 - Mode shapes and natural frequencies of rectangular plate; colour red indicates maximum deformation and colour blue, no deformation

### 3.2 Static analysis

When a DC voltage is applied to two single-layer piezoelectric actuators mounted on the rectangular plate, a static deformation results. A larger deformation is preferred to a

## Appendices

smaller one because of the thicker squeeze air film that it creates. Evidently the deformation is a function of the plate thickness.

Figure 8 shows the static deformation that appears on the rectangular plate when a 150 V DC was applied to the piezoelectric actuators with 0 V and 150 V on the respective bottom and top surfaces. A maximum deformation of  $0.21757 \mu\text{m}$  is seen to occur at two regions, as shown in red in Fig. 8, symmetrically disposed from the centre line parallel to the short sides of the plate.

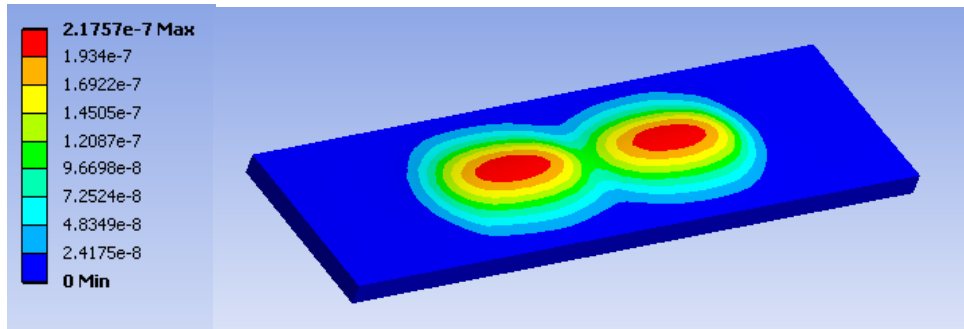


Figure 8 - Static deformation of rectangular plate when a 150V DC was applied to the two actuators

The relationship between the thickness of the plate and the deformation is shown in the Fig. 9. It is observed that the plate deflection increases disproportionately as the plate thickness decreases. The static deformation of a 1-mm thick plate is about 3 times as big as that of 2-mm thickness; however, as thickness increases from 3 to 4 mm, the static deformation hardly changes, being around  $0.1 \mu\text{m}$ .

Figure 9 - Relationship between maximum static deformation and plate thickness

### 3.3 Dynamic analysis

Dynamic analysis is used to determine the dynamic response of a structure under a sinusoidal excitation force. The excitation force in this case is created from the alternate expansion and compression of the piezoelectric actuators when they are driven by an AC voltage at 75V on top of a DC offset also at 75V. To take advantage of the mechanical gain at resonance, the excitation frequency was chosen to coincide with the Mode 1 frequency of 23606 Hz, as identified in Section 3.1, in order to achieve maximum dynamic response, thus giving a better floating performance as suggested by Fig. 3.

## Appendices

Figure 10 shows the dynamic response of the rectangular plate when excited at 23606 Hz with the AC 75 V and the DC offset 75V as occurring at the central region (shown in red) where the amplitude is  $1.936 \mu\text{m}$  [4]. As expected the response of the plate is of the same shape as mode shape 1. By varying the beam thickness from 1 to 4mm, the maximum amplitude of response is seen to decrease in an exponential manner as shown in Fig.11, similar to that observed in the static analysis (Fig.9). A comparison between the two analyses is presented in Fig.12: the difference in magnitude is striking; for a 2-mm thick plate, the dynamic deformation is about 9 times as large as the static deformation.

If maximum dynamic deformation was the only design criterion, then the thinner the plate the better. But the modal frequency drops as the plate thick decreases. Thus, for example, the 1-mm thick plate has a mode 1 frequency of 11.835 kHz, which is well below the threshold frequency of 15 kHz, thus creating substantial end leakage (Fig. 2) and a long transition time to equilibrium (Fig. 5); furthermore the resulting strain in the driving piezoelectric actuators may be too high to cause them to fracture.

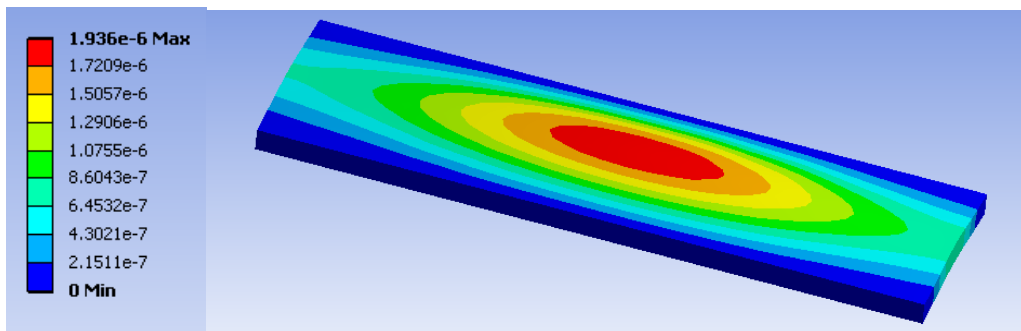


Figure 10 - Dynamic response of plate when driven at the fundamental natural frequency of 23606 Hz.

Figure 11 - Dynamic deformation versus plate thickness when excited at natural frequency of plate

## Appendices

Figure 12 - Comparison between static and dynamic plate deformations

### 3.4 Experimental results for the designed Squeeze film air journal bearing

Based on the results of the static and dynamic analyses and of the three design rules formulated in Section 3, the final design is created, which is as shown in Fig.13. The journal bearing is made from the material AL2024-T3, and has a diameter of 20.02 mm, a length of 60mm and a thickness of 2mm. Three fins, each 20 mm long, are positioned 120° apart on the outer circumference of the bearing tube; they are designed to provide a desirable modal shape of a triangular cross-section when excited by the actuators. This enables the air gap underneath the actuators to behave effectively as a squeeze air film. The round bar has a diameter of 19.99 mm and the surface was produced by cylindrical grinding.

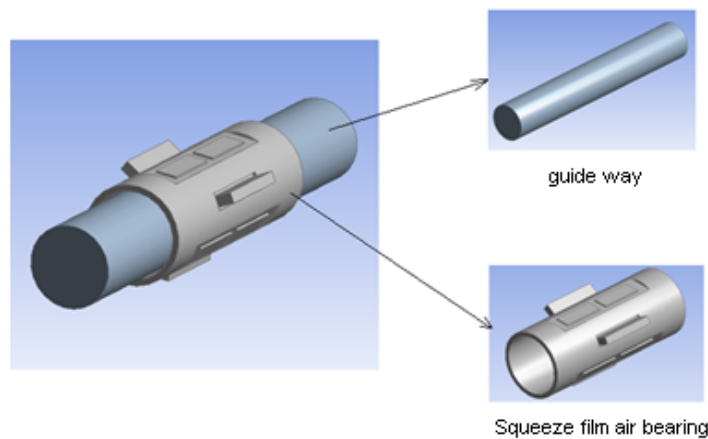


Figure 13 - Squeeze film air journal bearing with six single-layer piezoelectric actuators mounted on three milled flat surfaces, shown with the guide way in the shape of a round bar.

From the FEA modal modelling, the Mode 13 was identified to have the desired deformed geometry of a triangle and it has the modal frequency of 16.37 kHz, which is above the 15 kHz threshold. The corresponding mode shape is as shown in Fig. 14 where the red end of the colour spectrum denotes greater deformation. It can be observed that the outer edges of the round sleeve do not appear to deform much while the middle section deforms noticeably.

## Appendices

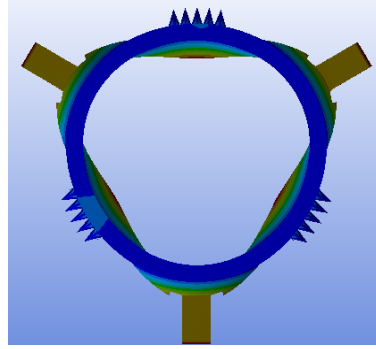


Figure 14 - Mode shape at Mode 13 of squeeze film air journal bearing

### 3.41. Experimental set up

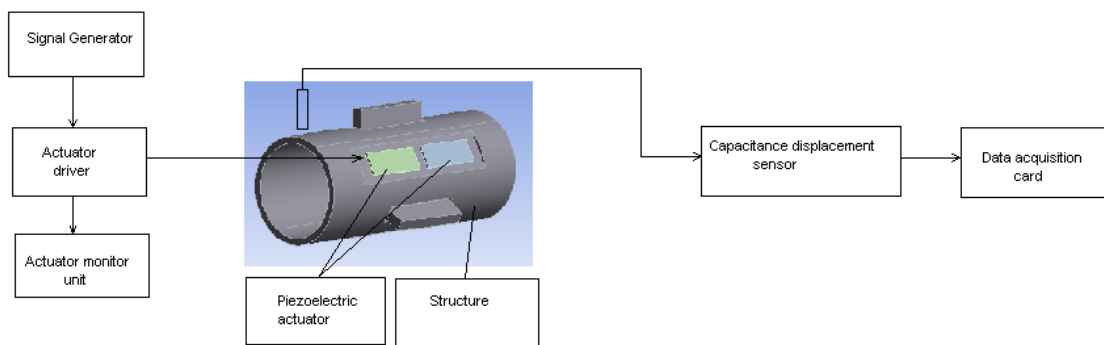


Figure 15 – Schematic diagram of the experimental set-up

Fig 15 shows the set up of equipment for the dynamic response experiment. The following items of equipment were used:

1. A signal generator – 0 to 5 V and 0 to 100 kHz (S J Electronics)
2. An actuator driver – ENP-1-1U (Echo Electronics)
3. An actuator driver monitor – ENP-50U (Echo Electronics)
4. A capacitance displacement sensor and a gauging module – MicroSense 5810; measurement bandwidth up to 100 kHz; measurement ranges  $\pm 100\mu\text{m}$ ; resolution  $\pm 49.69\text{ nm}$  (Ixthus)
5. A data acquisition card – PXI 6110 (National Instruments)

The signal generator created a sinusoidal wave which was amplified by the actuator driver and shaped by the actuator monitor to provide an excitation signal, with a 75V DC offset and a 75V peak-to-zero AC sinusoid. This excitation signal was used to drive the single layer piezoelectric actuators. The vibration response of the structure caused by the actuators was measured by the capacitance displacement sensor, whose

## **Appendices**

output was sampled into a PC via the data acquisition card driven by a LabVIEW program.

### **3.4.2 Oscillation amplitude on vibrating shell of journal bearing and excitation frequency**

The maximum amplitude of oscillation at the vibrating shell of the bearing was measured within a range of frequencies, 16.28 kHz to 16.55 kHz, in the vicinity of the predicted Mode 13 frequency of 16.37 Hz. The results are as shown in Figure 16. The measurements were made 10 times and it is the average that is shown on the graph; the corresponding error bar represents  $\pm 2$  standard errors. The narrow extent of the error bars suggests good measurement repeatability and high precision of the displacement amplitude obtained. From Figure 16, it is observed that the natural frequency for Mode 13 was 16.32 kHz; and that the amplitude of oscillation was 2.88  $\mu\text{m}$ , compared to the simulated result of 3.22 $\mu\text{m}$  from ANSYS Workbench modelling.

Figure 16 - Displacement amplitude at the centre of the bearing shell at Mode 13 versus excitation frequency at 75 V AC input with 75V DC coupling; error bars represent  $\pm 2$  standard errors

### **3.4.3 Mean film thickness and oscillation amplitude**

According to the second design rule the mean squeeze film thickness increases with the amplitude of oscillation of the shell. Experiments were conducted to validate this assertion. Figure 17 shows the relationship between the mean film thickness and the oscillation amplitude at three load levels. The loading was implemented by attaching a weight to the journal bearing and three loads were studied, namely 1.14 N, 1.64 N and 2.14 N. These loads were hung on the bottom fin – see Figure 14 – such that there was a squeeze air film at the top and another pair symmetrically disposed at 120° on either side. In Figure 17, it can be seen that the minimum film thickness increases in an exponential fashion with increasing oscillation amplitude for all three different loads.

## Appendices

Figure 17 – Mean film thickness versus oscillation amplitude at three load levels.

### 3.4.4 Comparison between experimental and theoretical mean squeeze film thicknesses

With the journal bearing loaded as described in Section 3.4.3 corresponding to the orientation of the three squeeze films as shown in Figure 14, an approximate simulation CFX model was formulated and analysed. Two simplifying assumptions were made:

1. As the surrounding sleeve is loaded, the squeeze film at the top has a thickness which is much smaller than that at the other two squeeze film situated towards the bottom (Figure 14), such that the levitation force created is solely due to the top squeeze film;
2. The top squeeze film is flat and there is no leakage when in operation; and
3. The upper plate of the top squeeze film translates bodily up and down with no deformation.

The CFX simulation modelled an air film which was 30mm long, 0.1 mm wide and 0.03  $\mu\text{m}$  thick using the same set of boundary conditions as that described in Section 2.3. Since the bearing shell of the top squeeze film did not oscillate as a rigid body but rather flexed itself at the Mode 13 natural frequency, the average amplitude of oscillation of 1.31 $\mu\text{m}$  was used in the simulation. This average was obtained by measuring the modal shape of the bearing shell at the top squeeze film with the bearing driven at the Mode 13 natural frequency of 16.32 kHz and then taking an arithmetical average from these measurements.

Figure 18 shows the results from the simulation as compared to those obtained from the experiment for different loadings. There is broad agreement between the two in terms of the trend and of the values of the mean film thickness, with better fit towards the higher loading. It is surmised that the better fit could be due to the fact that the first assumption becomes more correct as the loading increases; further work needs to be done in this area. The agreement between the theoretical and experimental results serves, in some way, to validate the simulation results in Section 2, from which the three design rules were derived.

Figure 18 – Comparison of theoretical and experimental for mean film thickness

## Appendices

### 4 Discussions

In this paper the flat rectangular plate was first studied in order to identify important design rules and parameters that would better inform subsequent design activity, leading to the design of a tubular bearing with fins. A comparison between the dynamic simulation results obtained from the flat plate and the curved shell is informative; Table 1 summarises the effort.

	<b>Flat Rectangular Plate</b> - 2 mm thick	<b>Tubular Bearing with Curved Shell</b> - 2 mm thick
<b>Natural frequency</b>	23606 Hz	16368 Hz
<b>Dynamic deformation</b>	1.99 $\mu\text{m}$	3.22 $\mu\text{m}$

Table 1 Comparison between flat plate and curved shell in respect of dynamic response

The flat plate is seen to have a higher natural frequency than the curved counterpart. This is due to two reasons: 1) the flat plate was subjected to a more severe end-fixing condition, namely built-in fixing along the full length, compared to the partial fixing via the foreshortened fins, which themselves are free to move radially, on the curved shell; 2) the curved shell has a milled flat for the actuators, which reduces the shell's stiffness in bending locally.

The foreshortened fins can be responsible for the larger dynamic response at 3.22  $\mu\text{m}$  compared to the 1.99  $\mu\text{m}$  on the severely edge-constrained plate.

### 5 Conclusions

Three design rules for squeeze air film bearings were produced and verified from the research:

1. To ensure a greater film thickness and to reduce end leakage, the oscillation frequency imposed on the air film should be high, preferably above 15 kHz (Figure 2).
2. The greater the oscillation amplitude of the air film, the greater is its mean thickness (Figure 3).
3. With a greater oscillation frequency of the air film, the bearing reaches its stable equilibrium position much more quickly (Figure 5).

Based on the design rules, a journal squeeze air film bearing was designed (Figures 13 and 14) and analysed. The bearing was designed to be driven at its 13<sup>th</sup> mode at the



## **Appendices**

frequency of 16.37 kHz at which the amplitude response was 3.22  $\mu\text{m}$  and the modal shape produced a squeezing action on the air film between the journal shell and the bearing shaft.

These three design rules were validated from experiments conducted on the journal squeeze air film bearing, as demonstrated in Figures 17 and 18.

## **Reference**

- [1] Stolarski, T.A. and Chai, W. (2006) ‘Load-carrying capacity generation in squeeze film action’, *International Journal of Mechanical Sciences*, 48 (3) PP.736-741.
- [2] Stolarski, T.A. and Woolliscroft, S.P. (2007) ‘Performance of a self-lifting linear air contact’, *Journal of Mechanical Engineering Science*, 221, PP.1103-1115.
- [3] Yoshimoto, S., Anno, Y., Sato, Y and Hamanaka, K.: Floating characteristics of squeeze-film gas bearing with elastic hinges for linear motion guide, *International Journal of JSME*, 60,2109-2115,1995.
- [4] Yoshimoto, S., Kobayashi, H. and Miyatake, M.: Floating characteristics of a squeeze –film bearing for a linear motion guide using ultrasonic vibration, *Journal of Tribology International*, 40,503-511, 2006
- [5] Ono, Y., Yoshimoto, S., and Miyatake, M.: Impulse-Load dynamics of squeeze film gas bearings for a linear motion guide, *Journal of Tribology*, 131,1-6, 2009
- [6] Stolarski, T.A.: Numerical modelling and experimental verification of compressible squeeze film pressure, *Journal of Tribology International*, 43,356-360, 2009
- [7] Stolarski, T.A. and Chai, W.: Self-levitation sliding air contact, *International Journal of Mechanical Sciences*, 48, 601-620, 2006.
- [8] Wang, C. And Au, Y. H. J.: Levitation Characteristics of a Squeeze Film Air Journal Bearing at its Normal Modes, *Journal of Advanced Manufacturing Technology* [submitted in Jan 2011].
- [9] Ha, D.N., Stolarski, T.A. and Yoshimoto, S.: An aerodynamic bearing with adjustable geometry and self-lifting capacity. Part 1: self-lift capacity by squeeze film, *International Journal of Engineering Tribology*, 219, 33-39, 2005.
- [10] Zhao, S. and Wallaschek, J.: Design and modelling of a novel squeeze film journal bearing, in: *Proceedings of the 2009 IEEE International Conference on Mechatronics and Automation*, Changchun, China, 9-12 August 2009, 1054-1059, 2009.

## Appendices